Particle Physics Probes from Cosmology

by

Anthony Fradette
B.Sc., McGill University, 2010
M.Sc., University of Victoria, 2012

A Dissertation Submitted in Partial Fulfillment of the
Requirements for the Degree of

DOCTOR OF PHILOSOPHY

in the Department of Physics and Astronomy

Particle Physics Probes from Cosmology

by

Anthony Fradette
B.Sc., McGill University, 2010
M.Sc., University of Victoria, 2012

Supervisory Committee

---

Dr. Maxim Pospelov, Supervisor
(Department of Physics and Astronomy)

---

Dr. Adam Ritz, Departmental Member
(Department of Physics and Astronomy)

---

Dr. Alexandre Brolo, Outside Member
(Department of Chemistry)

## ABSTRACT

In this dissertation, we explore the cosmological sensitivity of well-motivated extensions of the Standard Model (SM) of particles. We focus on two specific models, the vector portal and the Higgs portal, that can connect the SM to a dark sector of new hidden particles. We find that both portals have sensitivity in the ultra-weak coupling regime, where the relic abundance is set by the freeze-in mechanism. Provided that the mediators of the portal interactions decay into the SM, we derive the constraints on masses and couplings of such states from precision cosmology. As a primary source of constraints, we use Big Bang Nucleosynthesis (BBN), the Cosmic Microwave Background (CMB) and the diffuse X-ray background. For the Higgs portal scalar, we improve the relic abundance calculation in the literature and provide an estimate of thermal corrections to the freeze-in yield. We find that the cosmological bounds are relatively insensitive to improvements in the abundance accuracy, and a full finite-temperature calculation is not needed.

We also investigate the BBN constraints for hypothetical long-lived metastable scalars particles $S$ that can be produced at the Large Hadron Collider from decays of the Higgs boson. We find that for viable branching ratios $\mathrm{Br}(h \to SS)$, the early universe metastable abundance of $S$, regulated by its self-annihilation through the Higgs portal, is so large that the lifetime of $S$ is strongly constrained to $\tau_S < 0.1$ s to maintain the consistency of BBN predictions with observations. This provides a useful upper bound on the lifetimes of $S$ particles that a purposely-built detector, such as the one suggested in the MATHUSLA proposal, seek to discover.

We also investigate the viability and detectability of freeze-in self-interacting fermionic dark matter communicating with the SM via a vector portal. We focus on the parameter where the $\chi\bar{\chi} \to A'A'$ is negligible, as required by a variety of indirect detection constraints. We find that planned upgrades to the direct detection experiments will be able to probe the region of parameter space that can alleviate small scale structure problems of dark matter via self-interactions for a dark fine structure constant as small as $\alpha_d = 10^{-4}$. We forecast the sensitivity for Lux-ZEPLIN, XENONnT and PandaX-4T.

# Contents

# List of Tables

# List of Figures

# List of Abbreviations

| | |
|---|---|
| **BBN** | Big bang nucleosynthesis |
| **BE** | Bose-Einstein |
| **CDM** | Cold dark matter |
| **CMB** | Cosmic microwave background |
| **CP** | Charge-parity |
| **D** | Deuterium |
| **DD** | Direct detection |
| **DM** | Dark matter |
| **DS** | Dark sector |
| **EW** | Electroweak |
| **FD** | Fermi-Dirac |
| **H** | Hydrogen |
| **$^3$He** | Helium-3 |
| **$^4$He** | Helium-4 |
| **ΛCDM** | Standard cosmological model, cold dark matter with dark energy |
| **LHC** | Large hadron collider |
| **$^7$Li** | Lithium-7 |
| **MB** | Maxwell-Boltzmann |

| | |
|---|---|
| **n** | neutron |
| **NP** | New physics |
| **NWA** | Narrow-width approximation |
| **p** | proton |
| **QCD** | Quantum chromodynamics |
| **QED** | Quantum electrodynamics |
| **QSE** | Quasi-static equilibrium |
| **QSO** | Quasi-stellar object (quasar) |
| **R.H.S.** | Right-hand side |
| **SBBN** | Standard big bang nucleosynthesis |
| **SIDM** | Self-interacting dark matter |
| **SM** | Standard model |
| **T** | Temperature or tritium |
| **VDP** | Very dark photon |
| **vev** | vacuum expectation value |
| **WIMP** | Weakly interacting massive particle |

# ACKNOWLEDGEMENTS

Throughout the duration of my stay at the University of Victoria, numerous friends and colleagues have provided invaluable support, whether scientific or emotional, which helped me accomplish the work needed for my PhD. I am thankful for the guidance, patience and wisdom or my graduate advisor, Maxim Pospelov. My physics friends, Tony, Sam, Allison, Matthias, Alex and Patrick, have made sure I enjoyed my work and leisure time. My non-physics friends, Julia, Dom and Beth-Anne have greatly contributed to my amazing time in Victoria. My parents, Diane and Guy, have always supported my interests and goals and I would not have pursued physics this far without their never-ending encouragements. Finally, Cate has been by my side every day, listened to me, encouraged me and, most importantly, was there for me. Thank you all, it would have been much harder without you.

# DEDICATION

Pour Diane, Guy et Cate

# Chapter 1

# Introduction

Elementary particle physics is a mature scientific field; generations of scientists and philosophers have been trying to answer one simple question : *What is matter made of?* This rather basic question has lead to the initial discovery of the electron by J.J. Thomson in 1897 [1], followed by many breakthroughs in the last century that challenged our knowledge and perception of the world we live in.

Our current understanding of particles was established in the late '70s. The particles were classified by their properties with interactions described in the language of quantum field theory. This Standard Model (SM) of particle physics has proved to be an excellent tool to predict and describe experimental data. It reached an unprecedented level of experimental proof with the discovery of its last ingredient, the Higgs boson, at the Large Hadron Collider (LHC) in 2012 [2, 3].

Despite its undeniable success, the SM is known to be incomplete and new physics must be invoked to explain some phenomena. For instance, we know that the observation of neutrino oscillations imply a massive neutrino structure [4] that is not present in the SM. There are also a few high precision measurements that are incompatible with the SM theoretical predictions, notably the muon anomalous magnetic moment [5] and the proton charge radius determined from muonic hydrogen [6]. These examples of experimental results might be suggesting that additional ingredients with subdominant contributions to the SM are needed to provide small corrections to account for these discrepancies.

The situation is much more dramatic if we look in the sky, beyond our small planet. If the SM answers the original question *What is matter made of?*, it should provide a description of *all* matter, across the universe, from its infancy to current times. Yet, the existence of our universe and the breakthroughs of precision cosmology during the

last two decades tell us there must be more; Dark Matter (DM) contributes 25.8% of the total energy density and a dark energy filling 69.2% of the current energy density of the universe [7]. The existence of our universe also requires an asymmetry of matter over antimatter, otherwise the entirety of matter would have annihilated into radiation. Baryogenesis, the mechanism that generates this asymmetry in the early universe, requires a Charge-Parity (CP) violation which is present but too small in the SM [8]. This brings the need for extending the SM to another level; the SM is only a tiny fraction of the total energy of the universe and if it were its only constituent, the universe would be a sea of photons without planets, stars and galaxies!

The evidence for DM is now overwhelming [9] and essentially comes from a missing gravitational pull from ordinary matter (*e.g.* stars, galaxies, gas, etc.). Its influence is required on different scales, explaining the famous flat rotation curve velocity at large radii [10] on galactic scales to the anisotropies of the cosmic microwave background [7] and the structure formation [11] on cosmological scales. It would be perfectly consistent with observations if DM were to interact with the SM only through gravity and its relative abundance is set via an inexplicably tuned initial condition. The small difference of energy densities of dark and ordinary (*i.e.* SM) matter can instead suggest a common origin for both ingredients in the far past that would provide a "universal" initial condition. Such scenarios typically posit a significant amount of interaction between the two sectors that would keep them in equilibrium throughout the very early stages of the universe's history [9]. From a particle physics perspective, this is an exciting opportunity to find other experimental signatures of the SM-DM non-gravitational interactions and have a window into the fundamental properties of DM.

Although the contribution of SM particles is currently subdominant in terms of cosmological energy density, it is quite remarkable that its microphysics correctly predict relative abundances of light nuclei, which are unaffected by the DM and dark energy [12]. On the other hand, the strongest evidence for the need of an ameliorated SM comes from cosmology. The interplay between macrophysics and microphysics, cosmology and particle physics, is crucial for the progress in each field. In recent years, observational cosmology has reached a precision level that can provide better sensitivity to some particle physics parameters than more conventional particle experiments. For example, the best upper bound for the sum of neutrino masses currently comes from cosmological data [13].

The incompleteness of the SM and the complementarity of cosmology with labora-

tory experiments motivate the research efforts presented in this dissertation. We aim to harness the power of precision cosmology in order to explore possible extensions of the SM. Given the minimal signs of new physics from the LHC, precision cosmology provides an alternative search avenue from traditional collider experiments. Before diving into the specific details of the models investigated, we review some building blocks needed for studying particle physics effects within a cosmological framework.

## 1.1 Thermal history of the universe

The Big Bang picture of the early universe is an incredibly simple and successful theory as a post-inflation initial condition to the universe. With the simple requirements of a universe was once hot, dense, in thermal equilibrium and a nearly-scale invariant primordial spectrum of fluctuations, one can mathematically predict the properties of the expanding universe, retrieving in a natural way the general features of the universe we live in [14]. Thermal distributions of particles and an almost smooth background metric allow for simple analytic solutions at linear order of all physics, until the gravitational collapse of matter and formation of large structures in the universe.

Assuming an isotropic and homogeneous cosmology, the abundance of all particles that interact with a thermal bath are described by a master equation, the Boltzmann equation [14],

$$\dot{n}_i + 3Hn_i = \frac{g_i}{(2\pi)^3}\int C\left[f_i(\mathbf{p_i}, t)\right]\frac{\mathrm{d}^3\mathbf{p_i}}{E_i}, \tag{1.1}$$

where $n_i$ is the number density of the particle at a given time $t$, $H$ is the Hubble rate and $C$ describes the collisions or interactions it has with other particles, integrated over the distribution of the particle $f_i$. The left-hand side has the extra Hubble term that takes into effect the $n_i$ dilution from the expansion of the universe. Since entropy $s$ is comovingly conserved, it is customary to define $Y_i = n_i/s$, which simplifies the right-hand side to $\dot{n}_i + 3Hn_i = \dot{Y}_i$. The right-hand side is process dependent and needs to be computed for all types of interactions that are relevant.

The evolution of the Universe includes multiple thermal transitions, where some constituents begin as freely moving and then annihilate or bind to other particles. These transitions happen at very precise times, when the ambient temperature is of the same order as the binding energy of the bound objects. The binding energy hierarchy of the different substructures allows for well-defined outcomes of each

cooling stage. This separation of energy scales isolates the treatment of each stage and simplifies the understanding of the underlying physics. We proceed to review three main applications of the Boltzmann equation that will be used throughout this dissertation: the determination of the relic abundance of particles, the synthesis of light nuclei (named Big Bang Nucleosynthesis) and the emission of photons from the last-scattering surface (the Cosmic Microwave Background).

### 1.1.1 Relic densities

At high temperatures, particles are kept in thermal equilibrium by the efficient interaction rates with the thermal bath. Once the scattering rate drops below the Hubble rate, it is no longer maintained in equilibrium and the abundance departs from the equilibrium value. The archetype example is a species $i$ coupled to the SM bath with $2 \leftrightarrow 2$ interactions. The Boltzmann equation (1.1) takes a simple form

$$\dot{n}_i + 3Hn_i = -\langle \sigma v_{\rm rel} \rangle \left( n_i^2 - n_{i,\rm eq}^2 \right) , \tag{1.2}$$

where $\langle \sigma v_{\rm rel} \rangle$ is the thermally averaged cross section. The $-n_i^2 \langle \sigma v_{\rm rel} \rangle$ term accounts for the depletion from self-annihilations while the other term $n_{i,\rm eq}^2 \langle \sigma v_{\rm rel} \rangle$ takes care of the production of species $i$ from the inverse reaction. Because the $i$ production comes from particles in thermal equilibrium, detailed balanced can be used to represent the number densities of the bath particles as the equilibrium value $n_{i,\rm eq}$ [14]. The equation can be written more simply as

$$\frac{dY_i}{dT} = \langle \sigma v_{\rm rel} \rangle \frac{s}{HT} \left( Y_i^2 - Y_{i,\rm eq}^2 \right) , \tag{1.3}$$

with $\langle \sigma v_{\rm rel} \rangle$ as the only input to obtain the final abundance. We show in Fig. 1.1 the qualitative behaviour as a function of a constant $\langle \sigma v \rangle$ (although it can have a velocity dependence [14]). The particle initially starts in equilibrium, and when the annihilation rate drops below the expansion rate, the depletion from annihilations becomes inefficient and the abundance *freezes out* of the thermal bath. Stronger interactions maintain the abundance in equilibrium to lower temperatures, thus delaying the decoupling and decreasing the final abundance. In the freeze-out scenario, the final abundance is inversely proportional to the cross section $Y_{\rm f-o} \propto 1/\langle \sigma v \rangle$. The relic abundance matches the measured cold dark matter value for $\langle \sigma v \rangle \sim 1$ pb over a wide range of masses. This order of magnitude is typical of interactions induced by

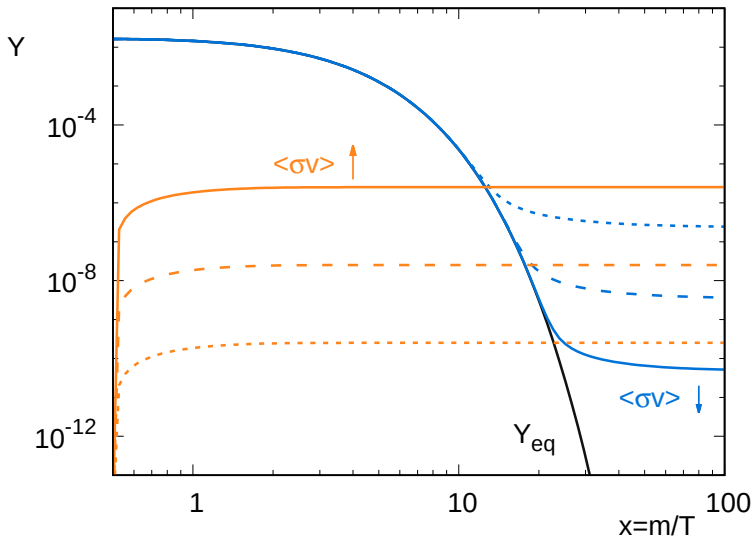


Figure 1.1: Schematic representation of the normalized particle density evolution in a freeze-out (blue) and freeze-in (orange) scenario. Dotted, dashed and solid lines demonstrated increasing cross sections.

the weak force and consequently defines a popular type of dark matter candidate : the Weakly Interacting Massive Particle (WIMP).

Large interaction rates with the thermal bath guarantee the thermalization of a species, irrespective of an initial condition on the abundance. An alternative scenario yet considers interaction rates that remain below the Hubble rate at all times [15]. In this case, if the species is initially absent, it gets populated from the thermal bath while never reaching thermal equilibrium. The $Y_{\rm eq}$ term in Eq. (1.3) can then be neglected and $Y$ is never depleted through annihilations. As shown in Fig. 1.1, the abundance *freezes in* and the surviving abundance is proportional to the cross section $Y_{\rm f-i} \propto \langle \sigma v \rangle$.

It should be emphasized that the empty initial abundance required for the freeze-in is an important initial condition for model building. It cannot be significantly populated by another mechanism, an inflaton decay for example. In this case, it would not interact enough to lower its abundance through annihilation and might overclose the universe. With this caveat in mind, the correct abundance for DM can be obtained in two regimes; through the freeze-in mechanism with a small coupling and via the standard freeze-out with a large coupling constant. As depicted in Fig. 1.2, in the intermediate regime, when couplings are sufficient to thermalize the DM, but

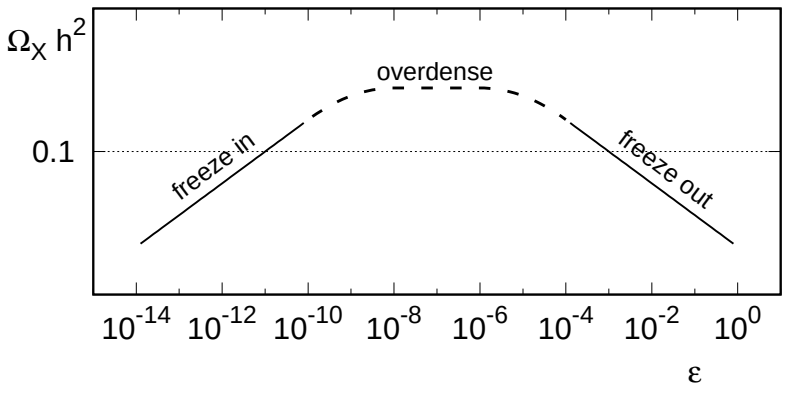


Figure 1.2: Schematic representation of the relic density relationship with respect to the coupling strength with the bath.

not sufficient enough to provide a weak-scale annihilation cross section, we have *too much* DM left, which is ruled out by observations. If additional interactions are present besides the $2 \leftrightarrow 2$ scenario, the Boltzmann equation requires more terms and the situation can be more complex than the basic freeze-in freeze-out picture [16, 15].

### 1.1.2 Big bang nucleosynthesis

Arguably the earliest probe of our Universe[1], the cosmological creation of light elements, referred to as Big Bang Nucleosynthesis (BBN), provides precise abundance predictions for the elements between Hydrogen (H) and Lithium-7 ($^7$Li) and their isotopes. The standard theory of BBN (see [12] for example) entails the evolution of abundances via the network of nuclear reactions that have carefully been calculated and/or measured in nuclear physics experiments (Fig. 1.3).

The abundance of each species $i = \{p, n, \mathrm{D}, {}^4\mathrm{He}, ...\}$ can be calculated with a set of coupled Boltzmann equations

$$\frac{dY_i}{dt} = -H(T)T\frac{dY_i}{dT} = \sum \left(\Gamma_{ij}Y_j + \Gamma_{ijk}Y_jY_k + ...\right), \tag{1.4}$$

where $Y_i = n_i/n_b$ is normalized on the baryon number density $n_b$. Each possible reaction in the network is represented via the corresponding rate $\Gamma_{ij...}$. The resulting

[1] In early 2014, the Bicep2 collaboration claimed detection of B-mode polarization [17] which could be interpreted as a signature of the inflationary era. The interpretation was under a heated debate and was then discarded through a joint analysis from Bicep2, Planck and Keck Array data [18].

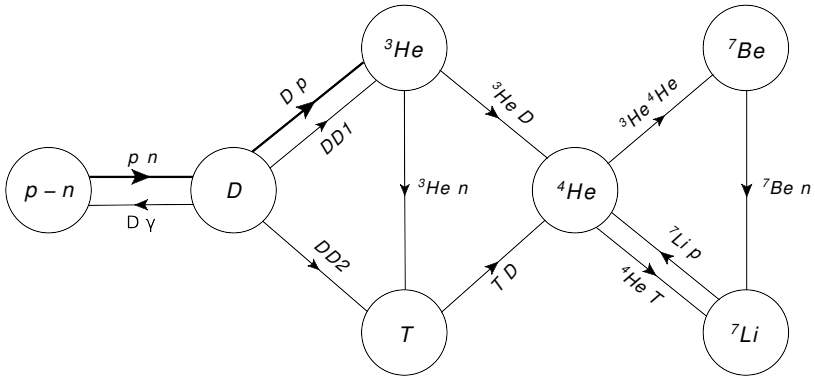


Figure 1.3: Network of main reactions in BBN. Each line is labeled by the reactants. $DD1$ corresponds to $D + D \to {}^3He + n$ and $DD2$ to $D + D \to T + p$.

evolution is shown in Fig. 1.4. The only external input parameter to determine the final abundances is $\eta_b$ the baryon-to-photon ratio, which is carefully measured in the CMB [7].

To qualitatively describe the sequence of events during the BBN, we note that the Universe is initially[2] filled with protons and neutrons in thermal equilibrium as a small addition to the energetically dominant electrons, positrons, neutrinos and photons. As decreasing temperatures make the rest energy difference between protons and neutrons relevant, the weak force shifts towards reducing the neutron abundance. Not too far from this temperature scale, interaction rates between neutrons and protons become smaller than the expansion rate and the neutron fraction freezes out to $X_n \equiv \frac{n_n}{n_n+n_p} \simeq 0.158$ at $T_{\text{freeze}} \simeq 0.84$ MeV. The production of the next lightest element, deuterium (D), is however delayed due to the high number of photons ($\eta_b \equiv n_b/n_\gamma \sim 10^{-10}$) which quickly destroys any heavier element. The neutron freeze-out fraction $X_n$ slightly decreases via $\beta$-decays to protons and residual weak interaction scattering processes. The onset of nuclear reactions is delayed by the shallowness of the deuteron binding energy (as compared to the typical nuclear binding energy scale) and the D production is eventually effective around $T \simeq 100$ keV. The remaining species in the nuclear network rapidly populate, with neutrons ending mostly in the element with the largest binding energy, $^4$He, allowing a straightforward estimate for its final

[2]This *initial* time is taken with respect to BBN. At earlier times, asymptotic freedom [19, 20] tells us that quarks should be freely propagating, but the high confinement energy $T \simeq 150$ MeV [21], compared to the beginning of BBN at $T \simeq 1$ MeV renders the details irrelevant.

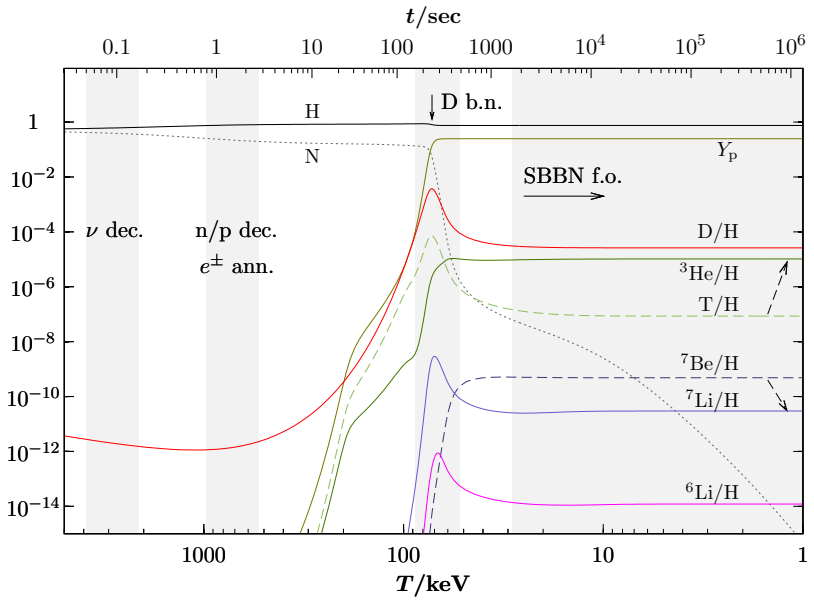


Figure 1.4: Time-dependence of the light nuclei abundances relative to hydrogen. Helium-4 is indicated as relative abundance by mass $Y_p$ defined in (1.5). The dotted lines are species that will freeze out from BBN, but eventually decay into a stable nucleus. Reproduced with permission from [12].

relative abundance by mass

$$Y_p \equiv \frac{m_{^4\mathrm{He}} n_{^4\mathrm{He}}}{m_b n_b} = 2X_n \simeq 0.25. \tag{1.5}$$

With the exception of the $^7$Li abundance, all theoretical predictions (with a baryon-photon ratio $\eta_b$ input from CMB observations) of primordial values agree with astrophysical observations [22]. The $^7$Li prediction from standard BBN remains a factor of 3-5 higher than the primordial value extrapolated from metal-poor stars [23]. The lithium problem is still unresolved, with potential solutions from new physics or astrophysical mechanisms altering its concentration in the atmospheres of old stars and thus modifying the extrapolation to a primordial value [22].

### 1.1.3 Cosmic microwave background

After BBN that is limited to a very early epoch (1 to 100 seconds), the next major cosmological event is the recombination of free electrons with the charged nuclei, transforming the Universe from free ions to neutral atoms. The Universe then becomes

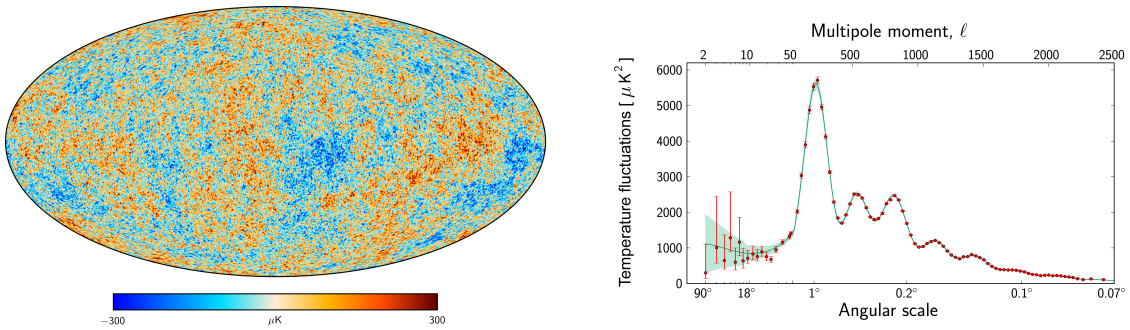


Figure 1.5: *Left:* Temperature anisotropies in the CMB measured by the Planck satellite [7]. The red (blue) spots correspond to regions in the sky with up to $10^{-4}$ K above (below) the average temperature $T_0 = 2.7255$ K. *Right:* Temperature power spectrum associated with the Planck data on the left. The red dots with errors and the measurements and the shaded green zone is the ΛCDM model prediction. Courtesy of the ESA and the Planck Collaboration

transparent, allowing the propagation of light over long distances. This remnant light, the CMB, is now detectable [24, 25], with a blackbody spectrum at $T = 2.73$ K and minuscule angular fluctuations at the $10^{-4}$ level (shown in Fig. 1.5). Deviations from the average temperature are a signature of a nearly scale-invariant spectrum of small fluctuations and evolved with the pressure-gravity oscillation of the baryon-photon plasma [26]. They thus encode rich information about the constituents of our Universe, and have recently been studied to high precision with the WMAP [24] and Planck [25] satellites to provide the present picture of a flat Universe, dominated by dark energy and cold dark matter with a nearly scale-invariant spectrum of primordial fluctuations (the $\Lambda CDM$ model).

As the Universe does not instantaneously become transparent, the CMB photons do not come from the exact same emission time and we observe an integrated picture over a range of last scattering times, effectively weighted by a function of the ionized fraction of the Universe. The neutralization process is most efficient through a cascading recombination with the free $\rightarrow 2S \rightarrow 1S$ perturbative transition[3] and can be evaluated with another form of the Boltzmann equation [27, 28]

$$\frac{dX_H}{dt} = C_r \left\{ (1 - X_H)\, \beta - X_H^2 n_b \alpha^{(2)} \right\}, \tag{1.6}$$

[3]The direct recombination to the ground state (and similarly via the $2P$ state) emit a photon that will ionize (excite) another neutral hydrogen and will result in no net change.

where $X_H = n_e/n_b$ is the ionized hydrogen fraction, $n_b = n_p + n_H$ the number of hydrogen nuclei, $\beta$ the ionization rate, $\alpha^{(2)}$ the recombination rate through $2\gamma$ decays from the $2S$ state and $C_r$ a correction factor accounting for ionization of excited states before they decay. Meanwhile, the Thomson scattering rate cannot keep the baryons in thermal equilibrium with radiation, the matter temperature $T_b$ drops relative to the photon temperature $T_\gamma$ [29].

Factoring out the convolution of the photon emission process in the temperature anisotropy, we can understand the origin of the fluctuations. The primordial quantum fluctuations that were left on large scales by inflation provided minuscule energy over(under)-densities. After the matter-radiation equality around $T \sim 0.2$ eV, the over(under)-densities start growing due to the DM. These provide gravitational potential wells for the baryon-photon fluid to clump together. As the local density increases, the photon pressure eventually counterbalances the gravitational force, inducing acoustic oscillation in the baryon-photon fluid. Performing a statistical analysis over the sky in Fourier space, the temperature anisotropies can be completely parametrized in the $C_l^{TT}$ power spectrum

$$\left\langle \Delta T(\vec{n}) \Delta T(\vec{n'}) \right\rangle = \frac{1}{4\pi} \sum_l (2l+1) C_l^{TT} P_l(\mu), \tag{1.7}$$

where $\mu = \vec{n} \cdot \vec{n'}$ and $P_l$'s are the Legendre polynomials. As shown in Fig. 1.5, the power spectrum decomposition clearly illustrates the acoustic oscillations. As the oscillations depend on the amount of matter, photons, the primordial fluctuations and the expansion history of the Universe, we can fit a 6-parameter model in the data and obtain the standard ΛCDM parameters [7]

$$\begin{array}{ccc} \Omega_b h^2 = 0.0223 & \Omega_c h^2 = 0.1186 & \Omega_\Lambda = 0.692 \\ n_s = 0.968 & A_s = 2.21 \times 10^9 & \tau = 0.066 \end{array}$$

where $\Omega_b$, $\Omega_c$, $\Omega_\Lambda$ are the normalized energy densities of baryons, cold dark matter and dark energy over the critical energy density ($\Omega_i = \rho_i/\rho_{\rm crit}$, $\rho_{\rm crit} = 3H_0^2/8\pi G_N$) , $n_s$ and $A_s$ are the spectral index and amplitude of the scalar primordial fluctuations, $\tau$ is the reionization optical depth and $h = 0.678$ is a parametrization of the Hubble rate $H_0 \equiv 100\ h$ km/s/Mpc.

The observed CMB photons also carry polarization, with $E$ modes (curl-free) generated after recombination through the residual late scatterings of the photons with

the quadrupole moment of the anisotropy. In a similar fashion to the TT spectrum, the EE and TE spectra provide additional source of information and reinforce the ΛCDM model [30]. The $B$-mode polarization (curl-containing or parity odd) on the other hand may provide evidence for non-scalar (*e.g.* tensor) perturbations if they have a primordial origin. Its claimed detection by the BICEP2 collaboration [17] in March 2014 was later ruled out by a joint analysis with the Planck and Keck Array collaborations. They demonstrated that the BICEP2 signal was coming from dust contamination as a galactic foreground [18] and pushes back the (potential) detection to future experiments.

## 1.2 The dark sector

The energy densities of baryonic and non-baryonic matter (respectively 4.8% and 25.8% of the total energy density [7]) could easily arise from comparable initial conditions in the early Universe, but their similar values motivate the existence of a mechanism governing their relic density. In fact, if we assume a particle theory of dark matter which was in thermal equilibrium with the SM particles in the far past, we can get a correct freeze-out relic density with a weak scale annihilation cross section, the so-called WIMP miracle [26]. It therefore makes sense to expand the SM with new interactions, which can be parametrized in a very specific way, and can already be probed with the current technology. We call the Dark Sector (DS) the ensemble of particles that are not charged under the SM forces or interact with the known forces in such a feeble way that they have so far escaped all experimental constraints. In its simplest realization, it could be comprised of a single new particle, such as the WIMP, or have a more complex structure with a multitude of particles and new forces.

### 1.2.1 Experimental motivation

The WIMP miracle has lead to a strong experimental effort in search for a direct detection of WIMPs. Various potential signals in the GeV mass range from the DAMA, CRESST, CDMS and CoGeNT collaborations (mostly inconsistent with each other, see Ref. [31] for a review) provided some early enthusiasm, but they were all later ruled out by the Xenon100 [32], LUX [33] and PandaX [34] groups.

In parallel to the hunt for a direct interaction between a dark matter particle and a

SM particle in a controlled experiment, there have been a few astrophysical anomalies, unexplained by the current astrophysical knowledge, that could potentially arise from the annihilation of dark sector particles. Recent (still unresolved) examples include the rise of positron-to-electrons fractions at high energies in cosmic-rays [35, 36, 37] and the observation of an unexplained emission line at 3.55 keV in different galaxy clusters [38, 39]. Moreover, $N$-body simulations of collisionless DM are in tension with observations on small galactic scales, and DM with self-interactions has been suggested to resolve the tension [40].

Moreover, the discrepancy between the theoretical and experimental values of the muon anomalous magnetic moment [41] may be hinting at a DS component with a completely different phenomenology than dark matter candidates [42]. All these tensions between experimental observations and SM prediction hint at a solution arising from new interactions with a yet-undiscovered sector of particles and forces. The DS could thus have a complex structure of its own, and searches should not be restricted to a single state that would explain the DM abundance by itself.

### 1.2.2 Dark Sector Portals

The symmetries in the SM restrict the form of operators for new particle interactions. From very generic field-theoretic principles, any new interactions that can connect to SM state, *i.e.* that can serve as mediators to the DS, will have the lagrangian form [43]

$$\mathcal{L}_{\text{mediator}} = \sum \frac{\mathcal{O}_{\text{NP}}^{(k)} \mathcal{O}_{\text{SM}}^{(l)}}{\Lambda^{k+l-4}}, \tag{1.8}$$

where $\mathcal{O}$ encodes the particle operators of the New Physics (NP) or the SM with their respective dimensionality $(k, l)$. As the action must be dimensionless, the lagrangian density must have units of $(\text{length})^{-4}$ (using units where $\hbar = c = 1$) and all higher-dimensional interactions must be suppressed by an energy breaking scale $\Lambda^{k+l-4}$, often taken at prohibitively high energy. As such, only very few operators do not receive that suppression, where $k+l \leq 4$, and serve as the most promising avenues the detect new physics with limited experimental power. They could provide the strongest new physics interactions with the SM, while also possibly mediating a new force in the DS. The SM only allow for three generic forms of such portals, with either a relevant or marginal operator [44]:

| Portal | Particles | Operators |
|---|---|---|
| Higgs | Dark scalars | $(AS + \lambda S^2)\, H^\dagger H$ |
| Vector | Dark photons | $\frac{\epsilon}{2\cos\theta_W} B_{\mu\nu} F'^{\mu\nu}$ |
| Neutrino | Sterile neutrinos | $y_N L H N$ |

The singlet scalar $S$ has been recognized early on as a simple extension of the SM to provide a dark matter candidate, provided that its stability is protected on cosmological times by a discrete $Z_2$ symmetry ($A = 0$) [45, 46]. If the $Z_2$-breaking term ($ASH^\dagger H$) is allowed, the new state $S$ mixes with the SM Higgs and becomes unstable through a Yukawa coupling with all SM massive states. Since the discovery of the SM Higgs [2, 3], there has been a increased interest in the Higgs portal scalar, with a clear experimental plan to probe the parameter space with mixing angle $\theta \lesssim 1$ [43, 47]. The appeal comes from the fact that the Higgs boson mass is now well measured to $m_h = 125$ GeV [48], thus removing a degree of freedom in the parameter space. More fundamentally, before the Higgs discovery, no scalar elementary particle had been observed in nature yet. Establishing the existence of the Higgs boson tells us that scalar particles can be realized in nature and justifies even further the possibility of new scalar states coupled to the SM. We will devote Part II of this dissertation to the scalar portal, utilizing cosmology as a powerful tool to complement the laboratory searches.

The dark photon $A'$ has a rich but simple phenomenology. The dark photon stress field tensor $F'_{\mu\nu} = \partial_\mu A'_\nu - \partial_\nu A'_\mu$ couples with SM electroweak stress field tensor $B_{\mu\nu}$ that combines the neutral gauge bosons, the photon and the massive $Z$ boson. For a dark photon with a negligible mass relative to $m_Z$, the $Z$ component can be neglected and A' couples to all SM electric charges, with the simple effective charge rescaling $e' = \epsilon e$. For $m_{A'} < 2m_e$, the only available decay channel is through the suppressed 3-photon channel and has a much different signature than the heavier case, where it decays into a pair of charged particles ($e^+e^-$, etc.). The experimental program to search for $A'$ is even richer than the scalar portal [49, 43, 47], simply because this particle (unlike the Higgs portal related states) couples to all particles democratically and most experiments are performed with light initial states (electrons, protons, etc.). Part I of this dissertation will explore the physics of the vector portal, again using cosmology as a probe to the lowest coupling regions of the parameter space.

Finally, sterile neutrinos received wide attention due to anomalies in neutrino oscillation experiments and an apparent mild preference for a higher number of relativistic degrees of freedom in previous cosmological measurements (see Ref [50] for

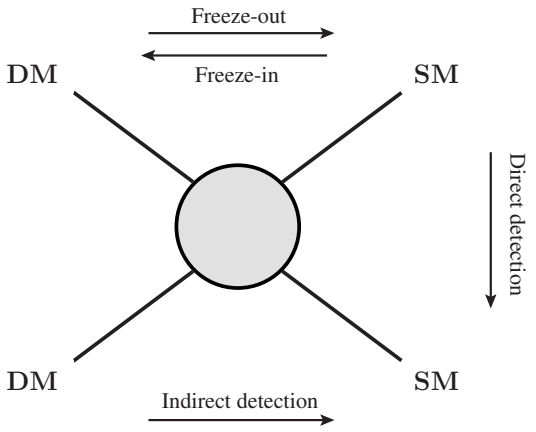


Figure 1.6: Illustration of the connection between the interactions for the relic density, direct and indirect detection.

a review). The number of relativistic degrees of freedom measured by Planck is now in better agreement with the 3 SM neutrinos [7], but the reported reduction of antineutrino flux in reactors remains an open issue [51]. Although the neutrino portal presents interesting opportunities for new physics phenomenology [43, 47, 50], this avenue will not be explored in this dissertation.

### 1.2.3 Dark Matter searches

A beautiful feature of the particle dark matter hypothesis is that the relic density is fixed by the interaction strength and automatically gives us experimental targets to detect DM and measure its properties [52]. As illustrated in Fig. 1.6, the connection between the relic abundance and its interaction with the SM suggests many avenues to have other experimental signals that guide us to its properties.

*Direct detection* experiments attempt to measure the recoil energy deposited by a scattering of dark matter on heavy nuclei. They consist of large volumes of heavy stable elements being carefully monitored for any unambiguous signal of energy deposition. The expected rate can be calculated from the local dark matter density and velocity and places constraints with minimal model dependence on the cross section off baryons or electrons [53]. The strongest constraints come from a combination of PandaX-II [54] and XENON-1T [55] with a spin-independent maximal sensitivity of WIMP-nucleon interaction of $\sigma_n = 7.7 \times 10^{-47}$ cm$^2$ for a 35-GeV WIMP.

Since the interaction rate is so low, these experiments are typically performed

in deep underground laboratories, profiting from the natural shielding of the rocks to minimize the background noise. The next generation of experiments (LZ [56], PandaX-4T [57] and XENON-nT [58] for example) will improve sensitivity by increasing their fiducial volume, thereby raising the expected number of events. It will potentially improve the sensitivity by more than an order of magnitude, approaching an irreducible source of background associated with scattering of the so-called atmospheric and supenova neutrinos on nuclei, also known as the "neutrino floor" [52].

On the other hand, *indirect detection* methods consist of looking for products of DM decays or annihilations [59]. These will be seen as energy releases that are unaccounted for by SM physics. Natural places to look for these energy releases are cosmological and astrophysical systems, where we expect a dense population of DM. On the cosmological side, both BBN [12] and the CMB [7] (discussed in the next section) impose strong constraints on additional energy during their active eras. Locally, the Fermi telescope provides strong bounds on gamma ray emissions from the Milky Way [60] and the AMS-02 instrument on the International Space Space limits WIMP annihilation from cosmic rays observations [61, 62].

It is tempting to attribute deviations from the predictions of fiducial astrophysical models as indirect DM signals and consider DM models that could account for them. Amongst popular examples, the PAMELA satellite first observed a cosmic ray positron excess [35], then confirmed by both Fermi [36] and AMS-02 [37], that could be explained by a heavy DM with leptonic decays. Such solutions are disfavored by CMB bounds and other gamma-ray observations [59]. Another anomaly comes from the galactic center, with an observed excess of gamma rays in the GeV range [63, 64] which could be explained by DM annihilation to quarks. This observation comes with large systematic uncertainties and could be sourced by other SM mechanisms [59]. More recently, a 3.5 keV X-ray excess was observed in galaxy clusters [38, 39]. The simplest explanation is a 7 keV decaying sterile neutrino DM [65], but there is still an ongoing debate over possible contaminations from atomic lines [66].

## 1.3 Cosmological probes of the dark sector

In a typical high-energy particle physics experiment, we can study the properties of an unstable particle if we satisfy two basic requirements:

- There must initially be *enough energy* to produce the unstable particle.

- The detector must be able to *record a signature*.

These requirements are somewhat flexible, but nevertheless correspond to the broad features of a successful experiment. In cosmology, the initial energy is very easily achieved. The thermal evolution from the Hot Big Bang picture implies that the temperature of the Universe was nearly arbitrarily high in the earliest moments. The kinetic energy of ambient particles is enough to create heavy interacting particles via thermal collisions, with a decreasing production rate as the Universe cools down. Depending on the stability of the particle, a relic abundance could survive or a delayed destruction could happen through decays, annihilations or other collisions.

In general, we expect the lifetime of an unstable particle to be inversely proportional to its production rate, unless they are due to different interaction types. Short lifetimes are then readily probed in experiments with high production rates and near detectors, akin to displaced interaction vertex searches at the LHC [67, 68]. Slightly longer decay lengths can be probed with purposely-built detector away from the production point, typically $\mathcal{O}(100\text{ m})$, the so-called beam dump experiments [43]. Longer lifetimes or decay lengths are beyond the terrestrial experimental reach because of their prohibitive probabilities to decay within a detector volume. As mentioned, early cosmology provides the energy and collision rate to thermally produce dark sector particles with very feeble coupling to the SM, for example through the freeze-in mechanism. Luckily, we have well-defined epochs in the evolution of the universe producing measurable outcomes that are sensitive to energy injection, serving as *detectors*. In particular, BBN and CMB measurements are sensitive to unstable particles with the following lifetimes:

$$\tau_{\text{new}} \simeq \begin{cases} 1\text{ s} - 1\text{ yr} & \text{BBN}, \\ 3\times 10^5\text{ yr} - 10^8\text{ yr} & \text{CMB}. \end{cases} \tag{1.9}$$

These properties render cosmology an excellent complementary search avenue for long-lived unstable particles. Since we will extensively use these two probes, we briefly summarize the effects of energy injection, with additional details provided in the relevant sections of the remainder of the dissertation.

### 1.3.1 Energy injection in BBN

The simplicity of BBN with its single input parameter $\eta_b$ inferred from the CMB anisotropies, coupled to the many astrophysical measurements of the abundances,

allow the use of BBN as the earliest probe for NP [12]. In particular, any energy injection from a DS source in the network of nuclear reactions (see Fig. 1.3) can modify the interactions and alter the final abundances. The decay or annihilation of new particles into SM particles can be characterized into two qualitatively different categories.

- *Electromagnetic energy injection.* Additional electrons, positrons or muons rapidly thermalize through inverse Compton scattering and yield high energy photons. The energy dissipates through creations of $e^{\pm}$ pairs with the ambient photons, until the energy is smaller than the thermal mass threshold $E_{\rm pair} \simeq m_e^2/(22T)$. Subsequently, the excess energy can only be diluted in the nuclei, thus changing the number densities and final products of BBN with additional photodestructions of elements. Solving for the temperature at which the energy threshold equals the binding energy of various nuclei, we can estimate the cosmic time when the energy injection will have a significant impact on the final abundances:

$$t_{\rm ph} \simeq \begin{cases} 2\times10^4 \text{ s}, & {}^7\text{Be}+\gamma \to {}^3\text{He}+{}^4\text{He} \quad (1.59 \text{ MeV}), \\ 5\times10^4 \text{ s}, & \text{D}+\gamma \to n+p \qquad\qquad\quad (2.22 \text{ MeV}), \\ 4\times10^6 \text{ s}, & {}^4\text{He}+\gamma \to {}^3\text{He/T}+n/p \quad (20 \text{ MeV}). \end{cases} \tag{1.10}$$

- *Hadronic energy injection.* The multiple strong interactions between mesons and nucleons with the ambient protons and nuclei render this category more complex and harder to model. The complete exposition of additional hadronic particles can be found in [69]. The dominant features used in this dissertation are modifications to the neutron abundance, with a increase in $n/p$ ratio (altering the final $^4$He abundance) via $\pi^- + p \to \pi^0 + n$ before the deuterium bottleneck and later destruction of $^4$He through $\pi^- + {}^4\text{He} \to T + n$ for examples.

### 1.3.2 Energy injection in the CMB

The CMB power spectra depend on the angular fluctuations, convoluted with the ionized fraction of hydrogen and helium, integrated over time. Ionization from an additional energy source will modify the recombination rate and the ionized fraction function. This will in turn influence the CMB angular power spectra, which we can use to constrain the energy input from decaying or annihilating particles [70, 71].

The main effects come from additional scatterings at lower redshift from a higher residual ionized fraction, washing out the temperature correlations at small scales and increasing the polarization on large scales.

Decaying particles provide an energy release rate related to the lifetime $\Gamma^{-1}$ of the parent particle, which can generically be parametrized as [72]

$$\frac{dE}{dtdV} = f_{\text{eff}} N \Gamma e^{-\Gamma t}, \tag{1.11}$$

where there is a metastable abundance of $N$ particles with an ionizing efficiency $f_{\text{eff}}$. CMB measurements provide an upper bound on the ionizing energy deposition $f_{\text{eff}} N\Gamma$ as a function of the lifetime of the unstable particle. To translate these parameters into bounds on specific dark sector models, one needs to solve for the ionizing efficiency $f_{\text{eff}}$, which depends on the decay products, their energy and time of injection [73, 72].

## 1.4 Structure of the dissertation

In the dissertation, we utilize cosmological probes to constrain and test various DS models. Part I of the dissertation focuses on the dark photon portal. More specifically, we will analyze two models.

**Chapter 2** explores the minimal set of constraints on the dark photon parameter space above the di-electron threshold from cosmology. We calculate the minimal abundance from the freeze-in mechanism and analyze the corresponding effects from its decays into BBN and the CMB. The resulting constraints are very robust and apply to a general dark sector connected to the SM via the dark photon, provided that the dark photon does not decay invisible to some dark sector light state. This chapter was published in Physical Review D as "Cosmological Constraints on Very Dark Photons" [74].

**Chapter 3** expands the dark sector to include a fermionic dark matter particle. This DM particle can have significant self-interactions mediated by the dark photon and can potentially alleviate the small scale structure discrepancy between observed and simulated dark matter profiles. This specific model from a freeze-out relic is already excluded from indirect detection measurements [75], but could possibly be evaded if the relic is set by the freeze-in mechanism. We analyze

this possibility and forecast the future sensitivity of planned direct detection upgrades on the parameter space.

Part II of the dissertation is devoted to the scalar portal. In a similar spirit, we explore the power of cosmology to bound the low coupling regime with the SM.

**Chapter 4** analyzes the parameter space of the scalar $S$ as a long-lived particle at the LHC from Higgs decays. The MATHUSLA detector has been proposed to experimentally test the possibility of long-lived unstable particles at a distance $\mathcal{O}(100\text{ m})$ away from the interaction point. We point out that the production and decay rates of these particles at the LHC can be related to a metastable abundance in the universe that is strongly restricted to lifetimes $\tau_S \lesssim 0.1$ s from BBN, thus providing a an upper bound on the lifetimes that need to be probed at MATHUSLA. This chapter was published in Physical Review D as "BBN for the LHC: constraints on lifetimes of the Higgs portal scalars" [76].

**Chapter 5** circles back to Chapter 2 and comprises of a similar analysis of the minimal cosmological constraints from the freeze-in abundance of the $S$ particle. The situation is however conceptually different because of the enhanced couplings to heavy SM particles, the freeze-in production epoch is much earlier, near the electroweak phase transition. We provide a more comprehension calculation of the abundance and correct some previous erroneous results reported in the literature. We clarify and quantify the source of uncertainty in the relic abundance and provide an improved analysis of the cosmological probes across the parameter space.

Finally, we conclude the dissertation in **Chapter 6** with a short conclusion, providing a brief outlook on the way forward to explore the DS.

# Part I

# Vector Portal

# Chapter 2

# Very Dark Photons in Cosmology

This chapter was published as: **A. Fradette, M. Pospelov, J. Pradler and A. Ritz. Physical Review D 90, 035022 (2014)**, with an update in Region I of Fig. 2.4 and its description in section 2.4.

## 2.1 Abstract

We explore the cosmological consequences of kinetically mixed dark photons with a mass between 1 MeV and 10 GeV, and an effective electromagnetic fine structure constant as small as $10^{-38}$. We calculate the freeze-in abundance of these dark photons in the early Universe and explore the impact of late decays on BBN and the CMB. This leads to new constraints on the parameter space of mass $m_V$ vs kinetic mixing parameter $\kappa$[1].

## 2.2 Introduction

In the past two decades, there has been impressive progress in our understanding of the cosmological history of the Universe. A variety of precision measurements and observations point to a specific sequence of major cosmological events: inflation, baryogenesis, BBN, recombination and the decoupling of the CMB. While our knowledge of inflation and baryogenesis, likely linked to the earliest moments in the Universe, is necessarily more uncertain, BBN and the CMB have a firm position in

[1]Since the publication of this chapter, the nomenclature was standardized to $A'$ for a dark photon and $\epsilon$ the kinetic mixing coupling. $V$ is this chapter refers to $A'$ and $\kappa = \epsilon$.

cosmic chronology. This by itself puts many models of particle physics to a stringent test, as the increasing precision of cosmological data leaves less and less room for deviations from the minimal scenario of standard cosmology. In this chapter, we adhere to the standard cosmological model, taking as given the above sequence of the main cosmological events. Thus we assume that the Universe emerged from the last stage of inflation and baryogenesis well before the onset of BBN. These minimal assumptions will allow us to set stringent bounds on very weakly interacting sectors of new physics beyond the SM.

Neutral hidden sectors, weakly coupled to the SM, are an intriguing possibility for new physics. They are motivated on various fronts, e.g. in the form of right-handed neutrinos allowing for neutrino oscillations, or by the need for non-baryonic dark matter. While the simplest hidden sectors in each case may consist of a single state, various extensions have been explored in recent years, motivated by specific experimental anomalies. In particular, these extensions allow for models of dark matter with enhanced or suppressed interaction rates or sub-weak scale masses.

From a general perspective, we would expect leading couplings to a neutral hidden sector to arise through relevant and marginal interactions. There are only three such flavor-universal 'portals' in the SM: the relevant interaction of the Higgs with a scalar operator $\mathcal{O}_S H^\dagger H$; the right-handed neutrino coupling $LHN_R$; and the kinetic mixing of a new U(1) vector $V_\mu$ with hypercharge $B_{\mu\nu}V^{\mu\nu}$. Of these, the latter vector portal is of particular interest as it leads to bilinear mixing with the photon and thus is experimentally testable, and at the same time allows for a vector which is naturally light. This portal has been actively studied in recent years, particularly in the 'dark force' regime in which the vector is a loop factor lighter than the weak scale, $m_V \sim$ MeV–GeV [43].

The model for this hidden sector is particularly simple. Besides the usual kinetic and mass terms for $V$, the coupling to the SM is given by [77]

$$\mathcal{L}_{\rm V} = -\frac{\kappa}{2} F_{\mu\nu} V^{\mu\nu} = e\kappa V_\mu J^\mu_{\rm em}. \tag{2.1}$$

Thus all phenomenological consequences of the model, including the production and decay of new vectors, are regulated by just two parameters, $\kappa$ and $m_V$. This makes the model a very simple benchmark for all light, weakly interacting, particle searches. There are, however, options with regard to the origin of the mass of $V$, either a new Higgs mechanism, or $m_V$ as a fundamental parameter—the so-called Stueckelberg

mass. In this chapter, we will concentrate on the latter option for simplicity.

The SM decay channels of $V$ are well known. In the mass range where hadronic decays are important, one can use direct experimental data for the $R$-ratio to infer couplings to virtual time-like photons, and hence to determine the decay rate $\Gamma_V$ and all the branching ratios. In a wide mass range from $\sim 1 - 220$ MeV, the vector $V$ decays purely to electron-positron pairs with lifetime

$$\tau_V \simeq \frac{3}{\alpha_{\rm eff} m_V} = 6 \times 10^5 \text{ yr} \times \frac{10\,\text{MeV}}{m_V} \times \frac{10^{-35}}{\alpha_{\rm eff}} \tag{2.2}$$

where we have introduced the effective electromagnetic fine structure constant, absorbing the square of the mixing angle into its definition,

$$\alpha_{\rm eff} \equiv \alpha\kappa^2. \tag{2.3}$$

Importantly, we assume no light hidden sector states $\chi$ charged under U(1), so that there are no "dark decays" of $V \to \chi\bar{\chi}$ that would erode the visible modes and shorten the lifetime of $V$.

The normalization of the various quantities in (2.2) roughly identifies the region of interest in the $\{\kappa, m_V\}$ parameter space for this chapter. We will explore the cosmological consequences of these hidden U(1) vectors with masses in the MeV-GeV range, and lifetimes long enough for the decay products to directly influence the physical processes in the universe following BBN, and during the epoch of CMB decoupling. These vectors have a parametrically small coupling to the electromagnetic current, and thus an extremely small production cross sections for $e^+e^- \to V\gamma$,

$$\sigma_{\rm prod} \sim \frac{\pi\alpha\alpha_{\rm eff}}{E^2_{\rm c.m.}} \sim 10^{-66} - 10^{-52}\ \text{cm}^2, \tag{2.4}$$

where we took $E_{\rm c.m.} \sim 200$ MeV and the range is determined by our region of interest,

$$\alpha_{\rm eff} \sim 10^{-38} - 10^{-24}. \tag{2.5}$$

Such small couplings render these vector states completely undetectable in terrestrial particle physics experiments, and consequently we refer to them as *very dark photons* (VDP). As follows from the expression (2.2) for the lifetime, the lower limit of the above range for $\alpha_{\rm eff}$ is relevant for CMB physics, while the upper limit is important for BBN.

The production cross section (2.4) looks prohibitively small, but in the early Universe at $T \sim m_V$ every particle in the primordial plasma has the right energy to emit $V$'s. The cumulative effect of early Universe production at these temperatures, followed by decays at $t \sim \tau_V$, can still inject a detectable amount of electromagnetic energy. A simple parametric estimate for the electromagnetic energy release per baryon, omitting $\mathcal{O}(1)$ factors, takes the form

$$E_{\text{p.b.}} \sim \frac{m_V \Gamma_{\text{prod}} H^{-1}_{T=m_V}}{n_{b,T=m_V}} \sim \frac{\alpha_{\text{eff}} M_{\text{Pl}}}{10\,\eta_b} \sim \alpha_{\text{eff}} \times 10^{36}\,\text{eV}. \tag{2.6}$$

Here the production rate per unit volume, $\Gamma_{\text{prod}}$, was taken to be the product of the typical number density of particles in the primordial plasma and the $V$ decay rate, $\tau_V^{-1} n_{\gamma,T=m_V}$. This production rate is active within one Hubble time, $H^{-1}_{T=m_V}$, leading to the appearance of the Planck mass in (2.6), along with another large factor, the ratio of photon to baryon number densities, $\eta_b^{-1} = 1.6 \times 10^9$. One observes that the combination of these two factors is capable of overcoming the extreme suppression by $\alpha_{\text{eff}}$. Given that BBN can be sensitive to an energy release as low as $O(\text{MeV})$ per baryon, and that the CMB anisotropy spectrum allows us to probe sub-eV energy injection, we reach the conclusion that the early Universe can be an effective probe of VDP! The cosmological signatures of the decaying VDP were partially explored in [78, 69], but to our knowledge the CMB constraints on this model were not previously studied.

In the remainder of this chapter, we provide detailed calculations to delineate the VDP parameter regions that are constrained by BBN and CMB data. In the process, we provide in section 2 an improved calculation of the 'freeze-in' abundance in the Early Universe (using some recent insight about the in-medium production of dark vectors [79, 80]; see also [81]). In section 3, we explore the BBN constraints in more detail, including the speculative possibility that the currently observed over-abundance of $^7$Li can be reduced via VDP decays. Then in section 4 we consider the impact of even later decays on the CMB anisotropies. A summary of the constraints we obtain in shown in Fig. 2.1, and more detailed plots of the parameter space are shown in sections 3 and 4. We finish with some concluding remarks in section 5. Several supplementary sections contain additional calculational details.

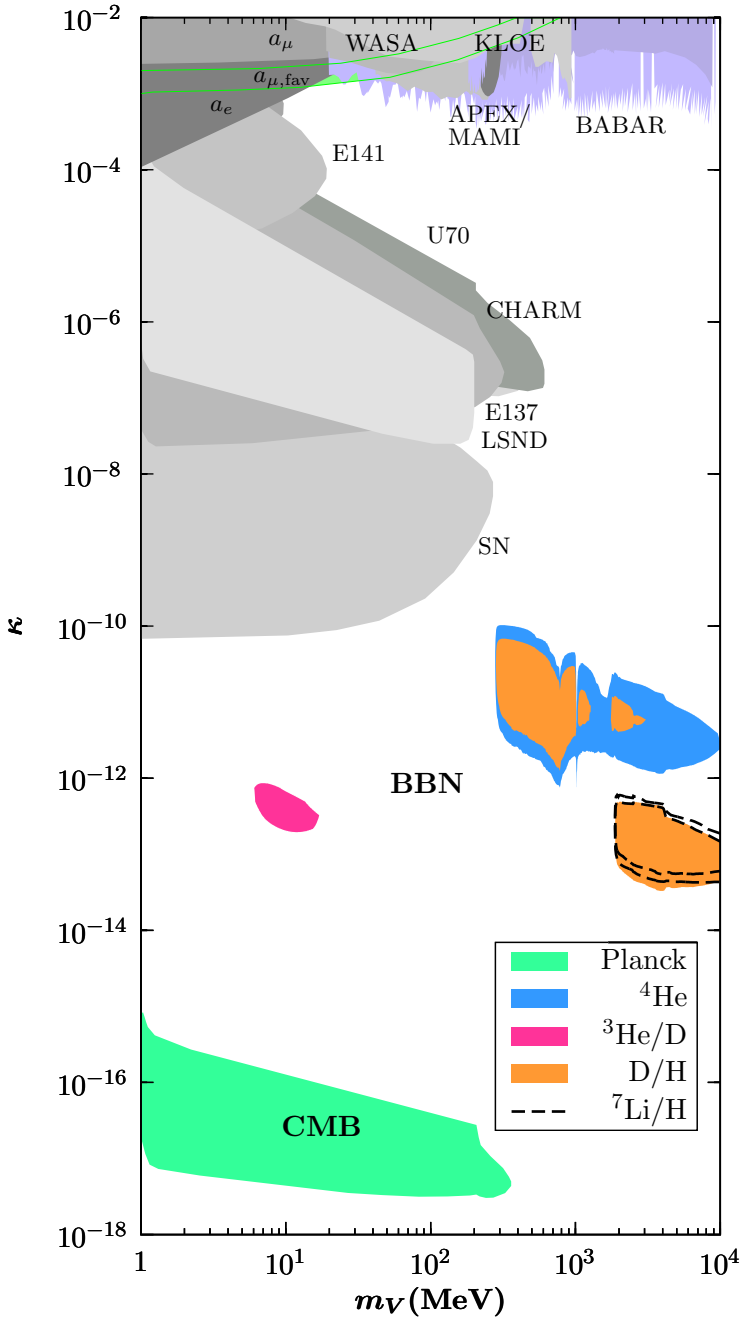


Figure 2.1: An overview of the constraints on the plane of vector mass versus kinetic mixing, showing the regions excluded due to their impact on BBN and the CMB anisotropies, in addition to various terrestrial limits [43, 82, 42, 83, 84, 85, 86, 87, 88, 89, 90, 91, 92, 93, 94, 95, 96, 97, 98, 99, 100, 101]. These excluded regions are shown in more detail in later sections.

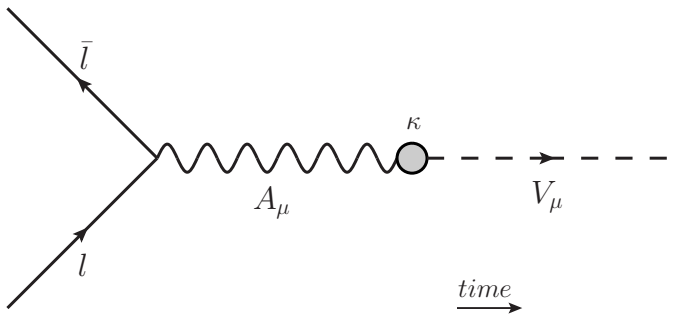


Figure 2.2: Illustration of the coalescence production of the dark photon $V$ via an off-shell photon.

## 2.3 Freeze-in abundance of VDP

The cosmological abundance of long-lived very dark photons is determined by the freeze-in mechanism. While there are several possible production channels, the simplest and most dominant is the inverse decay process. When quark (or more generally hadronic) contributions can be neglected, the inverse decay proceeds via coalescence of $e^\pm$ and $\mu^\pm$, $l\bar{l} \to V$, shown in Fig. 2.2.

The Boltzmann equation for the total number density of $V$ takes the form

$$\begin{aligned} \dot{n}_V + 3Hn_V &= \prod_{i=l,\bar{l},V} \int \left( \frac{d^3\mathbf{p}_i}{(2\pi)^3 2E_i} \right) N_l N_{\bar{l}} \\ &\quad \times (2\pi)^4 \delta^{(4)}(p_l + p_{\bar{l}} - p_V) \sum |M_{l\bar{l}}|^2, \end{aligned} \tag{2.7}$$

where the right hand side assumes the rate is sub-Hubble so that $V$ never achieves an equilibrium density. The product of Fermi-Dirac (FD) occupation numbers, $N_{l(\bar{l})} = [1 + \exp(-E_{l(\bar{l})}/T)]^{-1}$, is usually considered in the Maxwell-Boltzmann (MB) limit, $N_l N_{\bar{l}} \to e^{(E_l + E_{\bar{l}})/T}$. Although this is not justified parametrically, numerically the FD→MB substitution is quite accurate, because as it turns out the peak in the production rate (relative to entropy) is at $T < m_V$ [78].

The matrix element $\sum |M_{l\bar{l}}|^2$ is summed over both initial and final state spin degrees of freedom. In general, it should include the in-medium photon propagator in the thermal bath, and the fermion wave functions. Among these modifications the most important ones are those that lead to the resonant production of dark photon states. However, resonant production occurs at much earlier times [78], at temper-

atures $T_r^2 \geq 3m_V^2/(2\pi\alpha) \simeq (8m_V)^2$, and turns out to be parametrically suppressed relative to continuum production; the details of the corresponding calculation are included in supplementary section 2.7. The dominant continuum production corresponds to temperatures of $m_V$ and below where the $T$-dependence of $\sum |M_{l\bar{l}}|^2$ can be safely neglected. In the present model it is given by

$$\sum |M_{l\bar{l}}|^2 = 16\pi\alpha_{\rm eff} m_V^2 \left(1 + 2\frac{m_l^2}{m_V^2}\right). \tag{2.8}$$

The same matrix element determines the decay width,

$$\Gamma_{V\to l\bar{l}} = \frac{\alpha_{\rm eff}}{3} m_V \left(1 + 2\frac{m_l^2}{m_V^2}\right)\sqrt{1 - 4\frac{m_l^2}{m_V^2}}. \tag{2.9}$$

The right hand side of (2.7), that can be understood as the number of $V$ particles emitted per unit volume per unit time. In the MB approximation, it can be reduced to

$$\frac{1}{(2\pi)^3}\frac{1}{4}\int_{\text{Eq. 2.11}} dE_l\, dE_{\bar{l}}\, e^{-\frac{E_l+E_{\bar{l}}}{T}} \sum |M_{l\bar{l}}|^2, \tag{2.10}$$

where the integration region is given by

$$\left|\frac{m_V^2}{2} - m_l^2 - E_l E_{\bar{l}}\right| \leq \sqrt{E_l^2 - m_l^2}\sqrt{E_{\bar{l}}^2 - m_l^2}. \tag{2.11}$$

In the approximation where only electrons are allowed to coalesce and their mass neglected, $m_l \ll m_V < 2m_\mu$, (2.11) reduces to $E_l E_{\bar{l}} \geq m_V^2/4$ and the integration leads to the familiar modified Bessel function,

$$s\dot{Y}_V = \dot{n}_V + 3Hn_V = \frac{3}{2\pi^2}\Gamma_{V\to l\bar{l}} m_V^2 T K_1(m_V/T), \tag{2.12}$$

where $Y_V = n_V/s$ is the number density normalized by the total entropy density, and $\Gamma_{V\to l\bar{l}} = \alpha_{\rm eff} m_V/3$, without $(m_l^2/m_V^2)$-suppressed corrections, is used for consistency. The final freeze-in abundance via a given lepton pair is given by

$$Y_{V,f}^l = \int_0^\infty dT \frac{\dot{Y}_V^l}{H(T)T}. \tag{2.13}$$

The integrals are evaluated numerically using

$$H(T) \simeq 1.66\sqrt{g_*(T)}\frac{T^2}{M_{\rm pl}}; \qquad s(T) = \frac{2\pi^2}{45}g_*(T)T^3, \tag{2.14}$$

where $g_*(T)$ is the effective number of relativistic degrees of freedom, evaluated with the most recent lattice and perturbative QCD results (see appendix A for details).

For the simplest case of the MB distribution, with only relativistic electrons and positrons contributing and away from particle thresholds that change $g_*(T)$, the final integral can be evaluated analytically, and we have

$$Y^e_{V,f} = \frac{9}{4\pi}\frac{m_V^3\Gamma_{V\to e\bar{e}}}{(Hs)_{T=m_V}} = 0.72\frac{m_V^3\Gamma_{V\to e\bar{e}}}{(Hs)_{T=m_V}}. \tag{2.15}$$

This number reduces somewhat if the FD statistics is used, $0.72_{\rm MB} \to 0.54_{\rm FD}$, but receives a $\sim 20\%$ upward correction from the transverse resonance (see supplementary section 2.7). Our numerical integration routine includes both the correct statistics and the addition of resonant production.

While the treatment of leptonic VDP production might be tedious but straightforward, hadronic production in the early universe is not calculable in principle, as one cannot simply extrapolate measured rates for the conversion of virtual photons to hadrons above temperatures of the QCD and/or chiral phase transitions. While the generic scaling captured by Eq. 2.15 holds, one needs to make additional assumptions about the treatment of the primordial hadron gas. It seems reasonable to assume that at high temperatures, when all light quarks are deconfined, the individual quark contribution $Y^q_{V,f}$ can be added by imposing a lower cutoff at the confinement scale $T_c$ in the integral (2.13) and multiplying the matrix element (2.8) by the square of the quark electric charge $Q_q^2$. Below $T_c$ we will use a free meson gas as an approximation for the hadronic states, and production via inverse charged pion and kaon decays $\{\pi^+\pi^-, K^+K^-\} \to V$ is included using a scalar QED model (see supplementary section 2.8).

The VDPs when produced are semi-relativistic, and the subsequent expansion of the Universe quickly cools them so that at the time of decay $E_V = m_V$. The decay deposits this energy into $e^\pm$, $\mu^\pm$ and $\pi^\pm$ pairs, and more complicated hadronic final states when $m_V$ is above the $\rho$-resonance. Thus, the energy stored per baryon (before

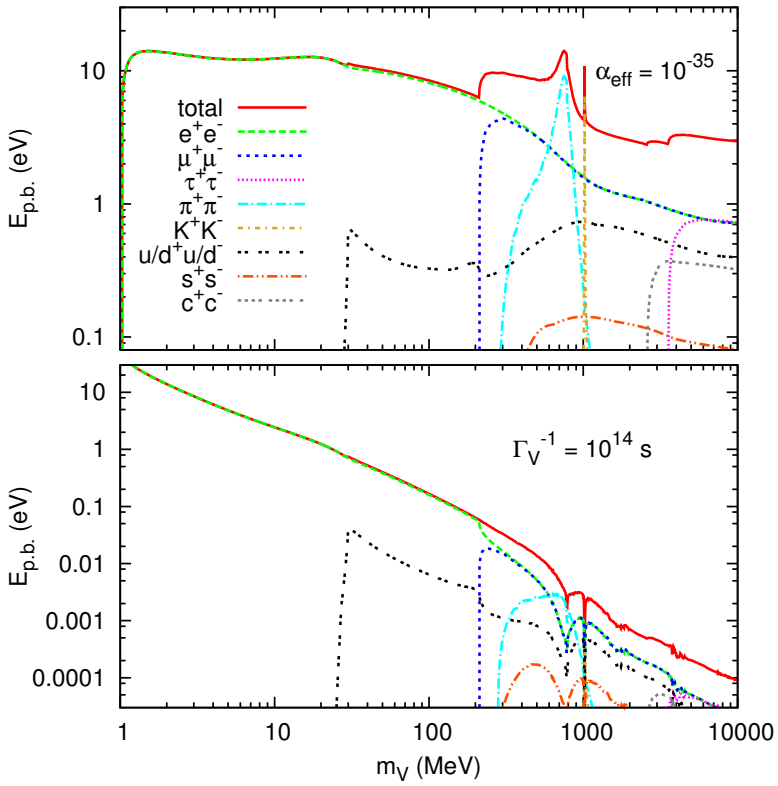


Figure 2.3: Total energy stored per baryons for $\alpha_{\rm eff} = 10^{-35}$ (upper) and $\Gamma_V^{-1} = 10^{14}$s (lower) from the various production channels as labeled.

the characteristic decay time) is given by

$$E_{\rm p.b.} = m_V Y_{V,f} \frac{s_0}{n_{b,0}}, \tag{2.16}$$

where $n_{b,0}/s_0 = 0.9 \times 10^{-10}$ is the baryon-to-entropy ratio today. $E_{\rm p.b.}$ is shown in two separate panels in Fig. 2.3. The top panel shows it as a function of $m_V$ at fixed $\alpha_{\rm eff}$, and the lower panel fixes the VDP lifetime to $\tau_V = 10^{14}$s. We illustrate the contributions from the different production channels. Using this calculated VDP energy reservoir we are now ready to explore its consequences for BBN and the CMB.

## 2.4 Impact on BBN

Late decays of dark photons affect the epoch of primordial nucleosynthesis after cosmic time $t \gtrsim 1$ sec in a variety of ways. The resulting constraints are governed by a combination of lifetime and abundance, and both have complementary trends with respect to $m_V$; $\tau_V$ ($Y_V$) decreases (increases) with growing mass. Therefore we generally expect constraints to be bounded and localized islands in parameter space with the relevant combination of $m_V$ and $Y_V$ to ensure BBN sensitivity.

Prior to decay, $V$ contributes to the matter content substantially, $n_V/n_b \lesssim 10^8$ for $\tau_V < 1$ sec. Whereas the modification of the Hubble rate is generally small, the decays of $V$ imply the injection of electrons, muons, pions, etc., in numbers larger than baryons. The effects on BBN are best described by partitioning the decay into electromagnetic and hadronic energy injection and in the following we provide a lightning review of those modes separately.

MeV-scale dark photons with $m_V < 2m_\pi$ provide a prototypical model of electromagnetic energy injection because the dominant kinematically accessible decay modes are $V \to e^+e^-, \mu^+\mu^-$. Muons decay before interacting weakly, and electron-positron pairs are instantly thermalized via rapid inverse Compton scattering on background photons. An electromagnetic cascade forms in energy degrading interactions of photons and electrons. The large number of photons created gives rise to a non-equilibrium destruction and creation of light elements.

The most important feature of the injected photon energy spectrum $f_\gamma(E_\gamma)$ is a sharp cut-off for energies above the $e^\pm$ pair-creation threshold on ambient photons, $E_{\rm pair} \simeq m_e^2/(22T)$. High-energy photons are efficiently dissipated before they can interact with nuclei, so that to good approximation $f_\gamma(E_\gamma) = 0$ for $E_\gamma > E_{\rm pair}$. In contrast, less energetic photons below the pair-creation threshold can interact with the light elements. Equating $E_{\rm pair}$ against the thresholds for dissociation of the various light elements informs us about the temperature and hence cosmic time $t_{\rm ph}$ at which to expect the scenario to be constrained:

$$t_{\rm ph} \simeq \begin{cases} 2\times 10^4\,{\rm sec}, & {}^7{\rm Be}+\gamma \to {}^3{\rm He}+{}^4{\rm He} \quad (1.59\ {\rm MeV}), \\ 5\times 10^4\,{\rm sec}, & {\rm D}+\gamma \to n+p \qquad\qquad\quad (2.22\ {\rm MeV}), \\ 4\times 10^6\,{\rm sec}, & {}^4{\rm He}+\gamma \to {}^3{\rm He}/{\rm T}+n/p \quad (20\ {\rm MeV}), \end{cases}$$

where the binding energy of the nucleus against destruction has been given in parentheses. If $V$ has a long lifetime and $m_V$ is light enough, it is possible that the initially

released energy is already below the pair-creation threshold, $E_e = m_V/2 < E_{\rm pair}$. The cascade will then produce less energetic photons $E_\gamma < E_{\rm pair}$. In this case, the emitted electron thermalizes in the Thomson scattering regime producing many soft photons, rather than a smaller number with high energy. This situation happens for $\tau \gtrsim 3 \times 10^6$s and the photo-dissociation is much less efficient [102]. Finally, note that we also find that neutrino injection from muon decay does not yield observable changes in the light element abundances—a facinating story in itself [69].

Once $m_V > 2m_\pi$, the hadronic channels open in the decay of $V$ and the effects on BBN become more difficult to model. A major simplification is that only long-lived mesons $\pi^\pm$, $K^\pm$, and $K_L$, with lifetime $\tau \sim 10^{-8}$ sec, and (anti-)nucleons have a chance to undergo a strong interaction reaction with ambient protons and nuclei. The relevant reactions are charge exchange, *e.g.* $\pi^- + p \to \pi^0 + n$, and absorption with subsequent destruction of light elements, *e.g.* $\pi^- + {}^4{\rm He} \to T + n$. Prior to the end of the deuterium bottleneck at $T \simeq 100$ keV only the former reactions are possible. They change the $n/p$ ratio that determines the primordial $^4$He value. Later, once elements have formed, charge exchange creates "extra neutrons" on top of the residual and declining neutron abundance. Moreover, spallation of $^4$He with non-equilibrium production of mass-3 elements and secondaries, *e.g.* through ${\rm T} + {}^4{\rm He}_{\rm bg} \to {}^6{\rm Li} + n$, are important. We model all such reactions in great detail, include secondary populations of pions from kaon decays, and various hyperon producing channels from reactions of kaons on nucleons and nuclei. A detailed exposition of the hadronic part along with a discussion of all included reactions can be found in Ref. [69]. More details are provided when discussing our findings below as well as in supplementary section 2.9.

We now proceed to review the light element observations that form the basis of our adopted limits. Probably the most notable recent developments in the determination of light element abundances are two precision measurements of D/H from high-$z$ QSO absorption systems [103, 104]. Both have error bars that are a factor $\sim 5$ smaller than the handful of previously available determinations. Taken together, the mean observationally inferred primordial D/H value now reads [104],

$$ {\rm D/H} = (2.53 \pm 0.04) \times 10^{-5}. \tag{2.17} $$

Nonetheless, systematically higher levels of primordial D/H are conceivable, in spite of the above error bar. For example, D may be astrated or absorbed on dust grains. Indeed, values as high as $4 \times 10^{-5}$ have been reported [105, 106], so as a conservative

upper limit we employ,

$$\mathrm{D/H} < 3 \times 10^{-5}. \tag{2.18}$$

On the flip side, underproducing D yields a robust constraint since no known astrophysical sources of D exist. We account for this constraint either by adopting the nominal lower $2\sigma$-limit from (2.17) or by demanding,

$$^3\mathrm{He/D} < 1. \tag{2.19}$$

The latter limit employs the solar system value [107] and arises from the consideration that D is more fragile than $^3$He, and hence a monotonically increasing function of time. Despite the uncertain galactic chemical evolution of $^3$He, (2.19) can therefore be considered robust.

The inference of the primordial mass fraction $Y_p$ from extragalactic H-II regions proved to be systematically uncertain in the past [108, 109] and values in the range

$$0.24 \leq Y_p \leq 0.26 \tag{2.20}$$

have been reported. We adopt this range as our cosmologically viable region.

Finally, what is believed to be the primordial value of $^7$Li/H, the so-called Spite plateau [110], is a factor of 3-5 lower than the lithium yield from standard BBN, $^7\mathrm{Li/H} = (5.24^{+0.71}_{-0.67}) \times 10^{-10}$ [23]. We deem the lithium problem solved in this model if we can identify a region in parameter space where lithium is reduced to the Spite plateau value,

$$10^{-10} < {}^7\mathrm{Li/H} < 2.5 \times 10^{-10}. \tag{2.21}$$

We take an opportunity to comment that the status of the lithium problem is somewhat controversial: while it is possible that new physics is responsible for its solution, the astrophysical lithium depletion mechanisms can also be invoked (see Ref. [22] for a review of this subject).

We are now in a position to present our results in Fig. 2.4 where a scan over the $m_V, \kappa$ parameter space is shown, and contours of constant lifetime, $\tau_V$ and relic abundance $n_V/n_b$ prior to decay are shown by the diagonal solid and dotted lines, respectively. Three distinct regions labeled I-III are identified as being in conflict

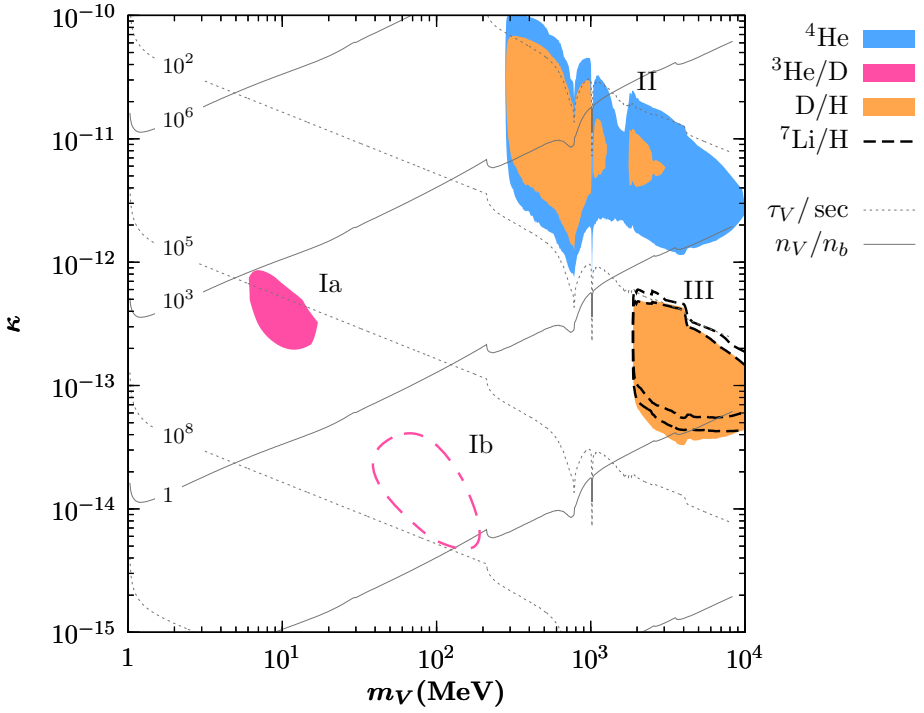


Figure 2.4: Effects on BBN from the decay of relic dark photons as a function vector mass of $m_V$ and kinetic mixing parameter $\kappa$. The diagonal gray lines are contours of lifetime $\tau_V$ (solid) and abundance per baryon $n_V/n_b$ prior to decay (dotted). Shaded regions are excluded as they are in conflict with primordially inferred light element abundances. The black dashed black lines are contours of decreasing $^7$Li/H abundance, $4\times10^{-10}$ and $3\times10^{-10}$, going from the outside to the inside, respectively. The pink dashed line is a mild increase in $^3$He/D, but not beyond the observational limit.

with observations. They arise from distinct physical processes which we now proceed to describe.

**Regions I:** In the regions labeled I the dark photon exclusively decays to $e^+e^-$. They are associated with pure electromagnetic energy injection.

In region Ia, the lifetime is $\tau_V \sim 10^5$ sec resulting in the destruction of $^7$Be and D. Deuterium is underproduced and the dark photon is ruled out by the constraint $^3\mathrm{He/D} < 1$ in the pink shaded region. An equivalent bound from the requirement $\mathrm{D/H} > 10^{-5}$ coincides with this one and is not shown.

In region Ib, with a $V$ lifetime of $\sim 10^7$ sec, $^4$He is being mildly dissociated. The efficiency is greatly reduced because of the softer spectrum of photons, a consequence of the Thomson scattering thermalization. Although there is a feeble increase in

$^3$He/D, it remains safely in the unconstrained region [102].

**Region II:** Now we turn to the low-lifetime/high-abundance region II. The lifetime of $V$ is below 100 sec and hence marks a choice of parameters where the dark photon decays before the end of the D-bottleneck ($T \sim 100$ keV). The injection of pions and—if kinematically allowed—of kaons and nucleons, induces $n \leftrightarrow p$ interconversion. It has the general effect that the $n/p$-ratio rises. The elevated number of neutrons that in turn become available at the end of the D-bottleneck allow for more D-formation and subsequently more $^4$He. The region is therefore challenged by the constraints $Y_p \leq 0.26$ and $\mathrm{D/H} \leq 3 \times 10^{-5}$.

**Region III:** Finally, region III is characterized by the presence of "extra neutrons" that appear right after the main stage of nucleosynthesis reactions at cosmic times $t \sim 10^3$ sec. The origin of those neutrons is twofold. First, there is a direct injection of $n$ from the decay $V \to n\bar{n}$. Second, there is indirect production, from charge exchange of $\pi^-$ on protons, $\pi^- p \to n\pi^0$ or $\pi^- p \to n\gamma$, and from hyperon production by "s-quark" exchange of $K^-$ on protons with subsequent hyperon decay. We note in passing that $K^- p \to \bar{K}^0 n$ has positive $Q$-value and is not allowed for stopped kaons; conservatively, we neglect this reaction.

The elevated neutron abundance leads to a chain of reactions that depletes the overall lithium abundance,

$$\text{step 1:} \quad {}^7\mathrm{Be} + n \to {}^7\mathrm{Li} + p, \tag{2.22}$$

$$\text{step 2:} \quad {}^7\mathrm{Li} + p \to {}^4\mathrm{He} + {}^4\mathrm{He}. \tag{2.23}$$

In the first step, $^7$Be charge exchanges with the neutron and forms $^7$Li. In a second step, $^7$Li, because it has one less unit of charge, is more susceptible to being destroyed by protons. The result of this mechanism is shown in Fig. 2.4 by the dashed curves. Most of the extra neutrons are, however, intercepted by protons so that this potential solution to the lithium problem is always accompanied by an elevated D-yield. The D/H constraint (2.18) is shown by the (orange) solid region.

A more detailed description of the calculations used to obtain these results is provided in supplementary section 2.9.

## 2.5 Impact on the CMB

Later decays of VDP, which occur after recombination if $\tau_V \gtrsim 10^{13}$s, can leave an imprint on the CMB. In particular, as discussed in [71, 70], the altered ionization history tends to enhance the TE and EE spectra on large scales, while the TT temperature fluctuation is damped on small scales. Consequently, precision CMB data can be used to further constrain the VDP parameter space in regimes where the late decays impact the ionization history.

The energy injection of a decaying species can be generically parametrized as [71, 70]

$$\frac{dE}{dtdV} = 3\zeta m_{\rm p}\Gamma e^{-\Gamma t}, \tag{2.24}$$

with $(1-x_e)/3$ of this energy going to ionization and $(1+2x_e)/3$ heating the medium, $x_e$ representing the ionized fraction. The energy output of each decay is $3\zeta m_{\rm p}$, the normalization chosen so that (2.24) gives the ionizing energy after recombination ($x_e \to 0$). Using CLASS [111] to obtain the CMB power spectra and MONTEPYTHON [112] as a Monte Carlo Markov Chain driver, we determine the $2\sigma$ limits from the Planck 2013 results [113] (which also incorporates the low-$l$ polarization likelihood from WMAP9 [30]). The limits are shown in Fig. 2.5, with constraints similarly derived from WMAP7 [114] + SPT [115], along with the WMAP3 and 2007 Planck forecast fits from [70]. The cutoff at $\Gamma^{-1} = 10^{13}$s appears since Ref. [70] used a purely matter-dominated approximation for the elapsed time $\left[t(z) \sim (1+z)^{-3/2}\right]$ in the exponential of (2.24) and assumed that decay lifetimes shorter than $10^{13}$ seconds happen before recombination and do not impact the CMB. In our calculations, we use the exact time from ΛCDM cosmology and obtain a more accurate picture for shorter lifetimes.

The energy output $\zeta$ can be related to the VDP parameters as follows,

$$\zeta = \frac{f}{3}\frac{\Omega_V}{\Omega_b} = \frac{f}{3}\frac{E_{\rm p.b.}}{m_p}. \tag{2.25}$$

The pre-factor $f$ determines the overall efficiency with which the deposited energy goes into heating and ionization. The thermalization of an energetic particle depends on the species, initial energy and redshift [116, 117]. Ref. [118] provides transfer functions $T(z_{inj}, z_{dep}, E)$ giving the fractional amount of energy deposited at $z_{dep}$ for

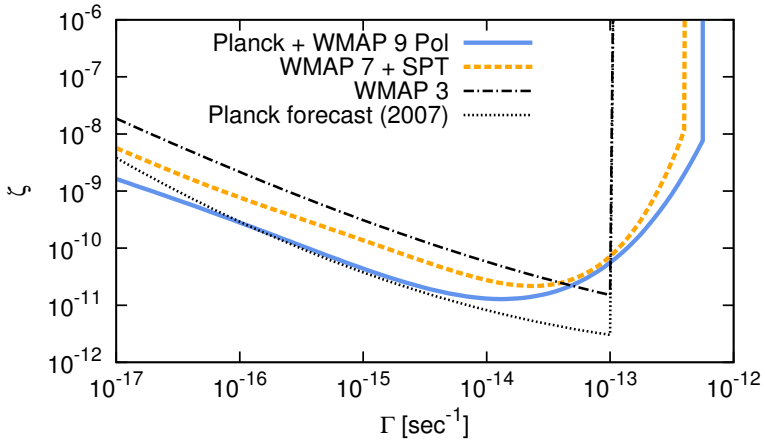


Figure 2.5: CMB constraints on the energy injection parameters $\zeta$ and $\Gamma$. For comparison, we include the WMAP3 curve and the Planck forecast (2007) from Ref. [70].

an energy injection $E$ at $z_{inj}$ for both $\gamma$ and $e^+e^-$ final states. With this information, we can numerically solve for the deposition efficiency of the injected energy from decaying particles [118],

$$f(z) = \frac{\frac{dE}{dz}\big|_{\rm dep}(z)}{\frac{dE}{dz}\big|_{\rm inj}(z)} \tag{2.26}$$

$$= \frac{H(z)\sum_{\rm species}\int_z^\infty \frac{d\ln(1+z_{\rm in})}{H(z_{\rm in})}\int T(z_{\rm in},z,E)E\frac{d\tilde{N}}{dE}dE}{\sum_{\rm species}\int E\frac{d\tilde{N}}{dE}dE}, \tag{2.27}$$

where $\frac{d\tilde{N}}{dE}$ is the normalized energy distribution of the $e^+e^-$ or $\gamma$ in the decaying particle rest frame. This strategy has been used in Refs. [117, 119] to analyze dark matter annihilation and decay to standard model particles for $m_\chi > 1$ GeV. An effective deposition efficiency $f_{\rm eff}$ is found by averaging $f(z)$ over the range $800 < z < 1000$. We compute $f_{\rm eff}$ for VDP in the mass range 1-500 MeV where the decay channels are $V \to \{e^+e^-, \mu^+\mu^-, \pi^+\pi^-\}$ [120]. The results for $f_{\rm eff}(m_V)$, along with each decay channel contributions and their branching ratios, are shown in Fig. 2.6 for $\Gamma_V^{-1} = 10^{14}$s. The low efficiency of $\mu^\pm$ and $\pi^\pm$ is due to the neutrinos radiating away a large fraction of the energy. For $e^\pm$ with $E \gtrsim 100$ MeV, the longer cooling time lowers the efficiency [118], which is clearly seen in the $f_{\rm eff}^{e^\pm}$ curve.

Using the result (2.16) with $f_{\rm eff}$ in (2.25), we find that our CMB constraints on

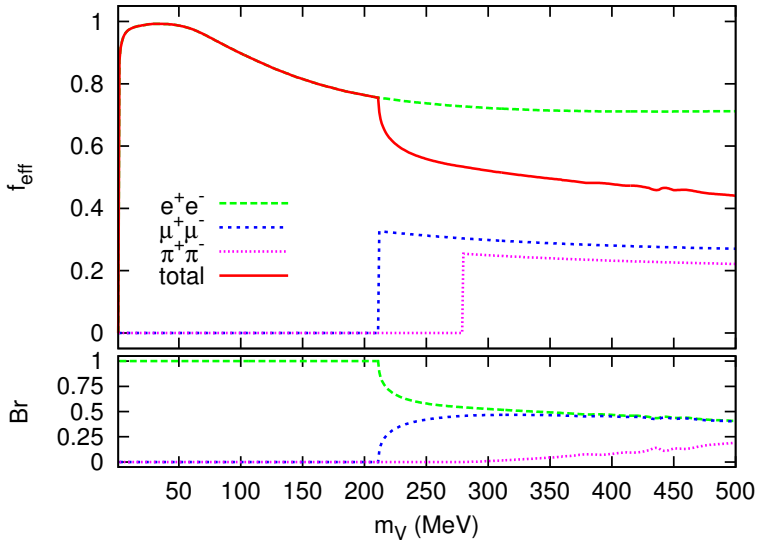


Figure 2.6: Effective deposition efficiency for each decay channel with the sum weighted by the branching ratios for $\Gamma_V^{-1} = 10^{14}$s.

$\Gamma - \zeta$ lead to the excluded region of parameter space shown in Fig. 2.7. We find this to be a rather remarkable sensitivity to an effective electromagnetic coupling as small as $\alpha_{\rm eff} \sim 10^{-37} - 10^{-38}$!

## 2.6 Concluding Remarks

The kinetic mixing portal is one of the few renormalizable interaction channels between the SM and a neutral hidden sector. As such, it is of interest to understand the full spectrum of limits on dark photons coupled through this portal. In this chapter, we have determined the cosmological constraints due to the impact of late decays on BBN and the CMB; the sensitivity extends to remarkably small effective electromagnetic couplings. In this concluding section, we comment on possible indirect signatures in the present day universe from the decay of relic dark photons, and other potential extensions.

It is important to emphasize that the constraints derived in this work rely only on the thermal production of VDP and the minimal cosmological history of the Universe. For the mass range of VDP considered here, the constraints will hold as long as temperatures $T \sim \mathcal{O}(1) - \mathcal{O}(100)$ MeV were attained at an early epoch. Any additional contributions to the abundance of VDP, such as production of $V$ through

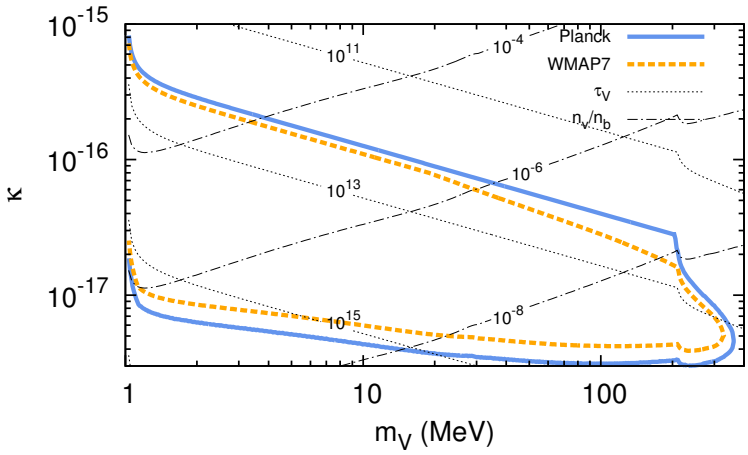


Figure 2.7: The solid contour lines bound the regions excluded by the CMB constraints on VDP. Contours of the lifetime in seconds and relative number density of dark photons to baryons prior to their decay are also shown.

other portals, or nonthermal contributions to $m_V^2\langle V_\mu^2\rangle$ due to vacuum misalignement mechanisms, will enhance the VDP abundance, and correspondingly strengthen the bounds on $\kappa$.

The analysis in this chapter assumed that the vector mass was above the electron threshold. For lower masses, $V$ naturally has a lifetime well in excess of the age of the universe and can play the role of dark matter [121, 78]. In this regime its relic abundance is fixed instead by Thomson-like scattering, $e+\gamma \to e+V$. As discussed in [121], for $m_V \sim 100$ keV, indirect constraints still allow this cosmological abundance with $\kappa \sim 10^{-11}$, but photoelectric absorption in dark matter detectors would leave a detectable ionization signal. The electronic background data from XENON100 in the 1-100 keV range [122] indicated no signal, thus appearing to close this window, as discussed in more detail in [123]. Very recently, these limits have also been improved by XMASS [124]. Nevertheless, minimal extensions of VDP in this mass range can provide viable models of superweakly-interacting massive particle dark matter. One option is to have a dark Higgs $h'$ responsible for breaking $U(1)_V$ and generating the dark photon mass. In the $m_{h'} < m_V$ regime, this will lead to extremely long-lived $h'$ particle states since $\Gamma_{h'} \propto \kappa^2$ [120]. In this case, one would require somewhat larger values of $\kappa$ to ensure a more efficient $e^-e^+ \to Vh'$ production channel. Another option is simply a new state state $\chi$, which is stable and charged under $V$. The analysis of these very light dark matter models goes beyond the scope of the present chapter.

We can also consider a higher mass range, e.g. TeV-scale dark photons, whose present-day decays could provide signatures in antimatter, gamma-ray and neutrino observations [125]. With a more massive dark vector, the full kinetic mixing with hypercharge should be included, $\mathcal{L}_{\rm V} = -\frac{\tilde{\kappa}}{2} B_{\mu\nu} V^{\mu\nu} = -\frac{\kappa}{2} F_{\mu\nu} V^{\mu\nu} + \frac{\kappa \tan\theta_w}{2} B_{\mu\nu} Z^{\mu\nu}$, where $\tilde{\kappa} = \kappa \cos\theta_w$ to keep the same normalization as before. Fermions then acquire both vector and axial vector couplings to $V$, modifying both the production and decays rates. Assuming $m_V \gg m_Z$, and generalizing (2.8) by summing over all degrees of freedom for $\gamma$ and $Z$ mediation, leads to

$$\Gamma_V \simeq 10^{-17}\mathrm{s}^{-1} \left(\frac{\alpha_{\rm eff}}{10^{-45}}\right) \left(\frac{m_V}{1\ \mathrm{TeV}}\right). \tag{2.28}$$

In the MB approximation, freeze-in production is analogous to (2.15), and using $g_\star \simeq 100$ and summing over the channels, we find

$$Y_{V,f} \simeq 10^{-31} \left(\frac{\Gamma_V}{10^{-17}\mathrm{s}^{-1}}\right) \left(\frac{\mathrm{TeV}}{m_V}\right)^2. \tag{2.29}$$

This is minuscule compared to the cold dark matter energy density

$$\frac{n_V m_V}{\rho_{\rm CDM}} \simeq 10^{-19} \left(\frac{\Gamma_V}{10^{-17}\mathrm{s}^{-1}}\right). \tag{2.30}$$

Decaying dark matter of that mass range, with 100% leptonic branching, requires a lifetime of $\tau_{\rm DM} = 10^{26}$s [125] to contribute to the increasing positron fraction in cosmic rays observed by PAMELA [35] and AMS-02 [37]. The VDP scenario thus falls short by many orders of magnitude. Similar conclusions follow for neutrino experiments, where decaying dark matter with mass $10 - 10^{15}$ TeV requires a lifetime of $\mathcal{O}(10^{26} - 10^{28})$s [126, 127]. Very long-lived dark photons are therefore too feebly coupled in this minimal scenario to contribute to these indirect detection signals.

Finally, we note that the analysis performed in this chapter can easily be extended to other cases of "very dark" particles. For example, super-weakly interacting singlet scalars $S$, coupled to the SM via the renormalizable Higgs portals $ASH^\dagger H + \lambda S^2 H^\dagger H$ can be probed via BBN [69] and the CMB. While the main cosmological constraints will be very similar to the VDP case, the details of the production from the Higgs portal are different, and shifted to the earlier electroweak epoch. The analysis of this minimal scalar model is presented in chapter 5.

## 2.7 Supplementary: Resonant Production

Here we demonstrate that the thermal effects, and the associated resonant production, create a parametrically suppressed contribution to $Y_{V,f}$, although numerically it may constitute as much as 30%.

### 2.7.1 Relativistic Case

We begin the analysis by choosing the simplest case of electron-positron coalescence and use MB statistics. Since thermal effects are going to be important at higher temperatures than $m_V$, $m_e$ is negligible and can be set to 0 from the start. Furthermore, we break up the matrix element into the longitudinal and transverse pieces according to the polarization of the $V$ boson produced with four-momentum $(\omega, \vec{q})$ to derive the right-hand side of the Boltzmann equation (2.7). After direct calculation we obtain

$$\begin{aligned} \text{R.H.S.} = \frac{3}{2\pi^2} m_V \Gamma_{V\to e\bar{e}} \int_{m_V}^{\infty} d\omega \sqrt{\omega^2 - m_V^2}\, e^{-\omega/T} \\ \times \left\{ \frac{1}{3} \frac{m_V^4}{|m_V^2 - \Pi_L|^2} + \frac{2}{3} \frac{m_V^4}{|m_V^2 - \Pi_T|^2} \right\}. \end{aligned} \tag{2.31}$$

The polarization tensors $\Pi_{T(L)}$ are complex functions of $\omega, |\vec{q}|$ and $T$, and originate from the virtual photon propagators. In the limit of vanishing plasma density, $\Pi_{T(L)} \to 0$, the expression inside $\{...\}$ tends to 1, and the R.H.S. becomes identical to that of (2.12), as it should be. The expressions for $\Pi_{T(L)}$ can be found in the thermal field theory literature, and we use the results of [128], with the more symmetric definition of the longitudinal polarization tensor [79], $\Pi_L^{\text{this work}} = \frac{m_V^2}{\omega^2 - m_V^2} \Pi_L^{\text{Ref. [128]}}$.

For a one-component ultra-relativistic plasma (again neglecting muon and pion contributions etc.), the expressions for the real parts of the polarization tensors are given by [128],

$$\begin{aligned} \text{Re}\Pi_T(\omega) &= \omega_p^2 \frac{3\omega^2}{2\vec{q}^2} \left( 1 - \frac{m_V^2}{\omega^2} \frac{\omega}{2|\vec{q}|} \log \frac{\omega + |\vec{q}|}{\omega - |\vec{q}|} \right), \\ \text{Re}\Pi_L(\omega) &= 3\omega_p^2 \frac{m_V^2}{\vec{q}^2} \left( \frac{\omega}{2|\vec{q}|} \log \frac{\omega + |\vec{q}|}{\omega - |\vec{q}|} - 1 \right), \end{aligned} \tag{2.32}$$

where all the factors of $|\vec{q}|$ can be replaced with $\sqrt{\omega^2 - m_V^2}$. The plasma frequency

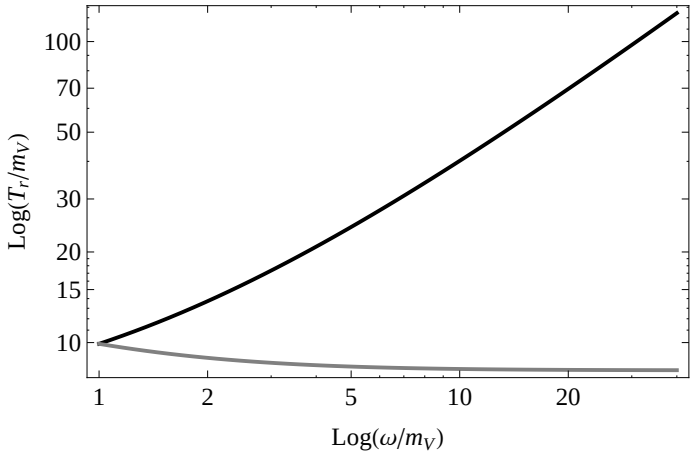


Figure 2.8: The dependence of the resonant temperatures $T_{r,L}$ (black) and $T_{r,T}$ (gray) on frequency $\omega$, all in units of $m_V$. The transverse resonance frequency asymptotes to $T_{\rm min} = m_V(3/(2\pi\alpha))^{1/2}$.

of the electron-positron fluid is given by

$$\omega_p^2 = \frac{4\pi\alpha}{9}T^2. \tag{2.33}$$

The imaginary parts of the polarization tensors are related to the massive photon decay rate in vacuum, $\Gamma_0 = \alpha m_V/3$,

$$\mathrm{Im}\Pi_{T(L)} = -\Gamma_0 m_V \left(1 - \exp(-\omega/T)\right). \tag{2.34}$$

(The VDP decay rate in vacuum is $\kappa^2\Gamma_0$ in this approximation.) Armed with these expressions, we can derive the conditions for a resonance, that is the point in $\{T, \omega\}$ where the denominator of (2.31) is minimized,

$$\mathrm{Re}\Pi_{T(L)}(\omega, T_{r,T(L)}) = m_V^2. \tag{2.35}$$

The dependence of $T_{r,T(L)}(\omega)$ is plotted in Fig. 2.8. The most important point is that all resonance frequencies are parametrically larger than $m_V$, and there is a minimum frequency at which the resonance can happen,

$$T_{\rm min} = m_V \left[\frac{3}{2\pi\alpha}\right]^{1/2} \simeq 8.1\, m_V. \tag{2.36}$$

Thus all resonances occur at temperatures that are parametrically larger (by a factor of $\alpha^{-1/2}$) than $m_V$, where the Hubble expansion rate is significantly greater than at $T < m_V$. We proceed by calculating the resonant contributions by using the narrow width approximation, that is we approximate the ratios inside the {...} of Eq. (2.31) by delta functions,

$$\frac{m_V^4}{|m_V^2 - \Pi|^2} \simeq \frac{3\pi}{2\alpha} \frac{T_r(\omega)\delta[T - T_r(\omega)]}{e^{\omega/T} - 1}. \tag{2.37}$$

This expression holds for both the $T$ and $L$ resonances.

The resonant contribution to the VDP abundance comes from evaluating two integrals, over $T$ and $\omega$. If the integral over the temperature is performed first, one finds

$$\begin{aligned} \Delta Y_{f,r} &= Y_T + Y_L, \\ Y_{T(L)} &= \frac{3 g_{T(L)}}{4\pi\alpha} \frac{m_V^3 \Gamma_{V\to e\bar{e}}}{(Hs)_{T=m_V}} \int_{m_V}^{\infty} \frac{m_V^3 \sqrt{\omega^2 - 1} d\omega}{(T_{r,T(L)}(\omega))^5 [e^{\omega/T} - 1]}, \end{aligned} \tag{2.38}$$

where $g_{T(L)} = 2(1)$ are the multiplicity factors. Performing the remaining integral we arrive at the following result,

$$\Delta Y_{f,r} \simeq \Delta Y_T \simeq 0.17 \times \frac{m_V^3 \Gamma_{V\to e\bar{e}}}{(Hs)_{T=m_V}}. \tag{2.39}$$

The longitudinal resonance turns out to be negligible on account of the large value of $T_{r,L}$ when $\omega \sim T_{r,L}$. (This is in contrast with the stellar production of very light dark photons, where the $L$-resonance dominates [79].) We now see that although the resonant contribution (2.39) is parametrically suppressed, by $O(\alpha^{1/2})$, relative to the continuum contribution (2.15), it can reach 20% of the total. Repeating the same calculations with FD statistics changes the coefficient only slightly, $0.17_{\rm MB} \to 0.15_{\rm FD}$.

### 2.7.2 Nonrelativistic Corrections

The analytical treatment of resonant production above is only valid for massless particles in the loop. In our numerical calculations, we include the $\Pi_{T,L}$ effects for all leptons of mass $m < 10$ GeV and charged pions for $T < T_c$. Ref. [128] provides analytical approximations for $\mathrm{Re}\Pi_{T,L}$, which interpolate smoothly between the 'classical'

(nonrelativistic) and relativistic limits,

$$\mathrm{Re}\Pi_{\mathrm{T}} = \omega_p^2 \frac{3}{2v_\star^2}\left(\frac{\omega^2}{k^2} - \frac{\omega^2 - v_\star^2 k^2}{k^2}\frac{\omega}{2v_\star k}\log\frac{\omega + v_\star k}{\omega - v_\star k}\right), \tag{2.40}$$

$$\mathrm{Re}\Pi_{\mathrm{L}} = \omega_p^2 \frac{3m_v^2}{v_\star^2 k^2}\left(\frac{\omega}{2v_\star k}\log\frac{\omega + v_\star k}{\omega - v_\star k} - 1\right), \tag{2.41}$$

where

$$\omega_p^2 = \frac{8\alpha}{\pi}\int_0^\infty dp\frac{p^2}{E}\left(1 - \frac{1}{3}\frac{p^2}{E^2}\right)n_F(E), \tag{2.42}$$

$$w_1^2 = \frac{8\alpha}{\pi}\int_0^\infty dp\frac{p^2}{E}\left(\frac{5}{3}\frac{p^2}{E^2} - \frac{p^4}{E^4}\right)n_F(E), \tag{2.43}$$

$$v_\star = \frac{w_1}{w_p}. \tag{2.44}$$

The parameter $v_\star$ can be interpreted as the typical velocity of the fermion at that given energy. We recover the relativistic limit (2.32) with $v_\star \to 1$ and the 'classical' (nonrelativistic) limit with $v_\star \to \sqrt{5T/m_f}$.

In general, the imaginary part of the polarization tensor is given by [129],

$$\mathrm{Im}\Pi = -\omega\Gamma^{\mathrm{Prod}}\left(e^{\frac{\omega}{T}} - 1\right), \tag{2.45}$$

$$\Gamma^{\mathrm{Prod}} = \frac{1}{2\omega}\int\frac{d^3p}{2E_p}\frac{d^3q}{2E_1}\frac{(2\pi)^4}{(2\pi)^6}\delta^4(k - p - q) \tag{2.46}$$

$$\times\left|\mathcal{M}_{1,2\to V}\right|^2 n_1 n_2. \tag{2.47}$$

Here $\Gamma^{\mathrm{Prod}}$ represents the production rate, with $\mathcal{M}_{1,2\to V}$ the matrix element for the particles coalescing into $V$ and $n_1$ and $n_2$ their respective statistical distributions. Separating the T and L parts of matrix element,

$$\left|\mathcal{M}^{T,L}_{l\bar{l}\to V}\right|^2 = 16\pi\alpha(F^T + F^L), \tag{2.48}$$

$$F^T = -2p^2\sin^2\theta + m_V^2, \tag{2.49}$$

$$F^L = -\frac{2}{m_V^2}\left(kE_p - \omega p\cos\theta\right)^2 + \frac{m_V^2}{2}, \tag{2.50}$$

we find

$$\Gamma^{\rm Prod}_{T(L)} = \frac{\alpha}{\omega k}\int_{\frac{\omega}{2}-\frac{k}{2}\sqrt{1-4\frac{m_f^2}{m_V^2}}}^{\frac{\omega}{2}+\frac{k}{2}\sqrt{1-4\frac{m_f^2}{m_V^2}}} dE_p \times \tag{2.51}$$

$$\times\, F^{T(L)}(\omega,p,\theta)\; n(E_p)n(\omega-E_p), \tag{2.52}$$

where $k$ relates to the dark vector, $p/q$ to the fermions in the loop and $\cos\theta = \frac{\omega E_p}{kp} - \frac{m_V^2}{2pk}$.

## 2.8 Supplementary: Hadronic Production

To model hadronic freeze-in production, we treat the coalescence of charged pions into dark photons as a scalar QED process. The spin-summed matrix element is

$$\sum |\mathcal{M}_{s\bar{s}}|^2 = 4\pi\alpha_{\rm eff}^{\pi\pi} m_V^2 \left(1 - 4\frac{m_s^2}{m_V^2}\right), \tag{2.53}$$

with the massless limit being a factor of 4 smaller than the fermionic case (2.8). We include the $\rho$-resonance in the charged-pion interaction via an effective scalar electromagnetic coupling which becomes $m_V$ dependent, $\alpha_{\rm eff}^{\pi\pi}(m_V) = \kappa^2\alpha^{\pi\pi}(\sqrt{s} = m_V)$. The coupling function $\alpha^{\pi\pi}(\sqrt{s})$ is extracted numerically from the $e^+e^- \to \gamma^* \to \pi^+\pi^-(\gamma)$ cross section measured by BaBar collaboration [130], and similarly for the charged kaons [131].

In accounting for thermal effects, the imaginary part of the polarization tensor can be found in the same manner as in section 2.7.1, by separating the matrix element into the different propagation modes for scalars,

$$F_s^T = p^2\sin^2\theta, \tag{2.54}$$

$$F_s^L = \frac{1}{m_V^2}\left(kE_p - \omega p\cos\theta\right)^2, \tag{2.55}$$

and (2.52) can be used with Bose-Einstein statistics.

The real part of the polarization tensor needs to be derived from first principles in finite-temperature field theory as the $\omega/k$ scaling of (2.40) (2.41) does not generally hold. However, it is known [132] that the high temperature limit is the same as (2.32), since the statistics integrals $\int_0^\infty dp\; p\, n_B(p) = 2\int_0^\infty dp\; p\, n_F(p)$ compensate

for the missing spin degrees of freedom [133]. On account of the high resonant temperature (2.36), we find that we can maintain good numerical accuracy with the simple rescaling,

$$\mathrm{Re}\Pi^{\mathrm{s}}_{\mathrm{T(L)}} = \frac{\mathrm{Re}\Pi_{\mathrm{T(L)}}}{2} \frac{\int dp\, \frac{p^2}{E} n_B(E)}{\int dp\, \frac{p^2}{E} n_F(E)}. \tag{2.56}$$

## 2.9 Supplementary: BBN Analysis

Here we provide some additional details regarding the treatment of BBN; the analysis of meson injection draws in large parts from Ref. [69] to which we refer the reader for an exhaustive discussion. The Boltzmann code that we use is based on Ref. [134], but incorporates some significant improvements and updates. These are likewise detailed in [69]. Our SBBN yields are in excellent agreement with those presented in [23] at the WMAP value of $\eta_b = 6.2 \times 10^{-10}$ and with a neutron lifetime of $\tau_n = 885.7\,\mathrm{s}$.

Below the di-pion threshold, $m_V \leq 2m_{\pi^\pm} = 279$ MeV, only electromagnetic energy injection from $V$-decays is relevant. As discussed in section 2.4, the formation of a photon cascade $f_\gamma(E_\gamma)$ gives way to photodissociation of nuclei. The rate of destruction of a species $N$ with number density $n_N$ is then given by

$$\Gamma_{\mathrm{ph}}(T) = 2n_N \int_{E_{\mathrm{thr}}}^{E_{\mathrm{max}}} dE_\gamma\, f_\gamma(E_\gamma) \sigma_{\gamma+N\to X}(E_\gamma), \tag{2.57}$$

where $\sigma_{\gamma+N\to X}(E_\gamma)$ is the photo-dissociation cross section for $\gamma + N \to X$ with threshold $E_{\mathrm{thr}}$. The factor of two accounts for the back-to-back $e^\pm$ pair forming two independent cascades, each with a maximum energy of $E_{\mathrm{max}} = \max\{E_{\mathrm{pair}}, E_{\mathrm{inj}}/2\}$. We take into account all relevant light element reactions listed in [135] and we also include secondary processes which may result in production of $^6$Li. The Boltzmann equations describing the temperature evolution of the light elements in the presence of energy injection are straightforward to obtain.

With regard to the injection of mesons and nucleons, we restrict ourselves to reactions at threshold, assuming that charged pions and kaons are thermalized before reacting. Likewise we assume that neutrons will be slowed down by their magnetic moment interaction with electrons, positrons and photons and neglect neutral kaons altogether because of their inability to stop and the associated uncertainty in reaction cross section.

We expect such an approximation to result in more conservative constraints. Incomplete thermalization for charged mesons only happens on the whole for temperatures $T < 40$ keV, for which the plasma stopping power diminishes. Away from threshold, pion-nucleon reactions can proceed resonantly, *e.g.* $\pi^- p \to \Delta^0 \to \pi^0 n$, with an efficiency up to $\sim 20 - 30$ times the value for stopped pions. Likewise, the total inelastic $\pi^-$-$^4$He cross section becomes significantly larger for pion kinetic energies of $\sim 150$ MeV. Such enhancements as well as non-thermal neutrons with spallating power lead to stronger departures from the standard case and are therefore more strictly constrained. There is, however, the beneficiary effect of reducing the cosmological lithium abundance towards observationally favored values through the production of "extra neutrons". As pointed out in [69], this process can also be boosted by the above resonances. However, this solution of the lithium problem is challenged by the simultaneous tightening of the D/H constraint, especially in light of the new D/H determinations discussed in the BBN section. For the interested reader, we point out that a detailed quantitative discussion of incomplete stopping can be found in Ref. [69].

Finally, baryon/anti-baryon pairs can be produced directly in the decay of the vector for $m_V \gtrsim 2$ GeV. Upon injection, resonances and hyperons decay to (anti)protons and (anti)neutrons—possibly accompanied pions and kaons—before interacting with the ambient medium. The fate of the final state nucleons is then as follows: $\bar{n}$ and $\bar{p}$ will preferentially annihilate on protons which are the most abundant target in the Universe with an annihilation cross section $\langle \sigma_{\rm ann} v \rangle \sim m_{\pi^\pm}^{-2}$. Depending on the $n/p$ ratio, they also annihilate with neutrons with a similar cross section. The annihilation on protons is faster than the Hubble rate at all relevant temperatures and—if annihilating on protons—the injection of $n\bar{n}$ results in one net $p \to n$ conversion with associated energy injection of $m_p + m_n$. Likewise, if annihilating on neutrons, $p\bar{p}$ injection results in one net $n \to p$ conversion. Assuming equal cross sections, the relative efficiencies for those processes are $p/(n+p)$ and $n/(n+p)$ respectively and we treat this sequence of events as being instantaneous.

Neutron injection during BBN in the decay $V \to n\bar{n}$ and close to the threshold $m_V \gtrsim 2m_n$ can be studied by utilizing the (only) measurement of electron-positron annihilation to the neutron-antineutron final state, $e^+e^- \to n\bar{n}$ [136]. At threshold, $\sigma_{e^+e^- \to n\bar{n}} \sim 1\,\text{nb}$ is reported. With a total hadronic cross section $\sigma_{e^+e^- \to \text{had}} \sim 50\,\text{nb}$ this points to a branching fraction $\sim 2\%$. In our actual analysis we use a more conservative value that arises from a joint extraction of the neutron Sachs electric

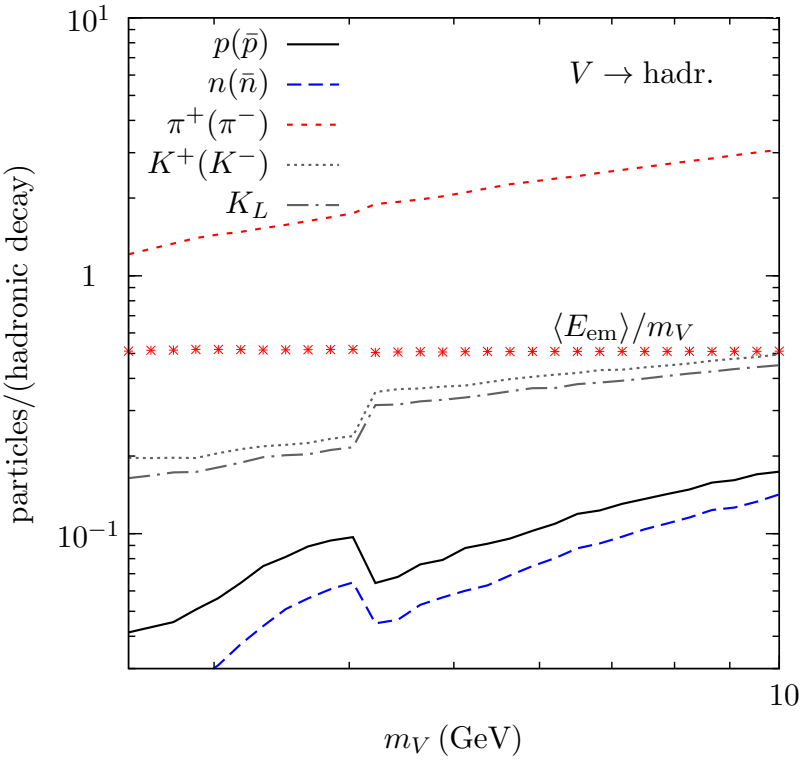


Figure 2.9: The average number of particles per $V$ decay with $m_V > 2.5$ GeV, from a Pythia simulation. Also shown is the average electromagnetic energy injected after all particles have decayed to electrons and photons ($e^+$ are assumed to have annihilated on $e^-$.) When including leptonic channels, to a good approximation 1/3 of the energy is carried away in the form of neutrinos. Resonances like $J/\psi$ are not captured by the resolution of the simulation and we neglect such isolated points in the parameter space.

(magnetic) form factor $|G^n_{E(M)}(q^2)|$ in the time-like and space-like regions; for us, the momentum transfer is time-like with $q^2 = m_V^2$ and

$$\sigma_{e^+e^-\to n\bar{n}} = \frac{4\pi\alpha^2}{3q^2}\sqrt{1-\frac{4m_n^2}{q^2}} \times \left[|G^n_M(q^2)|^2 + \frac{2m_n^2}{q^2}|G^n_E(q^2)|^2\right]. \tag{2.58}$$

At threshold we use the solid black line of Fig. 11 of [137] and the $V$-width is then given by

$$\Gamma_{V\to n\bar{n}} = \kappa^2 \frac{m_V^3}{4\pi\alpha}\sigma_{e^+e^-\to n\bar{n}}(q^2 = m_V^2). \tag{2.59}$$

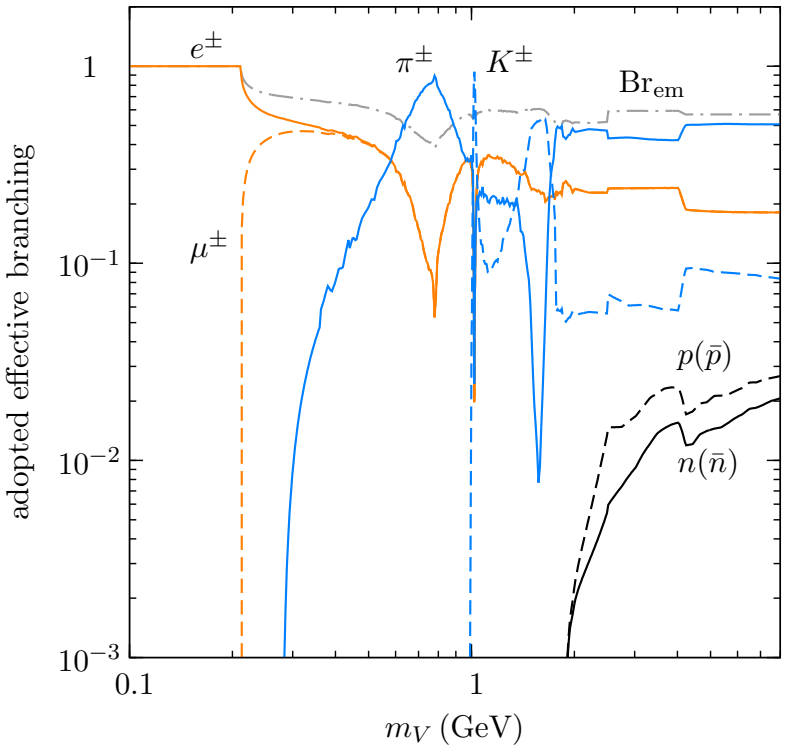


Figure 2.10: The adopted effective branching ratios into the various final states that are relevant for BBN considerations. As multi-pion and kaon states become relevant in the kinematically allowed region, we stitch together BaBar measurements of the $e^\pm \to \pi^\pm$ and $e^\pm \to K^\pm$ cross sections up to $m_V = 1.8$ GeV with our Pythia simulation for $m_V \geq 2.5$ GeV. In this plot, any branching to $K_L$ was neglected. Also shown is the fraction of vector mass that is converted into EM-energy, denoted $\mathrm{Br_{em}}$.

Away from threshold, we simulate the complex decays of $V$ with Pythia. In particular, multi-pion(kaon) production and decays to hyperons and baryonic resonances become relevant. The yield of phenomenologically relevant final states, $\pi^\pm, K^\pm$, $K_L$, and nucleons is shown in Fig. 2.9 for $m_V \geq 2.5$ GeV. Narrow resonances like $J/\psi$ are not captured by the resolution of the simulation. The dots in Fig 2.9 show the average electromagnetic energy injected after all particles have decayed to electrons and photons; $e^+$ are assumed to have annihilated on $e^-$. One can see that to a significant fraction of the energy is carried away by neutrinos.

At lower energies, even though the Pythia simulation is not available, the topology of the decay events becomes simpler, and is eventually dominated by two body decays. Above the di-pion (di-kaon) threshold, we therefore use BaBar precision mea-

surements of the $e^{\pm} \to \pi^{\pm}$ and $e^{\pm} \to K^{\pm}$ cross section until an energy $\sqrt{s} = m_V = 1.8$ GeV. Above that energy we stitch the data together with our simulation above, expecting to capture the overall importance of various final states qualitatively correctly. The resulting effective effective branching ratios that are relevant for BBN considerations are shown in Fig. 2.10. For simplicity, and as alluded to above, we neglect the $K_L$ contribution. Also shown is the fraction of vector mass that is converted into EM-energy in the hadronic decay, denoted by $\mathrm{Br}_{\mathrm{em}}$.

# Chapter 3

# Self-interacting dark matter from freeze-in

## 3.1 Abstract

We analyze the viability and detectability of Self-Interacting Fermionic Dark Matter (SIDM) with a freeze-in dark photon portal to the Standard Model. The freeze-in relic is possible for $\alpha'\alpha_d \sim 10^{-26}$. To evade strong constraints from $\chi\bar{\chi} \to A'A'$ annihilations, we focus on $\alpha_d \lesssim 10^{-4} \times (m_\chi/2\text{ GeV})$ region, where reannihilations are negligible. Although current Direct Detection (DD) limits on spin-independent cross sections are too weak to constrain the parameter space, we compute the DD forecasts for freeze-in SIDM and find that XENON1T with design sensitivity and future experiments LUX-Zeplin, XENONnT and PandaX-4T will have the reach to cover the region of interest for SIDM for $\alpha_d = 10^{-4}$. The requirements on the dark photon parameter space are near supernova constraints that suffer large systematics and do not robustly exclude the parameter space with the current understanding of their cores.

## 3.2 Introduction

DM has been a main driver behind the quest for new physics in recent decades. Its existence is undeniable and often interpreted as a particle in the Cold Dark Matter (CDM) paradigm [138]. The CDM model, through its gravitational interactions only, allows for many particle models that work with most DM signals, notably on the large

scales [9]. Numerical simulations of collisionless CDM have shown a discrepancy with observations on the small scales: the inner region of a halo density profile shows a core instead of the cusp predicted by simulations [139], the number of observed satellites [140] in the Local Group and subhaloes [141] in the Milky Way are lower than predicted, in addition to observed alignment of the satellites that is not explained with CDM [142].

Many solutions have been proposed to solve these problems. The inclusion of baryon feedback seems very promising and tends to show the tensions arose from the missing supernova in the simulations [143, 144]. It is however uncertain if cores do exist [145, 146] or whether the full baryonic effects are under control and additional work is needed to corroborate these results [147, 148]. Warm DM has also been suggested to smear out the density profile and reduce structure formation [149, 150], but fails to predict correct rotation curves (see [148] for a short review). Finally, SIDM has also been proposed to alleviate the issues [151, 152] (see Ref. [40] for a recent review). The self-interactions allow for core formation and correct the formation of satellites and substructure, while reproducing the large scale successes of CDM [153]. Large self-interactions (over dark matter mass) are ruled out by the viscosity of galaxy mergers $\sigma_{\rm SI}/m_\chi \lesssim 1$ cm/g [154, 155, 156], but values in the range

$$\sigma_{\rm SI}/m_\chi \sim 0.1 - 10 \text{ cm/g} \tag{3.1}$$

seem to correctly fit the DM data [157, 153, 158]. For a velocity-independent cross section, the upper range is hence ruled out, while a mild velocity dependence in $\sigma/m$ provides a better fit, allowing large self-interactions in smaller systems and providing the required smaller cross section on the galaxy and cluster scales [159, 160, 161, 162, 163].

Building a viable SIDM particle model that interacts with the SM is not trivial. The well-known freeze-out cross section for a correct DM relic density around the weak scale $\sigma \sim 10^{-36}$ cm$^2$ (compared to $\sigma \sim 10^{-24}$ cm$^2 \times m_\chi/$ GeV for self-interactions) rules out WIMP candidates [160]. Hidden sectors models with a stable DM particle naturally provide SIDM candidates and in the standard freeze-out scenario, only the 10 - 500 MeV mass range for a scalar or Majorana dark matter coupled with a slightly heavier gauge boson are potential viable candidates [164]. Some other regions of parameter space with special features have been shown to both accommodate a DM relic density and the right level of self-interaction. For example, models of strongly

interacting DM with a freeze-out governed by $3 \to 2$ annihilations [165, 166, 167], a non-abelian hidden sector [168], asymmetric DM [160, 161] and DM with a freeze-in relic density [169, 170, 171] have all been shown to provide the correct relic density with DM self-interactions in the favoured range to solve the small scale anomalies.

One of the simplest models of dark matter is to extend the SM with a dark quantum electrodynamic sector containing a Dirac fermion pair and a massive vector boson that kinetically mixes with the SM photon. Its (freeze-out) thermal relic is set via $s$-wave annihilation and is excluded for $m \lesssim 10$ GeV from CMB energy injection constraints [7]. In the context of SIDM, $m_{A'}/m_\chi \simeq 10^{-3}$ is typically required to obtain the correct level of self-interactions between dwarf and cluster scales [40]. In this case, the $s$-wave annihilation are enhanced by the Sommerfeld effect and the SIDM region of interest (100 MeV $< m_\chi <$ 100 TeV and 1 MeV $< m_{A'} <$ 1 GeV) is ruled out by indirect detection bounds from Planck, AMS-02 and Fermi [75]. These limits can be relaxed under a few conditions. For example, it was recognized that if the DM does not thermalize with the SM, SIDM is asymmetric or $A'$ has a mass mixing with $Z$ can all evade the indirect detection constraints [75, 40].

In this chapter, we explore the first option to evade the strong indirect detection constraints. We consider a Dirac DM particle, coupled feebly to the SM via a massive $A'$ kinetically mixed with the photon. We provide a discussion of freeze-in dark fermion with a U(1) mediator in the context on SIDM, exploring cosmological, astrophysical and direct detection consequences. Freeze-in portals with a massless (or ultralight) dark photon have previously been discussed in terms of direct detection sensitivity [16, 172, 173, 174], but not in the context of a MeV range mediator mass with SIDM. The freeze-in production of a fermionic DM with a dark photon was first derived in Ref. [16] in which they recognize the discovery potential at Xenon1T. We update their result, improve the DD forecasts and provide explicit detection benchmarks by different experiments in the context of the SIDM parameter space.

In section 3.3, we define the model and discuss the freeze-in production in section 3.4, providing analytical approximations where appropriate. We review the SIDM parameter space in section 3.5. In section 3.6, we cover both direct and indirect experimental probes of the parameter space. We provide a discussion and a summary in sections 3.7 and 3.8.

## 3.3 Model and Set-up

As mentioned, in this work we consider an extension of the SM symmetry group with an additional $\mathrm{U}(1)_X$ gauge group, broken at an arbitrary large energy scale and kinetically mixed with the SM hypercharge, neglecting a mass mixing with the $Z$ boson. For simplicity, we assume a Stueckelberg symmetry breaking to generate the vector boson mass (see [175] for a general discussion), although a similar study can be made with a Higgs mechanism in the dark sector.

The dark photon $A'$ is coupled to a DS containing a fermion-antifermion pair $\chi-\bar{\chi}$ with a vector coupling $g_d$ (no axial coupling), analogous to a dark quantum electrodynamics theory. The kinetic mixing of strength $\epsilon/\cos\theta_W$ with the SM hypercharge serves as a portal to the DS. For $m_{A'} \ll m_Z$, the phenomenology is dominated by the photon mixing and the relevant lagrangian is

$$\begin{aligned}\mathcal{L}_{\mathrm{dark}} = -\frac{1}{4}F'_{\mu\nu}F'^{\mu\nu} + \frac{m^2_{A'}}{2}A'_\mu A'^\mu \\ + \frac{\epsilon}{2}F'_{\mu\nu}F^{\mu\nu} + \bar{\chi}(i\not{D} - m_\chi)\chi,\end{aligned} \tag{3.2}$$

where $A'$ and $\chi$ denote the dark photon and dark fermion respectively, $F^{(\prime)}_{\mu\nu} = \partial_\mu A^{(\prime)}_\nu - \partial_\nu A^{(\prime)}_\mu$ are the related field strength tensors and the covariant derivative takes the form $D_\mu = \partial_\mu - ig_d A'_\mu$.

The model has 4 free parameters $\{m_{A'}, \epsilon, m_\chi, g_d\}$ and we define new fine structure constants, $\alpha' = \epsilon^2\alpha$ and $\alpha_d = g_d^2/4\pi$, for electromagnetic forces between the two sectors and within the DS respectively.

## 3.4 Production of the dark sector

The final relic abundance of the constituents of a DS is determined by the thermal interactions with the SM particles. The number density of each particle evolves according to the Boltzmann equation for $1+2 \leftrightarrow 3+4$ interactions and takes the form

$$\begin{aligned}a^{-3}\frac{d(n_3 a^3)}{dt} = \int\left(\prod_{i=1\ldots4}\frac{d^3p_i}{(2\pi)^3 2E_i}\right)\times \\ \times\,(2\pi)^4\delta^4(p_1+p_2-p_3-p_4)\,|\mathcal{M}|^2\,(N_1N_2 - N_3N_4)\,,\end{aligned} \tag{3.3}$$

where $N_i$ is the statistical distribution of species $i$ and we have neglected the Bose enhancement and Pauli blocking effects. The evolution of number densities is more easily expressed with the dimensionless parameter $Y = n/s$, where $s$ is the entropy density of the Universe. We can then substitute the right-hand side of (3.3) with $s\dot{Y}_3$ and we can relate $Y_\chi(t = t_0)$ to the present number density of the dark fermions and its corresponding energy abundance

$$\Omega_\chi h^2 = \frac{m_\chi Y_\chi(t_0) s_0}{\rho_{\rm crit}/h^2}, \tag{3.4}$$

where $s_0 = 2891.2$ cm$^{-3}$ is the present entropy density and $\rho_{\rm crit}/h^2 = 1.054 \times 10^{-2}$ MeV cm$^{-3}$ [176].

For couplings large enough such that the interactions rate between the visible and dark sectors is faster than the Hubble rate at any given time, both sectors quickly reach thermal equilibrium and the final $\chi$ abundance is determined by the inefficiency of annihilations, with $\Omega_\chi \propto 1/\langle\sigma v\rangle$ [9].

On the other hand, assuming an empty DS in the infinite past with arbitrary weak couplings, $\chi$ never reaches an equilibrium and $\Omega_\chi \propto \langle\sigma v\rangle$ [177], which is the production scenario considered here. Although the relic is proportional to $\alpha'\alpha_d$, there is a mass-dependent upper bound on $\alpha_d$ that cannot be compensated by simply decreasing $\alpha'$. Indeed, for large dark couplings and light mediators, the DS produced through freeze-in can be depleted via $\chi\bar{\chi} \to A'A'$ annihilations, a regime of reannihilation [16]. After computing the freeze-in parameter space for a correct DM relic, we quantify the reannihilation to find the range of applicability of our freeze-in relic results.

### 3.4.1 Freeze-in regime

Assuming an empty DS as an initial condition in the infinite past, the light dark fermions will be generated through $s$-channel annihilation of electrically charged SM particles. By definition of the freeze-in regime, the destruction rate is negligible and we can take $N_3, N_4 \to 0$ in (3.3) to evaluate the final abundance. In the Maxwell-Boltzmann approximation, the integrals simplify to [178]

$$s\dot{Y}_\chi = \frac{T}{2(2\pi)^4} \int_{4m^2}^{\infty} ds\ \sigma\sqrt{s}\left(s - 4m^2\right) K_1\left(\frac{\sqrt{s}}{T}\right), \tag{3.5}$$

where $s = (p_1 + p_2)^2$, $K_1$ is the modified Bessel function of the second kind and $m$ is the mass of the SM annihilating particles. Details of the analytical estimates and the cross section $\sigma$ for the reaction $1 + 2 \to \chi + \bar{\chi}$ are given in supplementary section 3.9. The final abundance is found by integrating

$$Y = \int_0^\infty dT \frac{\dot{Y}}{H(T)T}, \tag{3.6}$$

with the usual entropy density and Hubble rate

$$s(T) = \frac{2\pi^2}{45} h_\star(T) T^3, \qquad H(T) \simeq 1.66 \sqrt{g_\star(T)} \frac{T^2}{M_{\rm pl}}, \tag{3.7}$$

for the effective number of relativistic (entropy) degrees of freedom $g_\star$ ($h_\star$), which in the spirit of the freeze-in mechanism, only comprises SM particles. The following set of analytical yields we derived are accurate at 5% where $g_\star(m_\chi)$ and $h_\star(m_\chi)$ are mostly constant to 40% when $m_\chi \sim 10 - 20$ MeV.

For $m_{A'} \ll 2m_e$ or $2m_\chi$, the production rate is restricted by the phase-space of the non-relativistic fermions and we obtain the analytical approximation

$$Y^{\text{imag } A'}_{\chi+\bar{\chi},\text{f}-\text{i}} \simeq 2 \times \frac{9\alpha'\alpha_d}{128\pi} \frac{m_{hf}^4}{(Hs)_{T=m_{hf}}}, \tag{3.8}$$

where $m_{hf} = \text{Max}(m_e, m_\chi)$ is the mass of the heavier fermion in the reaction.

For $2m_e, 2m_\chi \ll m_{A'} < 2m_\mu$, the reaction is resonantly enhanced at the $A'$ mass pole, and we can estimate the freeze-in yield from an on-shell dark photon

$$Y^{\text{real } A'}_{\chi+\bar{\chi},\text{f}-\text{i}} \simeq 2 \times \frac{3}{4\pi} \frac{\alpha'\alpha_d}{\alpha' + \alpha_d} \frac{m_{A'}^4}{(Hs)_{T=m_{A'}}}. \tag{3.9}$$

In addition to the annihilation channels, the decay of the SM $Z$ boson dominates the production for 1 GeV $\lesssim m_\chi < m_Z/2$ [16, 172]. Recalling the mixing in (3.2) is with the hypercharge field tensor $B_{\mu\nu} = \cos\theta_W F_{\mu\nu} - \sin\theta_W Z_{\mu\nu}$, the dark photon also obtains a kinetic mixing with the $Z$ boson with a $\epsilon \tan\theta_W$ mixing coupling (see supplementary section 3.10 for a short review of the field rotations and couplings). The decay rate is

$$\Gamma_{Z\to\chi\bar{\chi}} = \epsilon^2 \tan^2\theta_W \Gamma^{m_{A'}=m_Z}_{A'\to\chi\bar{\chi}} \simeq 10^{-22}\ \text{GeV} \frac{\alpha'\alpha_d}{10^{-25}}, \tag{3.10}$$

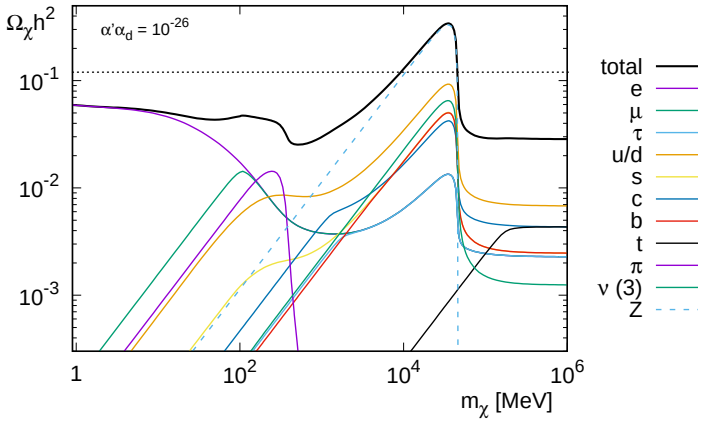


Figure 3.1: Contribution of each production channels in the freeze-in relic with a light mediator ($m_{A'} \ll m_Z$) as a function of dark matter $m_\chi$ for $\alpha'\alpha_d = 10^{-26}$. The dotted line shows the CDM relic density. The dashed lines demonstrated that the $Z$ decay estimate matches the Breit-Wigner cross sections used.

where we neglected the phase-space suppression of a massive $\chi$. The production rate is straightforward

$$s\dot{Y}_\chi = 3 \times \int \frac{d^3p_Z}{(2\pi)^3}\frac{m_Z}{E_Z}\Gamma_{Z\to\chi\bar{\chi}}N_Z, \tag{3.11}$$

and the resulting $\chi\bar{\chi}$ yield is

$$Y^{Z\text{ decay}}_{\chi+\bar{\chi},\text{f}-\text{i}} \simeq 2 \times 2.5 \times 10^{-14}\frac{\alpha'\alpha_d}{10^{-25}}\left(m_Z^2 + 2m_\chi^2\right)\sqrt{1-\frac{4m_\chi^2}{m_Z^2}}. \tag{3.12}$$

Our numerical results use the MB approximation ($N_i = e^{-E_i/T}$) and include all charged leptons, free quarks (free pions and kaons) above (below) the QCD confinement temperature following the prescription in [74]. The contribution of quarks is similar to equations (3.8-3.9) with the additional colour number and quark charge $N_c Q_q^2$ factor. We include the $Z$-mediated diagram, with a Breit-Wigner width that correctly reproduces Eq. 3.12 when summed over all production channels. The relic abundance for $m_{A'} \ll m_\chi, m_Z$ is shown in Fig. 3.1.

Using the most recent CDM density measurement from the Planck satellite [7]

$$\Omega_{\text{CDM}}h^2 = 0.1198 \pm 0.0015, \tag{3.13}$$

the estimates for a freeze-in $\chi$ relic become (from one electron-type production chan-

nel)

$$\alpha'\alpha_d \simeq 6\times 10^{-28}\frac{m_{hf}}{m_\chi}h_\star^{hf}\sqrt{g_\star^{hf}} \qquad \text{off-shell } A', \tag{3.14}$$

$$\alpha' \simeq 5\times 10^{-29}\frac{m_{A'}}{m_\chi}h_\star^{A'}\sqrt{g_\star^{A'}} \qquad \text{on-shell } A'. \tag{3.15}$$

The number of relativistic degrees of freedom $g_\star$ and entropic relativistic degrees of freedom $h_\star$ are accordingly evaluated at the heavy fermion $hf$ or dark photon $A'$ mass and we assumed that the on-shell $A'$ decay is dominated by the dark sector fermions $\alpha_d \gg \alpha'$. Including all channels, $\Omega_\chi = \Omega_{\rm CDM}$ is achieved for $\alpha'\alpha_d \sim 10^{-26}$ for $m_{A'} \ll m_\chi, m_Z$.

### 3.4.2 Dark thermalization and reannihilation

If we have a freeze-in production dominated by the portal coupling rather than the DS coupling $\alpha' \ll \alpha_d$ (as implied by the SIDM framework), it is possible to have a significant amount of DM depletion without the dark sector itself with annihilations into dark photons, a regime of reannihilation [16]. This situation is possible even if the DS has not reached full equilibrium with the SM. The onset of this regime is appears when the annihilation is cosmologically efficient

$$\langle\sigma_{\rm ann}v\rangle n_\chi(T_{\rm DS}) \gtrsim H(T_\gamma), \tag{3.16}$$

where $\langle\sigma_{\rm ann}v\rangle$ is the $\chi\bar{\chi}\to A'A'$ thermal cross section, evaluated at the DS temperature $T_{\rm DS} < T_\gamma$. To obtain $T_{\rm DS}$, we first solve the energy transfer to the DS (see supplementary section 3.11 for details). Equipped with the dark sector $T_{\rm DS}(T_\gamma)$, we can augment the Boltzmann equation to include the depletion within the DS [16]

$$\frac{dY}{dT} = \frac{s(T_\gamma)}{H(T_\gamma)T_\gamma}\Big[\langle\sigma_{\rm prod}v\rangle_{T_\gamma}\left(Y_{\rm eq}^2(T_\gamma) - Y^2\right) + \tag{3.17}$$

$$+\langle\sigma_{\rm ann}v\rangle_{T_{\rm DS}}\left(Y_{\rm eq}^2(T_{\rm DS}) - Y^2\right)\Big], \tag{3.18}$$

where $\langle\sigma v\rangle_{T_i}$ is evaluated at temperature $T_i$ and $\sigma_{\rm prod}$ includes all SM production channels. Numerical solutions of $Y(T)$ are shown in Fig. 3.2 for $m_\chi = 100$ GeV with the freeze-in relic versus the reannihilation scenario. Conceptually, $Y$ initially follows the equilibrium curve $Y_{\rm eq,DS}$ reduced from the would-be SM equilibrium $Y_{\rm eq}$ since $T_{\rm DS} \ll T_\gamma$. At some point, the source from the SM maintains a $\chi$ population above

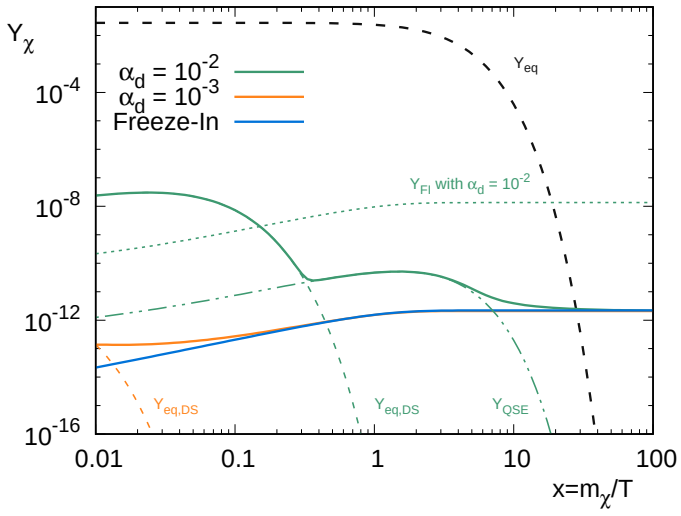


Figure 3.2: Thermal evolution of the normalized number density $Y = n/s$ for $m_\chi = 100$ GeV with a strong reannihilation, ($\alpha_d = 10^{-2}$, solid, green), negligible reannihilation ($\alpha_d = 10^{-3}$, solid, orange) and from freeze-in only (solid blue). Dashed lines are used to show analytical solutions for $Y$ is thermal equilibrium with the SM $Y_{\rm eq}$ or with the DS with a small temperature $Y_{\rm eq,DS}$. The dotted line shows the would-be freeze-in yield with the same $\alpha'\alpha_d$ as the $\alpha_d = 10^{-2}$ curve, except neglecting reannhilation. The dashed-dotted line follows in the quasi-static equilibrium.

$Y_{\rm eq,DS}$ and the abundance follows a Quasi-Static Equilibrium (QSE), an intermediate abundance weighing the still-efficient annihilations depletion with the influx of $\chi$ from the SM bath given by [179, 16]

$$Y_{QSE} = \sqrt{\frac{\langle\sigma_{\rm prod} v\rangle_{T_\gamma}}{\langle\sigma_{\rm ann} v\rangle_{T_{\rm DS}}}} Y_{\rm eq}. \tag{3.19}$$

This is clearly seen as the second *bump* for the $\alpha_d = 10^{-2}$ curve in Fig. 3.2. The relic then decouples as a standard freeze-out, with and effective cross section $\langle\sigma_{\rm eff} v\rangle = \sqrt{\langle\sigma_{\rm prod} v\rangle\langle\sigma_{\rm ann} v\rangle}$. Our numerical solution for reannihilation does not use an empty far past as an initial condition (as opposed to the freeze-in scenario) but rather with $Y_{\rm ini} = Y_{\rm eq,DS}$. This has no impact on the final abundance as the would-be abundance for the same $\alpha'\alpha_d$ crosses $Y_{\rm eq,DS}$ before the transition to $Y_{\rm QSE}$ (see dotted line in Fig. 3.2). In other words, thermalization to $Y_{\rm eq,DS}$ is guaranteed to happen. Finally, the freeze-in relic is attained if $Y$ freezes out of $Y_{\rm QSE}$ before the $\sigma_{\rm prod}$ becomes inefficient, as exemplified in the $\alpha_d = 10^{-3}$ curve.

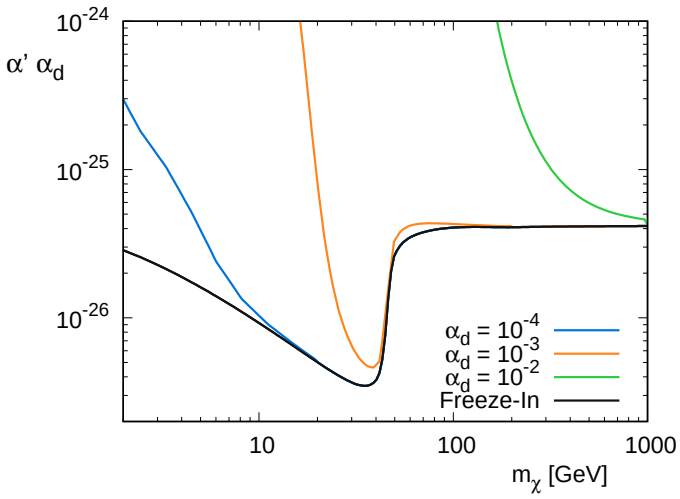


Figure 3.3: Values of $\alpha'\alpha_d$ needed for the correct relic density in the frozen-in fermionic SIDM model with a dark photon mediator.

The non-relativistic thermally averaged cross section for annihilations to $A'A'$ is

$$\langle \sigma v \rangle = \frac{\pi \alpha_d}{2m_\chi^2} \tag{3.20}$$

and the reannihilation regime is consequently more important for light DM masses. The required value of $\alpha'\alpha_d$ to generate the correct relic abundance therefore increases from the freeze-in value $\alpha_d/m_\chi \lesssim 10^{-5}/\text{GeV}$ as shown in Fig. 3.3. For a fixed value of $\alpha_d$, $\alpha'\alpha_d$ cannot be arbitrarily increased to compensate a stronger reannihilation for smaller values of $m_\chi$. Larger values of $\alpha'\alpha_d$ increase $T_{\text{DS}}$, or equivalently $Y_{\text{eq,DS}}$ which eventually connects the two baths thermally (when $Y_{\text{eq,DS}} = Y_{\text{eq}}$). In this case, the relic is set by the standard freeze-out, with a final abundance inversely proportional to Eq. (3.20), independently of the $\alpha'\alpha_d$ product. Finally, this dark freeze-out serves as a lower bound on $m_\chi$ for a fixed $\alpha_d$ for the possibility of a freeze-in or reannihilation relic. Using the crude freeze-out requirement $\langle \sigma v \rangle \sim 1$ pb we find the approximate bound

$$m_\chi \gtrsim 200 \text{ GeV} \times \frac{\alpha_d}{10^{-2}}, \tag{3.21}$$

for a viable freeze-in or reannihilation-type relic, which is representative of our numerical results shown in Fig. 3.3.

## 3.5 Self-Interactions

The mechanics and interesting parameters space for self-interactions with respect to the small scale anomalies have been formulated in a series of papers [160, 161]. We simply review the analytical features and replicate the results in terms of dark photons from Ref. [161]. While the exact solution is found by numerically solving the Schrödinger equation, we simplify our task by utilizing the analytical approximations provided in the different regimes. This reduces the resolution of the resonant peaks in the parameter space, but does not change our overall result.

In astrophysical systems, dark matter scatterings are non-relativistic and well described by a Yukawa potential

$$V(r) = -\frac{\alpha_d}{r} e^{-m_{A'} r}. \tag{3.22}$$

The momentum transfer cross section

$$\sigma_T = \int d\Omega (1 - \cos\theta) \frac{d\sigma}{d\Omega}, \tag{3.23}$$

is known in the Born ($\alpha_d m_\chi \ll m_{A'}$) and classical limit ($m_{A'} \ll m_\chi v$), while the remaining parameter space can be studied through the Schrödinger equation. In particular, the nonperturbative region allows resonances for

$$\frac{\alpha_d m_\chi}{\kappa m_{A'}} = n^2 \,, \qquad n = 1,\, 2,\, 3,\, ... \tag{3.24}$$

where $\kappa \simeq 1.6$. An analytic approximation for this regime is available by solving the Hulthen potential

$$V(r) = -\frac{\alpha_d \kappa m_{A'} e^{-\kappa m_{A'} r}}{1 - e^{-\kappa m_{A'} r}}, \tag{3.25}$$

as a proxy to the Yukawa potential.

The resonances present sharp patterns in the velocity-dependence, which can affect different astrophysical systems through the velocity dispersion of their particles. In general, a system in thermal equilibrium can be described in the velocity-averaged cross section

$$\langle \sigma_T \rangle = \int \frac{d^3 v}{(2\pi v_0^2)^{3/2}} e^{-\frac{v^2}{2v_0^2}} \sigma_T(v), \tag{3.26}$$

where $v_0$ is the typical velocity of the particles. The compelling SIDM parameter space is found with the following requirements

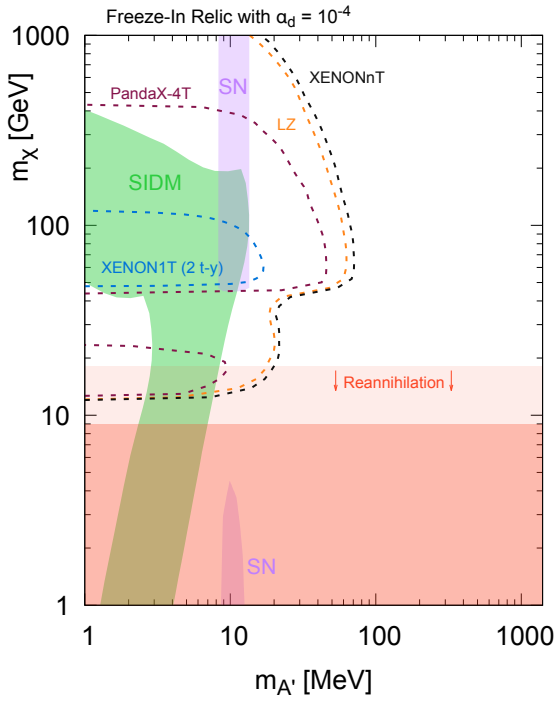


Figure 3.4: SIDM parameter space for $\alpha_d = 10^{-4}$ with current constraints and forecasted sensitivity of DD experiments. At each point, $\alpha'$ is chosen to give the correct relic density. The region highlighted in red cannot generate a freeze-in relic; the dark region thermalizes with the SM and the pale region has a small reannihilation contribution. The green region is favoured by the DM small scale anomalies. BBN and conservative SN constraints from the dark photon parameter space are shown in purple. The dashed lines represents future sensitivity for XENONnt, LUX-Zeplin (LZ), PandaX-4T and XENON1T at design sensitivity.

- $0.1 < \langle\sigma_T\rangle/m_\chi < 1$ cm$^2/g$ on dwarf scales with $v_0 = 30$ km/s,
- $\langle\sigma_T\rangle/m_\chi < 1$ cm$^2/g$ on the cluster scales with $v_0 = 3000$ km/s,

to alleviate the small scale anomalies. The region for $\alpha_d = 10^{-4}$ is shown in Fig. 3.4 along with the current constraints and future experimental sensitivity to be explained in the next section.

## 3.6 Probes and Constraints

The established program for DM direct detection provides an opportunity to observe a symmetric SIDM with $\alpha_d = 10^{-2}$ and $\epsilon \sim 10^{-10}$ [162, 163, 180]. These values are

near the freeze-in range and form an interesting possibility to experimentally observe the freeze-in SIDM. Additionally, since the SIDM favours a light mediator, the dark photon will populate (at lower temperatures) through the freeze-in production and known constraints (partially derived in chapter 2) on visibly decaying dark photons apply (see [181] for a recent overview). In this section, we first derive the direct detection signal for our model and then summarize the indirect detection restrictions of the dark photons.

### 3.6.1 Direct Detection

The low-momentum ($q = 0$) spin-independent cross section with a nucleon

$$\sigma_{\chi n}^{\mathrm{SI}} = \frac{16\pi\alpha'\alpha_d(Z/A)^2\mu_{\chi n}^2}{m_{A'}^4} \tag{3.27}$$

combined with the freeze-in relic density requirement

$$\alpha'\alpha_d \simeq 10^{-26}, \tag{3.28}$$

imply that the model is near the direct detection sensitivity

$$\sigma_{\chi n}^{\mathrm{SI}} \sim 10^{-46} \times \mathrm{cm}^2 \left(\frac{20\ \ \mathrm{MeV}}{m_{A'}}\right)^4, \tag{3.29}$$

and we thus expect the freeze-in SIDM to be within the projected detection range of the upcoming generation of experiments. This scattering cross section assumes point-like interactions and does not apply directly to the long-range behaviour of light mediators. If the mediator is lighter than the momentum transfer ($q \sim 50$ MeV for a Xenon experiment), the $R \propto m_{A'}^{-4}$ scaling of the event rate is saturated and instead depends on the nuclear recoil energy of the experiment [182, 183].

More precisely, the differential cross section with a target nucleus is [182]

$$\frac{d\sigma(v, E_R)}{dE_R} = \frac{m_T}{2\mu_{\chi p}^2}\sigma_{\chi n}^{\mathrm{SI}}\frac{A^2}{v^2}\frac{F^2(E_R)}{\left(1 + \frac{2m_T E_R}{m_{A'}^2}\right)^2}, \tag{3.30}$$

where $m_T$ is the target mass, $\mu_{\chi p}$ is the DM-proton reduced mass, $A$ is the atomic nucleon number of the target, $v$ is the DM velocity, $F$ the Helm nuclear form factor

and $E_R$ the recoil energy of the nucleus. Integrating over the local DM distribution[1], the differential recoil rate becomes

$$\frac{dR}{dE_R} = C_{T\chi}\sigma_{\chi n}^{\rm SI}\frac{F^2(E_R)\,\eta\left[v_{min}(E_R)\right]}{\left(1+\frac{2m_T E_R}{m_{A'}^2}\right)^2}, \tag{3.31}$$

where the detector parameters and local mass density have been incorporated in $C_{T\chi}$ and the velocity dependence is

$$\eta \equiv \int_{v\geq v_{min}(E_R)} d^3v \frac{f_M(\vec{v})}{v} \tag{3.32}$$

with $f_M$ as the normalized isotropic Maxwellian velocity distribution in the galaxy in Earth's frame, truncated at $v_{esc}$, while neglecting the annual modulation. The lower bound is given by the minimal DM velocity that can induce a given recoil energy in the target $v_{min} = \sqrt{m_T E_R/2\mu_{\chi T}^2}$.

For each direct detection experiment, an analysis must be performed to transform the theoretical rate into an observed signal rate and apply the relevant cuts to optimize the statistics. This task was executed by other authors in Ref. [180] in the context of dark photons/fermions without the freeze-in relic and obtained exclusion regions from the LUX experiment 2013 results [33] and SuperCDMS [184].

Instead of going through the experimental modelling, we can simply utilize the nuclear recoil efficiency $\epsilon_R(E_R)$ provided by each collaboration with the strongest constraints (LUX [185], XENON1T [55] and PandaX-II [34]). The experimental event rate is then straightforward

$$R = C_{T\chi}\sigma_{\chi n}^{\rm SI}\int dE_R \frac{F^2(E_R)\,\eta\left(v_{min}\right)}{\left(1+\frac{2m_T E_R}{m_{A'}^2}\right)^2}\epsilon_R\left(E_R\right). \tag{3.33}$$

The published exclusion regions in the $m_\chi - \sigma_{\chi n}^{\rm SI}$ space by experiments assume heavy mediators and we can translate them into light mediators constraints via

$$\sigma_0^{\rm SI}(m_\chi) = \sigma_{\chi n}^{\rm SI}(m_\chi, m_{A'})\frac{\mathcal{I}\left(m_\chi, m_{A'}\right)}{\mathcal{I}\left(m_\chi, \infty\right)}, \tag{3.34}$$

with $\sigma_0^{\rm SI}(m_\chi)$ representing the provided experimental cross section limit and $\mathcal{I}$ the

[1]We use the standard astrophysical parameters $v_0 = 220$ km/s, $v_\odot = 232$ km/s and $v_{esc} = 544$ km/s.

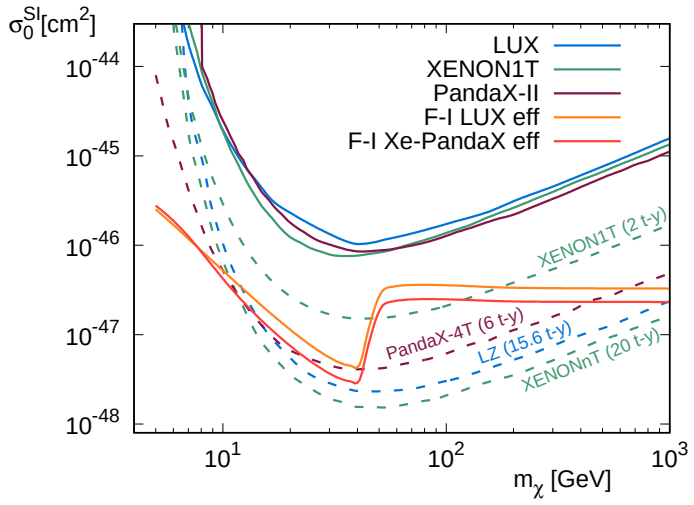


Figure 3.5: Spin-independent cross section limits from current DD experiments and projected sensitivity for future upgrades. The maximal cross section in the light mediator limit is shown for the freeze-in SIDM with the energy recoil efficiency used in the LUX (orange) and XENONnT experiments (red). PandaX is indistinguishable from the XENONnT efficiency.

integral in equation (3.33). Using the same experimental and astrophysical parameters, this strategy reproduces the general features of the full study in Ref. [180], with our exclusion regions being more conservative.

We display the nuclear recoil efficiencies with a saturated low mediator mass limit in Fig. 3.5 (the Xenon1T and Panda-X efficiencies are similar and combined in the figure), along with the present strongest limit from LUX [185], XENON1T [55], PandaX-II [54], the forecasted sensitivities for the design sensitivity of XENON1T [58] and future experiments the LUX-Zeplin (LZ) [186] and PandaX-4T [57]. DD experiments can probe the freeze-in DM when they attain the red and orange lines of saturated low mediator mass. These low-mass limit show the largest cross section testable for a given DM mass. A heavier mediator is eventually suppressed by $m_{A'}^{-4}$ when $m_{A'}$ becomes larger than the transferred momentum. The forecasted reach of each experiments in shown in Fig. 3.4 for $\alpha_d = 10^{-4}$. For this benchmark, both LZ and XENONnT should have the experimental reach to fully probe the large $m_\chi$ region of SIDM. Both PandaX-4T and XENON1T at full design sensitivity (current constraints are early results with 34.2 live days of data [55]) will partially probe the SIDM parameter space.

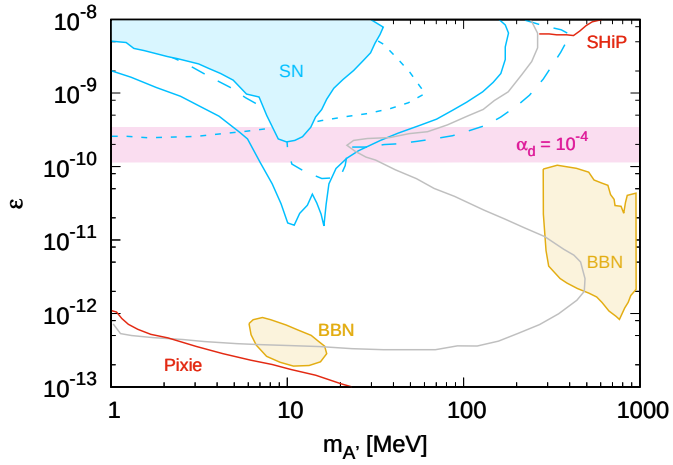


Figure 3.6: Dark photon parameter space with robustly excluded regions in solid colours. The solid and dashed blue lines are potentially excluded by SN arguments, while the grey lines show older (outdated) SN constraints (see text for details.) The red lines show future regions of sensitivity by the Pixie satellite and the SHiP experiment. The horizontal band shows the spread in $\epsilon$ that gives the correct relic density for 1 GeV $< m_\chi <$ 1 TeV and $\alpha_d = 10^{-4}$.

### 3.6.2 Indirect Detection

The mild velocity dependence favoured by the SIDM parameter space implies a light mediator, visibly decaying into the SM. Regardless of the structure of the (heavier) dark sector, there are multiple constraints from cosmology, astrophysical and experimental results on the parameter space, shown in Fig. 3.6. By focusing on $\alpha_d = 10^{-4}$, the strong indirect detection signals from Sommerfeld enhanced $A'A'$ annihilations only affect lighter masses $m_\chi \lesssim 20$ GeV. The constraints on the remainder of the parameter space will come for the freeze-in $A'$ relic which subsequently decays and influences the cosmology, as derived in chapter 2. The solid coloured regions are robustly excluded, while the lined regions correspond to either future experimental sensitivity or systematic uncertainties in the constraints. The range of values of $\epsilon$ that provide the correct relic density for $\alpha_d = 10^{-4}$ is highlighted in the pink band. For a given $\alpha_d$, the upper limit in the $\epsilon$ band is for $_\chi > m_Z$, while the lower range is due to the larger production from $Z$ decays at $m\chi \lesssim m_Z/2$.

For the specific choice of $\alpha_d = 10^{-4}$, all viable values of $\epsilon$ with the relic force the $A'$ to decay before the BBN sensitivity. The only indirect detection measurement that affects this parameter space comes from supernova.

The bounds from supernova energy loss have recently been updated to include the finite-temperature and density effects in the dark photon propagation [187, 188]. While both references broadly agree, Ref. [187] showed that varying the temperature and density profile of the progenitor can significantly affect the final constraints. As such, we show in solid blue their *robust* exclusion region, while their largest variation (solid blue line) and result from [188] (dashed blue line) serve as systematic uncertainties. Another recent calculation without finite-temperature effects is shown in dotted blue, which overestimates the sensitivity at low $A'$ masses [189]. We additionally show older constraints [190, 191] in grey in Fig. 3.6. The upper grey blob ($\epsilon \sim 10^{-10} - 10^{-7}$) is the region that was updated and comes from energy loss arguments that would decrease the neutrino luminosity below the observed signal. The lower region ($\epsilon \sim 10^{-12} - 10^{-10}$) is due to $A'$ decays just outside the progenitor's surface that would emit an unobserved electromagnetic signal[2].

We also show the potential future sensitivity of the SHiP experiment [47] that will be able to probe $m_{A'} > 300$ MeV and complement other beam dump experiments (see [43] for a review).

## 3.7 Discussion

Large values of $\alpha_d$ are often discussed in the SIDM literature. While reannihilation of the DS considerably reduce the viable freeze-in parameter space, we find that $\alpha_d \sim 10^{-4}$ is still a plausible candidate to the DM existing in nature. It is quite remarkable that many DD collaborations will have the sensitivity to cover the region of interest. The forecasts are based on the fact that they will be able to at least match the nuclear recoil detection efficiency of previous analyses. The reach into low $E_R$ is important so as to obtain a sensitivity into light mediators. As long as $m_{A'} \gtrsim 2m_T E_R \sim 50$ MeV, the event rate goes as $m_{A'}^{-4}$ and the experimental sensitivity is purely determined by the $\sigma_{\chi n}^{\rm SI}$ limits of the experiments. Further reach in the heavy mediator direction requires tremendous efforts, as an improvement of an order of magnitude in $\sigma_{\chi n}^{\rm SI}$ limit translates in a $10^{1/4} \sim 1.7$ improvement in $m_{A'}$. For example, an optimal sensitivity at the neutrino coherent scattering floor would have a reach to $m_{A'} \sim 150$ MeV at its maximal point.

[2]We note that a portion of this constraint should be still valid, but the full phenomenology with plasma effects has not be determined yet. In particular, we expect the lower bound to be $\propto \epsilon^2 m_{A'}^2$ instead of being flat in $m_{A'}$, in a similar fashion to the updated neutrino luminosity argument [187].

On the other hand, as $m_\chi$ is lowered below 50 MeV, a combination of the raw $\sigma^{\rm SI}_{\chi n}$ and the low-$E_R$ acceptance rate influences the reach into the model. The LUX collaboration made a significant leap in lowering the minimum recoil energy acceptance to 1.1 keV with a new calibration technique by injecting tritium $\beta$ source [192]. The derived photon and electron emission model is transferrable to other xenon experiments and both XENON and PandaX collaborations are profiting from this technique, providing similar low-$E_R$ efficiency [58]. We see from Fig. 3.5 that the XENON1T will be the first experiment to have sensitivity to the SIDM freeze-in dark fermion-photon model if they achieve their design sensitivity. Looking further in time, XENON1T's next phase XENONnT [58], LZ and PandaX-4T will be able to go further even further in sensitivity. As all these next generation experiments are built on same the knowledge and expertise, we expect the efficiency to further increase and consider our forecast to be conservative.

Taking advantage of the light mediator $m_{A'}^{-4}$ enhancement for small $E_R$, direct detection of DM scatterings on electron can additionally constrain sub-GeV DM. Many experimental avenues have been identified (for example through electron ionization, excitation or molecular dissociation [172]) which potentially allow $E_R$ down to the eV range. In this case, the scattering cross section is [172]

$$\sigma^{\rm SI}_{\chi e} = \frac{16\pi\alpha'\alpha_d\mu^2_{\chi e}}{\left(m^2_{A'} + \alpha^2 m_e^2\right)^2} \sim 10^{-42} \times {\rm cm}^2 \left(\frac{0.1\ {\rm MeV}}{m_{A'}}\right)^4, \tag{3.35}$$

and is saturated in light $m_{A'}$ by the electronic wavefunction around the nuclei. The electron response to the scattering involve quantum mechanical simulations and the freeze-in relic with a very light dark photon $m_{A'} \ll$ keV mediator has been explicitly featured as an achievable sensitivity target [172]. In particular, both DAMIC [193] and SuperCDMS-silicon [194] will be able to probe freeze-in DM in the range $m_\chi \sim 10^0 - 10^6$ MeV with ultralight dark photons [173]. A hypothetical molecular $N_2$-based detector could also detect the same model with $m_\chi$ $10^2 - 10^6$ MeV through chemical-bond breaking [174]. These experimental efforts can be interesting for the non-resonant SIDM, where the region with correct self-interactions with smaller $\alpha_d$ is located as smaller $m_\chi - m_{A'}$.

Finally, the recent work on dark photons produced in a supernova has demonstrated the large systematic uncertainties that affect the $m_{A'} - \epsilon$ parameter space [187, 188, 189]. We utilize the most conservative results, but advancement on that front can potentially rule out most of the SIDM parameter space for $\alpha_d = 10^{-4}$ if the

physical processes lie further in the systematic errors range.

## 3.8 Summary

In this work, we presented the parameter space for a frozen-in Dirac fermion DM with a dark photon mediator. We find that the complementary relationship between direct detection experiments and the indirect detection constraints on the dark photon will cover some of the self-interaction parameter space, demonstrating $\alpha_d = 10^{-4}$ as a benchmark that will be fully probed. The direct detection sensitivity is heavily impeded for heavy mediators, but supernova constraints on the dark photon can rule out most of the model if proto-neutron stars profiles are better understood and improve systematic uncertainties.

## 3.9 Supplementary: Analytical freeze-in yields

Assuming the production rate is sub-Hubble, chemical equilibrium is never reached and $\chi$ is produced via the freeze-in mechanism. The $\chi$ destruction in the Boltzmann equation is negligible, from the lack of $\chi$ to annihilate, and we take $N_3, N_4 \to 0$ in (3.3).

$$
\begin{aligned}
s\dot{Y}_\chi = &\int \frac{d^3p_1}{(2\pi)^3 2E_1}\frac{d^3p_2}{(2\pi)^3 2E_2}\frac{d^3p_3}{(2\pi)^3 2E_3}\frac{d^3p_4}{(2\pi)^3 2E_4}\times \\
&\times (2\pi)^4\delta^4(p_1+p_2-p_3-p_4)\,|\mathcal{M}|^2\,N_1N_2, &(3.36)\\
\equiv &\int \frac{d^3p_1}{(2\pi)^3}\frac{d^3p_2}{(2\pi)^3}\sigma v N_1N_2 \equiv n_1n_2\langle\sigma v\rangle &(3.37)\\
= &\frac{T}{2(2\pi)^4}\int_{4m_e^2}^{\infty} ds\;\sigma\sqrt{s}\left(s-4m_e^2\right)K_1\left(\frac{\sqrt{s}}{T}\right), &(3.38)
\end{aligned}
$$

where we assumed MB statistics of the initial particles, $s = (p_1+p_2)^2$ and $K_1$ is the modified Bessel function of the first kind. For $f\bar{f} \to \chi\bar{\chi}$, the spin-summed photon-

mediated squared matrix element and cross section are

$$|\mathcal{M}|^2 = 64\pi^2\alpha'\alpha_d \frac{s^2}{(s-m_{A'}^2)^2 + m_{A'}^2\Gamma_{A'}^2}\left\{1 + \frac{4m_e^2}{s} + \frac{4m_\chi^2}{s} + \right. \tag{3.39}$$

$$\left. + \left(1 - \frac{4m_e^2}{s}\right)\left(1 - \frac{4m_\chi^2}{s}\right)\cos^2(\theta)\right\}, \tag{3.40}$$

$$\sigma = \frac{16\pi}{3}\alpha'\alpha_d \frac{s}{(s-m_{A'}^2)^2 + m_{A'}^2\Gamma_{A'}^2} \frac{\sqrt{1-\frac{4m_\chi^2}{s}}}{\sqrt{1-\frac{4m_e^2}{s}}}\left(1 + \frac{2m_e^2}{s}\right)\left(1 + \frac{2m_\chi^2}{s}\right), \tag{3.41}$$

where $\Gamma_{A'} \simeq \frac{\alpha_d m_{A'}}{3}$ is the decay rate of $A' \to \chi\bar{\chi}$ and the final abundance is given by (3.6). Although we numerically obtain our results, we here provide analytical approximation to the $\chi$ yield via freeze-in production.

**On-shell resonance of** $A'$. For $m_{A'} > 2m_e, 2m_\chi$, the virtual $A'$ becomes on-shell and the production hits a resonance. Using the narrow-width approximation of the Breit-Wigner distribution

$$\frac{1}{(s-m_{A'}^2)^2 + m_{A'}^2\Gamma_{A'}^2} \approx \frac{\pi}{m_{A'}\Gamma_{A'}}\delta(s - m_{A'}^2), \tag{3.42}$$

the centre of energy integral (3.38) becomes trivial and we get the estimate

$$s\dot{Y}_\chi^{\text{real } A'} = \frac{1}{2\pi^2}\alpha' T m_{A'}^3 K_1\left(\frac{m_{A'}}{T}\right), \tag{3.43}$$

when using relativistic approximations. This is the same result as the production of an on-shell dark photon from the thermal bath of electrons as in [74]. The same argument follows and the final abundance from a single lepton coalescence channel is

$$Y_{\chi+\bar{\chi},\text{f-i}}^{\text{real } A'} \simeq 2 \times \frac{3\alpha'}{4\pi}\frac{m_{A'}^4}{(Hs)_{T=m_{A'}}}, \tag{3.44}$$

where the factor of 2 comes from the associated production of $\bar{\chi}$.

**Off-shell** $A'$. For $m_{A'} \ll 2m_{hf}$, $m_{hf}$ being the heavier fermion in the initial or final state, the production rate shuts off at low temperature from the phase-space exponential suppression of non-relativistic heavier fermions. Neglecting $m_{A'}$ and the lighter $m_f$, the integrand of (3.38) can be evaluated analytically and we find the

simplified estimates

$$s\dot{Y}_{\chi}^{\text{imag }A'} = \frac{\alpha'\alpha_d}{6\pi^3} T m_{hf}^2 \left[ 4TK_1^2\left(\frac{m_{hf}}{T}\right) + \right. \\ \left. + \sqrt{\pi} m_{hf} G_{1,3}^{3,0}\left( \frac{m_{hf}^2}{T^2} \middle| \begin{matrix} 1 \\ -\frac{1}{2}, -\frac{1}{2}, \frac{1}{2} \end{matrix} \right) \right], \tag{3.45}$$

where $G_{p,q}^{m,n}\left( z \middle| \begin{matrix} a_1, ..., a_p \\ b_1, ..., b_q \end{matrix} \right)$ is the Meijer G function. Integrating over the simplified thermal history $sH \propto T^5$ , we find the estimate

$$Y_{\chi+\bar{\chi},\text{f}-\text{i}}^{\text{imag }A'} \simeq 2 \times \frac{9\alpha'\alpha_d}{128\pi} \frac{m_{hf}^4}{(Hs)_{T=m_e}}, \tag{3.46}$$

accurate at the 5-percent level.

## 3.10 Supplementary: Field rotations and couplings

In this supplementary section, we provide a review of the field rotations and coupling constants arising from a feeble kinetic mixing ($\epsilon \ll 1$). The exact results for any $\epsilon$ values are given in Ref. [195]. After diagonalizing the kinetic mixing and electroweak symmetry breaking, the $Z_0 - A'_0$ mass matrix is ($\delta \equiv m_{A',0}/m_{Z,0}$)

$$m_V^2 = m_{Z,0}^2 \begin{pmatrix} 1 & \epsilon\tan\theta \\ \epsilon\tan\theta & \delta^2 \end{pmatrix}. \tag{3.47}$$

While the photon remains massless, the physical $Z - A'$ are found by diagonalizing the mass matrix

$$\begin{pmatrix} Z \\ A' \end{pmatrix} = \begin{pmatrix} \cos\alpha & \sin\alpha \\ -\sin\alpha & \cos\alpha \end{pmatrix} \begin{pmatrix} Z_0 \\ A'_0 \end{pmatrix} \tag{3.48}$$

and $\tan\alpha = \epsilon\tan\theta/(\delta^2 - 1)$. The mass eigenstates are as expected $m_Z = m_{Z_0}$, $m_{A'} = \delta m_Z = m_{A',0}$ (corrections appear at $\mathcal{O}(\epsilon^2)$). The vector couplings between $Z$

and the fermions become

$$g_{Zf\bar{f}} = \frac{g}{\cos\theta}\left[\cos\alpha(t^3\cos^2\theta - Y\sin^2\theta)\right. \tag{3.49}$$
$$\left. +\epsilon\sin\alpha\tan\theta\, Y\right],$$
$$g_{A'f\bar{f}} = \frac{g}{\cos\theta}\left[-\sin\alpha(t^3\cos^2\theta - Y\sin^2\theta)\right. \tag{3.50}$$
$$\left. +\epsilon\cos\alpha\tan\theta\, Y\right], \tag{3.51}$$

with the standard $t^3$ weak isospin and $Y$ hypercharge value of each fermion. The axial coupling remains unchanged from the SM. Unless $m_{A'} \sim m_Z$ ($\epsilon \sim |1-\delta^2|$), the $Z$ interactions are at their SM values (up to $\mathcal{O}(\epsilon^2)$). On the other hand, the dark photon couplings differ in the low and high $m_{A'}$ mass limits

$$g_{A'f\bar{f}} \to \begin{cases} -\epsilon e Q & \text{for } m_{A'} \ll m_Z \\ \frac{\epsilon e Y}{\cos^2\theta} & \text{for } m_{A'} \gg m_Z \end{cases}, \tag{3.52}$$

and thus couples to neutrinos at high masses. The couplings on the dark sector side are given by

$$g_{A'\chi\bar{\chi}} = g_d\cos\alpha \tag{3.53}$$
$$g_{Z\chi\bar{\chi}} = g_d\sin\alpha \tag{3.54}$$

## 3.11 Supplementary: Dark sector energy flow

By definition of the freeze-in regime, the DS does not thermalize at an arbitrary early time and entropy conservation arguments for the temperature decoupling do no apply. Instead, we compute the energy transfer to the DS with the Boltzmann equations. We numerically solve for the energy conservation equations [196]

$$\dot{\rho}_{\rm SM} + 3H\left(\rho_{\rm SM} + P_{\rm SM}\right) = -\mathcal{E} \tag{3.55}$$
$$\dot{\rho}_{\rm DS} + 3H\left(\rho_{\rm DS} + P_{\rm DS}\right) = \mathcal{E} \tag{3.56}$$

in the relativistic approximation $P_{\rm DS} = \rho_{\rm DS}/3$, with the energy density flow $\mathcal{E}$ given by

$$\mathcal{E} = \int \left( \prod_{i=1\ldots4} \frac{d^3 p_i}{(2\pi)^3 2E_i} \right) (2\pi)^4 \delta^4(p_1 + p_2 - p_3 - p_4) \times \\ \times \Delta E \ |\mathcal{M}|^2 \left( N_1 N_2 - N_3 N_4 \right), \tag{3.57}$$

with the energy transfer $\Delta E = \sqrt{s}$.

In the freeze-in limit, we find the following estimates

$$\mathcal{E}^{\text{real } A'} = \frac{1}{2\pi^2} \alpha' T m_{A'}^4 K_1 \left( \frac{m_{A'}}{T} \right), \tag{3.58}$$

$$\mathcal{E}^{\text{imag } A'} = \frac{\alpha' \alpha_d}{2\pi^2} T^3 \left( 2m_{hf}^2 + 2m_{hf} T + T^2 \right) e^{-\frac{2m_{hf}}{T}}. \tag{3.59}$$

In these cases, the energy density flow equation (3.56) can be solved exactly (with the $P_{\rm DS} = \rho_{\rm DS}/3$ and $H \sim T^2$ assumptions) and the attractor solutions for an empty DS initial condition in the far past are

$$\rho_{\rm DS}^{\text{real } A'}(T) = \frac{\alpha' m_{A'}^6}{8\pi^2 H_{m_{A'}} T} G^{2,1}_{1,3} \left( \frac{m_{A'}}{2T}, \frac{1}{2} \middle| \begin{matrix} -\frac{3}{2} \\ -\frac{1}{2}, \frac{1}{2}, -\frac{5}{2} \end{matrix} \right), \tag{3.60}$$

$$\rho_{\rm DS}^{\text{imag } A'}(T) = \frac{3\alpha' \alpha_d}{4\pi^2} \frac{m_{hf} T^4}{H_{m_{hf}}} \left( 1 - g\left( \frac{m_{hf}}{T} \right) e^{-\frac{2m_{hf}}{T}} \right), \tag{3.61}$$

where $g(x) = 1 + 4x/3 + 2x^2/3$ and $H_m$ is the Hubble rate evaluated at $H(T = m)$. By construction we solved for relativistic species ($P_{\rm DS} = \rho_{\rm DS}/3$) and the decoupled behaviour at low-temperature goes as

$$\rho_{\rm DS}^{\text{real } A'}(T) \sim \frac{8\alpha'}{\pi^2} \frac{m_{A'}}{H_{m_{A'}}} T^4, \tag{3.62}$$

$$\rho_{\rm DS}^{\text{imag } A'}(T) \sim \frac{3\alpha' \alpha_d}{4\pi^2} \frac{m_{hf}}{H_{m_{hf}}} T^4. \tag{3.63}$$

# Part II

# Higgs Portal

# Chapter 4

# Long-Lived Scalars at the LHC

This chapter was published as: **A. Fradette and M. Pospelov. Physical Review D 96, 075033 (2017)**. Section 4.6 was added for this dissertation.

## 4.1 Abstract

LHC experiments can provide a remarkable sensitivity to exotic metastable massive particles, decaying with significant displacement from the interaction point. The best sensitivity is achieved with models where the production and decay occur due to different coupling constants, and the lifetime of exotic particles determines the probability of decay within a detector. The lifetimes of such particles can be independently limited from standard cosmology, in particular, the BBN. In this chapter, we analyze the constraints on the simplest scalar model coupled through the Higgs portal, where the production occurs via $h \to SS$, and the decay is induced by the small mixing angle of the Higgs field $h$ and scalar $S$. We find that throughout most of the parameter space, $2m_\mu < m_S < m_h/2$, the lifetime of an exotic particle has to be less than 0.1 s, while below $2m_\mu$ it could grow to about a second. The strong constraints on lifetimes are induced by the nucleonic and mesonic decays of scalars that tend to raise the $n/p$ ratio. Strong constraints on lifetimes of the minimal singlet extensions of the Higgs potential are welcome news for the MATHUSLA proposal that seeks to detect displaced decays of exotic particles produced in the LHC collisions. We also point out how more complicated exotic sectors could evade the BBN lifetime constraints.

## 4.2 Introduction

The absence of readily discoverable NP at the LHC has presented the physics community with a formidable puzzle. While the arguments for NP "not too far" from the weak scale still loom large, there is a distinct desire to explore wider (and wilder) theoretical options away from a simply realized weak-scale supersymmetry, or extra space dimensions. One possible strategy to look for new physics is to abandon theoretical preconceptions and to start looking for nonstandard signatures that the NP could present.

Large classes of models offer promising avenues for a nonstandard signal in the production of new exotic particles (possibly of electroweak-scale mass) with subsequent decay away from the interaction point (see *e.g.* [197, 198, 199, 200]). While both ATLAS and CMS have performed corresponding studies in a variety of contexts and for different ranges of displacement [67, 68, 201], it has recently been pointed out that a dedicated and relatively inexpensive detector [202] could extend the physics reach into cases where the decay lengths are on the order of $O(100\,\mathrm{m})$ and beyond.

When both the production and the decay of an exotic state $S$ occur through one and the same coupling constant, the chances of detecting such NP at the LHC experiments are not great. Indeed, a large displacement implies a very small value for the coupling, which in turn leads to very inefficient production rates. Therefore, an ideal case for the collider studies would be when the production and decay occur through different coupling constants, and $\lambda_{\mathrm{production}} \gg \lambda_{\mathrm{decay}}$. For the pair-produced exotics, such a hierarchy can be made "natural" as the $\lambda_{\mathrm{decay}} \to 0$ limit could lead to an enhanced symmetry.

If the main signal to search for is an *appearance* of abnormal energy deposition or exotic vertex some distance from the interaction point, it is then very important to know how small $\lambda_{\mathrm{decay}}$ is allowed to be. In more practical terms, one would like to know if there is an external to the LHC physics constraint on the lifetimes $\tau_S$ of such exotic particles. An obvious source for such a constraint can be early cosmology. The BBN, and its overall agreement with observations [203] (apart from the unclear status of $^7$Li) can provide a limit on the lifetimes of such particles. To derive such limits, one would have to make a fairly natural assumption that the Universe was indeed as hot as $T \sim m_S \sim$ electroweak scale at some point in its history. Subsequent thermal evolution to the BBN temperatures involves self-depletion via $SS \to \mathrm{SM}$ due to $\lambda_{\mathrm{production}}$, in an expected WIMP-type annihilation process, and late-time decay of

$S \to$ SM where depending on lifetimes and the properties of the decay products the BBN outcome may get affected. These mechanisms are well understood in the BBN literature (see *e.g.* [204, 12] for reviews). We will require that the late decay of $S$ provides a small and acceptable perturbation to the standard BBN (SBBN) outcome, which in turn will limit $\tau_S$.

In this chapter, we analyze a fairly minimal model, where a new singlet scalar has predominantly a quadratic coupling to the Higgs boson that regulates both its production at colliders and the intermediate cosmological abundance at $T_{\rm BBN} \ll T \ll m_S$. Given that the model is very predictive, it allows one to place robust bounds on lifetimes of such particles with a minimum amount of model dependence. We find that for most of the analyzed parameter space with $m_S < m_h/2$, the intermediate abundance of such particles is large enough to affect the neutron-proton freeze-out ratios at relevant temperatures. This allows us to set fairly robust bounds on lifetimes of such particles, which come out to be remarkably strong, and shorter than 0.1 s. In what follows, we describe the model and the cosmological history of $S$ (section 4.3), derive the impact on the BBN (section 4.4), present our results (section 4.5), estimate the number of events at the MATHUSLA detector (section 4.6) and provide an overall discussion (section 4.7).

## 4.3 The minimal Higgs portal model

We consider the simplest extension of the SM by a singlet scalar field $S$. A new singlet scalar $S$ can have two interaction terms with the SM at the renormalizable level, in addition to trilinear and quartic self-interactions. In this scenario, the Lagrangian of the singlet sector (including the SM) generically takes the form

$$\mathcal{L}_{H/S} = \mu^2 H^\dagger H - \lambda_H \left(H^\dagger H\right)^2 - V(S) - ASH^\dagger H - \lambda_S S^2 H^\dagger H + \text{kin. terms}. \quad (4.1)$$

The Higgs expectation value $v = 246$ GeV is assumed to correspond to a global minimum. The self-interaction potential $V(S) = \lambda_4 S^4 + \lambda_3 S^3 + \frac{m_{S0}^2}{2} S^2$ can be redefined in such a way that the linear term is absent. It is important that the $A,\ \lambda_3 \to 0$ and $\langle S \rangle = 0$ limit would correspond to the case of stable $S$ particles. To simplify the discussion without sacrificing much generality, we take $\lambda_{3,4} \to 0$ and assume $Av \ll m_{S0}^2,\ \lambda_S v^2$.

The physical mass of $S$ receives a contribution from the electroweak symmetry

breaking, $m_S = \sqrt{m_{S0}^2 + \lambda_S v^2}$. At linear order in $A$, the mixing angle $\theta$ between physical excitations $S$ and $h$ is

$$\theta = \frac{Av}{m_h^2 - m_S^2}\left(1 - \frac{\lambda_S v^2}{m_S^2}\right). \tag{4.2}$$

The $\lambda_S$ term arises because the $S$ field develops a small $A$-controlled vacuum expectation value. The mixing parameter $\theta$ leads, via the $A$ coupling constant, to the decay of $S$ particles, which can readily be derived from

$$\mathcal{L}_{\text{decay}} = S \times \theta \sum_{\text{SM}} O_h, \tag{4.3}$$

where $O_h$ is the set of the standard Higgs interaction terms, with the Higgs field removed: *e.g.* $O_h = (m_f/v)\bar{f}f$ for an elementary SM fermion $f$.

This Yukawa-type coupling to the SM has been tested in rare meson decays [205, 206, 44, 207, 208] and in proton fixed-target experiments [47]. The model is mostly ruled out for large mixing angles $\theta \gtrsim 10^{-4} - 10^{-2}$ over the $m_S \sim$ MeV - 5 GeV mass range. The proposed experiment SHiP could potentially improve current sensitivity down to $\theta \sim 10^{-6}$ for $m_S \sim$ few GeV [47] and there are additional islands of sensitivity at even lower mixing angles from BBN and the CMB [102].

In the limit of $\theta \to 0$, $S$ is stable and could be the dark matter [209, 45, 46]. Various limits arise from searches in direct and indirect detection if the particle is stable (see Refs. [210, 211] for recent reviews), but $\lambda_S$ is generically bounded from the constraints on invisible Higgs decay, independently of the direct detection limits. The SM Higgs has a well-predicted decay rate into SM particles of $\Gamma_{\text{SM}} = 4.07$ MeV. So far, the properties of 125 GeV resonance are remarkably consistent with the SM Higgs, and therefore there is little doubt that its width is close to $\Gamma_{\text{SM}}$. The invisible branching ratio of Higgs decay to the $SS$ final state is

$$\Gamma_{h\to SS} = \frac{\lambda_S^2 v^2}{8\pi m_h}\sqrt{1 - \frac{4m_S^2}{m_h^2}}, \tag{4.4}$$

$$Br(h \to SS) = \frac{\Gamma_S}{\Gamma_S + \Gamma_{\text{SM}}} \simeq 10^{-2}\left(\frac{\lambda_S}{0.0015}\right)^2, \tag{4.5}$$

where in the last line we assumed $Br(h \to SS) \ll 1$ and $m_S \ll m_h$. The experimental upper bound on the invisible branching ratio of a SM Higgs is 0.19 (at $2\sigma$) [212], which

translates into an upper bound on $\lambda_S$,

$$\lambda_S \lesssim \frac{0.007}{\left(1-\frac{4m_S^2}{m_h^2}\right)^{1/4}}. \tag{4.6}$$

If $S$ is to be stable, such small couplings would lead to an excessive abundance of $S$, which invalidates the $Z_2$ symmetric case and forces us to include the decay term. From now on, we will consider $\theta \neq 0$, or in other words the case of unstable $S$ particles. Since our analysis is motivated by the LHC physics, we will use $Br(h \to SS)$ as an input parameter and substitute $\lambda_S$ everywhere employing (4.4) and (4.5).

### 4.3.1 Decay products

Since $S$ interacts with the SM in the same fashion as the Higgs with an additional $\theta$ mixing factor (4.3), its decay properties are similar to those of a light Higgs boson. For the derivations of the actual limits on the lifetime of $S$, we need to know its mesonic and nucleonic decay branching ratios.

The decay channels of a light Higgs have been considered in the early years of the Weinberg-Salam electroweak model [213], with additional refinements as SM particles and hadronic resonances were being discovered and final-state interactions were becoming better understood [214, 215, 216]. Hadronic decays in the mass range $2m_\pi < m_S \lesssim 4$ GeV are still poorly understood, with models varying by as much as a few orders of magnitude near the di-kaon threshold [208].

The leptonic decay channels are straightforward, with the decay rate given by

$$\Gamma_{S\to l\bar{l}} = \frac{\theta^2}{8\pi}\frac{m_l^2}{v^2} m_S \left(1-\frac{4m_l^2}{m_S^2}\right)^{3/2}. \tag{4.7}$$

If the decaying product is a pair of heavy quarks, there are $\mathcal{O}(1)$ corrections coming from the 1-loop QCD vertex correction [210], which yields the following correction factor [217] to the fermionic expressions (4.7)

$$f_q = 3\left[1+\frac{4\alpha_s}{3\pi}\left(\frac{9}{4}+\frac{3}{2}\ln\frac{m_q^2}{m_S^2}\right)\right] \tag{4.8}$$

and the factor of 3 comes from the number of color charges. For better accuracy, we use the higher order perturbative results from the HDECAY code [218] for $m_S >$

2.5 GeV.

Metastable mesons, such as $\pi^{\pm}$ and $K^{\pm}, \bar{K}^0, K^0$ are "important" decay products, as they can participate in the charge-exchange reactions with nucleons and shift the $n-p$ balance, hence affecting the whole nucleosynthetic chain. In the mass range where the perturbative QCD calculations are no longer valid, we base our baseline calculations on Ref. [219]. The scalar-pion interaction can be extracted from the low-energy expansion of the trace of the QCD energy-momentum tensor (see, *e.g.*, [220, 221]) by integrating out the three heavy quarks and using chiral perturbation theory on the remainder, yielding the effective Lagrangian [219]

$$\mathcal{L}_{S\pi\pi} = \frac{4}{9}\frac{\theta}{v} S \left( \frac{1}{2}\partial_\mu \pi^0 \partial^\mu \pi^0 + \partial_\mu \pi^+ \partial^\mu \pi^- \right) - \frac{5}{3}\frac{\theta m_\pi^2}{v} S \left( \frac{1}{2}\pi^0\pi^0 + \pi^+\pi^- \right), \tag{4.9}$$

where we have inserted the SM numerical values for the number of heavy quarks and the first coefficient of the QCD beta function. This leads to decay width to charged pions

$$\Gamma_{S\to\pi^+\pi^-} = 2\Gamma_{S\to\pi^0\pi^0} = \frac{\theta^2}{16\pi}\frac{m_S^3}{v^2}\left(\frac{2}{9} + \frac{11}{9}\frac{m_\pi^2}{m_S^2}\right)^2 \sqrt{1 - \frac{4m_\pi^2}{m_S^2}}. \tag{4.10}$$

This result, however, is not applicable far above the pion threshold, as final-state resonances would drastically affect this prediction. Instead, we use the pion and kaon decay width described in Ref. [222], where the authors matched the next-to-leading order corrections of the low-energy theorems to the dispersion results from the $\pi\pi$ phase-shift analysis above 600 MeV from the CERN-Munich group [223]. The photon decay channel is added with the prescription detailed in Ref. [224]. Finally, there is a gap for 1.4 GeV $< m_S <$ 2.5 GeV where no analytical treatment is entirely trustworthy, as this includes new resonances strongly coupled to $\eta\eta$ and other potential hadronic channels. We simply follow Ref. [219] and interpolate between the two regimes, under the assumption that there is no order of magnitude deviation in this mass range. The branching ratios and the lifetime for $\theta = 10^{-6}$ are displayed in Fig. 4.1.

As an alternative decay spectrum model, we also display the perturbative spectator approach [225, 226, 47], where the relative decay widths above the kaon threshold are given by

$$\Gamma_{\mu^+\mu^-} : \Gamma_{KK} : \Gamma_{\eta\eta} = m_\mu^2\beta_\mu^3 : 3\frac{9}{13}m_s^2\beta_K^3 : 3\frac{4}{13}m_s^2\beta_\eta^3, \tag{4.11}$$

with $\beta_i = \sqrt{1 - 4m_i^2/m_S^2}\Theta(m_S - 2m_i)$, $\Theta$ being the step-function, and we adopt the

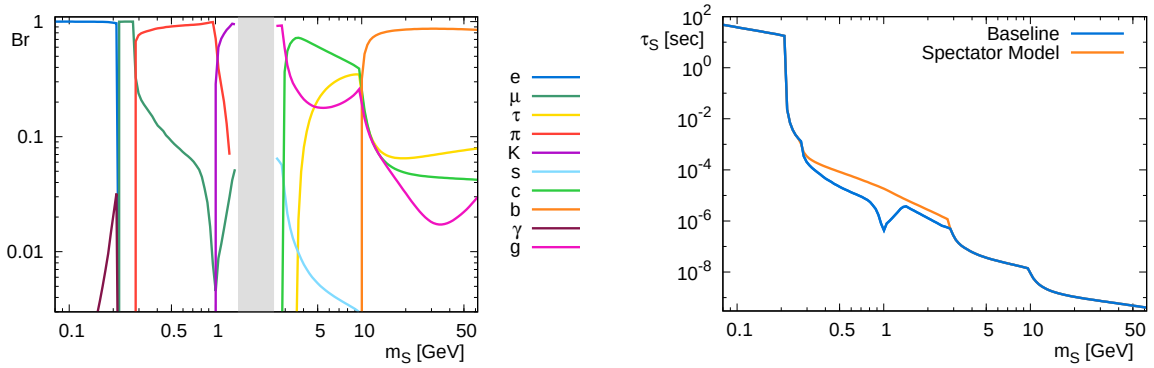


Figure 4.1: *Left*: Branching ratios of the scalar $S$ in our baseline decay model. See text for details. *Right*: Scalar $S$ lifetime of our baseline model and the spectator model for the mixing angle $\theta = 10^{-6}$.

running of $s$ quark mass following Ref. [224]. The pion contribution is kept as in Eq. (4.10) and then we use the HDECAY output at the $c$-quark threshold and above to match our baseline model.

For $m_S$ of several GeV and heavier, decays with final state nucleon-antinucleon pairs are possible. Even though the branching to such states are generally lower than 10%, the effect on BBN can be quite significant, and therefore these are by far the most important channels for $\tau_S \gtrsim 1$ s. On top of direct and for the most part subdominant contributions from $S \to \bar{n}n, ...$, we need to take into account the (anti)nucleon states that emerge from the hadronization of the quark decay products and heavy $B$-meson fragmentations.

### 4.3.2 Cosmological metastable abundance

After the temperature drops below $m_S$, the interaction of $SS$ pairs with the SM shifts toward the annihilation, resulting in an intermediate (metastable) population of $S$ bosons. In the mass range that we consider, the $S$ annihilation is dominated by the $s$-channel reactions $SS \to h^* \to XX$, where on the receiving end are the pairs of the SM states $XX$ created by a Higgs-mediation process. The annihilation cross

section $\sigma v$ generically takes the form

$$\sigma v(s) = \frac{8\lambda_S^2 v^2}{(s-m_h^2)^2 + m_h^2 \Gamma_{\mathrm{SM}+S}^2} \frac{\Gamma_{\mathrm{SM}}^{m_h \to \sqrt{s}}}{\sqrt{s}}, \tag{4.12}$$

$$\langle \sigma v \rangle = \frac{\int_{4m_S^2}^{\infty} ds\ \sigma v(s)\ s\sqrt{s-4m_S^2} K_1\left(\frac{\sqrt{s}}{T}\right)}{16 T m_S^4 K_2^2\left(\frac{m_S}{T}\right)}. \tag{4.13}$$

This formula recast the rate in terms of a Higgs width $\Gamma_{\mathrm{SM}}^{m_h \to \sqrt{s}}$ with a fictitious mass of $\sqrt{s}$. This form encompasses both perturbative and nonperturbative channels in the $h^*$ decay rate (with the substitution $m_h^* \to \sqrt{s}$), which we have described above. In the standard WIMP freeze-out paradigm, a DM particle freezes out at $T_{\mathrm{f.o.}} \sim m_{\mathrm{DM}}/20$, $\langle \sigma v \rangle$ is simply the nonrelativistic limit $\sigma v(\sqrt{s} = 2m_{\mathrm{DM}})$ and the relic density can be conveniently approximated as $\Omega_{\mathrm{DM}} h^2 \sim 0.11 \times 1\mathrm{pb}/\langle \sigma v \rangle$. This result emerges as a solution to the Boltzmann equation[1] [227]

$$\frac{dY}{dx} = \frac{s\langle \sigma v \rangle}{Hx} \left[1 + \frac{1}{3}\frac{d(\ln h_{\mathrm{eff}})}{d(\ln T)}\right] \left(Y_{\mathrm{eq}}^2 - Y^2\right), \tag{4.14}$$

when the freeze-out occurs in the exponentially falling region of the equilibrium density $Y_{\mathrm{eq}}(T)$. For a much smaller annihilation cross section, $\langle \sigma v \rangle \ll 1$ pb, $Y$ departs from the equilibrium value earlier, possibly near the relativistic plateau $Y_{\mathrm{eq}} = n_{\mathrm{eq}}/s \to 45\zeta(3)/2\pi^4 h_{\mathrm{eff}}(T)$ for $x \ll 1$. Since the nonrelativistic annihilation cross section in the minimal Higgs portal model ranges from $10^{-3}$ to $10^{-14}$ pb for $m_S \sim 1$ MeV $- 60$ GeV and $Br(h \to SS) \sim 0.1 - 0.001$, we numerically integrate Eq. (4.14) to determine the metastable $S$ abundance. The results are shown in Fig. 4.2, normalized to the baryon number density for a more intuitive interpretation of its impact on BBN in the following section.

For $m_S \simeq m_h/2$, the $\sigma v$ cross section evaluated at $s = 4m_S^2$ is a poor approximation, as it fails to capture the strong energy dependence of the cross section near the resonance at $\sqrt{s} = m_h/2$ [228]. The sharp drop in the abundance above $m_S \sim 45$ GeV is due to the resonant contribution to the thermally averaged cross section, leading to a delayed freeze-out and drastic decrease in metastable $S$ abundance. Our numerical results agree with the semianalytic treatment of Ref. [210]. For very light $m_S$, one can

[1] We use the standard variable definitions, where $Y = n_S/s$ is the $S$ abundance normalized on the entropy density $s$, $x = m/T$ is the dimensionless inverse temperature, $H$ is the Hubble rate, $h_{\mathrm{eff}}$ is the number of entropic relativistic degrees of freedom and $Y_{eq}$ is the normalized thermal equilibrium $S$ number density.

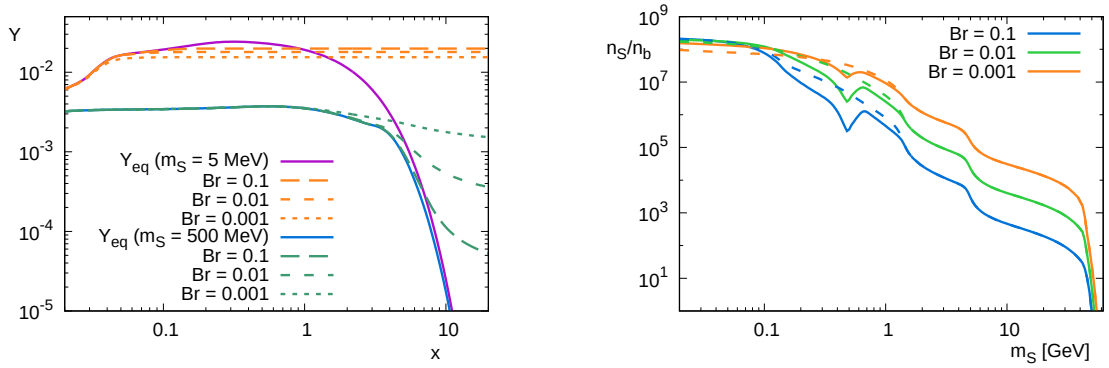


Figure 4.2: *Left*: Temperature evolution ($x = m/T$) of the $Y_S$ intermediate abundance for $m_S = 5$ MeV and 500 MeV for the three benchmark Higgs branching ratios. *Right*: Metastable abundance of $S$ prior to its decay normalized over the baryon density. Values shown for $Br(h \to SS) = 10^{-1}$, $10^{-2}$ and $10^{-3}$. The dashed lines correspond to the perturbative spectator model.

see that the freeze-out abundances are large, and the relative spread between different input values of $Br(h \to SS)$ gets smaller, as the annihilation cross section becomes very small and the freeze-out happens in the semirelativistic regime $x_{\text{f.o.}} \sim \mathcal{O}(1)$ with an asymptote at the $Y_{\text{eq}}$ relativistic plateau for small $m_S$. The only difference at the lightest masses is from $Y_{\text{eq}}^{\text{rel}} \propto 1/h_{\text{eff}}(T)$. Since $h_{\text{eff}}$ is a monotonic function of temperature, weaker annihilation cross sections freeze out earlier, at a higher temperature, thus yielding smaller abundances (as seen in the $m_S = 5$ MeV curves in Fig. 4.2). This is in contrast with the standard freeze-out in the nonrelativistic regime, with final abundances inversely proportional to the cross section. We note in passing that the strong-interaction-related uncertainty "propagates" outside the $m_S \sim 2m_\pi - 2m_c$ window. For example, because of the relativistic freeze-out, for $m_S$ smaller than $2m_\pi$ the hadronic channels may turn out to be important.

Corrections to the metastable abundance from the $Z_2$-breaking mixing angle are negligible. Parametrically, we will be interested in values of $\theta$ that have $\Gamma_S^{\text{dec}} \sim (0.1 - 1\text{ s})^{-1}$. Modifications to the relic abundance would arise from decay or inverse decay processes with approximately

$$\left.\frac{\delta n_S}{n_S}\right|_\theta \sim \frac{\Gamma_S^{\text{dec,inv}-\text{dec}}}{H(t_{fo})} \ll 1, \tag{4.15}$$

which justifies neglecting $\theta$ at the time of metastable $S$ freeze-out.

## 4.4 Big Bang Nucleosynthesis

The formation of light nuclei is one of the earliest probes of NP in cosmology along with far less certain constraints imposed by the inflationary framework. BBN is well understood within SM physics, and its outcome agrees with observational data for $^4$He and D. $^7$Li has an outstanding factor of $\sim 2-3$ discrepancy between theory and observations [203], with the caveat that the observed abundances may have been affected by stellar evolution. Nevertheless, the overall success over a wide range of abundances can be used to constrain various types of NP [12].

The initial BBN stage is the neutron-proton ratio $n/p$ freeze-out. Maintained in equilibrium by electroweak interactions at high temperatures, the neutron abundance follows $n/p \sim e^{-Q/T}$, where $Q = m_n - m_p - m_e \simeq 1.293$ MeV, until the epoch when the weak processes decouple around temperatures of 0.7 MeV. The outcome, $n/p \simeq 1/6$, is quasistable, decreasing to $n/p \simeq 1/7$ at the end of the "deuterium bottleneck." The latter terminology is used to indicate a much delayed onset of nuclear reactions controlled by a relatively shallow $n-p$ binding energy. Once the Universe runs out of photons that can efficiently dissociate deuterium, the bulk of the nucleosynthetic reactions occurs at $t_{\rm deut} \sim 200$ s. $^4$He has a large binding energy per nucleon, and the reactions leading to it are less Coulomb-suppressed than for heavier elements. Consequently, most neutrons end up in the final $^4$He abundance (expressed in mass fraction from the total baryon mass) $Y_p \simeq 2(n/p)/\left(1+n/p\right) \simeq 0.25$.

Traces of neutrons and incomplete nuclear burning of $A = 2,\ 3$ nuclei light nuclei result in the leftover abundances of $^3$He and D. Beyond the $^4$He atomic number, the deepest bound nucleus is $^{12}$C, but its formation is completely suppressed since it would need to be produced by a triple $^4$He collision. The $2 \to 2$ reactions $p + {}^4$He and $^4$He + $^4$He are also ineffective at producing heavier nuclei as the $A = 5$ and $A = 8$ elements are all unstable. The only remaining possibilities are $^4\mathrm{He} + {}^3\mathrm{He} \to {}^7\mathrm{Be} + \gamma$ followed by an electron capture to yield $^7$Li/H $\sim \mathcal{O}(10^{-10})$ and $^6$Li formed at the $^6$Li/H $\sim \mathcal{O}(10^{-14})$ via $^4$He-D fusion. For the problem at hand - the determination of the upper limit on the $S$ lifetime - few of these details matter. This is because of relatively large metastable abundances affecting the earliest stages of nucleosynthesis, primarily via the $n/p$ ratio.

### 4.4.1 Neutron enrichment

Ample abundances of $S$ particles ($n_S \sim 10^2 - 10^9 \times n_b$) flood the Universe with final state mesons and nucleons that in turn could spoil the final light nuclei abundances. For example, at temperatures $T \sim 0.5$ MeV, the protons are $\sim 6$ times more abundant than neutrons, but this ratio can easily be changed due to meson-induced charge exchange reactions. At these temperatures, the probability of $p \to n$ conversion from charged pions is

$$P_{n\to p} \simeq n_p \langle \sigma v \rangle_{pn} c\tau_{\pi^+} \simeq 2 \times \frac{10^{21}}{\mathrm{cm}^3} \times 1.5 \text{ mb} \times 2.6 \times 10^{-8} \text{ s} \times c \simeq 2.5 \times 10^{-3}. \quad (4.16)$$

It is then clear that injection of $O(10^3)$ mesons per nucleon at these temperatures can drastically increase the $n/p$ freeze-out abundance. Similarly, direct baryonic injection of $n\bar{n}$ and $p\bar{p}$ will have a comparable effect on the $n/p$ ratio. On the other hand, if $S$ decays happen before the $n/p$ freeze-out, the additional $p \to n$ conversions would not be as efficient, being washed out by the ongoing weak interaction conversions.

The limit of the exclusion region in the $Y_S/\tau_S$ parameter space ($Y_S \equiv n_S/n_b$ from now on) is determined by solving the Boltzmann equation with the injection of charge exchange inducing particles. Given that the abundances of $S$ particles are large, the main constraints can be derived from the $n/p$ freeze-out ratio. To that effect, we would not need a complete BBN framework, but only a subset of the whole code that deals with $n \leftrightarrow p$ conversions. We follow the semianalytic treatment by Mukhanov [229] that approximates $n \leftrightarrow p$ weak conversion rates by a few integrals over thermal distributions and assumes a "steplike" disappearance of charged leptons below $T = m_e$,

$$\Gamma_{n\nu_e\to pe^-} = \frac{1+3g_a^2}{2\pi^3} G_F^2 Q^5 J(1;\infty), \qquad \Gamma_{pe^-\to n\nu_e} = e^{-Q/T}\Gamma_{n\nu_e\to pe^-}, \quad (4.17)$$

$$\Gamma_{ne^+\to p\bar{\nu}_e} = \frac{1+3g_a^2}{2\pi^3} G_F^2 Q^5 J(-\infty;-\frac{m_e}{Q}), \qquad \Gamma_{p\bar{\nu}_e\to ne^+} = e^{-Q/T}\Gamma_{ne^+\to p\bar{\nu}_e}, \quad (4.18)$$

$$J(a,b) \equiv \int_a^b \sqrt{1-\frac{(m_e/Q)^2}{q^2}} \frac{q^2(q-1)^2\, dq}{(1+e^{\frac{Q}{T_\nu}(q-1)})(1+e^{-\frac{Q}{T}q})}, \quad (4.19)$$

where $g_a \simeq 1.27$ is the standard nucleon axial-vector coupling, $Q = m_n - m_p - m_e \simeq 1.293$ MeV, and $G_F$ is the Fermi constant. The reverse reaction rates are found by detailed balance. We evaluate $J$ numerically and solve for the electron-neutrino temperature $T_\nu$ by entropy conservation, assuming a $\nu_e$ decoupling temperature of

2 MeV, which reproduces the correct entropy degrees of freedom at lower temperature [230]. It is then straightforward to solve numerically the differential equation for $X_n = n_n/n_b$,

$$\frac{dX_n}{dT} = \frac{\Gamma_{n\nu_e\to pe^-} + \Gamma_{ne^+\to p\bar{\nu}_e}}{TH(T)}\left(X_n - (1-X_n)e^{-Q/T}\right) + \frac{\Gamma_n X_n}{TH(T)}, \tag{4.20}$$

where the last term represents the neutron decay with $\Gamma_n^{-1} = 880$ s. This equation is approximately valid until the rapid switch-on of the nuclear reaction rates at the end of the deuterium bottleneck. Within this approximation, one can determine the final temperature where the equation is valid by starting with $X_n = 1/2$ at early times, and solving for the deuterium bottleneck temperature by imposing $Y_p = 2X_n(T_{\rm deut}) = 0.25$. This results in $T_{\rm deut} \simeq 0.068$ MeV or $t_{\rm deut} \simeq 276$ s. We take this approximation as our baseline SBBN model, which is then modified by the inclusion of extra sources and sinks for $n$, $p$, and new $n \leftrightarrow p$ reactions. To constrain the parameter space of a species decaying into charged mesons or baryons, we proceed by solving the Boltzmann equation that includes new interactions. We will require that $Y_p$ does not deviate from SBBN by more than 4%,

$$\Delta Y_p \equiv |Y_p - Y_p^{\rm SBBN}| < 0.01, \tag{4.21}$$

which is a rather generous allowance for the errors, considering the tight observational constraints on primordial helium abundance [203]. Consequently, it will result in conservative limits of $\tau_S$.

### Meson-mediated mechanism

Only long-lived mesons have an opportunity to interact with the baryon bath and induce proton-neutron conversions. As such, only $\pi^\pm$, $K^\pm$ and $K_L$ have lifetimes in excess of $\tau \sim 10^{-8}$ s, and can induce $p \leftrightarrow n$ via strong interactions. For temperatures relevant for the $n/p$ freeze-out, the density of charged leptons is very high, and mesons are efficiently stopped by the primordial plasma. We assume that they are efficiently thermalized, and take the relevant pion-induced reactions at threshold [231, 69] ($c =$

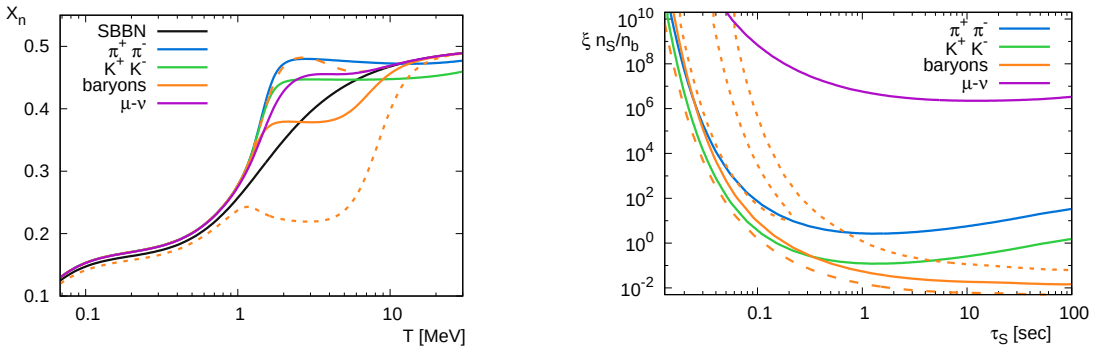


Figure 4.3: *Left*: $X_n$ evolution for the SBBN and the injection of pions, kaons, baryons and muons (neutrinos) as described in the text (see supplementary section 4.8.1 for the muon case) for lifetimes of 0.05 s with the initial $Y_S$ abundance tuned to yield $\Delta Y_p = 0.01$ (maximum allowed shift of $Y_p$). The baryonic injection is taken at $\kappa = 0.5$ (full line); the lines for $\kappa = 1$ (dashed) and $\kappa = 0.2$ (dotted) are also displayed. *Right*: Limit of injected pairs for each channel as a function of the $S$ lifetime. The upper-right dotted line for $\kappa = 0.2$ is at $Y_p = 0.26$, and the upper-left dotted island yields $Y_p = 0.24$.

1),

$$\pi^- + p \to n + \gamma: \qquad (\sigma v)^{\pi^-}_{pn(\gamma)} \simeq 0.57 \text{ mb}, \qquad Q = 138.3 \text{ MeV}, \tag{4.22}$$

$$\pi^- + p \to n + \pi^0: \qquad (\sigma v)^{\pi^-}_{pn(\pi^0)} \simeq 0.88 \text{ mb}, \qquad Q = 3.3 \text{ MeV}, \tag{4.23}$$

$$\pi^+ + n \to p + \gamma: \qquad (\sigma v)^{\pi^+}_{np(\gamma)} \simeq 0.44 \text{ mb}, \qquad Q = 140.9 \text{ MeV}, \tag{4.24}$$

$$\pi^+ + n \to p + \pi^0: \qquad (\sigma v)^{\pi^+}_{np(\pi^0)} \simeq 1.26 \text{ mb}, \qquad Q = 5.9 \text{ MeV}. \tag{4.25}$$

The reverse reactions are irrelevant due to the short lifetime of $\pi^0$'s and the need for nonthermal $\gamma$'s of $\sim 140$ MeV energy. The $\pi^-$ reactions are to be added to the right-hand side of the Boltzmann Eq. (4.20) via the additional term

$$\left.\frac{dX_n}{dT}\right|_{\pi-} = \frac{-1}{TH(T)} n^{\rm inj}_{\pi^-} \left( \langle \sigma v \rangle^{\pi^-}_{pn(\pi^0)} + \langle \sigma v \rangle^{\pi^-}_{pn(\gamma)} \right) (1 - X_n), \tag{4.26}$$

and similarly for the $\pi^+$ reactions. The ambient population of injected pions from a $S$ decay with $Br(S \to \pi^+\pi^-) = \xi_{\pi^\pm}$ is $n^{\rm inj}_{\pi^\pm} \simeq \xi_{\pi^\pm} \Gamma_S \tau_{\pi^\pm} Y_S n_b(T) e^{-t\Gamma_S}$, where we take $t \simeq 2.42$ s $(\text{MeV}/T)^2/\sqrt{g_\star}$ and the thermal cross sections at their threshold value $\langle \sigma v \rangle^{\pi^+}_{np} = (\sigma v)^{\pi^+}_{np}$. Reactions with pairs of charged particles in the initial states, such as $\pi^- p$, will be somewhat enhanced due to the Coulomb attraction, which provides a small but non-negligible correction. We account for it following Ref. [69].

The implementation of the charged kaon reactions is similar to the pion case, but the dominant reactions are rather different. The direct charge exchange between neutral and charged kaons is

$$\bar{K}^0 + n \to K^- + p: \qquad (\sigma v)^{\bar{K}^0}_{pn(K^-)} \simeq 10 \text{ mb}, \qquad Q = 5.3 \text{ MeV}, \tag{4.27}$$

with similar cross section for a charge-conjugated reaction, $K^0 p \to K^+ n$. For neutral kaons, the effects induced by $K_L$ are the most important, and we use $\sigma(K_L n \to K^- p) \simeq \frac{1}{2}\sigma(\bar{K}^0 n \to K^- p)$ and (4.27) to find $(\sigma v)^{\bar{K}^0}_{pn(K^-)} \simeq 4.5$ mb. Additionally, efficient reactions can also proceed via $s$-quark being incorporated inside an unstable hyperon and a pion

$$K^- + p \to \Sigma^{\pm}\pi^{\mp}, \Sigma^0\pi^0, \Lambda\pi^0, \tag{4.28}$$

$$K^- + n \to \Sigma^-\pi^0, \Sigma^0\pi^-, \Lambda\pi^-, \tag{4.29}$$

with the hyperon subsequently decaying into $p/n + X$. The inclusive threshold cross sections found by weighting each hyperon-producing cross sections by their branching ratios to $p/n$ are [69]

$$K^- + p \to n + X: \qquad (\sigma v)^{K-}_{pn} \simeq 32 \text{ mb}, \tag{4.30}$$

$$K^- + n \to p + X: \qquad (\sigma v)^{K-}_{np} \simeq 13 \text{ mb}, \tag{4.31}$$

$$K_L + p \to n + X: \qquad (\sigma v)^{K-}_{pn} \simeq 6.5 \text{ mb}, \tag{4.32}$$

$$K_L + n \to p + X: \qquad (\sigma v)^{K-}_{np} \simeq 16 \text{ mb}. \tag{4.33}$$

Notice the absence of corresponding hyperon reactions initiated by $K^+$ due to the presence of an anti-$s$ quark.

Representative examples of $X_n(T)$ evolutions and the sensitivity to $\xi_{\pi^\pm} Y_S/\tau_S$ parameter space are shown in Fig. 4.3. The left panel displays significant modifications to the evolution of neutron abundance at $\tau_S$ =0.05 s with adjustable initial abundance, yielding $\Delta Y_p = 0.01$. The departure from $X_n = 0.5$ at high temperatures is clearly visible. [In fact, for short $\tau_S$, the kaon injection channel at early times leads to a shift of the equilibrium value of $X_n$ to $(\sigma v)^{K^-+K_L}_{pn}/((\sigma v)^{K^-+K_L}_{pn} + (\sigma v)^{K^-+K_L}_{np}) \simeq 0.45$.] As the temperature lowers, the Coulomb-enhanced reaction becomes stronger. For meson injection, these reactions enhance the $p \to n$ conversion, keeping $X_n$ away from the SBBN value. The right panel gives a boundary of the exclusion regions for dif-

ferent injection modes. In addition to the already described channels, charged kaons also give rise to a population of secondary charged pions that should also be included in the analysis of $p \leftrightarrow n$ transitions. Since the constraints are already stronger than for the charged pion case, we neglect this effect, which leads to more conservative bounds.

**Direct baryonic injection mechanism**

If $S$ is heavy enough, the end products after hadronization of the primary decay products (*e.g.* $b$ or $c$ quarks) may contain baryons. Since $S$ has no baryon number, one should expect an equal number of baryons and antibaryons in the final states. Therefore, one should expect the injection of $n\bar{n}$, $p\bar{p}$, $\bar{n}p$ and $p\bar{n}$ pairs, as well as (in principle) baryonic states with higher multiplicities. The hadronization process and decay of heavy quarks produce many more light mesons than baryons, and a complete analysis must include a Monte Carlo study of the hadronization process (see Ref. [232] for benchmarks of heavy unstable particles decaying into 2 hadronic + 1 leptonic jets in the early BBN epoch). Assuming that the heavy quarks inside baryons decay due to the "main" weak decay sequence, $b \to c \to s \to u$, one should also expect a somewhat large number of the final states with a proton or antiproton over neutron or antineutron. We will tune the branching models of $S$ to available particle data on proton production, and take $N_n = \kappa N_p$ and $N_{\bar{n}} = \kappa N_{\bar{p}}$. Furthermore, because of a more frequent appearance of the up-quark at the end of the decay chain, we would take $\kappa \simeq 0.5$ on average.

As in the case of mesons, the thermalization of baryonic decay products is quick (see *e.g.* [233]). As a baryonic pair is created in the decay, the baryon is added to the existing population of $n$ or $p$. The antibaryon will, however, annihilate with either $p$ or $n$ and dissipate into lighter mesons. If it annihilates with its own antiparticle, there is no net change in $n/p$, but an annihilation with the other species induces a net $n - p$ change. The probability $P_{k\bar{l}}^{i\to j}$ of a net charge exchange $i \to j$ from a $k\bar{l}$ injection is simply given by the weighted annihilation rates

$$P_{p\bar{p}}^{n\to p} = \frac{X_n \langle\sigma v\rangle_{n\bar{p}}}{X_n \langle\sigma v\rangle_{n\bar{p}} + (1 - X_n)\langle\sigma v\rangle_{p\bar{p}}}, \qquad P_{p\bar{n}}^{n\to p} = \frac{(1 - X_n)\langle\sigma v\rangle_{p\bar{n}}}{X_n \langle\sigma v\rangle_{n\bar{n}} + (1 - X_n)\langle\sigma v\rangle_{p\bar{n}}} \tag{4.34}$$

and similarly for the $n\bar{p}$ and $n\bar{n}$ injections. The baryonic annihilation rates are given

by [231]

$$\langle\sigma v\rangle_{n\bar{n}} = \langle\sigma v\rangle_{p\bar{p}}/C = 37 \text{ mb}, \qquad \langle\sigma v\rangle_{n\bar{p}} = \langle\sigma v\rangle_{p\bar{n}} = 28 \text{ mb}, \tag{4.35}$$

where the $p\bar{p}$ has the low-$v$ Coulomb correction $C(v)$. The implementation of these processes in the Boltzmann equation then require additional terms

$$\left.\frac{dX_n}{dT}\right|_{pn} = \frac{-\xi_p \Gamma_S e^{-t\Gamma_S}}{TH(T)} \left(-P_{p\bar{p}}^{n\to p} - \kappa P_{p\bar{n}}^{n\to p} + \kappa P_{p\bar{n}}^{n\to p} + \kappa^2 P_{n\bar{n}}^{n\to p}\right). \tag{4.36}$$

As before, the outcome is displayed in Fig. 4.3. Again, for short $S$ lifetimes and large $Y_S$, the large numbers of injected particles completely dictate the early $X_n$ value. The constraint on $Y_S$ goes up more sharply in the short $S$ lifetime limit. There is a significant dependence on $\kappa$ for $\tau_S \gtrsim 0.1$ s, which is washed out by the SM electroweak interactions at earlier times. If we take the extreme limit $\kappa \to 0$, no neutrons are injected and the $p\bar{p}$ pair can only further decrease the $n/p$ ratio, thus constrained by the lower $Y_p$ limit 0.24. On the other hand, a symmetric injection $\kappa = 1$ enhances the $n/p$ ratio as the antibaryon mostly annihilates on protons, more abundant than neutrons by a factor of $\sim 6-7$ after the standard $n/p$ freeze-out. For $\kappa \gtrsim 0$, the final $Y_p$ can be either increased or decreased, depending on whether the $S$ particles decay away before or after the displaced $X_n$ equilibrium crosses the SBBN $n/p$ freeze-out curve. As shown for $\kappa = 0.2$ in Fig. 4.3, there is a $Y_p = 0.24$ exclusion island at low lifetimes and larger lifetimes are constrained by $Y_p = 0.26$. We use $\kappa = 0.5$ as our baryonic injection constraint benchmark.

Similar results were found in Ref. [234] in the context of MeV-scale reheating with hadronic energy injection. The importance of hadron injection on $Y_p$ completely dominates the second order effects of incomplete neutrino thermalization after late reheating. Even though we have checked that $S$ does not reheat the SM bath in our model, $\rho_S \ll \rho_{\rm SM}$, the importance of hadronic injection reinforces the validity of our treatment even in the absence of the full treatment of Boltzmann equation for neutrinos.

### Meson injection from residual annihilations

In addition to its decay products, $S$ can also inject particles in the cosmic medium via $SS$ annihilations to charged pions. The injected pions interact with the cosmic medium in the same way as from the $S$ decays described above. The Boltzmann

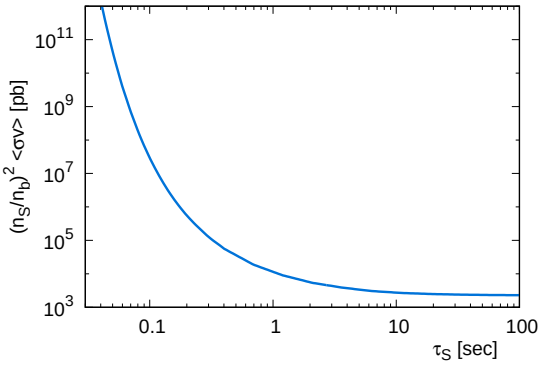


Figure 4.4: Constraints on $Y_S^2\langle\sigma v\rangle_{\pi^+\pi^-}$ from $SS$ annihilations into charged pions from the BBN $^4$He abundance at $Y_p = 0.26$.

equation takes the addition term (4.26), with the injected pion density now given by

$$n_{\pi^\pm}^{\rm ann} = \tau_{\pi^\pm} n_S^2(T)\,\langle\sigma v\rangle_{\pi^+\pi^-} = \tau_{\pi^\pm} Y_S^2 n_b^2(T) e^{-2t\Gamma_S}\,\langle\sigma v\rangle_{\pi^+\pi^-}\,, \tag{4.37}$$

where $\langle\sigma v\rangle_{\pi^+\pi^-}$ is the nonrelativistic annihilation cross section $\sigma v(2m_S)$ as per Eq. (4.12), rescaled by the pionic branching ratio at $\sqrt{s} = 2m_S$. The $n_{\pi^\pm}^{\rm ann} \propto n_S^2 \propto T^6$ dependence implies a much stronger impact at high energies, enforcing the displaced initial condition $X_n^i \simeq 0.47$. As $S$ decays away, its impact on $X_n(T)$ is even more rapidly exponentially suppressed and its constraints are less stringent than decays at very short lifetimes. The bounds from annihilation are given in the $Y_S^2\langle\sigma v\rangle_{\pi^+\pi^-} - \tau_S$ parameter space and displayed in Fig. 4.4.

### 4.4.2 Energy density requirements

The resultant BBN abundances depend on the nuclear reaction rates and how efficient they are as the Universe expands. One by one, the reaction rates drop out of equilibrium, as the Universe expands and cools. If the Hubble rate is increased due to a large energy density locked in a DS, the active reaction time would shorten, potentially spoiling the SBBN results. For our study, the most important effect is the change of the Hubble rate during the $n/p$ freeze-out, which again affects $Y_p$. However, we can also use as a constraint a well-measured quantity in cosmology, the total energy density carried by neutrinos.

The neutrinos decouple from thermal processes at $T \sim 2$ MeV. If the decaying particle is heavy and does not decay into neutrinos, it will reheat electron-photon

fluid with respect to the neutrinos, decrease $T_\nu/T_\gamma$ and equivalently lower $N_{\rm eff}$. The Planck Collaboration measured $N_{\rm eff} = 3.04 \pm 0.33$ at $2\sigma$, including their CMB results and external cosmological data [7], which imposes $N_{\rm eff} > 2.71$ as a lower bound. In the extreme case of a full reheating of the SM bath in the 1-10 MeV temperature range, numerical solutions show a decrease in $N_{\rm eff}$ due to inefficient thermalization of neutrinos [235], which slows down the Hubble rate resulting in a decreased $Y_p$ [234]. In our model, we verified *a posteriori* that $S$ never dominates the cosmic energy density $\rho_S < \rho_{\rm SM}$ prior to its decay. We can then treat the energy injection as a perturbation around the standard case, without the need for a full numerical machinery of the neutrino thermalization.

The energy densities and Hubble rate form a closed system of differential equations

$$\dot{\rho}_S + 3H\rho_S = -\Gamma_S \rho_S, \qquad \dot{\rho}_{\rm rad} + 4H\rho_{\rm rad} = \Gamma_S \rho_S, \qquad H^2 = \frac{8\pi G}{3}\left(\rho_{\rm rad} + \rho_S\right), \tag{4.38}$$

where we have assumed a nonrelativistic $S$ and omitted the variation in relativistic degrees of freedom. Assuming steplike decoupling and changes in relativistic degrees of freedom, the $T$ evolution separates into three regions. For $T > T_\nu^{\rm decoup}$, neutrinos are in equilibrium with the electromagnetic bath and $\rho_S$ is injected equally in $e^\pm$'s, $\nu$'s and $\gamma$'s. For $T_\nu^{\rm decoup} > T > T_{m_e}$, the neutrinos are simply redshifted while the electron-photon bath is heated by the $S$ decays. For $T_{m_e} > T$, electrons become nonrelativistic and transfer their entropy to photons, additionally heating the photon bath compared to the neutrino bath.

If $S$ does not dominate the energy density of the Universe before its decay, we can write $\rho_S = \delta_S \rho_{\rm rad}^{\rm SM}$, $\rho_{\rm rad} = \rho_{\rm rad}^{\rm SM}(1+\delta_{\rm rad})$ and expand (4.38) around the $\delta$ perturbations to solve the system analytically. At linear order, we find the solutions

$$\rho_S(t) = \frac{c_S}{t^{3/2}} e^{-\Gamma_S t}, \qquad \rho_{\rm rad}(t) = \frac{c_{\rm rad}^i}{t^2}\left[1 + F(t)\right], \tag{4.39}$$

$$F(t) = \frac{c_S}{c_{\rm rad}^i \sqrt{\Gamma_S}} \frac{1}{\Gamma_S t}\left[\Gamma_{3/2}(\sqrt{\Gamma_S t}) - \Gamma_{5/2}(\sqrt{\Gamma_S t}) + \frac{\sqrt{\pi}}{4}\right] \tag{4.40}$$

where $\Gamma_{3/2}$, $\Gamma_{5/2}$ are incomplete Gamma functions and the integration constants $c_S$, $c_{\rm rad}$ are set to have $\rho_S = m_S n_S$ and $\rho_{\rm rad} = \rho_{\rm rad}^{SM}$ at some early time $\Gamma_S t \ll 1$. After the neutrinos decouple, the injected energy is distributed to the photon-electron bath

and its energy density departs for the neutrino bath,

$$\rho_\gamma^{\rm mid}(t) = \tilde{g}_{\gamma+e}\frac{c^i_{\rm rad}}{t^2}\left[1+F(t)\right] + \tilde{g}_\nu\frac{c^i_{\rm rad}}{t^2}\left[G(t)-G(t_\nu^{\rm decoup})\right], \tag{4.41}$$

$$\rho_\nu^{\rm mid}(t) = \tilde{g}_\nu\frac{c^i_{\rm rad}}{t^2}\left[1+F(t)-G(t)+G(t_\nu^{\rm decoup})\right], \tag{4.42}$$

where $\tilde{g}_i \equiv g_i/(g_{\gamma+e}+g_\nu)$ is the fraction of relativistic degrees of freedom of each bath, $t_\nu^{\rm decoup}$ the neutrino decoupling time and

$$G(t) = \frac{c_S}{2c^i_{\rm rad}}\sqrt{\frac{\pi}{\Gamma_S}}\,{\rm erf}\left(\sqrt{\Gamma_S t}\right) - \frac{c_S}{c^i_{\rm rad}}\sqrt{t}e^{-\Gamma_S t}. \tag{4.43}$$

Finally, after the electrons become nonrelativistic, they effectively transfer their entropy to the photon bath. Assuming an instantaneous transition, entropy continuity implies an increase of energy density by a factor of $\delta = (g_e+g_\gamma)^{1/3}/g_\gamma^{1/3} = (11/4)^{1/3}$. Matching boundary conditions, the energy densities at late times are

$$\rho_\gamma^{\rm late}(t) = \tilde{g}_{\gamma+e}\delta\frac{c^i_{\rm rad}}{t^2}\left[1+\alpha F(t)+c\frac{t_e}{t}\right] + \tag{4.44}$$

$$+\,\tilde{g}_\nu\alpha\frac{c^i_{\rm rad}}{t^2}\left[G(t)-G(t_e)+\delta\left(G(t_e)-G(t_\nu^{\rm decoup})\right)\right], \tag{4.45}$$

$$\rho_\nu^{\rm late}(t) = \tilde{g}_\nu\frac{c^i_{\rm rad}}{t^2}\left[1+\alpha\left\{F(t)-G(t)+G(t_e)+\delta(G(t_\nu^{\rm decoup})-G(t_e))\right\}+c\frac{t_e}{t}\right], \tag{4.46}$$

with $\alpha = 1/(\delta\tilde{g}_{\gamma+e}+\tilde{g}_\nu)$ and $c$ a boundary condition that is irrelevant in the $t\to\infty$ limit.

The temperature-time dependence is found via $\rho_{\rm rad}(t) = \pi^2 g_\star T^4/30$. Since the neutrino interaction rate scales as $\Gamma_{\nu_e}\sim T^5$, we find the neutrino decoupling time in the modified cosmology by equating $(T_\nu^{\rm decoupl})^5/H(T_\nu^{\rm decoupl}) = (T_\nu^0)^5/H_0(T_\nu^0)$, with $H$ the perturbed Hubble rate and $T_\nu^0$ the neutrino decoupling temperature in the SM. In the Maxwell-Boltzmann approximation, $T_\nu^0 = 2$ MeV, but thermal refinements in the interaction rates and phase space tend to yield a lower value $T_\nu^0 = 1.4$ MeV [236].

Then, at $\Gamma_S t \gg 1$, we can evaluate $T_\nu/T_\gamma$ and find

$$N_{\rm eff} = 3\left(\frac{T_\nu}{T_\gamma}\right)^4\left(\frac{11}{4}\right)^{4/3} \tag{4.47}$$

$$\simeq 3\times\frac{\delta\tilde{g}_{\gamma+e}+\tilde{g}_\nu-\frac{c_S}{2c^i_{\rm rad}}\sqrt{\frac{\pi}{\Gamma_S}}+(1-\delta)G(t_e)+\delta G(t_\nu^{\rm decoup})}{\delta\tilde{g}_{\gamma+e}+\tilde{g}_\nu+\frac{\tilde{g}_\nu}{\delta\tilde{g}_{\gamma+e}}\left(\frac{c_S}{2c^i_{\rm rad}}\sqrt{\frac{\pi}{\Gamma_S}}-(1-\delta)G(t_e)-\delta G(T_\nu^{\rm decoup})\right)} \tag{4.48}$$

to constrain energy injection into electrons. We display in Fig. 4.5 the departure from $N_{\rm eff}=3$ as a function of time for $\tau_S = 0.1$ s and the two neutrino decoupling temperature benchmarks. The limits are also shown in units of stored energy density $m_S n_S/n_b$, where $m_S$ is in MeV. If the $S$ decay happens after the neutrino decoupling, all energy is deposited in the photon bath and the result is independent of our choice of $T_\nu^0$. If decays happen earlier, the photon and neutrinos are potentially still coupled and the energy emitted in $S$ decays only influences $N_{\rm eff}$ after decoupling. As such, the constraints has a $t\propto(1/T_\nu^0)^2$ dependence. We adopt the conservative side[2], $T_\nu^0 = 1.4$ MeV, as our bounds on the $m_S-\tau_S$ parameter space. Notice the constraints for $SS$ annihilations to pions are much stronger and will be dominant when the pionic annihilation channel is open, *i.e.* for $m_\pi < m_S < 2m_\pi$.

### 4.4.3 Late-time energy injection

In the example of the $S$ particles coupled through the Higgs portal, the most stringent constraints on lifetime come from the considerations of $n/p$ freeze-out. In other models, with additional channels of annihilation that can suppress metastable abundances, the constraints on lifetime would not be as stringent and would mostly come from the considerations of late energy injection. For completeness, we also discuss these constraints here. Modification of BBN by unstable particles with lifetimes in excess of 200 s has been considered in detail, both through hadronic [231, 237], electromagnetic [135] or combined [233, 238, 69] energy cascades.

Hadronic injection after $t\gtrsim 200$ s is most efficient at modifying the final yields of the less abundant light nuclei D, $^3$He, $^6$Li, and $^7$Li. After most of $^4$He has been syn-

[2]The neutrino decoupling temperature is not a well-defined quantity as the weak cross section with electrons scales as $E^2$ resulting in energetic neutrinos remaining coupled slightly longer, in addition to the $\nu_\mu$ and $\nu_\tau$ decoupling slightly earlier [236]. Our choice of $T_\nu^0 = 1.4$ MeV is on the lowest end of decoupling temperatures, underestimating the energy fraction going into the electromagnetic bath as higher generations of neutrinos and lower energy electron-neutrinos have already decoupled. A full Boltzmann evolution of the neutrino spectrum will yield stronger constraints.

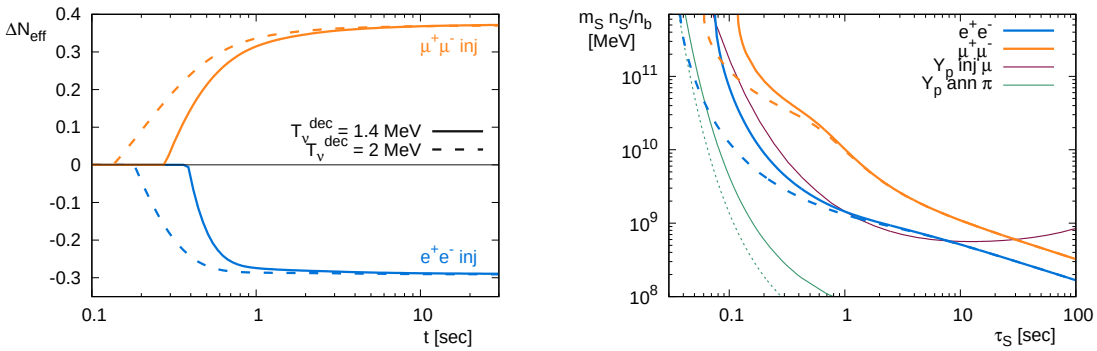


Figure 4.5: *Left*: Departure from the SM $N_{\rm eff}$ as the Universe cools down for electron injections (blue lines) and muon injections (orange lines, see supplementary section 4.8.2 for details). The extrema of the neutrino decoupling temperature ranges are shown in full lines and dashed lines as labeled in the figure. *Right*: Bound of maximal stored energy decaying into electrons or muons as a function of particle lifetimes. The full lines and dashed lines represent the neutrino decoupling temperatures as on the left. We also show for comparison some benchmark bounds in this parameter space from the BBN $Y_p$ results. The thin olive curves are the neutron enrichment constraint from annihilation into pions for $m_S = 140$ MeV (solid lines) and $m_S = 275$ MeV (dotted lines). The thin purple line is the $Y_p$ constraint for a $m_S = 250$ MeV particle decaying into muons.

thesized, the BBN enters the regime ($T \sim 50$ keV) when neutrons are rare, $O(10^{-5})$ or so, yet their abundances are critical in determining the final abundance of deuterium. At that stage, any additional neutrons brought into the system through external processes such as heavy particle decays lead to the increase of the deuterium abundance. (Incidentally, it also leads to the suppression of $^7$Be and consequently of $^7$Li [231].) The increase of D production can be exacerbated by the hadro-dissociation of $^4$He in the process of slowing down of injected hadrons. Additional production of $^3$He through spallation can also affect the $^3$He/D ratio [239]. Secondary and tertiary processes may also generate $^6$Li and $^9$Be [240, 241]. Detailed studies of the ensuing constraints [238] show strong sensitivity to hadronic (mostly nucleonic) decays of metastable particles with lifetimes in the hundreds of seconds and longer, and initial abundances comparable to or even smaller than that of baryons. In recent years, these constraints have only gotten stronger, primarily due to steady observational progress in determination of primordial D/H [104].

If for some reason, hadrons and specifically nucleons are absent from the decay chains, the abundances of light elements can be modified by the late injection of electromagnetic energy. At early times this mechanism is inefficient, as radiation

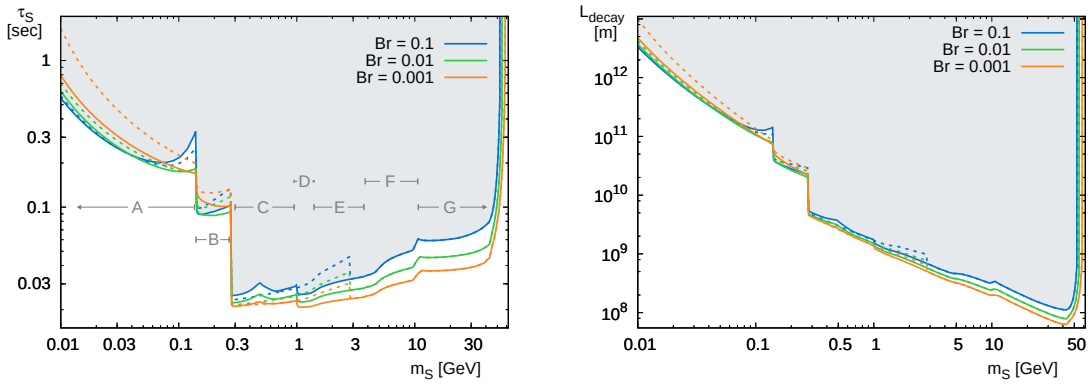


Figure 4.6: *Left*: Lifetime constraint as a function of the $S$ mass for three $h \to SS$ branching ratios. The lettered regions represent different assumptions or physics and are described in the text. The dotted lines correspond to the perturbative spectator model. *Right*: Same as left, except transposed in the decay length of $S$, assuming it is boosted to $E_S = 200$ GeV.

quanta with energy in excess of nuclear binding are quickly energetically degraded by ambient plasma. The photodissociation therefore sets in at late times leading to a suppression D ($t \gtrsim 10^4$ s) and additional production of $^3$He for $t \gtrsim 10^6$ s. Since typically 45% of hadronic energy injection is dissipated electromagnetically in the hadronization cascade [238], the late-time energy injection constraints on a heavy particle are dominated by the electromagnetic reactions in the BBN network.

## 4.5 Results

We are now in a position to perform a scan in parameter space of the minimal Higgs model, constrained by the consistency with BBN. In Fig. 4.6, we display the parameter space, in both the lifetime and an effective decay length $L_{\rm dec} = c\tau_S\beta_S(E_S/m_S)$. We assume an average $E_S$ of 200 GeV, from a Higgs typically boosted at 400 GeV at the LHC. The resulting constraints, along with the assumptions considered in each mass range are described below.

- **Region A** $2m_e < m_S < 2m_\mu$ : The constraint comes from the decrease in $N_{\rm eff}$ with the entropy dump in the SM bath after neutrino decoupling. We take the neutrino decoupling temperature to be $T_\nu^0 = 1.4$ MeV as a conservative limit.

- **Region B** $m_\pi < m_S < 2m_\pi$ : This region is dominated by the $SS$ annihilation to $\pi^+\pi^-$. We also derived the same constraint as region A from $N_{\rm eff}$ up to $m_S =$

$2m_\mu$, in addition to the raised $N_{\text{eff}}$ from decays into muons in the $2m_\mu < m_S < 2m_\pi$ and the $Y_p$ constraints from $S$ decaying into muons (see supplementary section 4.8 for muon injection considerations). They all yield weaker bounds than the $SS \to \pi^+\pi^-$ constraints, of $\tau_S > 0.3$ s or longer.

- **Region C** $2m_\pi < m_S < 2m_K$ : The abundance $Y_S$ weighted by the pion branching ratio constrains the region via direct charged pion decays. We assume 2/3 go into charged pions and 1/3 is radiated away in $\pi^0$.

- **Region D** $2m_K < m_S < 1.4$ GeV : The abundance $Y_S$ weighted by the kaon branching ratio constrains the region via direct charged kaon decays. We assume 1/2 go into charged kaons and 1/2 into $K^0\bar{K}^0$. Only half of the neutral kaons survive as $K_L$, creating similar in numbers metastable populations of $K_L$, $K^+$ and $K^-$.

- **Region E** 1.4 GeV $< m_S < 2m_D$ : By strangeness conservation, we assume that all $s$ quarks yield a kaon, half charged and half neutral. Since we do not have model-independent branching ratios of $S$ in this mass regime, we vary the description according to the assumptions in each decay model. For the baseline model, we assume that 100% decays to the kaons and apply our kaon injection constraints. For the perturbative spectator model, the kaon branching ratio is given by (4.11), with non-negligible contributions from decays to pions, muons and eta mesons, resulting in weaker bounds until the $c$-quark threshold. At $m_S = m_c$ the hadronic modeling dependence largely goes away.

- **Region F** $2m_D < m_S < 2m_b$ : We utilize the branching fractions of $c\bar{c}$ from $e^+e^-$ at $\sqrt{s} = 10.5$ GeV into $D$ mesons from Ref. [242] and weight each channel by its inclusive $K^\pm$ branching ratios to find a hadronization yield of 0.63 $K^+K^-$ pair per $S$ decay into $c$ quarks. Rescaled by $Br(S \to c\bar{c})$, the same constraints from kaon injection apply. Above the $2m_{\Lambda_c}$ threshold, a $c\bar{c}$ typically forms a $c$ baryon with a 0.06 probability [242], which then hadronizes to $p$ or $n$. We find this constraint weaker than the kaons injection and use the $K^+K^-$ result across this entire range.

- **Region G** $m_S > 2m_b$ : The main decay channel here are pairs of $b\bar{b}$ quarks. The charged pion, charged kaons and proton multiplicities in the $b\bar{b}$ decay of a $Z$ boson are measured to be 18.44±0.63, 2.63±0.14 and 1.00±0.08, respectively, by

the ALEPH Collaboration [243]. We assume the ratio holds in the hadronization of lower center-of-mass decays into $b\bar{b}$ and scale by the mean charge multiplicity fit [244]

$$N_{ch}(s) = -0.577 + 0.394\ln(s/s_0) + 0.213\ln^2(s/s_0) + 0.005(s/s_0)^{0.55}, \quad (4.49)$$

where $s_0 = 1$ GeV$^2$. This fit agrees well in both $e^+e^-$ and $p\bar{p}$ collisions between $\sqrt{s} \sim 2$ GeV $- 2$ TeV. This gives us an estimate for the baryon injection of the $b\bar{b}$ branching fraction of $S$. We further assume a 50% smaller injection of $n(\bar{n})$ to utilize our baryon injection constraints. The accompanying pions and kaons also independently yield comparable constraints, not shown in the figure.

## 4.6 Events at MATHUSLA

The number of events at the boundary of our constraints can easily be estimated with

$$N_{\text{obs}} \sim N_h \times \text{Br}(h \to SS) \times \epsilon_{\text{geometric}} \times \frac{L_{\text{det depth}}}{L_{\text{dec}}}, \quad (4.50)$$

where $N_h$ is the expected number of Higgs bosons produced, $\epsilon_{\text{geometric}}$ is the geometric acceptance (percentage of solid angle covered) of the detector and $L_{\text{det depth}}$ is the depth of the decay chamber of the detector, linear from the direction of $S$ travel. A possible configuration for MATHUSLA is a (200 m)$^2$ detector at the surface (100 m away from the LHC beam) with a 20 m decay chamber depth [202] corresponding to $\epsilon_{\text{geometric}} \sim 0.1$. A high-luminosity upgrade to the LHC is expected to produce $N_h \sim 1.5 \times 10^8$ Higgs bosons, where we assumed an integrated luminosity of 3000 fb$^{-1}$ [245] and a Higgs boson production cross section of $\sigma_h \simeq 50$ pb at 14 TeV [246]. The expected number of events is shown in Fig. 4.7, which is one order of magnitude shorter than 1 in the optimal $m_S = 10 - 50$ GeV range. Given that the suggested configuration is based on a target goal of a few events for decay lengths of $c\tau \sim 10^7$ m [202], our estimate is in line with the limit BBN $c\tau_S \sim 10^8$ m shown in Fig. 4.6. To reduce the cosmic background in the detector, $S$ events will be triggered with the coincidence of the emission of a Higgs boson with a high transverse momentum, which will further decrease the number of tagged $S$ events from our estimate.

To reduce

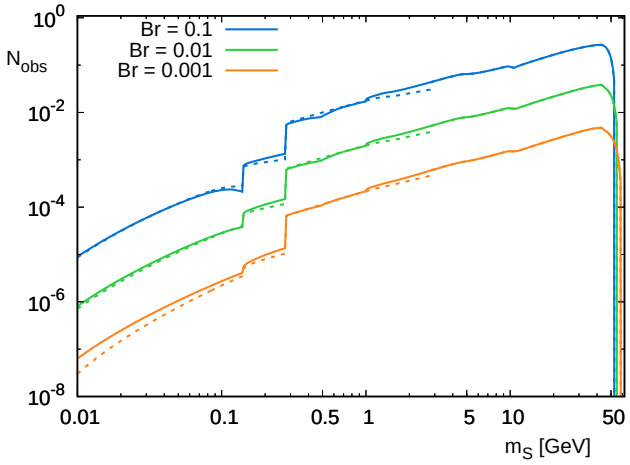


Figure 4.7: Estimate of the expected number of events at the BBN limit threshold in the proposed MATHUSLA detector.

## 4.7 Discussion

We have considered, in some detail, constraints on the lifetimes of the scalar particles, coupled to the higgs portal via a minimal set of couplings. To stay relevant for the LHC, we have concentrated on the $m_S < m_h/2$ case, that allows pair production of $S$ states in the decay of higgs bosons. The same coupling is responsible for the cosmological depletion of $S$ particles, leading to their metastable abundance in the early universe.

We find that throughout almost the whole mass range considered in this work, $2m_\mu < m_S < m_h/2$, the constraints on the lifetime of $S$ particles are stronger than 0.1 s. Moreover, the results have a relatively mild dependence on the $Br(h \to SS)$. The reason for that is as follows: the experimental limits on $Br(h \to SS)$ are already strong enough to limit the annihilation rate of $SS$ pairs to the SM states to be much less than one picobarn, and consequently the metastable abundance of $S$ particles per nucleon is quite high, $Y_p \gg 1$. This leads to a massive injection of nucleons and mesons at early times, which raises the $n/p$ ratio, and creates larger yields of $^4$He compared to SBBN. Contributions of very light $S$ particles to the Hubble rate during the $n/p$ freeze-out also raises $Y_p$. The limits on $\tau_S$ are robust, and have rather mild dependence on the uncertainties in our treatment. This is because the initial large metastable $Y_S$ abundance needs to be depleted prior to the $n/p$ freeze-out time $t_{n/p}$, leading to the requirement $\tau_S \ll t_{n/p}$. Consequently $O(1)$ variations in the yields of mesons and nucleons in the final states can be compensated by small variations in $\tau_S$,

parametrically on the order $\log^{-1}(t_{n/p}/\tau_S)$, to produce the same influence on BBN. For the same reasons, our limits are also very insensitive to the exact observational constraint on $\Delta Y_p$, and we take a rather conservative limit of 0.01 (allowing $\pm 0.01$ deviations from the observed/calculated mean). From the point of the LHC physics, the most promising is a scenario with a mass $m_S$ not far below $m_h/2$. In that case, the effective decay length has to be on the order of or smaller than $\sim 10^8$ m, (see Fig. 4.6), providing a $10^{-6}$ *minimum* probability for a decay within a 100 m length purposely built detector. Given that the high-luminosity LHC would produce copious numbers of the Higgs bosons, there is a chance to cover the entire lifetime range for masses within the $10 - 50$ GeV range.

In this chapter we have neglected the effect of $S$ self-interaction. It turns out that the obtained results are also robust to a self-interaction induced reduction in number densities. Retaining the approximate $Z_2$-symmetry considered, a quartic $\lambda_4 S^4$ interaction could be considered, which would lead to *e.g.* $4S \to 2S$ processes. Thus, large self-interaction can maintain chemical equilibrium within the DS through efficient number changing processes and further deplete the $S$ number density [165, 166] (see Ref. [247] for a realization of strongly interacting $Z_2$ Higgs portal dark matter). After thermal decoupling from the SM, entropy conservation in the $S$ bath with chemical equilibrium imposes the scaling $n_S \propto 1/a^3 \ln a$ [165], which implies an additional depletion of $Y_S \sim Y_S^{\rm fo,SM} \ln(a/a_{\rm fo,SM})$, where fo,SM denotes the values without the self-interaction. The $S$ metastable abundance will therefore be at most lowered by a factor of a few (certainly less than an order of magnitude), which would have a very limited impact on the $\tau_S$ limit.

It is easy to see that the above considerations can be generalized to other models of the Higgs-portal-coupled particles. For example, consider a fermion $\chi$, coupled to the Higgs via $H^\dagger H(\bar{\chi}\chi)$ or $H^\dagger H(\bar{\chi} i\gamma_5 \chi)$ dimension-five operators, and having a small decay term such as a neutrino portal $LH\chi$. The main analysis of our work can be recast for that model, especially in the part that connects Higgs decays with a metastable abundance of $\chi$. Evidently, for $Br(h \to \chi\bar{\chi}) \sim Br(h \to SS)$ input, one will end up with $Y_\chi \sim Y_S$. The only change will be in the yields of mesons and baryons in the decays of $\chi$ compared to $S$. However, it is well known that already for $m_\chi$ above 250 MeV, the yields of pions and kaons are substantial [47], giving confidence that for the most part the same constraints we have derived for $\tau_S$ will translate to similar limits on $\tau_\chi$.

The analysis performed in this chapter can easily be generalized to other models

of metastable particles, with different types of interactions, via $Z$, $Z'$ etc. In the limit when $Z'$ is outside of the LHC reach, one could have a set of effective operators connecting $\chi$ with the SM fields, such as $\frac{1}{\Lambda^2}\bar{\chi}\gamma_\mu\chi\bar{q}\gamma_\mu q$, where $\Lambda$ is some energy scale. The $\chi$ pair-production cross section in this case will scale as $\sigma_{q\bar{q}\to\chi\bar{\chi}} \propto E_q^2\Lambda^{-4}$, where $E_q$ is a typical (anti)quark energy, while the cosmological annihilation cross section has $\sigma_{\chi\bar{\chi}\to q\bar{q}}v \propto m_\chi^2\Lambda^{-4}$ scaling. Therefore, the LHC-relevant cross section can be enhanced relative to the annihilation rate by a parametrically large ratio, $E_q^2/m_\chi^2$ if $m_\chi$ is parametrically smaller than the TeV scale. Therefore, one can easily have a range of parameters with a relatively large $\chi\bar{\chi}$ pair-production cross section, while having very small annihilation rates, rendering $n_\chi/n_b \gg 1$, and resulting again in strong BBN constraints on lifetimes, $\tau_\chi < 0.1$ s. Therefore, we conclude that some simple $Z'$ mediated models of metastable particles can also be strongly restricted by cosmology, making them a perfect candidate for the searches of metastable particles at the LHC.

It is also instructive to consider models where constraints on the lifetime of metastable particles are *much weaker*. Clearly, one needs an effective new mechanism for the self-annihilation in the early universe, as the Higgs channel is too inefficient. Staying within the Higgs portal models, consider the following potential with two real scalars,

$$V(H,S_1,S_2) = H^\dagger H(\lambda_1 S_1^2+\lambda_2 S_2^2+A_1 S_1+A_2 S_2)+\lambda_{12}S_1^2S_2^2+V(S_1)+V(S_2)+V(H^\dagger H), \tag{4.51}$$

with the following hierarchy of couplings:

$$\lambda_1 \gg \lambda_2;\ A_1 \ll A_2;\ \lambda_{12}\sim O(1);\ m_{S_1} > m_{S_2}. \tag{4.52}$$

These choices will lead to a long-lived $S_1$, somewhat shorter-lived $S_2$, a predominant decay of the Higgs boson to pairs of $S_1$, and cosmological depletion of $S_1$ via $S_1S_1 \to S_2S_2$ annihilation before BBN (even if S1 has a lifetime $\tau_S \gg 1$ s) with potentially a large cross section due to a sizable $\lambda_{12}$ coupling. Most importantly, in this model the Higgs decay to pairs of $S_1$ does not result in a prediction of $Y_{S1}$ abundance, which can be quite small even for small values of $Br(H \to S_1S_1)$. If $Y_{S1} \ll 1$, there would not be enough decay mesons and nucleons to affect early $n/p$ freeze-out, and constraints on $\tau_{S1}$ will be coming only from the considerations of late decays with hadronic or electromagnetic energy injection. Instead of $\tau_S < 0.1$ s, one expects to have sensitivity

to $\tau_{S1} \sim 10^3$ s, or even worse, beyond $10^4$ s, if decays of $S_1$ are mostly leptonic. This example is not unique, and there are other models where constraints on lifetimes and decay lengths are relatively lax, provided that there are extra channels that ensure efficient cosmological annihilation of metastable particles.

## 4.8 Supplementary: Muon injections in early BBN

Although muon injection related constraints are relatively weak and do not affect our main result, Fig. 4.6, in this supplementary section we provide additional details concerning the effects of muon injections on $Y_p$ and $N_{\rm eff}$ to verify that they are subdominant to the residual annihilation to pions in the $m_\pi < m_S < 2m_\pi$ mass range.

### 4.8.1 Neutron enrichment

Muon injection physics differs from the previous scenarios of meson and baryon injection considered in section 4.4.1. The direct charge exchange is through the weak force, as opposed to the strong force in the other cases, and is completely negligible over the lifetime of the muon. Instead, the reactions can happen via the energetic neutrinos emitted by the muon decays. The general case for $\nu + X$ injection in BBN is treated in Ref. [248] and the specific case of muon injection after $t \sim 100$ s has been covered in Ref. [69], to which we refer the reader for details. Assuming stopped muons, the authors solved for the injected neutrino energy spectrum, including redshifting and averaged over flavor oscillations, to be integrated in the $n-p$ conversion rate. At earlier times, we know background neutrinos are coupled to $e^\pm$ down to $T \simeq 2$ MeV, and energetic injected neutrinos must accordingly deplete their energy efficiently as well. Summing over the possible interactions with the background neutrinos and $e^\pm$ [249], the collision rate of an injected electron neutrino with the bath is given by

$$\begin{aligned}\Gamma^{\nu_e}_{\rm coll}\left(E_\nu, T\right) &= \frac{7\pi}{135} G_{\rm F}^2 E_\nu \left[\left(5 + g_{\rm L}^2 + g_{\rm R}^2\right) T_\nu^4 + 4\left(g_{\rm L}^2 + g_{\rm R}^2\right)\eta(T)\, T_\gamma^4\right], \\ &\simeq \left(\frac{E_\nu}{32\ {\rm MeV}}\right)\left[\frac{5.7}{\rm sec}\left(\frac{T_\nu}{1\ {\rm MeV}}\right)^4 + \frac{1.3}{\rm sec}\eta(T_\gamma)\left(\frac{T_\gamma}{1\ {\rm MeV}}\right)^4\right], \end{aligned} \tag{4.53}$$

$g_{\rm L} = 1/2 + \sin^2\theta_{\rm w}$, $g_{\rm R} = \sin^2\theta_{\rm w}$, while $\eta(T) = 1$ for $T \gtrsim m_e$ and exponentially falls to 0 at lower temperatures. We follow the implementation of Ref. [69] and correct for the removal of energetic neutrinos coupled to the electromagnetic plasma by adding

an effective collision lifetime in the neutrino energy distribution (normalized on $n_b$)

$$f_e\left(T, E_\nu\right) = \Gamma_S Y_S \int_T^\infty \frac{dT_1\; e^{-t_1\Gamma_S}}{H(T_1)T_1} F_e\left(E_\nu, \frac{E_0 T}{T_1}\right) e^{-\int_T^{T_1} dT_2\; \frac{\Gamma_{\rm coll}(E_\nu \frac{T_2}{T}, T_2)}{H(T_2)T_2}}, \tag{4.54}$$

where $F_e$ is the distribution at injection time $T_1$, averaged over flavor oscillations. The charge-exchange rate to be inserted in the Boltzmann Eq. (4.20) is

$$\Gamma^\nu_{pn} = n_b(T) \int_0^{E_0} \sigma^{\bar\nu}_{pn} f_e(T, E_\nu)\; dE_\nu \tag{4.55}$$

and similarly for the reverse $np$ direction. The resulting constraints are shown in Fig. 4.3. Our results lean on the conservative side on a few assumptions. For simplicity, we assumed one collision for the neutrino thermalization, instead of following energy degradation over a shower of multiple interactions. Moreover, we took the collision time of the electron neutrino, even though there are muon neutrino states in the oscillations. Since $\Gamma^{\nu_e}_{\rm coll} > \Gamma^{\nu_\mu}_{\rm coll}$, we overestimate the actual collision time and the overall conversion rate should be slightly larger.

### 4.8.2 Energy injection partitioned between photon and neutrino baths (*e.g. muon injection*)

The case for energy injection from muons with respect to $N_{\rm eff}$ is somewhat interesting as its decay products, neutrinos and electrons, clearly deposit their energy in two different baths, once everything is decoupled. Both $T_\gamma$ and $T_\nu$ will rise, but since the 2 neutrinos carry more energy than the electron for a muon decay, we expect a rise in $N_{\rm eff}$. More precisely, we solve a similar set of equations as (4.38), except the photon bath absorbs a $\xi$ proportion of the $S$ decay energy and the neutrino bath gets the remaining $(1-\xi)$ portion. Before neutrino decoupling, the radiation bath evolves as in Eq. (4.40). Each decay product carries on average the energy [69]

$$\langle E_e\rangle = 37.0\text{ MeV}, \qquad \langle E_{\nu_e}\rangle = 31.7\text{ MeV}, \qquad \left\langle E_{\nu_\mu}\right\rangle = 37.0\text{ MeV}. \tag{4.56}$$

After neutrino decoupling, the energetic neutrinos can still collide with the ambient electrons until $\Gamma^{\nu_e}_{{\rm coll}-e} < H$, where $\Gamma^{\nu_e}_{{\rm coll}-e}$ is the collision rate with electrons only, the $T_\gamma$-dependent term in Eq. (4.53). Then, the energy distributed to the photon bath

separates into two regimes

$$\xi_1 = \frac{\langle E_e \rangle + \frac{\Gamma^{\nu_e}_{\text{coll}-e}}{\Gamma^{\nu_e}_{\text{coll}}} \langle E_{\nu_e} \rangle + \frac{\Gamma^{\nu_\mu}_{\text{coll}-e}}{\Gamma^{\nu_\mu}_{\text{coll}}} \langle E_{\nu_\mu} \rangle}{m_\mu} \simeq 0.47, \qquad \xi_2 = \frac{\langle E_e \rangle}{m_\mu} = 0.35, \quad (4.57)$$

where the muon neutrino collision term is given by

$$\Gamma^{\nu_\mu}_{\text{coll}}(E_\nu, T) = \frac{7\pi}{135} G_{\text{F}}^2 E_\nu \left[ \left(5 + (g_{\text{L}} - 1)^2 + g_{\text{R}}^2\right) T_\nu^4 + 4 \left( (g_{\text{L}} - 1)^2 + g_{\text{R}}^2 \right) \eta(T)\, T_\gamma^4 \right]. \quad (4.58)$$

Following the same procedure as in section 4.4.2, we find

$$N_{\text{eff}} = 3 \times \frac{\delta\tilde{g}_{\gamma+e+\tilde{g}_\nu} + \frac{c_S(\delta\tilde{g}_{\gamma+e}(1-\xi_2)-\xi_2\tilde{g}_\nu)}{2c_{\text{rad}}^2\tilde{g}_\nu}\sqrt{\frac{\pi}{\Gamma_S}} + \frac{C}{\tilde{g}_\nu}}{\delta\tilde{g}_{\gamma+e} + \tilde{g}_\nu - \frac{c_S(\delta\tilde{g}_{\gamma+e}(1-\xi_2)-\xi_2\tilde{g}_\nu)}{2c_{\text{rad}}^2\delta\tilde{g}_{\gamma+e}}\sqrt{\frac{\pi}{\Gamma_S}} - \frac{C}{\delta\tilde{g}_{\gamma+e}}}, \quad (4.59)$$

$$C = \delta(\xi_2 - \xi_1) G(t_{\text{coll}}) + \delta(\xi_1 - \tilde{g}_{\gamma+e}) G(t_\nu^{\text{decoup}}) + \xi_2(1-\delta) G(t_e), \quad (4.60)$$

with $t_{\text{coll}}$ found by solving $\Gamma^{\nu_e}_{\text{coll}-e} = H$. The physics is constrained by $N_{\text{eff}} < 3.37$. The time dependence of the departure from $N_{\text{eff}} = 3$ is shown for $\tau_S = 0.2$ s and the two choices of $T_\nu^0$ in Fig. 4.5. The corresponding constraints on the maximal stored energy for a given lifetime are shown on the right. For comparison with the muon-induced $Y_p$ bound, we display the curve for $m_S = 250$ MeV from neutron enrichment in purple. Independently from the choice of $T_\nu^0$, the $Y_p$ bounds from $\mu$ injections are more constraining for $\tau_S \gtrsim 0.2$ s than its $N_{\text{eff}}$ impact, while the annihilation to $\pi^+\pi^-$ provides the dominant constraint in the entire $2m_\mu < m_S < 2m_\pi$ range.

# Chapter 5

# Feeble Scalar Portal in Cosmology

## 5.1 Abstract

We explore the cosmological implications of the super-renormalizable Higgs portal scalar with a freeze-in abundance. We find that a combination of X-rays, CMB, spectral distortions and $N_{\text{eff}}$ excludes 10 orders of magnitude in mixing angle for 1 keV $\lesssim m_S \lesssim$ 200 MeV. The CMB sensitivity can reach up to $\theta \simeq 10^{-16}$. Above the di-pion threshold, large uncertainties in the $S$ decay rate for $2m_\pi < m_S \lesssim 2$ GeV generate significant systematic uncertainty in BBN and Pixie's spectral distortion forecast. BBN further constrains the parameter space up to $m_S \lesssim 180$ GeV. The combined excluded region covers a large section of the technically natural portion of the super-renormalizable Higgs portal scalar parameter space. We improve the freeze-in abundance calculation and discuss finite-temperature corrections. We find that cosmological constraints are insensitive to variations within our derived error range and a thermal field theory calculation is not required.

## 5.2 Introduction

Similar to the cosmological constraints of the dark photon in the weakly coupled limit presented in Chapter 2, we investigate the cosmological implications of a real dark scalar singlet $S$ coupled to the SM. From a pragmatic phenomenological mindset, if a new scalar were to exist in the universe, its leading interaction with the SM at a low energy should be through the super-renormalizable interaction $SH^\dagger H$. To guarantee its stability, one might protect decay interactions by a $Z_2$ symmetry. Since we are

interested in energy injections for decays, we forego this requirement and allow the super-renormalizable trilinear interaction $SH^\dagger H$. With a $SH^\dagger H$ interaction alone, $S$ is guaranteed to be produced in the early universe and potentially decay during cosmological transitions that are sensitive to energy injections. Recently, the relaxion, a new scalar mixing with the Higgs, has been suggested as a non-anthropic solution to the electroweak hierarchy problem [250, 251]. In this model, the relaxion-Higgs mixing can be very small in the sub-eV to GeV relaxion mass range. It is therefore interesting in our search for NP to investigate the $S$ phenomenology in the super-weak regime, where the abundance is determined by the freeze-in mechanism.

The $S$ freeze-in abundance and its cosmological probes for $m_S > 1$ MeV were first considered in Ref. [102], stating that the abundance is dominated by QCD interactions below the electroweak phase transition, finding :

$$Y_S^{\rm BJW} \sim 1.6 \times 10^{12} \theta^2, \tag{5.1}$$

where $\theta$ is the mixing angle with the SM Higgs. Independently, another group [251] estimated the $S$ lower bound from Primakoff and Compton processes at low temperatures $T < 20$ GeV in the context of relaxion-Higgs mixing and found

$$Y_S^{\rm FFFGP} \gtrsim 2.9 \times 10^{9} \theta^2, \tag{5.2}$$

with a complete analysis of cosmological probes below $m_S < 1$ MeV and crude estimates above $m_S > 1$ MeV. We are presenting an updated analysis with the following improvements.

- **Freeze-in yield**: We compute the tree-level freeze-in $S$ production for all electroweak and QCD channels, with varying electroweak vev $v(T)$ as a first approximation of thermal effects and provide an estimate on the precision of the calculation. We correct the QCD cross sections used in Ref. [102], resulting in a reduction of the yield from this particular channel by a factor of 20. We also estimate the accuracy of the Maxwell-Boltzmann approximation in the production calculation.

- **Decay rate**: We demonstrate the large uncertainty range in the constraints from the unknown $S$ decay rate to pions and kaons by showing two decay profiles. Additionally, we improve the $S \to \gamma\gamma$ decay rate, important for $m_S <$ 1 MeV, by including the light quarks contribution as mesonic loops, decreasing

(increasing) the decay rate by a factor of 4 over the typically used rate where $u, d, s$ are assumed to be massive (or neglected).

- **Early decays**: Ref. [102] performed a thorough analysis of BBN constraints, but mentioned that their analysis of early decays for $m_S < 2m_\pi$ does not consider energy density considerations from the large stored energy in the $S$ bath. We include a treatment of early decays, transitioning from the freeze-in abundance to the thermalized freeze-out relic, considering its impact on the relative neutrino and electromagnetic energy baths.

In this chapter, we first review the model and describe its features not mentioned in chapter 4 in section 5.3. Then, we discuss the freeze-in abundance calculation in section 5.4, providing details on many subtleties and particularities of the calculation. We provide a complete scan of the $S$ parameter space at small mixing angles in section 5.5, with details on the cosmological constraints updated in this work. Finally, we end the chapter with a general discussion on the robustness of our results in section 5.6.

## 5.3 The super-renormalizable Higgs portal model

We consider a subset of the minimal Higgs portal model presented in chapter 4, the super-renormalizable Higgs portal. The scalar part of the SM lagrangian is augmented by dimension 1 interactions with

$$\mathcal{L}_{H/S} = \mu^2 H^\dagger H - \lambda_H \left(H^\dagger H\right)^2 - \frac{m_S^2}{2} S^2 - A S H^\dagger H + \text{kin. terms}, \tag{5.3}$$

neglecting the self-interaction term $\lambda_3 S^3$ that would not produce $S$ particles in the freeze-in limit. As we saw in chapter 4, the $A$ term induces a small mixing angle $\theta$ between physical excitations $S$ and $h$,

$$\theta = \frac{Av}{m_h^2 - m_S^2}, \tag{5.4}$$

at linear order in $A$ and leads to interactions between $S$ and SM particles exactly like the Higgs boson, rescaled by a suppression factor $\theta$. In the unitary gauge of the broken electroweak phase, after rotating $h$ and $S$ to their physical states, we find the

scalar potential

$$V_{H/S} = \frac{m_h^2}{2}h^2 + \frac{m_S^2}{2}S^2 + \lambda v\, h^3 + \frac{\lambda}{4}h^4 + \left(\frac{A}{2} - 3\theta\lambda v\right) h^2 S - \theta\lambda\, h^3 S, \tag{5.5}$$

which shows the $hhS$ and $hhhS$ contact interactions.

### 5.3.1 $S \to \gamma\gamma$ decay rate

The $S$ decay channels for $m_S > 2m_e$ are discussed in section 4.3.1. Below the electron threshold, a Higgs-like particle decays to 2 photons through a loop of heavy particles. The leading order decay rate is found by summing over the massive charged particles entering the loop [252]

$$\Gamma(S \to \gamma\gamma) = \frac{\theta^2\alpha^2 m_S^3}{256\pi^3 v^2}\left|C\right|^2, \tag{5.6}$$

$$C = \sum_f N_c Q_f^2 A_f(\tau_f) + A_W(\tau_W) \tag{5.7}$$

where $\tau_i = m_S^2/4m_i^2$ and the $W$ contribution has an opposite interference sign

$$A_f(\tau) = \frac{2}{\tau^2}\left[\tau + (\tau-1)f(\tau)\right] \xrightarrow[\tau\to 0]{} 4/3, \tag{5.8}$$

$$A_W(\tau) = \frac{-1}{\tau^2}\left[2\tau^2 + 3\tau + 3(2\tau-1)f(\tau)\right] \xrightarrow[\tau\to 0]{} -7, \tag{5.9}$$

while

$$f(\tau) = \begin{cases} \arcsin^2\sqrt{\tau} & \tau \le 1 \\ -\frac{1}{4}\left[\ln\frac{1+\sqrt{1-\tau^{-1}}}{1-\sqrt{1-\tau^{-1}}} - i\pi\right]^2 & \tau > 1 \end{cases}. \tag{5.10}$$

In this prescription, the inclusion of light quarks $u$, $d$ and $s$ is rather ambiguous. Their masses are not physical rest masses since $m_{u,d,s} \ll \Lambda_{\rm QCD} \simeq 350$ MeV. Instead, they are determined as chiral symmetry breaking variables in QCD which generate the non-zero mass of the Goldstone bosons of the approximate symmetry, the pions, kaons and eta mesons [253]. A more appropriate interpretation of their contribution to $S \to \gamma\gamma$ is through a virtual loops of pions and kaons [254]. Adding the contributions

from all SM particles, for $m_S \ll 2m_e$ we find

$$C = \begin{cases} 11/3 & \simeq 3.67 & \text{for } 0+6 \text{ quarks} \\ 989/522 & \simeq 1.89 & \text{for } 2+4 \text{ quarks} \\ 50/27 & \simeq 1.85 & \text{for } 3+3 \text{ quarks} \\ 1 & = 1 & \text{for } 0+3 \text{ quarks} \end{cases} \tag{5.11}$$

where different scenarios of $a$ light + $b$ heavy quarks are shown and the true value should be around the 3+3 or 2+4 scenarios. Since the difference in decay rate between the two cases, $\mathcal{O}(4\%)$, is negligible for new physics, we simply choose $C = 50/27$.

### 5.3.2 Finite-temperature effects

In a vacuum, the SM masses are generated through the higgs mechanism and are proportional to the electroweak vacuum expectation value (vev) $v$. In the cosmological thermal bath, in particular near the electroweak symmetry restoration temperature, long-range interactions are screened by the plasma. Particles effectively develop a thermal mass as a representation of this screening. The mass of a particle at a given temperature $T$ can be generally written as [255]

$$m^2(T) = m_0^2(v) + m_T^2(T), \tag{5.12}$$

where $m_0$ is the tree-level mass that depends on the vev and $m_T$ is the thermal mass. Note that the vev depends on $T$, so that $m_0$ also has a temperature dependance. A simple analytic formulation of the high-$T$ higgs thermal mass is given by [256]

$$m_{h,T}^2(T) = c_h T^2, \qquad c_h = \frac{1}{16}\left(8\lambda_H + 4y_t^2 + 3g_2^2 + g_1^2\right). \tag{5.13}$$

Inserting the additional term $\frac{c_h}{2}T^2h^2$ in the lagrangian (5.3) to generate the equivalent thermal mass, we can solve for $v(T)$

$$v(T) = \sqrt{v_0^2 - \frac{c_h T^2}{\lambda_h}}, \tag{5.14}$$

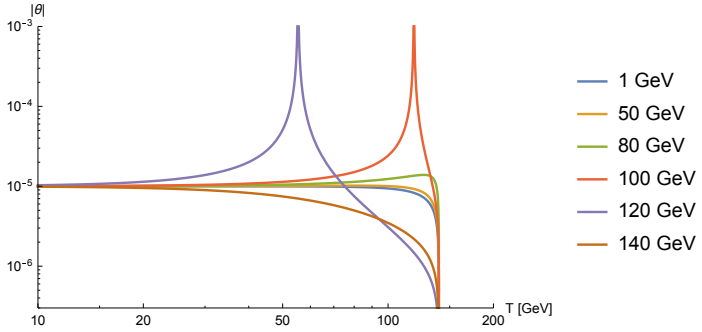


Figure 5.1: Mixing angle as a function of temperature for $\theta_0 = 10^{-5}$ and the listed values of $m_S$. A resonance appears for 90 GeV $\lesssim m_S \leq$ 125 GeV.

which predicts an electroweak symmetry restoration at the critical temperature $T_c \simeq$ 140 GeV[1]. The higgs thermal mass (5.13) is valid for the *SM flavour state*, meaning the unrotated state, not the mass eigenstates. As such, the mixing angle with $S$ becomes temperature-dependent

$$\theta(T) = \frac{A\, v(T)}{m_h^2(T) - m_S^2}. \tag{5.15}$$

and is shown for a few values of heavy $m_S$ in Fig. 5.1. A thermal resonance in the mixing angle appears for 90 GeV $\lesssim m_S \lesssim m_{h,0}$, at the specific temperature where $m_S = m_h(T)$. Smaller values of $m_S$ are shielded from this resonance by the $T^2$ mass term that prevents arbitrarily small values of $m_h(T)$ in the $v \to 0$ limit.

Since the relevant parameter space is in the *very small* mixing, the effect of $S$ on the SM thermal masses is negligible. Similarly, the $S$ thermal mass will be $m_S^2(T) \sim \theta^2 T^2$ and thus can be completely neglected for this study.

### 5.3.3 Higher order corrections to the thermal mixing angle

An interesting feature of the thermal mixing angle defined in Eq. 5.15 is the rapid shutoff at $T = T_c$ with $\theta(T > T_c) = 0$. Taken at face value, it suggests that vertices with Feynman rules proportional to $v$ are not allowed in the electroweak symmetric phase. This is only true at the tree-level and the surviving diagrams are generated at higher order in $A$ expansion. The first terms in the higher order expansion are shown in Fig. 5.2.

[1]This value is $\mathcal{O}(10\%)$ smaller than the full SM value of $T_c^{\rm SM} \simeq 160$ GeV from lattice simulations [257, 258], but since the bulk of the $S$ production will be from the $v(T) \gg T$ regime, we don't expect large yield difference from a $T$ expansion at higher order.

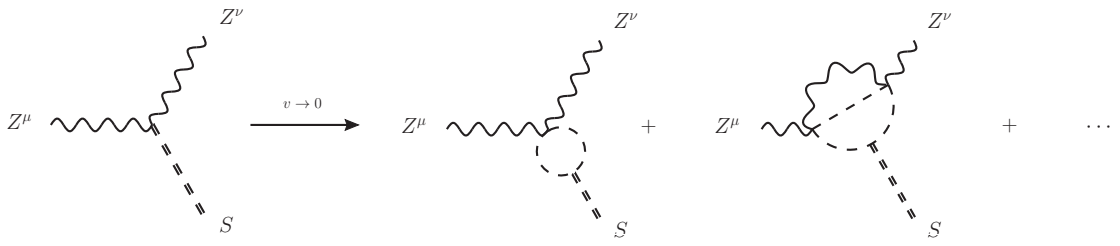


Figure 5.2: Survival of the ZZS vertex at higher order in the symmetric phase.

As a representative behaviour, we can look at the first thermal correction, with one loop in Goldstone bosons. Taking the soft $S$ limit such that Matsubara sum of the Golsdstone boson loop is easily tractable, we find the $T > 0$ of the first vertex correction to be

$$\Gamma^{\mu\nu}_{ZZS,T>0} \sim \frac{Ag^2}{4} g^{\mu\nu} \int \frac{d^3p}{(2\pi)^3} \frac{\beta\omega e^{\beta\omega} + e^{\beta\omega} - 1}{\omega^3 \left(1 - e^{\beta\omega}\right)^2}, \tag{5.16}$$

where $\beta = 1/T$ and $\omega$ is the energy of the boson in the loop. For a massless boson, this integral is infrared divergent, a well-known behaviour of finite-temperature corrections [132]. Expanding the integrand in low $\omega$, the divergence has the form

$$\Gamma^{\mu\nu}_{ZZS,T>0} \sim Ag^2 \; g^{\mu\nu} \frac{1}{(\text{loop})} \int \frac{d\omega}{\beta\omega^2}. \tag{5.17}$$

The bosons are however screened by the plasma with the effective thermal mass $m^2_{h,T} = c_h T^2$. The regulated corrections gives

$$\Gamma^{\mu\nu}_{ZZS,T>0} \sim Ag^2 \; g^{\mu\nu} \frac{1}{(\text{loop})} \frac{1}{\sqrt{c_h}}, \tag{5.18}$$

which is a loop factor smaller than the tree-level. The vertex therefore does not vanish, but is suppressed over the vacuum value.

## 5.4 Cosmological production via freeze-in

The cosmological production of a new species $S$ from $2 \to 2$ interactions is given by the Boltzmann equation

$$s\dot{Y} = \int \prod_{i=1}^{4} \left( \frac{d^3 \mathrm{p}_i}{2E_i(2\pi)^3} \right) \Lambda(f_1, f_2, f_3, f_4) |\mathcal{M}|^2 (2\pi)^4 \delta^4(p_1 + p_2 - p_3 - p_4), \tag{5.19}$$

where $\Lambda = f_1 f_2 (1 \pm f_3)(1 \pm f_4)$ represents the thermal distribution of each species and $|\mathcal{M}|^2$ is the spin-summed squared amplitude. In the MB approximation of the freeze-in mechanism, $\Lambda \to f_1^{\mathrm{MB}} f_2^{\mathrm{MB}} = e^{-\frac{(E_1+E_2)}{T}}$, and for 4 different species, Eq. 5.19 takes the form [259]

$$s\dot{Y}_{12\to 3S} = \frac{g_1 g_2}{8\pi^4} \, T \int_{\mathrm{Max}(m_1+m_2, m_3+m_4)^2}^{\infty} ds \; p_{12}^2 \sqrt{s} \sigma K_1 \left( \frac{\sqrt{s}}{T} \right), \tag{5.20}$$

$$p_{12}^2 = \frac{s}{4} \left( 1 - \frac{(m_1 - m_2)^2}{s} \right) \left( 1 - \frac{(m_1 + m_2)^2}{s} \right), \tag{5.21}$$

where $s$ is the entropy density, $Y = n_S/s$ and $\sigma = \sigma_{12\to 3S}$ is the standard cross section averaged over initial particles degrees of freedom.

The total $S$ is yield is found by summing all $12 \to 3S$ possible interactions where 1, 2 and 3 are SM particles. Production channels of the form $12 \to SS$ are suppressed by an extra factor of $\theta$ and are neglected. Since the $S$ particle preferably interacts with massive particles, we anticipate a large number of possible production channels around the electroweak scale. We classify the different channels by their asymptotic behaviour in the electroweak (EW) unbroken phase. According to the *Goldstone Boson Equivalence Principle* [260, 261], in $v^2/s \to 0$ limit, the behaviour has to be the same as simple Goldstone bosons interactions. Expanding the Higgs doublet with 4 massless bosons

$$H = \begin{pmatrix} \phi^+ \\ (h + i\phi^0)/\sqrt{2} \end{pmatrix}, \tag{5.22}$$

we find that the only $S$-producing interactions in the symmetric phase will be the $2 \to 2$ scattering $t_R Q_L \to HS$, $VH \to HS$ ($V$ is a SU(2)/U(1) gauge boson) and $t_R H \to Q_L S$, shown in Fig. 5.3. As such, we categorizes the $S$-producing interactions in 4 different types:

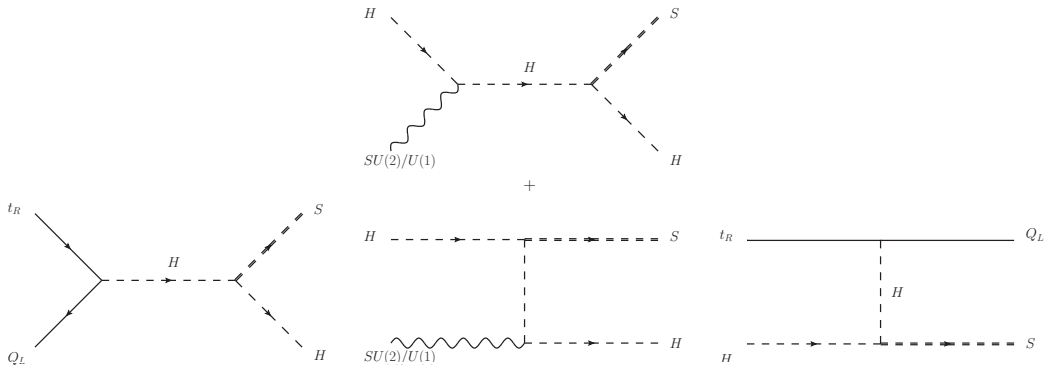


Figure 5.3: Feynman diagrams of the $S$-producing interactions in the electroweak symmetric phase. *Left :* Yukawa annihilations. *Center :* Gauge boson scatterings. *Right :* Compton-like scatterings.

- *QCD production*, which includes all diagrams with gluons.
- *Yukawa annihilation*, which includes the 4 reactions contributing to $t_R Q_L \to HS$.
- *Compton-like scattering*, which includes reactions with a quark scattering on a boson in the form of $t_R H \to Q_L S$.
- *Gauge boson scattering*, which includes the reactions purely with bosons.

We segment the production calculation in two regimes, first for $T \ll T_c$ with near-vacuum cross sections. Then, for $T > T_c$, the vacuum expectation value is negligible and the dimensionful SM couplings proportional to $v$ vanish. In all instances, we compute the cross sections at tree-level, with a few phenomenological improvements we justify below.

In the broken phase, we incorporate the the first correction of thermal effects by explicitly varying the EW vev as in (5.14) and treating all SM masses as vev-dependent variables

$$m_{SM}(T) = m^0_{SM} \times \frac{v(T)}{v_0}, \tag{5.23}$$

thus dropping the $T^2$ term in Eq. (5.12). For $m_h(T)$, the $T^2$ term is however retained for consistency in the definition of $v(T)$ and to make sure $\theta(T)$ does not have a divergence for small $m_S$. We expect this approximation to hold until $v(T) \gtrsim gT$, before the thermal masses are dominated by the plasma contributions.

In the symmetric phase, we retain the quark masses in the cross sections and promote them to the thermal mass acquired from the QCD plasma [132]

$$m_q^2(T) = \frac{g_s^2 C_F}{8} T^2 = \frac{g_s^2}{6} T^2, \tag{5.24}$$

which affects the kinematic phase space available for interactions. The Higgs doublet components all obtain the Higgs thermal mass (5.13). We neglect the gauge boson transverse mass. From a finite-temperature point of view, the magnetic thermal mass of a non-abelian SU(N) at one-loop is 0 [262]. A non-vanishing value is generated at higher order as a non-perturbative quantity of the order $m_T^2 \sim (g/3\pi)gT$ [263, 264], which is sub-leading compared to the other masses.

In the intermediate regime where a full finite-temperature calculation is needed $\frac{v(T)}{g} \lesssim T \leq T_c$, we extrapolate our two regions to obtain an uncertainty band for our model. In either case, we obtain a relic density uncertainty within a factor of 2, which is reasonable for the problem at hand.

Retaining the top quark Yukawa coupling $y_t$, the electroweak couplings $g, g'$ and the Higgs self-coupling $\lambda_H$ as the only non-zero coupling constants, the yield from each non-vanishing production channel in the $m_S \ll m_h$ limit are compiled in Table 5.1. Their respective emissivity as a function of temperature are shown in Figs. 5.4 and 5.5. We use FeynCalc [265, 266] to compute the cross sections. The QCD cross sections are expressed in section 5.4.1 and the large $s$ limit of the other channels are listed in supplementary section 5.7.

### 5.4.1 QCD production

The authors in Ref. [102] claimed the $S$ interactions with $t$ quarks and gluons dominate the freeze-in production. The cross sections for a gluon interaction with the top

| Production Channel $i$ | $Y_i^{v\gg 0}$ | $Y_i^{v\gtrsim 0}$ | $Y_i^{\text{sym}}$ | $Y_i^{\text{tot}}$ $[10^{10}\theta^2]$ |
|---|---|---|---|---|
| $t\bar{t} \to gS$ | 2.11 | 0.93 | 0 | 6.29 - 8.11 |
| $tg \to tS$ $(\times 2)$ | 4.17 | 0.90 | | |
| $t\bar{t} \to hS$ | 0.41 | 0.08 | 0.03 - 0.05 | 1.72 - 2.01 |
| $t\bar{t} \to ZS$ | 0.44 | 0.11 | | |
| $t\bar{b} \to W^+S$ $(\times 2)$ | 0.82 | 0.11 | | |
| $th \to tS$ $(\times 2)$ | 0.38 | 0.13 | 0.14 - 0.21 | 14.40 - 17.77 |
| $tZ \to tS$ $(\times 2)$ | 1.46 | 0.77 | | |
| $tW \to bS$ $(\times 2)$ | 3.66 | 1.43 | | |
| $bW \to tS$ $(\times 2)$ | 8.70 | 1.11 | | |
| $Zh \to ZS$ | 0.26 | 0.10 | 0.01 - 0.02 | 8.68 - 10.93 |
| $ZZ \to hS$ | 0.33 | 0.17 | | |
| $WW \to hS$ | 0.57 | 0.25 | | |
| $WW \to ZS$ | 3.47 | 0.89 | | |
| $Wh \to WS$ $(\times 2)$ | 0.46 | 0.16 | | |
| $WZ \to WS$ $(\times 2)$ | 3.57 | 0.69 | | |
| $hh \to hS$ | 0.01 | $< 0.01$ | 0 | |
| Total | 30.81 | 7.84 | 0.19 - 0.28 | 31.1 - 38.8 |

Table 5.1: $S$ freeze-in yield for each production channels in units of $10^{10}\theta^2$, separated by their near-vacuum contribution $Y_i^{v\gg 0}$ and addition yield $Y_i^{v\gtrsim 0}$ if extrapolated to the phase transition. The yield from each production category in the symmetric phase is shown as $Y_{rmcat}^{\text{sym}}$ with the range displaying the value above $T_c$ or extrapolated down.

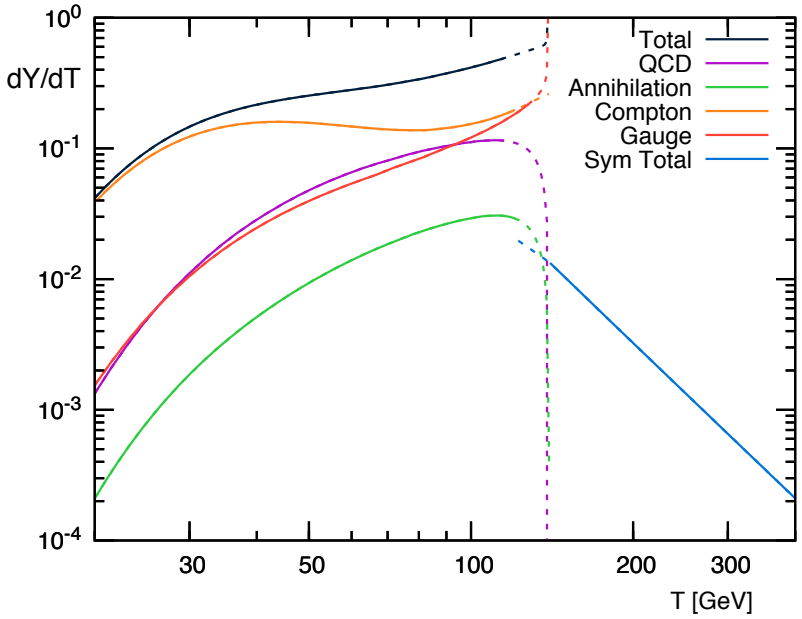


Figure 5.4: Total $S$ freeze-in emissivity and the contribution from each production channel category as a function of temperature for $\theta = 10^{-5}$.

quark to produce a $S$ (in the $m_S \to 0$ limit) are

$$\sigma_{t\bar{t}\to gS} = \frac{\alpha_s \theta^2 y_t^2}{9s}\left[\left(1-\frac{4m_t^2}{s}\right)\ln\left(\frac{1+\sqrt{1-\frac{4m_t^2}{s}}}{1-\sqrt{1-\frac{4m_t^2}{s}}}\right)+\frac{8m_t^2}{s\sqrt{1-\frac{4m_t^2}{s}}}\right] \tag{5.25}$$

$$\sigma_{tg\to tS} = \frac{\alpha_s \theta^2 y_t^2}{96s}\left[\frac{2s\left(s+3m_t^2\right)^2}{\left(s-m_t^2\right)^3}\ln\left(\frac{s}{m_t^2}\right)\right. \tag{5.26}$$

$$\left.-\frac{1}{\left(1-\frac{s}{m_t^2}\right)^3}\left(3+22\frac{m_t^2}{s}-20\frac{m_t^4}{s^2}-6\frac{m_t^6}{s^3}+\frac{m_t^8}{s^4}\right)\right], \tag{5.27}$$

where $y_t = 2m_t/v$ and $\alpha_s$ is the strong coupling constant, evaluated at the cosmic temperature $\alpha_s = \alpha_s(T)$. Including out $v(T)$ model, we find a total yield from the QCD reactions of

$$Y_{\rm QCD} \simeq 6.30 - 8.15 \times 10^{10}\ \theta^2, \tag{5.28}$$

where the uncertainty depends on whether we cut off the production at $T \leq v/g_s \simeq$ 121 GeV or we push the extrapolation to $T \leq T_c \simeq 140$ GeV. This yield is a factor

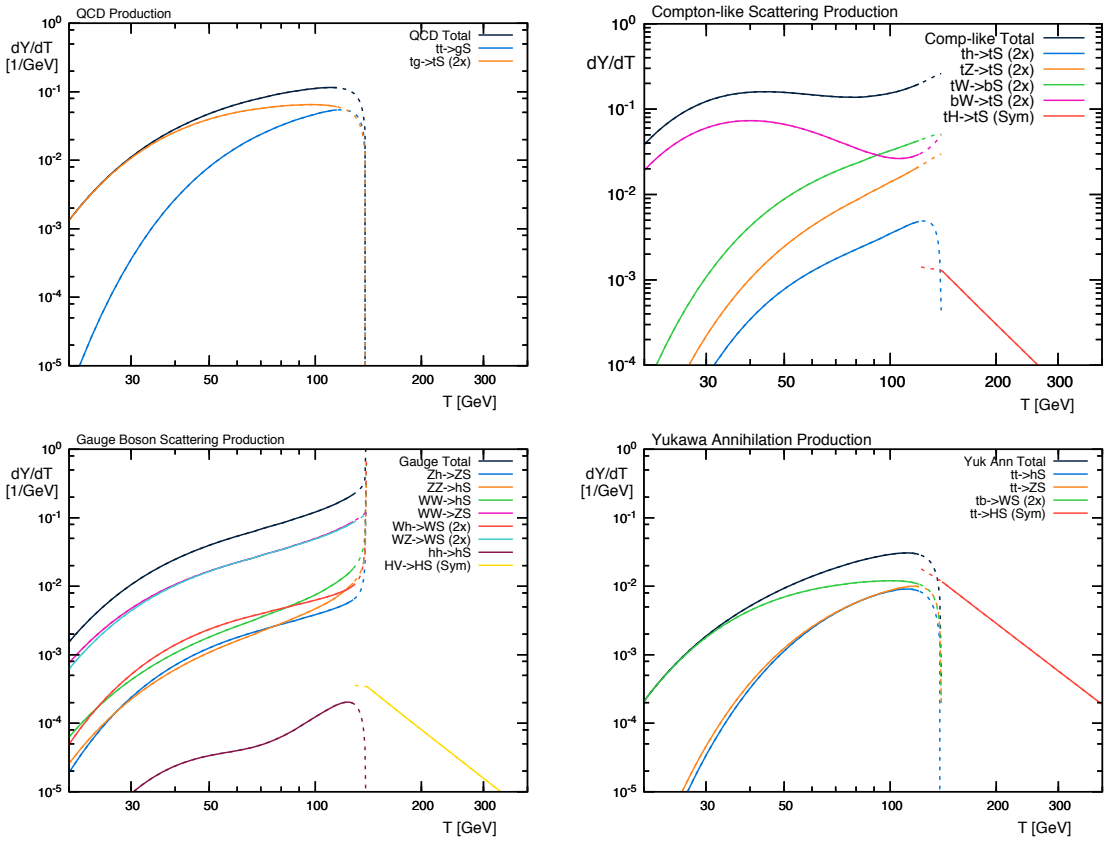


Figure 5.5: $S$ abundance yield from each production channels separated by each category. *Top left :* QCD production. *Top Right :* Compton-like scattering. *Bottom left :* Gauge boson scattering. *Bottom right :* Yukawa annihilation.

of approximately 20 smaller than the value quoted[2] in Berger et al. [102]. As listed in Table 5.1, we find many other channels with electroweak gauge bosons that contribute to the same level or more than these QCD-induced reactions.

### 5.4.2 Infrared divergences

There are two types of infrared divergences in the interactions that require special care, both present in the channel with the largest yield contribution, $bW \to tS$, schematically shown in Fig. 5.6.

At lower temperatures, where the vacuum cross sections are clearly applicable, the emission of a soft $S$ is enhanced from the near on-shell $t$ and $W$ mediators. Removing

[2]Both cross sections in Ref. [102] contain errors compared to (5.25-5.27) and their analytical estimate, equation (III-7) in [102] is dimensionally wrong.

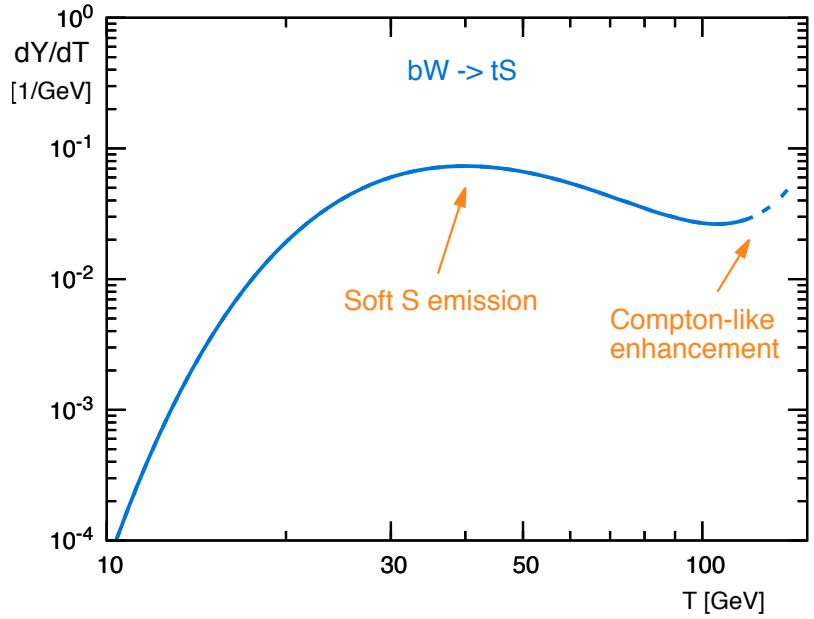


Figure 5.6: Emissivity of the production channel $bW \to tS$ showing the two types of IR divergences present in the calculations. The soft $S$ emission is physical and unique to this production channel. The Coulomb-like enhancement is present in all reactions with a $t$ or $u$-channel spin-1 mediator, is unphysical and signifies the breakdown of our calculations. See text for details.

the $S$ emission, the inverse decay process $bW \to t$ is kinematically allowed. Since we are considering an arbitrarily light scalar, $m_S \ll m_W, m_t$, the $2 \to 2$ reactions creating the $S$ have a kinematic cutoff of $s \geq (m_t + m_S)^2$, which approaches the propagator singularity $1/(s - m_t^2)$ as $m_S \to 0$. This type of divergence is regulated by the finite width of the propagator. For this channel, we promote the denominator of the $t$ quark and $W$ boson propagators to their Breit-Wigner equivalent

$$\frac{1}{p^2 - m_t^2} \to \frac{1}{p^2 - m_t^2 - i\Gamma_t m_t}, \qquad \frac{1}{p^2 - m_W^2} \to \frac{1}{p^2 - m_W^2 - i\Gamma_W m_W}, \tag{5.29}$$

where $\Gamma_i = \Gamma_i^0 \times \frac{v(T)}{v_0}$ is consistent with our $v(T)$ model throughout the calculation and the SM values are $\Gamma_t^0 = 1.4$ GeV and $\Gamma_W^0 = 2.1$ GeV [48]. Multiple schemes for calculating cross sections with unstable particles have been proposed beyond the simple substitution (5.29). The basic Breit-Wigner substitution is technically incompatible with gauge invariance and Ward identities [267, 268, 269], a problem that can lead to dramatic inconsistencies in the small-angle scattering away from the res-

onance [267]. We have explicitly compared the cross section with and without the substitution (5.29) away from the resonance. They differ by a factor of

$$\frac{\sigma^{BW}_{bW\to tS}}{\sigma^{0}_{bW\to tS}} \xrightarrow{s\gg m_t^2, m_W^2} \frac{m_W}{\Gamma_W}\arctan\frac{\Gamma_W}{m_W} = 0.9998 \tag{5.30}$$

which justifies the use of Breit-Wigner propagators in this reaction.

The second infrared divergences appear near $T_c$, where $v \to 0$. The exchange of a massless spin-1 particle in the $t(u)$-channels generates a well-known collinear divergence in the forward (backward) scattering [270]. This phenomenon is most easily demonstrated in scalar quantum electrodynamics, where for simplicity we consider the scattering of two distinguishable massless charged scalars, $s_1$ and $s_2$. The only Feynman diagram is the $t$-channel exchange of a photon. In the centre-of-mass frame, the differential cross section takes the form

$$\frac{d\sigma}{d\Omega} = \frac{4\alpha^2}{s}\left(\frac{3+\cos\theta}{1-\cos\theta}\right)^2, \tag{5.31}$$

which obviously diverges in the forward scattering $\theta = 0$. In practice, no experiment would have perfect resolution, the setup would have a angular cutoff $\theta \geq \theta_{\min}$ and $\theta = 0$ is never truly achieved. This resolution cutoff can alternatively be recasted in terms of a fictitious photon mass $m_\gamma$ and Eq. 5.31 becomes

$$\frac{d\sigma}{d\Omega_{\text{reg}}} = \frac{4\alpha^2}{s}\left(\frac{s(3+\cos\theta)}{s(1-\cos\theta)+2m_\gamma^2}\right)^2, \tag{5.32}$$

removing the singular pole of the denominator. The final cross section cannot depend on the fictitious $m_\gamma$. Its dependence perfectly cancels out when other reactions that have experimentally indistinguishable initial and final states are added, namely absorption and emission of soft photons with the same fictitious mass $m_\gamma$ [271, 272].

In the context of $S$ freeze-in production, the total cross sections with the $t$ or $u$-channel gauge boson propagators don't fall off as $1/s$ in the high energy limit (see supplementary section 5.7 for expressions). For the example shown in Fig. 5.6, we have

$$\sigma_{bW^+\to tS} \to \frac{\theta^2 m_W^2}{12\pi v^4} + \mathcal{O}\left(1/s\right). \tag{5.33}$$

At low temperatures, this asymptotic behaviour does not matter as large $s$ values are exponentially suppressed by the energy available in the initial particle distributions.

Writing the $W$ mass with its explicit vev dependance, Eq. 5.33 becomes

$$\sigma_{bW^+\to tS} \to \frac{\theta^2 g^2}{48\pi v^2} + \mathcal{O}\left(1/s\right), \tag{5.34}$$

which clearly diverges as $v \to 0$. Conceptually, this IR divergence should be regularized in the same fashion as the scalar QED example. It would then suffice to introduce a fiducial mass for the boson propagator and include diagrams with soft emissions and absorptions. In this case, the emissions and absorptions are connected to the thermal bath and the mass regulator is a physical quantity, the thermal mass. The Coulomb-like enhancement near $T \to T_c$ obtained from a simple extrapolation of the vacuum cross sections, with vev-dependant masses, (as in Eq. 5.23) signifies the breakdown of our calculations since the thermal effects are not incorporated. The formal strategy to deal with the collinear IR divergence in thermal field theory as been laid down by Braaten and Yuan [273] in the weak coupling limit $g \ll 1$. The strategy is to separate the hard and soft regimes at an intermediate momentum scale $gT \ll k_{\rm cut} \ll T$. The hard contribution for $k > k_{\rm cut}$ is calculated with tree-level diagrams in vacuum and the soft part is calculated with thermal field theory machinery. The $k_{\rm cut}$-dependent divergence cancels, obtaining a consistent finite result. We do not perform this full calculation, but simply use the limit $gT \lesssim v(T)$ as a boundary to our tree-level cross sections.

### 5.4.3 Resonant $S$ production

As seen in Fig. 5.1, the mixing angle obtains a physical resonance when $m_h(T) = m_S$. The resonance appears for 90 GeV $\lesssim m_S \leq$ 125 GeV with a decreasing resonance temperature $T_{\rm res}$ as $m_S$ approaches 125 GeV, as shown in Fig. 5.7. Physically, this resonance arises where the virtual Higgs that rotates into $S$ is allowed to become on-shell. This is equivalent to an unstable intermediate particle and can therefore be dealt with by promoting the Higgs propagator to its Breit-Wigner counterpart

$$\theta \to \theta_{\rm BW} = \frac{Av(T)}{m_h^2(T) - m_S^2 + i\Gamma_h(T) m_S}. \tag{5.35}$$

At low temperature, we have $\Gamma_h(T) = \Gamma_{h,0} v(T)/v_0$, with $\Gamma_{h,0} = 4.07$ MeV is the SM prediction. In the symmetric phase, the thermal width scales as $\Gamma_h(T) \sim 3g^2T^2/(256\pi m_h(T))$ [274, 275]. As an approximation of the Higgs thermal width,

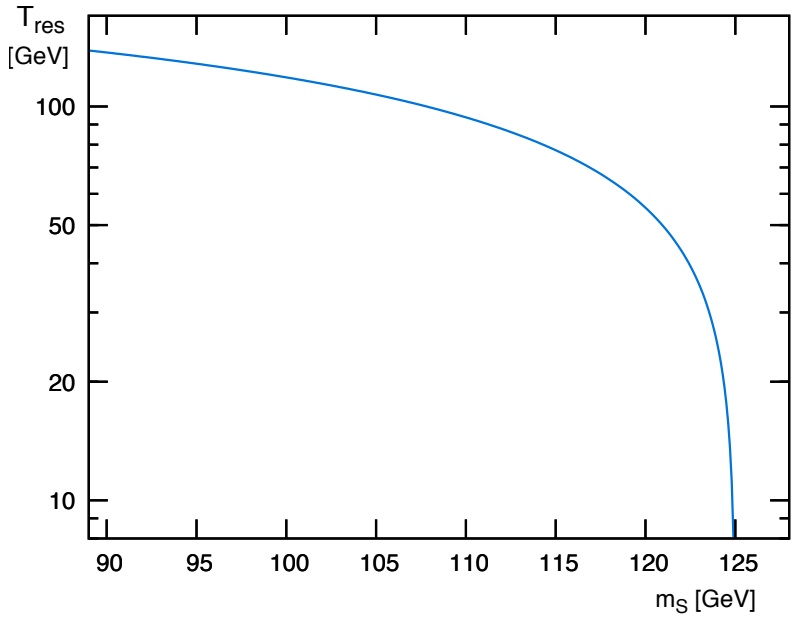


Figure 5.7: Resonance temperature as a function of $m_S$.

we extrapolate these two expressions in the intermediate range.

Since $\Gamma_h \ll m_h$, we can use the narrow-width approximation (NWA) to estimate the $S$ yield from the resonance. Substituing

$$\theta^2 \to \theta^2_{\rm NWA} = \frac{A^2 v^2(T_{\rm res})\pi}{2m_S^2 \Gamma_h(T_{\rm res})|m_h'(T_{\rm res})|}\delta\left(T - T_{\rm res}\right), \tag{5.36}$$

into Eq. (5.21), we find the simplified integral

$$Y_{\rm res} \simeq \frac{A^2 v_{\rm res}^2}{c_h T_{\rm res} m_S \Gamma_{\rm res} s_{\rm res} H_{\rm res}} \frac{g_1 g_2}{16\pi^3} \int ds p_{12}^2 \sqrt{s}\sigma_{\theta\to 1} K_1\left(\frac{\sqrt{s}}{T_{\rm res}}\right), \tag{5.37}$$

where we used the simplification $|m'_{h,rmres}| = c_h T_{\rm res}/m_S$. The resulting abundance is up to 1-2 orders of magnitude larger than non-resonance values depending on $T_{\rm res}$.

### 5.4.4 Thermalization of the $S$ sector with the SM

The freeze-in regime of the $S$ abundance applies for mixing angles small enough that the production rate remains below the Hubble rate

$$\Gamma_{\rm prod} = n_i \left\langle \sigma v \right\rangle_{12\to 3S} \lesssim H(T). \tag{5.38}$$

Summing all the production channels, we find that the freeze-in relic obtained with Eq. (5.21) is valid for

$$\theta \lesssim \theta_{\rm therm} \sim 10^{-6}. \tag{5.39}$$

Larger mixing angles completely thermalize with the SM bath before $S$ decouples and the relic is simply given by the standard freeze-out paradigm. In this case, $Y_S$ is maintained at its relativistic equilibrium value

$$Y_{\rm eq} = \frac{45\zeta(3)}{2\pi^2 g_\star(T)} \simeq \frac{0.28}{g_\star(T)}, \tag{5.40}$$

until $m_S$ becomes nonrelativistic, $T \lesssim m_S$, or the coannihilation rate becomes inefficient and $S$ decouples to its freeze-out abundance. Since $S$ interacts dominantly with heavy particles, $S$ remains relativistic while the coannihilating partners become nonrelativistic and the annihilation efficiency is exponentially lowered from the phase-space suppression of the other particles. Thus, $S$ freezes out according to Eq. (5.40) and the abundance only depends on the number of relativistic degrees of freedom $g_\star$ at the decoupling temperature. Above the QCD confinement scale $T_{\rm QCD} \sim 200$ MeV, $g_\star$ varies by at most of factor of 2, in the range of $g_\star \sim 205/4 - 427/4$. A conservative estimate for the thermalized $S$ relic abundance is therefore

$$Y_S^{\rm f-o} \simeq \frac{1}{400}. \tag{5.41}$$

### 5.4.5 Validity of the Maxwell-Boltzmann approximation

In the classic case of a WIMP freeze-out, the decoupling temperature of the species is typically in the non-relativistic regime $T_{\rm decoupl} \sim m/20$. The statistical distribution of the particles are well described by the MB distribution, which allows for an analytical simplification of the phase-space integrals in the Boltzmann equation. In the freeze-in scenario considered here, this simplification is not necessarily justified and we must verify its validity. We derive in supplementary section 5.8 the analytical 3-dimensional expression to be numerically integrated for the $S$ abundance including the correct statistical distribution of all particles.

Instead of proceeding with the full treatment, we can simply verify the MB approximation with a simpler integration. Keeping the exact statistical distributions in

the Boltzmann equation, we obtain [259]

$$s\dot{Y} = \frac{1}{32\pi^4}\int ds\; p_{ij}\sqrt{s}\;\sigma\int_{\sqrt{s}}^{\infty} dE_+ \int_{\frac{|m_1^2-m_2^2|E_+}{s}-2p_{ij}\sqrt{\frac{E_+^2-s}{s}}}^{\frac{|m_1^2-m_2^2|E_+}{s}+2p_{ij}\sqrt{\frac{E_+^2-s}{s}}} dE_-\; f_1 f_2(1\pm f_3), \quad (5.42)$$

where the initial energies were rewritten in terms of $E_+ = E_1 + E_2$, $E_- = |E_1 - E_2|$, $f_i$ is the Fermi-Dirac (FD) or Bose-Einstein (BE) distribution of species $i$ and the $+$ $(-)$ is chosen for bosons (fermions) in the last term. The MB approximation (5.20) arises as an analytic solution in the MB limit $f_{1,2} = e^{-E_{1,2}/T}$ and $(1 \pm f_3) \to 1$. We should stress that Eq. (5.42) is not mathematically correct as $E_3$ should have been included in the cross section phase-space integration over the end products. This integration is in general non-trivial and includes an additional angular dependence with $s$ (see supplementary section 5.8). Nonetheless, we can use Eq. 5.42 as an estimate to the full result. To obtain the first correction beyond the MB approximation, we can expand

$$f_i = \frac{1}{e^{E_i/T}\pm 1} \simeq e^{-E_i/T}\left(1 \mp e^{-E_i/T} + \cdots\right). \quad (5.43)$$

It is important to notice that the first order correction in the initial particles is equal to the MB limit of the $(1 \pm f)$ term. At first order in $e^{-E_i/T}$, we have

$$f_1 f_2(1\pm f_3) \simeq e^{-E_+/T}\left(1 + \kappa_1 e^{-(E_+ + E_-)/2T} + \kappa_2 e^{-(E_+ - E_-)/2T} + \kappa_3 e^{-E_3/T}\right), \quad (5.44)$$

where $\kappa_i = \pm 1$, $+$ $(-)$ for bosons (fermions). As expected, the bosonic distribution enhances the overall yield, while the fermionic distribution decreases it. In principle, $E_3$ is a function of the $\sqrt{s}$ and the angular kinematics of the end particles. As mentioned, the $1 \pm f_3$ should be included in the annihilation cross section and modify $\sigma$. However, we know by conservation of energy we have $E_1 + E_2 = E_3 + E_4$ and must have the following bounds on $E_3$

$$m_3 \le E_3 \le E_+. \quad (5.45)$$

To estimate the range of possible yield values with the first correction to the full quantum distribution, we can integrate (5.42) with (5.44) for each of the $E_3$ extrema values. The potential spread in total emissivity in shown in Fig. 5.8 with an estimated error range of

$$2.8\times 10^{11}\theta^2 < Y_S < 5.2\times 10^{11}\theta^2. \quad (5.46)$$

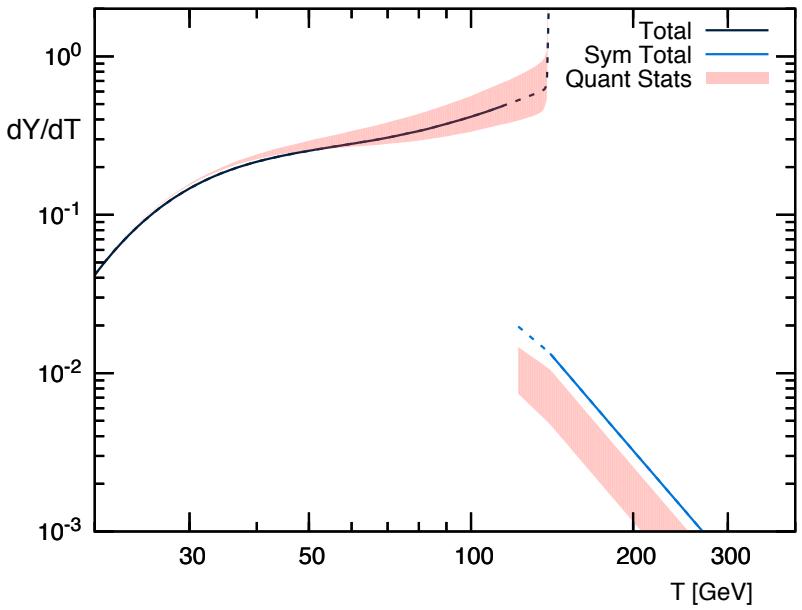


Figure 5.8: Total $S$ emissivity as a function of temperature, including the estimated range of error from the correct emissivity with quantum distributions of particles 1, 2 and 3.

The total error for the MB approximation is thus expected to be within a factor of 2. The first order correction band in the symmetric phase completely below the MB value, because the top quark thermal masses from the QCD plasma dominate and suppresses the available phase space in the Fermi-Dirac distribution.

## 5.5 Cosmological constraints

The small mixing angle abundance from freeze-in allows us to place the minimal set of bounds on the $S$ parameter space with $\theta \lesssim \theta_{\rm therm} \sim 10^{-6}$. We update and improve the cosmological constraints partially presented in both Ref. [102] and Ref. [251] and present the full low-$\theta$ parameter space in Fig. 5.9. The cosmological constraints that depend on $Y_S$ are discussed in the following subsections. Below $m_S \lesssim 5$ keV, the strongest constraint on $S$ comes from stellar cooling constraints [188] and even lighter scalars in the sub-eV range are excluded by $5^{\rm th}$ force experiments [276, 277, 278, 279]. We also show the projected sensitivity from the SHiP experiment [47] and an order-of-magnitude estimate of supernova energy loss [280]. Above the pion threshold, we will see that the constraints largely depend on the $S$ decay model. The colored exclusion

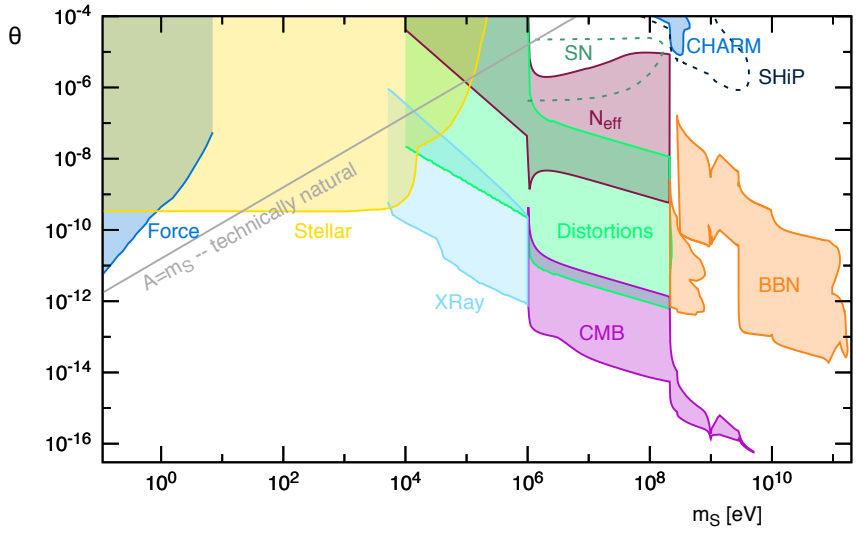


Figure 5.9: Overview of the excluded parameter space of the super-renormalizable Higgs portal scalar, including the updated constraints from the diffuse X-ray background (XRay), the CMB anisotropies, spectral distortions, $N_{\rm eff}$ and BBN derived in this chapter. Constraints from new short-range forces (Force) [276, 277, 278, 279] and stellar cooling [188] from other authors are shown. Below the thin grey line, $S$ is technically natural. We also display the SHiP projected sensitivity [47] and an estimate of supernova (SN) constraints [280].

regions presented in Fig 5.9 are using the baseline decay model, which has a larger or equal decay width than the spectator model. It thus corresponds to more conservative results due to the reduced abundance for a fixed lifetime. In the super-renormalizable Higgs portal, loop-corrections to the $S$ mass will be $\Delta m_S^2 \sim A^2 \log \Lambda_{\rm UV}$. The scalar is thus technically natural for $A \lesssim m_S$ [281], where the cosmological constraints lie in the parameter space.

### 5.5.1 Diffuse X-ray background

Many present-day satellites look for our galaxy's photon spectrum in various energy ranges and provide upper bounds on the luminosity of X-rays or Gamma-rays that can be emitted. This can be interpreted as a maximal photon source for decaying or annihilating dark matter. In particular, Ref. [282] computed the lifetime constraint on a scalar dark matter decaying into 2 photons in the 4 keV $< m_S <$ 10 GeV mass range assuming $\tau_S \gg \tau_{\rm universe}$. We can rescale their constraint from the HEAO-1 [283] and INTEGRAL [284] satellites to obtain an exclusion band for 4 keV $< m_S <$ 1 MeV

with $10^{16}\,\mathrm{sec} \lesssim \tau_S \lesssim 10^{22}\,\mathrm{sec}$ displayed as *X-Ray* in Fig. 5.9.

### 5.5.2 Cosmic Microwave Background

The precise measurement of the temperature and polarization anisotropies in the CMB by the WMAP [24] and Planck [7] satellites provide strong constraints on the energy injection that can ionize the cosmic neutral hydrogen after recombination [71, 285, 116, 70, 286, 72]. The raised ionized fraction at lower redshifts allows for delayed photons interactions, which modifies the visibility function that weighs the probability of last scattering of a given CMB photon at a specific time. This effectively damps the high-$l$ tail of the TT power spectrum and increases the low-$l$ E-mode polarization [71, 285].

The efficiency of energy deposition in the cosmic plasma at a redshift $z_{dep}$ by an energetic electron-positron pair or photons injected at an earlier redshift $z_{inj} > z_{dep}$ has been solved in Ref. [118] and updated in Ref. [73]. This update provides the energy fractions that go into ionizations, excitations, heating and emission of low-energy photons. Given the process-dependent $z$-dependent ionization efficiency, comparing the modified power spectra to the CMB data is computationally intense and not practical. In practice, principal component analysis of modified recombination histories show that a decaying particle is well described by a constant deposition efficiency taken at $z_{dep} = 300$ [73, 287]. We can then simply utilized our derived constraints from chapter 2 in Fig. 2.5 and translate to the current model with

$$\zeta = f_{\mathrm{eff}} \frac{m_S Y_S s_0}{m_p n_{b,0}}, \tag{5.47}$$

where $f_{\mathrm{eff}} = f(z = 300)$ is the ratio of energy absorbed into ionization over energy emitted at $z_{\mathrm{dep}} = 300$. In the mass range where $S \to \mu^+\mu^-$ is the main decay channel, we solve for $f_{\mathrm{eff}}$ by integrating over the electron decay from for the muon, which decreases the ionization efficiency by $\sim 3$ due to neutrinos radiating away energy. We repeat the procedure for the decay chain $S \to \pi^+\pi^- \to \mu^+\mu^-\nu\nu$, $S \to \pi^0\pi^0 \to \gamma\gamma\gamma\gamma$ and find that it is well approximated by evaluating the decay products at their average energy from the decay. We evaluate the efficiency of kaons by weighing the main branching ratios and the decay products by their average carried energy, percolating them down to their final $e^\pm - \gamma - \nu$ spectra. Above the di-charm threshold, the light quarks, charm quark and gluon all have similar deposition efficiencies that lie

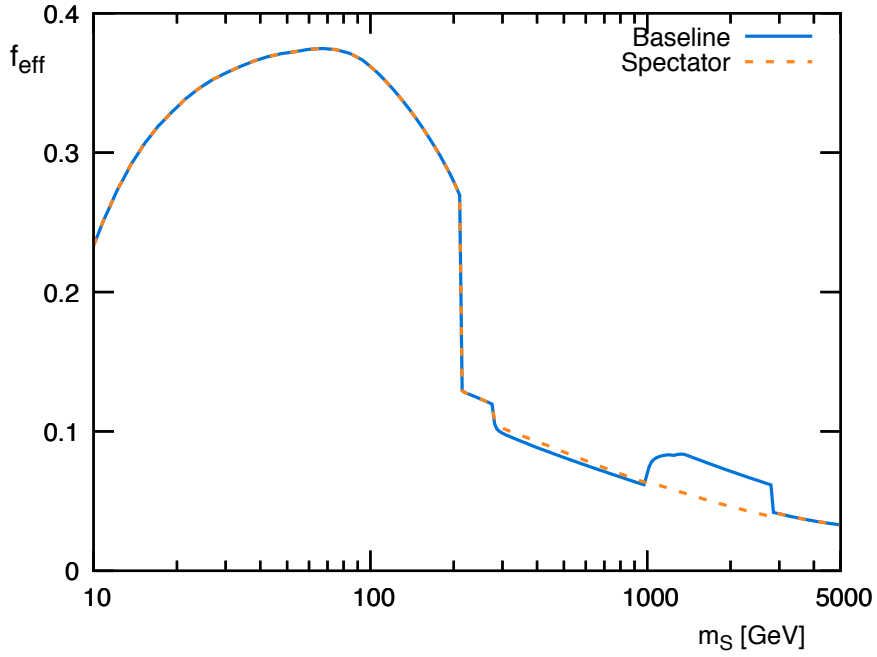


Figure 5.10: Effective fraction of energy deposited in ionization of the the cosmic plasma at $z = 300$ for $\Gamma_S = 10^{14}$ s, for both the baseline and spectator decay models.

somewhere between the electron and the muon injection efficiencies [72]. In general, for $m_S \lesssim 10$ GeV, the efficiency tends to approach the muonic case [119]. We adopt the same ionization efficiency as muons for conservative results. The overall $f_{\rm eff}$ for $S$ with $\tau_S = 10^{14}$ sec is shown in Fig. 5.10 for both the baseline and spectator decay models.

We do not extrapolate the CMB constraints for lifetimes $\tau_S < 10^{13}$ s because $f_{\rm eff}$ is not numerically stable for decays before recombination [73] and the on-the-spot approximation at $z_{\rm dep} = 300$ fails to represent the correct physics for short lifetimes [287]. The excluded band is shown in orange in Fig 5.11 for the baseline model, with the would-be exclusion region for the spectator decay model delimited by a thin gray line.

### 5.5.3 Spectral distortions

While energy injection after recombination can be seen in the CMB as variations in the anisotropies, earlier injections can induce spectral distortions from the blackbody distribution (see Ref. [289] for a recent review) and can be used as probes on decaying

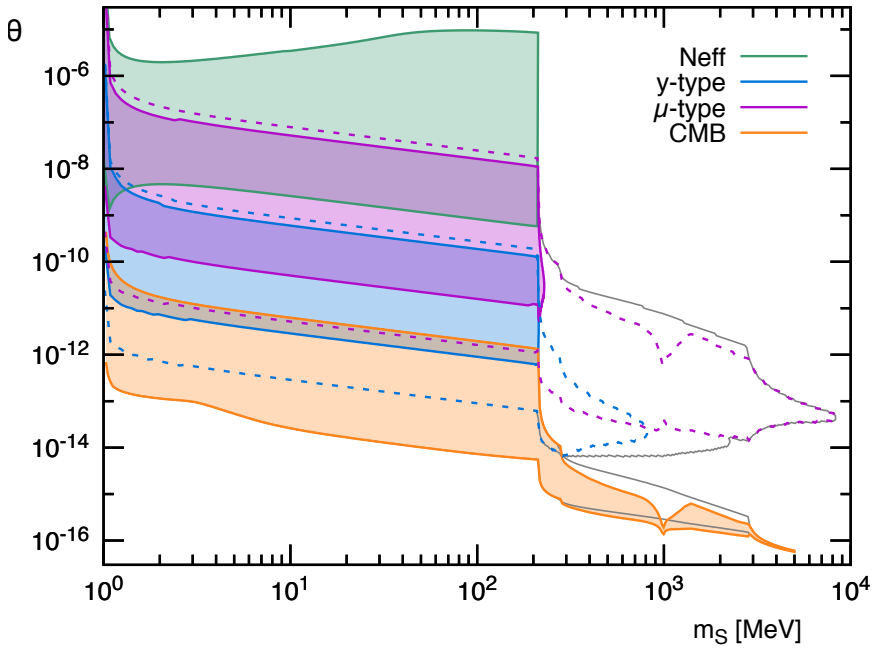


Figure 5.11: Detailed cosmological constraints on $S$ in the MeV mass range, excluding BBN (see Fig. 5.13). The solid lines and shaded areas represent the parameters excluded in the baseline decay model. Dashed lines are spectral distortions projection from Pixie [288] and the thin gray line demonstrate the would-be Pixie sensitivity in the spectator $S$ decay model.

particles [290, 291].

Cosmological thermalization is very efficient at arbitrarily early times and the photon plasma becomes susceptible to incomplete re-equilibration of its spectrum for energy releases at $z \lesssim z_\mu \simeq 2 \times 10^6$. The CMB photons are still efficient at redistributing their energy across the energy spectrum, but double Compton scattering and Bremsstrahlung interactions that adjust the number of photons become inefficient. The bath thus develops a non-zero chemical potential at high energies resulting in the $\mu$-distortion. At lower redshifts, $z \lesssim z_{\mu y} \simeq 5 \times 10^4$, Compton scatterings between electrons and photons fail to maintain both species at a common temperature. The photon bath gets a temperature diminution at low energies and the high frequencies obtain a relative gain in temperature, a phenomenon called the Compton $y$-distortion [289].

Distortions from arbitrary energy injections can be approximated by [292]

$$y = \frac{1}{4}\int_{z_{\rm rec}}^{z_{\mu y}} \frac{d(Q/\rho_\gamma)}{dz'}dz', \qquad \mu = 1.401\int_{z_{\mu y}}^{\infty} e^{-\left(\frac{z'}{z_\mu}\right)^{5/2}}\frac{d(Q/\rho_\gamma)}{dz'}dz', \tag{5.48}$$

where $z_{\rm rec} = 1000$ and the normalized injected electromagnetic energy is

$$\frac{d(Q/\rho_\gamma)}{dz'} = \frac{1}{\rho_\gamma}\frac{dE}{dtdV}Br_{\rm em}\frac{1}{H(1+z')}. \tag{5.49}$$

In this case, $\frac{dE}{dtdV}$ is the total energy injected and $Br_{\rm em}$ is the branching ratio to electromagnetic end products. In a radiation-dominated Universe, the $y$-distortion can be evaluated analytically with

$$y \simeq \frac{\sqrt{\pi}}{8}\frac{Y_S m_S s_0}{\rho_{\gamma 0}\sqrt{\Gamma_S t_0}}\, Br_{\rm em}\, \mathcal{I}(\Gamma), \tag{5.50}$$

with the current entropy density $s_0 = 2891\ {\rm cm}^{-3}$, the current photon energy density $\rho_{\gamma 0} = 0.26\ {\rm eV\ cm}^{-3}$, a time normalization of $t_0 = 2.4\times 10^{19}\,{\rm sec}$ and the integral $\mathcal{I}(\Gamma)$ is defined as

$$\mathcal{I}(\Gamma) = \frac{2}{\sqrt{\pi}}\int_{\frac{\Gamma t_0}{z_{\mu y}^2}}^{\frac{\Gamma t_0}{z_{\rm rec}^2}} e^{-\xi}\sqrt{\xi}\, d\xi \rightarrow \begin{cases} 1 & ,\text{if } 10^{-13} \lesssim \Gamma\times{\rm sec} \lesssim 10^{-10}, \\ 0 & ,\text{if } \Gamma \ll 10^{-13}\ {\rm sec}^{-1} \quad \text{or} \quad \Gamma \gg 10^{-10}\ {\rm s}^{-1}. \end{cases} \tag{5.51}$$

The measured bounds from Cobe/FIRAS and the projected sensitivity from PIXIE are

$$|y| \leq 1.5\times 10^{-5} \qquad |\mu| \leq 9\times 10^{-5} \qquad \text{for Cobe/FIRAS [293]}, \tag{5.52}$$

$$|y| \leq 2\times 10^{-9} \qquad |\mu| \leq 1\times 10^{-8} \qquad \text{for PIXIE [288]}. \tag{5.53}$$

We approximate the electromagnetic branching ratio by weighting the average energy carried by end products from initial decays at rest with their respective branching ratios from $S$. Since the averaged energy carried away by the electron in a muon decay is $\langle E_e\rangle/m_\mu = 0.35$ [69], we have $Br_{\rm em}^{S\rightarrow\mu^+\mu^-} = 0.35$. The heavier decay products can be built by cascading down the lighter products. We find the electromagnetic

branching ratios

$$E_{\rm em}^{\mu^\pm} \simeq 0.35 \times E_{\mu^\pm}, \qquad E_{\rm em}^{\pi^\pm} \simeq 0.27 \times E_{\pi^\pm}, \qquad E_{\rm em}^{\pi^0} = 1.00 \times E_{\pi^0}, \tag{5.54}$$

$$E_{\rm em}^{K^\pm} \simeq 0.29 \times E_{K^\pm}, \qquad E_{\rm em}^{K_S^0} \simeq 0.49 \times E_{K_S^0}, \qquad E_{\rm em}^{K_L^0} \simeq 0.48 \times E_{K_L^0}, \tag{5.55}$$

where we neglected the kaon decay channels that contribute less than 10% of the kaon decay width. The total electromagnetic branching ratio for the $S$ decay channels are

$$Br_{\rm em}^{S\to\mu^+\mu^-} = 0.35, \qquad Br_{\rm em}^{S\to\pi\pi} = 0.51, \qquad Br_{\rm em}^{S\to KK} = 0.39, \qquad Br_{\rm em}^{S\to q\bar{q},gg} = 0.45, \tag{5.56}$$

where 2/3 (1/3) of pions are charged (neutral), 1/2 (1/4+1/4) of kaons are charged (neutral short + long) and we assume the electromagnetic yield of high energy quarks and gluons of 0.45 is maintained for $c$-quarks. The total $Br_{\rm em}$ as a function of $m_S$ is shown for the baseline and the spectator decay models in Fig. 5.12. The excluded regions from Cobe/FIRAS are shown in Fig. 5.11, with a robust conservative overlap between all probes in the 1 MeV $< m_S < 2m_\mu$ mass range. Pixie will not change the constraints in the $m_S < 2m_\mu$ mass range, but has the potential to increase the sensitivity to $m_S \lesssim 8$ GeV, with a sensitivity band that somewhat depends on the $S$ decay model.

### 5.5.4 $N_{\rm eff}$

The amount of relativistic energy density in the Universe is well constrained by the CMB. The temperature of the photon bath determines its contribution to the total radiation energy density. Any additional component is parametrized in $N_{\rm eff}$, the effective number of neutrinos with a temperature $T_\nu = (4/11)^{1/3} T_\gamma$. The Planck collaboration measurement of $N_{\rm eff} = 3.04 \pm 0.33$ [7] at $2\sigma$ is in agreement with the SM predicted value of 3.046 [294].

The constraints on early injection $\tau_S < 1\,$sec of $S \to \{e^+e^-, \gamma\gamma\}$ or $S \to \mu^+\mu^-$ have been derived in chapter 4 including neutrino decoupling effects, which we apply using the freeze-out abundance from Eq. 5.41 in the mass range 10 MeV $\lesssim m_S < 2m_\mu$. For lower masses, the $S$ lifetime at the border of the exclusion band is longer than $\tau_S = 100$ s, the maximal range derived in chapter 4. For longer lifetimes, we simply compare the energy density of the $S$ sector with the SM energy densities in the neutrino and EM baths prior to the energy release (at $t = x\tau_S$) and assume an

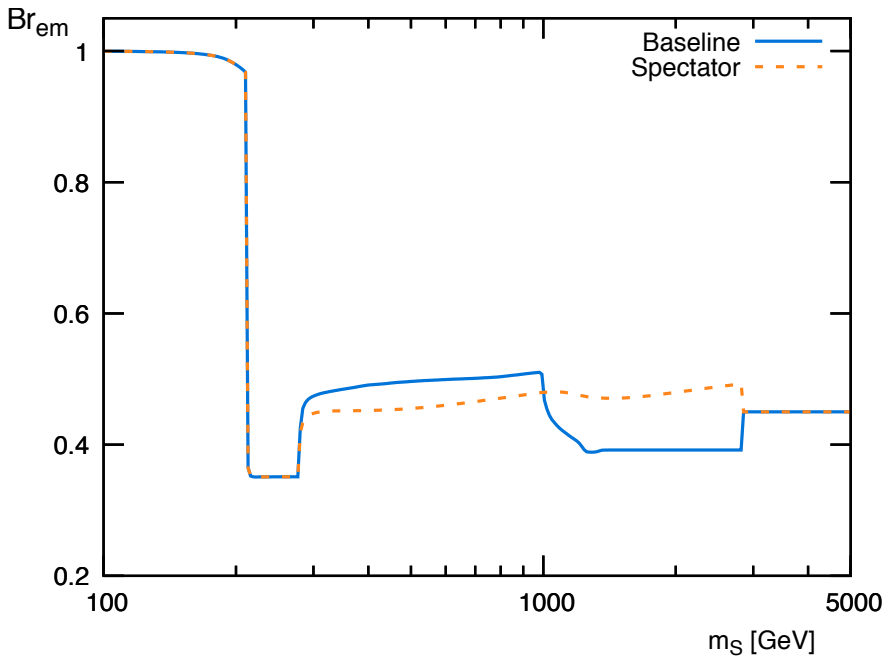


Figure 5.12: Fraction of $S$ rest energy decaying into electromagnetic energy as a function of its mass for the baseline and spectator decay models.

instantaneous decay. $N_{\rm eff}$ can then be estimated by comparing the relative energy density in the neutrino and EM baths

$$N_{\rm eff} = \frac{8}{7}\left(\frac{11}{4}\right)^{4/3} \frac{\rho_\nu^0 + \rho_\nu^S}{\rho_\gamma^0 + \rho_\gamma^S}, \tag{5.57}$$

where $\rho_\gamma^S = Br_{\rm em}\rho_S(t = x\tau_S)$, $\rho_\nu^S = (1 - Br_{\rm em})\rho_S(t = x\tau_S)$ and the electromagnetic/neutrino energy partition of the end products $Br_{\rm em}$ is taken from Fig. 5.12. We choose $x = 1/10$ that extrapolates to the $\tau_S < 100$ s constraints. The choice of $x = 1/10$ is conservative. The nonrelativistic $S$ energy density decreases less with time than the relativistic SM energy density and larger values of $x$ would yield stronger constraints. Using the $2\sigma$ range of $N_{\rm eff} = 3.04 \pm 0.33$, we find the constraints labelled $N_{\rm eff}$ in Figs. 5.9 and 5.11.

### 5.5.5 Big Bang Nucleosynthesis

The BBN of light nuclei is well understood, with final abundance of stable light nuclei in good agreement with predicted values (see for *e.g.* Refs. [203, 295] for recent

overviews and discussions of the discrepancy with $^7$Li). The concordance between predicted and observed abundances of $^4$He , $^3$He and D can be used to constrain electromagnetic and hadronic energy injections (see Refs. [204, 12, 296] for reviews).

The outcome of decaying particles in the BBN era depends on the ability of the decay products to efficiently interact with the light nuclei, which vary as the BBN reaction network evolves and the universe cools down. Early mesons decays were thoroughly discussed in chapter 4, effectively increasing the $n/p$ ratio before they freeze out, thus raising the $^4$He yield above its observational limit. After most neutrons have converted to $^4$He , the negatively charged mesons, $\pi^-$ and $K^-$ can dissociate the copious $^4$He , producing lighter $^3$He , T, D, $n$ and $p$ that are re-fed in the reaction network [69]. This mechanism was suggested to decrease the $^7$Li prediction by reducing the amount of $^7$Be and resolve the discrepancy with observations [69], but incidentally also raising the $D/H$ ratio above $3\times10^{-5}$ from inefficient $D$ burning, which is now excluded by observations [104, 297]. Beyond $\tau_S \gtrsim 10^4$ s, the mesonic interaction rate with ambient nuclei is suppressed by the expansion dilution below their decay rates. The mesons instead have enough survival time to decay away in a shower of electromagnetic energy. Photodissociation of nuclei becomes efficient when photons have cascaded down below the $e^+e^-$ thermal pair creation energy $E_{\rm th} = m_e^2/22T$. These $\gamma$-rays can photodissociate D with a binding energy of $E_{\rm D}^{\rm bind} = 2.2$ MeV at $t \sim 5\times10^4$ s and similarly for $^4$He with $E_{^4{\rm He}}^{\rm bind} = 19.8$ MeV at $t \sim 4\times10^6$ s [238].

We implement mesonic decays to $S\to\pi\pi$ and $S\to KK$ (charged and neutral) by weighing the freeze-in abundance by their respective branching ratios. We can then apply the early decays constraint from chapter 4, constraining the $S$ parameter space by an overproduction of $^4$He shown in blue in Fig. 5.13. Moreover, we use the $D/H < 3\times10^{-5}$ limit from Ref. [69], utilizing their stopped pions and kaons analysis for conservative results, displayed as the orange region on the $S$ parameter space. Longer lifetimes with electromagnetic showers constraints are shown in green. We weigh the $S$ abundance by the electromagnetic branching ratio from Fig. 5.12 and compare the value with the electromagnetic injection limit from Ref. [296]. The upper protruding band is from a decreased D/H ratio while the lower green region is from an increased $^3$He /D ratio. We have assumed 100% decays to kaons in the uncertain region, from $m_S \sim 1.4$ GeV to the di-charm threshold. The $S$ BBN constraint from mesonic decays have large uncertainties from the unknown decay spectrum. This is shown by the rather largely different exclusion region if the spectator decay model

was instead assumed, as shown by the thin gray line in Fig. 5.13.

Above the di-charm threshold, the $S$ decay products are well understood and the model allows for more accurate predictions. The BBN outcome is sensitive to the total energy injected via quark pairs, with a negligible dependence on the quark flavor [296]. The sensitivity is mostly dominated by the number of hadrons produced in the hadronic shower, with a $m_S^{0.3}$ dependence on the total energy input (assuming a nonrelativistic $S$). Constraints from quark injection therefore increase with a smaller $m_S$ [296]. We use the $b\bar{b}$ limits from a 30 GeV initial particle from Ref. [296] for $c\bar{c}$ and $b\bar{b}$ injections, both rescaled by their respective branching ratio. The resulting exclusion is shown in red in Fig. 5.13, with the upper $\theta$ range constrained by a $^4$He overabundance and the lower $\theta$ values excluded by a D overproduction. For $m_S \gtrsim m_h$, the freeze-in abundance is suppressed compared to the decay rate and the BBN sensitivity quickly shuts off near $m_S \lesssim 180$ GeV.

Electromagnetic injections below the pion threshold will also affect the BBN network, through decays to muons and electrons with a nontrivial dependence on the $S$ mass [102]. However, the $S$ decay rate is much weaker and requires $\theta$ values near the $S$ thermalization to decay during the active BBN epoch. The parameter space will have strong constraints from energy density requirements via $N_{\text{eff}}$, which is derived in section 5.5.4, along with the spectral distortions results from section 5.5.3. These already exclude the parameter space with $\tau_S \sim 0.1 - 10^{13}$ s for $2m_e < m_S < 2m_\mu$. We therefore don't need to perform a detailed analysis of the BBN constraints below the di-pion threshold and, by the same token, the potential solution to the $^7$Li problem tagged in Ref. [102] is also ruled out.

## 5.6 Discussion

We have improved the freeze-in production calculation of the Higgs portal scalar and shown that electroweak gauge bosons and the $t - b$ quarks have non-negligible contributions to the total yield. The dominant production channel is not through QCD interactions as previously thought [102]. We find the largest yield from the top quark coalescence with a soft $S$ emission, regulated by the top quark finite-width. Even for $m_S \ll m_h$, the favoured interactions with heavy particles push the bulk of the production just below the electroweak phase transition, in the 10 GeV $\leq T \leq T_c$ temperature range. Improvements in the precision of the calculation require the full finite-temperature quantum field theory machinery that models the phase transition

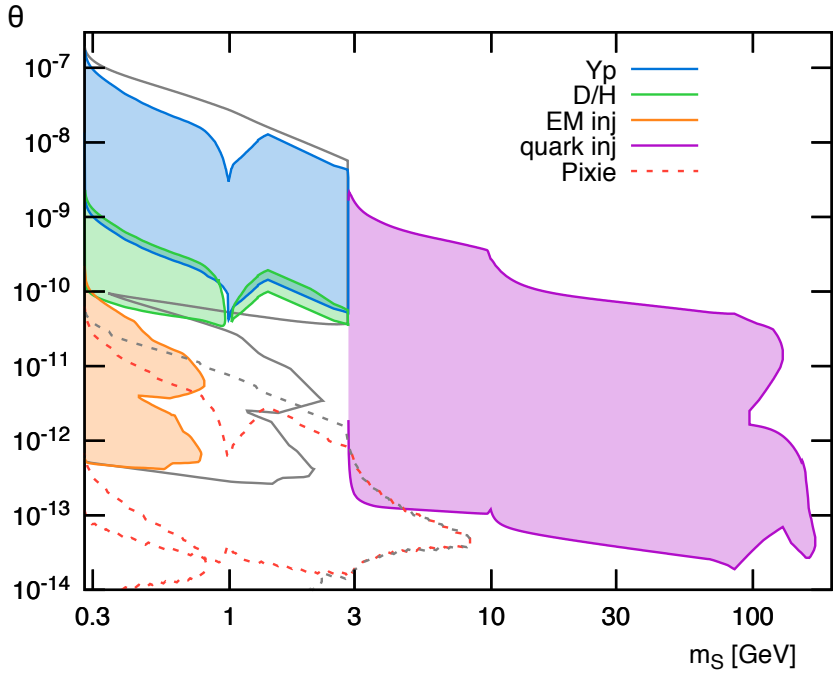


Figure 5.13: BBN constraints above the di-pion threshold. Solid lines and shaded areas are ruled out if $S$ follows the baseline decay model. Thin gray lines show the region for the spectator decay model instead. Dashed lines represent the future spectral distortion sensitivity from Pixie [288].

and includes plasma screening effects. This incremental effort is substantial and not necessarily justified for NP searches, especially because we are able to estimate our current accuracy around a factor of 2.

We provide a full parameter space scan of low mixing angle constraints, from sub-eV masses to 100 GeV. The cosmological constraints that depend on the primordial $S$ abundance appear for $m_S > 10$ keV. The Higgs portal scalar has well-defined decay products below the pion threshold. It allows for rigorous constraints in the 10 keV $< m_S < 2m_\mu$ range that fully cover 6 to 10 orders of magnitude in mixing angle. The low $\theta$ boundary is probed by the late decays seen in the diffuse X-Ray background and the CMB. In both cases, the lifetimes exceed the sensitive injection time window. This means that the number of decaying particles scales as $dN/dt \propto Y_S \Gamma_S \propto \theta^4$. A change in $S$ abundance by a factor of 2 would change the $\theta$ sensitivity by a factor of $2^{1/4}$, which is negligible. For this reason, improvements in the calculation of $Y_S$ would provide a minimal accuracy gain in sensitivity and our approximate framework with near-vacuum cross sections is justified, at least for

$m_S < 2m_\mu$. Similarly, the upper boundary for large $\theta$ is set by the freeze-out relic, rather than the freeze-in abundance. As explained in chapter 4, early cosmological energy injection has a logarithmic dependence on the $S$ primordial metastable abundance. This log dependence renders the exclusion region robust to variations by a few in $Y_S^{\mathrm{f-o}}$, confirming the accuracy of our conservative estimate, Eq. (5.41), without the need for a relativistic freeze-out computation.

Above the pion threshold, in the $2m_\pi < m_S \lesssim 2m_c$ mass range, we have derived the CMB, spectral distortion Pixie forecast and BBN constraints for two difference decay models, with significant differences in the exclusion bands. Especially near the kaon resonance, $m_S \sim 1$ GeV, sensitivity of each probe can vary by an order of magnitude in $\theta$. Given this poorly defined feature, we stress that improvements in the determination of the $S$ mesonic decay width are needed before finite-temperature abundance calculations are warranted to improve the accuracy of cosmological probes.

For higher masses, where $m_S$ predominantly decays to quarks, the large $\theta$ sensitivity boundary is sharply diverging for short lifetimes in the $m_S Y_S$ vs $\tau_S$ plane [296]. The $\theta$ constraint is insensitive to minor changes in $Y_S$. For $\tau_S > 10^4$ s, however, the required energy stored in the dark sector, $m_S Y_S$, is almost flat for increasing lifetimes. Changes in the freeze-in yield by a factor of 2 can thus be compensated by a factor of $2^{1/4}$ in the mixing angle, the same parametric dependence as the X-rays and CMB case. We therefore conclude that cosmological constraints on $S$ are robust to variations of $Y_S$ by a factor of a few, except where $S$ decays primarily to mesons, where the determination of the decay width results in a larger uncertainty.

The derived constraints are somewhat conservative with respect to the structure of the dark sector if a quartic interaction $\lambda_S S^2 H^\dagger H$ does not thermalize the DS. The only additional requirement is that $S$ decays visibly and not into some light dark state. In this case, the freeze-in production mechanism provides the minimal metastable abundance $S$ can have for a given lifetime. Any additional interactions with other states will increase its population, until it thermalizes with the SM. Large self-interactions can potentially dilute $Y_S$ before it decays, which would reduce the $S$ abundance by a factor of $\ln(a_{\tau_S}/a_{\mathrm{f-i}})$ [165]. Given that the freeze-in relic is set at $T_{\mathrm{f-i}} \sim 10$ GeV, this is a negligible factor of a few for early decays probed by BBN or $N_{\mathrm{eff}}$, but can potentially be more than an order of magnitude in $Y_S$ for lifetimes relevant to the CMB and X-rays measurements. Large self-interactions could therefore reduce the low $\theta$ sensitivity by a factor of a few.

## 5.7 Supplementary: Large energy limit of production cross sections

We collect here the large $s$ limit of the cross sections used in the freeze-in relic abundance. For the Yukawa annihilation type, we have

$$\sigma_{t\bar{t}\to hS} \to \frac{y_t^4\theta^2}{192\pi s}\left(\ln\frac{s}{m_t^2}-2\right), \tag{5.58}$$

$$\sigma_{t\bar{t}\to ZS} \to \frac{\theta^2}{576\pi v^4 s}\left[6m_t^2\left(2m_t^2+(1+c_v^2)m_Z^2\right)\ln\frac{s}{m_t^2}+m_Z^2\left((1+c_v^2)m_Z^2-24m_t^2\right)\right], \tag{5.59}$$

$$\sigma_{t\bar{b}\to W^+S} \to \frac{\theta^2}{288\pi v^4 s}\left[3m_t^2(m_t^2+2m_W^2)\ln\frac{s}{m_t^2}+2m_W^2-12m_t^2m_W^2-3m_t^2\right]. \tag{5.60}$$

The cross sections for Compton-like scatterings are

$$\sigma_{th\to tS} \to \frac{\theta^2 y_t^4}{128\pi s}\left(2\ln\frac{s}{m_t^2}+5\right), \tag{5.61}$$

$$\sigma_{tZ\to tS} \to \frac{\theta^2 m_Z^2}{48\pi v^4}(1+c_v^2)+\mathcal{O}\left(\frac{1}{s}\right), \tag{5.62}$$

$$\sigma_{tW^-\to bS} \to \frac{\theta^2 m_W^2}{12\pi v^4}+\mathcal{O}\left(\frac{1}{s}\right), \tag{5.63}$$

$$\sigma_{bW^+\to tS} \to \frac{\theta^2 m_W^2}{12\pi v^4}+\mathcal{O}\left(\frac{1}{s}\right) \tag{5.64}$$

and the boson scattering cross sections are

$$\sigma_{Zh\to ZS} \to \frac{\theta^2 m_Z^2}{12\pi v^4} \qquad \sigma_{ZZ\to hS} \to \frac{\theta^2 m_Z^2}{36\pi v^4} \tag{5.65}$$

$$\sigma_{W^+W^-\to hS} \to \frac{\theta^2 m_W^2}{18\pi v^4} \qquad \sigma_{W^+W^-\to ZS} \to \frac{\theta^2 m_W^2\,(8m_W^2+m_Z^2)}{18\pi m_Z^2 v^4} \tag{5.66}$$

$$\sigma_{W^\pm h\to W^\pm S} \to \frac{\theta^2 m_W^2}{36\pi v^4} \qquad \sigma_{W^\pm Z\to W^\pm S} \to \frac{\theta^2(20m_W^4-3m_W^2m_Z^2+m_Z^4)}{36\pi m_Z^2 v^4} \tag{5.67}$$

$$\sigma_{hh\to hS} \to \frac{9\theta^2\lambda^2}{8\pi s}. \tag{5.68}$$

## 5.8 Supplementary: Strategy to numerical integration with quantum statistics

This strategy is based of Ref. [298] which reduced the collision integral in the context of neutrino decoupling from 9D to 2D retaining the quantum distributions of particles. Since they have a heavy mediator in all cases, they don't have angular dependencies in the propagator denominators and can get further than us analytically. Nevertheless, we have a strategy to reduce the number of integrals we need to numerically integrate.

We want to integrate

$$s\dot{Y} = \int \prod_{i=1}^{4} \left( \frac{d^3\mathrm{p}_i}{2E_i(2\pi)^3} \right) \Lambda(f_1, f_2, f_3, f_4) |\mathcal{M}|^2 (2\pi)^4 \delta^4(p_1 + p_2 - p_3 - p_4), \tag{5.69}$$

where $\Lambda$ represents the thermal distribution of each species and $|\mathcal{M}|^2$ is the spin-summed squared amplitude. Let's go in the frame where species 1 travels in the $\hat{x}$ direction. Then, in general, we can define the four-vectors

$$p_1 = (E_1, \mathrm{p}_1, 0, 0), \tag{5.70}$$

$$p_2 = (E_2, \mathrm{p}_2 \cos\alpha, \mathrm{p}_2 \sin\alpha \sin\beta, \mathrm{p}_2 \sin\alpha \cos\beta), \tag{5.71}$$

$$p_2 = (E_3, \mathrm{p}_3 \cos\theta, 0, \mathrm{p}_3 \sin\theta), \tag{5.72}$$

$$p_4 = p_1 + p_2 - p_3, \tag{5.73}$$

where $\mathrm{p_i} = |\vec{p}_i|$ and we defined the angle between $\vec{p}_1/\vec{p}_2$ as $\alpha$ and $\vec{p}_1/\vec{p}_3$ as $\theta$. Both $\vec{p}_2$ and $\vec{p}_3$ have an azimuthal angle with $\vec{p}_1$, but there is an overall $2\pi$ symmetry and only the difference between the 2 azimuthal angles matters. We used this symmetry to fix the $\vec{p}_3$ azimuthal angle $\mu$ to 0. Then we have

$$d^3\mathrm{p}_1 d^3\mathrm{p}_2 d^3\mathrm{p}_3 = \mathrm{p}_1 E_1 dE_1 d\Omega_1 \; \mathrm{p}_2 E_2 dE_2 d(\cos\alpha) d\beta \; \mathrm{p}_3 E_3 dE_3 \; d(\cos\theta) \; d\mu \tag{5.74}$$

and our overall integral reduces to

$$s\dot{Y} = \frac{2(2\pi)^2}{8(2\pi)^8} \int \prod_{i=1}^{3} (\mathrm{p}_i dE_i) \, \frac{d^3p_4}{2E_4} d(\cos\alpha) \; d\beta \; d(\cos\theta) \; \Lambda(f_1, f_2, f_3, f_4) |\mathcal{M}|^2 \delta^4(p_1 + p_2 - p_3 - p_4), \tag{5.75}$$

where we performed the trivial integrals over $\Omega_1$ and $\mu$. We can recall that the

3-dimensional integral $d^3\mathrm{p}_4$ came from

$$\frac{d^3\mathrm{p}_4}{2E_4} = d^4p_4\delta(p_4^2 - m_4^2)\Theta(p_4^0) \tag{5.76}$$

and we can use the 4-d dirac delta to evaluate $d^4p_4$

$$s\dot{Y} = \frac{1}{4(2\pi)^6}\int\prod_{i=1}^{3}(\mathrm{p}_i dE_i)\ \ d(\cos\alpha)\ d\beta\ d(\cos\theta)\ \Lambda(f_1,f_2,f_3,f_4)|\mathcal{M}|^2\delta(p_4^2 - m_4^2)\Theta(p_4^0), \tag{5.77}$$

which fixes $p_4^2 = p_1^2 + p_2^2 + p_3^2 + 2(p_1\cdot p_2 - p_1\cdot p_3 - p_2\cdot p_3)$ from now on. The dot products can be evaluated from our angle definitions

$$p_1\cdot p_2 = E_1E_2 - \mathrm{p}_1\mathrm{p}_2\cos\alpha, \qquad p_2\cdot p_3 = E_2E_3 - \mathrm{p}_2\mathrm{p}_3(\cos\alpha\cos\theta + \sin\alpha\sin\theta\cos\beta), \tag{5.78}$$

$$p_1\cdot p_3 = E_1E_3 - \mathrm{p}_1\mathrm{p}_3\cos\theta, \qquad p_2\cdot p_4 = m_2^3 + p_1\cdot p_2 - p_2\cdot p_3, \tag{5.79}$$

$$p_1\cdot p_4 = m_1^2 + p_1\cdot p_2 - p_1\cdot p_3, \qquad p_3\cdot p_4 = -m_3^3 + p_1\cdot p_3 + p_2\cdot p_3. \tag{5.80}$$

The inside of the last delta function can be expressed as a function of $\beta$

$$f(\beta) = p_4^2 - m_4^2 \tag{5.81}$$

$$= \omega + 2\left(\mathrm{p}_2\mathrm{p}_3\cos\alpha\cos\theta + \mathrm{p}_2\mathrm{p}_3\sin\alpha\sin\theta\cos\beta - \mathrm{p}_1\mathrm{p}_2\cos\alpha\right) \tag{5.82}$$

$$\omega = Q + 2\left(E_1E_2 - E_1E_3 - E_2E_3 + \mathrm{p}_1\mathrm{p}_3\cos\theta\right) \tag{5.83}$$

$$Q = m_1^2 + m_2^2 + m_3^2 - m_4^2 \tag{5.84}$$

$$f'(\beta) = -2\mathrm{p}_2\mathrm{p}_3\sin\alpha\sin\theta\sin\beta. \tag{5.85}$$

The $\beta$ integral can evaluated, forcing $\beta\to\beta_0$, where

$$\cos\beta_0 = -\frac{\omega + 2\left(\mathrm{p}_2\mathrm{p}_3\cos\alpha\cos\theta - \mathrm{p}_1\mathrm{p}_2\cos\alpha\right)}{2\mathrm{p}_2\mathrm{p}_3\sin\alpha\sin\theta} \tag{5.86}$$

is found by solving $f(\beta_0) = 0$. There are actually 2 $\beta_0$ solutions given by $\sin\beta_0 = \pm\sqrt{1-\cos^2\beta_0}$. Since everything is symmetric in $\beta$ (all dot products are $\cos\beta$-dependent and the $\partial f/\partial\beta$ that appears in the dominator is in absolute values), we

can simply use the positive root and multiply by 2. Hence, we get

$$s\dot{Y} = \frac{1}{2(2\pi)^6}\int \prod_{i=1}^{3} (\mathrm{p}_i dE_i)\ d(\cos\alpha)\, d(\cos\theta)\, \Lambda(f_1, f_2, f_3, f_4) \times \tag{5.87}$$

$$\times\ \frac{|\mathcal{M}|^2 \Theta(p_4^0)\Theta(4\mathrm{p}_2^2\mathrm{p}_3^2 \sin^2\alpha \sin^2\theta \sin^2\beta_0)}{2\mathrm{p}_2\mathrm{p}_3 \sin\alpha \sin\theta \sin\beta_0}. \tag{5.88}$$

The extra step-function arises as an obligation to maintain $\beta_0$ in the physical phase-space

$$\cos^2\beta_0 \leq 0 \quad \leftrightarrow \quad (2\mathrm{p}_2\mathrm{p}_3 \sin\alpha \sin\theta \sin\beta_0)^2 \geq 0 \quad \leftrightarrow \quad \left|\frac{\partial f}{\partial \beta_0}\right|^2 \geq 0. \tag{5.89}$$

We can now focus on the angular integrations.

$$s\dot{Y} = \frac{1}{2(2\pi)^6}\int dE_1 dE_2 dE_3\ \mathrm{p}_1\mathrm{p}_2\mathrm{p}_3 \Lambda(f_1, f_2, f_3, f_4) \times \mathcal{I} \tag{5.90}$$

$$\mathcal{I} = \int d(\cos\theta) d(\cos\alpha)\ \frac{|\mathcal{M}|^2 \Theta(p_4^0)\Theta\left(\left|\frac{\partial f}{\partial \beta_0}\right|^2\right)}{\left|\frac{\partial f}{\partial \beta_0}\right|}. \tag{5.91}$$

We can expand $f'$ as

$$\left|\frac{\partial f}{\partial \beta_0}\right|^2 = a\cos^2\alpha + b\cos\alpha + c \tag{5.92}$$

$$a = -4\mathrm{p}_2^2\left(\mathrm{p}_1^2 + \mathrm{p}_3^2 - 2\mathrm{p}_1\mathrm{p}_3\cos\theta\right) \tag{5.93}$$

$$b = 4\mathrm{p}_2\left(\mathrm{p}_1 - \mathrm{p}_3\cos\theta\right)\omega \tag{5.94}$$

$$c = 4\mathrm{p}_2^2\mathrm{p}_3^2\sin^2\theta - \omega^2. \tag{5.95}$$

The step-function ensures that the denominator is real

$$\mathcal{I} = \int d(\cos\theta) \int_{\cos\alpha_-}^{\cos\alpha_+} d(\cos\alpha)\ \frac{|\mathcal{M}|^2 \Theta(p_4^0)\Theta\left(a\cos^2\alpha + b\cos\alpha + c\right)}{\sqrt{a\cos^2\alpha + b\cos\alpha + c}}. \tag{5.96}$$

Since $|\mathcal{M}|^2$ only consists of simple functions of $\cos\alpha$, the $\cos\alpha$ integration is an analytic solution, although process dependent. Since $a \leq 0$, the integration bounds

are set by the real-valued criterion, between which the quadratic function is positive

$$\cos\alpha_- = \frac{-b+\sqrt{b^2-4ac}}{2a}, \qquad \cos\alpha_+ = \frac{-b-\sqrt{b^2-4ac}}{2a}. \tag{5.97}$$

Notice that we always have $-1 \leq \cos\alpha_-$ and $\cos\alpha_+ \leq 1$. Finally, the $\theta$ integral can be performed. In a similar fashion, requiring $\cos\alpha_\pm$ to be real implies the condition

$$b^2-4ac \geq 0 \quad \rightarrow \quad \cos\theta_\pm = -\frac{Q+2\mathrm{p}_2^2+2\gamma \mp 2\mathrm{p}_2\sqrt{Q+\mathrm{p}_1^2+\mathrm{p}_2^2+\mathrm{p}_3^2+2\gamma}}{2\mathrm{p}_1\mathrm{p}_3}, \tag{5.98}$$

where we use the shorthand $\gamma = E_1E_2 - E_1E_3 - E_2E_3$ and we have

$$\mathcal{I} = \int_{\max(-1,\cos\theta_-)}^{\min(1,\cos\theta_+)} d(\cos\theta) \int_{\cos\alpha_-}^{\cos\alpha_+} d(\cos\alpha)\, \frac{|\mathcal{M}|^2\Theta(p_4^0)\Theta\left(a\cos^2\alpha+b\cos\alpha+c\right)}{\sqrt{a\cos^2\alpha+b\cos\alpha+c}}. \tag{5.99}$$

These 2 integrals can be done analytically for each reaction. The final integral to be performed numerically for the emissivity is 3-dimensional

$$s\dot{Y} = \frac{1}{2(2\pi)^6}\int dE_1dE_2dE_3\ \mathrm{p}_1\mathrm{p}_2\mathrm{p}_3\Lambda(f_1,f_2,f_3,f_4)\times\mathcal{I}\times\Theta(Q+\mathrm{p}_1^2+\mathrm{p}_2^2+\mathrm{p}_3^2+2\gamma) \tag{5.100}$$

$$\mathcal{I} = \int_{\max(-1,\cos\theta_-)}^{\min(1,\cos\theta_+)} d(\cos\theta) \int_{\cos\alpha_-}^{\cos\alpha_+} d(\cos\alpha)\, \frac{|\mathcal{M}|^2}{\sqrt{a\cos^2\alpha+b\cos\alpha+c}}. \tag{5.101}$$

The step-function here guarantees that the phase-space is physical and $\cos\alpha_\pm$ is real-valued.

# Chapter 6

# Conclusion

The ensemble of work presented in this dissertation used the complementarity of cosmology and standard particle physics experiments to further the search for NP interactions. It is quite fortuitous that the thermal history of the universe provides exactly what is lacking in terrestrial experiments to increase sensitivity to low couplings. The limited energy and luminosity available in colliders restricts the production of either massive states or super-weakly coupled particles. The conditions after the Big Bang circumvent both of these limitations; the high temperature provides the energy required for the rest mass of heavy particles and the high density guarantees a large number of collisions to produce super-weakly coupled particles. Long-lived particles require large-scale detectors with long decay chambers, typically distanced by $L = c\tau_X\beta_X$, which need to be prohibitively large for lifetimes $\tau_X \gtrsim 0.1$ s. The physics at BBN and the CMB emission provide natural detectors beyond this limit, offering sensitivity to the $\tau_X \sim 0.1\ \mathrm{s} - 10^8$ yr range. We have used these generic points to constrain both the dark photon and the Higgs portal scalar in regions of parameter space that would otherwise be unattainable by direct searches.

The cosmological constraints also provide a target maximal sensitivity needed to cover the parameter space. We could naively think that experimental technology will arbitrarily improve and after generations of new experiments the sensitivity would reach lower values of coupling for NP. We have seen that BBN defines the maximal lifetime needed to be probed to fully cover the parameter space of metastable particles populated through the Higgs boson decay. We derived specific constraints for the Higgs scalar portal, but they generally apply to a large class of models. This will be useful in the design of future experiments at the LHC.

Finally, we used a specific case of feeble coupling with the SM to study a model

of self-interacting dark matter that is not viable in the standard freeze-out scenario. Although it was already known that future direct detection experiments will partially probe the parameter space, we demonstrated which regions in $m_\chi - m_{A'}$ specific experiments will be sensitive to. In particular, we have shown that they will cover the entire range of interest to resolve tensions in small scale DM physics for $\alpha_d = 10^{-4}$.

With the advent of new experiments turning on, the absence of NP signals keeps restricting the properties of potential candidates for NP. The complexity of NP solutions to current problems (such as the origin of DM for *e.g.*) consistently increases with the addition of constraints from the continuous experimental effort. Luckily, this provides a balance between target goals for experimentalists and theoretical understanding for theorists and phenomenologists. It will always be possible that NP exists beyond our reach; we can only hope that Nature has new particles and forces that will one day be within our experimental grasp.

# Appendix A

# Relativistic degrees of freedom

Our evaluation of the number of relativistic degrees of freedom needed in the Hubble rate and entropy density follows the technique used in [299], updated with more recent theoretical QCD results.

The BMW lattice QCD group [300] provides a fitting function for the trace anomaly, from which we can extract the energy and entropy density. Their function incorporates the hadron resonance gas model below the pseudo-critical temperature $T_c$ and $n_f = 2 + 1$ lattice results up to 1000 MeV. At higher temperatures, we used the $n_f = 3$ three-loop result from hard-thermal-loop perturbation theory [301] with renormalization scale $\Lambda = 2\pi T$. The heavier quarks are modelled as an ideal gas, scaled by the ratio of the energy density of $n_f = 3$ QCD to the ideal gas value at the given temperature. This approximation has been used in [299] and is shown to be in good agreement with preliminary lattice results for $n_f = 2 + 1 + 1$ [302]. The resulting $g_\star(T)$ is shown in Fig. A.1.

The QCD phase transition is a cross-over [303], with a pseudo-critical temperature $T_c$ in the range of 150-170 MeV. For a given observable, $T_c$ is well-defined as the temperature of the maximal inflection point. In the present work, we used $T_c = 157$ MeV, the pseudo-critical temperature of the energy density [21].

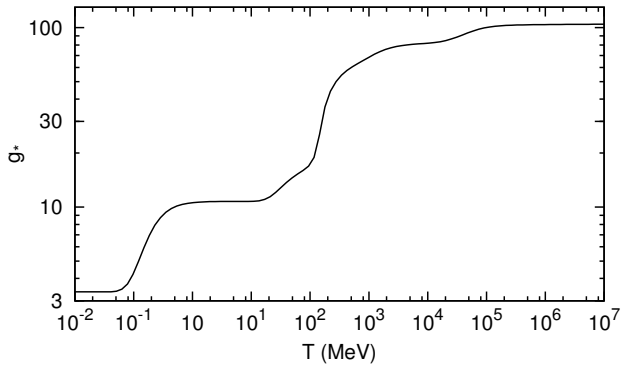


Figure A.1: Relativistic degrees of freedom as a function of temperature.

# Bibliography

[1] David Griffiths. *Introduction to elementary particles*. 2008.

[2] Georges Aad et al. Observation of a new particle in the search for the Standard Model Higgs boson with the ATLAS detector at the LHC. *Phys. Lett.*, B716:1–29, 2012.

[3] Serguei Chatrchyan et al. Observation of a new boson at a mass of 125 GeV with the CMS experiment at the LHC. *Phys. Lett.*, B716:30–61, 2012.

[4] Alessandro Strumia and Francesco Vissani. Neutrino masses and mixings and... 2006.

[5] James P. Miller, Eduardo de Rafael, B. Lee Roberts, and Dominik Stckinger. Muon (g-2): Experiment and Theory. *Ann. Rev. Nucl. Part. Sci.*, 62:237–264, 2012.

[6] Randolf Pohl, Ronald Gilman, Gerald A. Miller, and Krzysztof Pachucki. Muonic hydrogen and the proton radius puzzle. *Ann. Rev. Nucl. Part. Sci.*, 63:175–204, 2013.

[7] P. A. R. Ade et al. Planck 2015 results. XIII. Cosmological parameters. *Astron. Astrophys.*, 594:A13, 2016.

[8] James M. Cline. Baryogenesis. In *Les Houches Summer School - Session 86: Particle Physics and Cosmology: The Fabric of Spacetime Les Houches, France, July 31-August 25, 2006*, 2006.

[9] Gianfranco Bertone, Dan Hooper, and Joseph Silk. Particle dark matter: Evidence, candidates and constraints. *Phys. Rept.*, 405:279–390, 2005.

[10] K. G. Begeman, A. H. Broeils, and R. H. Sanders. Extended rotation curves of spiral galaxies: Dark haloes and modified dynamics. *Mon. Not. Roy. Astron. Soc.*, 249:523, 1991.

[11] Julio F. Navarro, Carlos S. Frenk, and Simon D. M. White. The Structure of cold dark matter halos. *Astrophys. J.*, 462:563–575, 1996.

[12] Maxim Pospelov and Josef Pradler. Big Bang Nucleosynthesis as a Probe of New Physics. *Ann. Rev. Nucl. Part. Sci.*, 60:539–568, 2010.

[13] Sunny Vagnozzi, Elena Giusarma, Olga Mena, Katherine Freese, Martina Gerbino, Shirley Ho, and Massimiliano Lattanzi. Unveiling $\nu$ secrets with cosmological data: neutrino masses and mass hierarchy. 2017.

[14] Patrick Peter and Jean-Philippe Uzan. *Primordial cosmology*. Oxford Graduate Texts. Oxford Univ. Press, Oxford, 2009.

[15] Nicols Bernal, Matti Heikinheimo, Tommi Tenkanen, Kimmo Tuominen, and Ville Vaskonen. The Dawn of FIMP Dark Matter: A Review of Models and Constraints. *Int. J. Mod. Phys.*, A32(27):1730023, 2017.

[16] Xiaoyong Chu, Thomas Hambye, and Michel H. G. Tytgat. The Four Basic Ways of Creating Dark Matter Through a Portal. *JCAP*, 1205:034, 2012.

[17] P. A. R. Ade et al. Detection of $B$-Mode Polarization at Degree Angular Scales by BICEP2. *Phys. Rev. Lett.*, 112(24):241101, 2014.

[18] P. A. R. Ade et al. Joint Analysis of BICEP2/$Keck?Array$ and *Planck* Data. *Phys. Rev. Lett.*, 114:101301, 2015.

[19] David J. Gross and Frank Wilczek. Ultraviolet Behavior of Nonabelian Gauge Theories. *Phys. Rev. Lett.*, 30:1343–1346, 1973.

[20] H. David Politzer. Reliable Perturbative Results for Strong Interactions? *Phys. Rev. Lett.*, 30:1346–1349, 1973.

[21] Szabolcs Borsanyi, Zoltan Fodor, Christian Hoelbling, Sandor D Katz, Stefan Krieg, Claudia Ratti, and Kalman K. Szabo. Is there still any $T_c$ mystery in lattice QCD? Results with physical masses in the continuum limit III. *JHEP*, 09:073, 2010.

[22] Brian D. Fields. The primordial lithium problem. *Ann. Rev. Nucl. Part. Sci.*, 61:47–68, 2011.

[23] Richard H. Cyburt, Brian D. Fields, and Keith A. Olive. An Update on the big bang nucleosynthesis prediction for Li-7: The problem worsens. *JCAP*, 0811:012, 2008.

[24] G. Hinshaw et al. Nine-Year Wilkinson Microwave Anisotropy Probe (WMAP) Observations: Cosmological Parameter Results. *Astrophys. J. Suppl.*, 208:19, 2013.

[25] P. A. R. Ade et al. Planck 2013 results. XVI. Cosmological parameters. *Astron. Astrophys.*, 571:A16, 2014.

[26] Scott Dodelson. *Modern Cosmology.* Academic Press, Amsterdam, 2003.

[27] P. J. E. Peebles. Recombination of the Primeval Plasma. *Astrophys. J.*, 153:1, 1968.

[28] Chung-Pei Ma and Edmund Bertschinger. Cosmological perturbation theory in the synchronous and conformal Newtonian gauges. *Astrophys. J.*, 455:7–25, 1995.

[29] Sara Seager, Dimitar D. Sasselov, and Douglas Scott. A new calculation of the recombination epoch. *Astrophys. J.*, 523:L1–L5, 1999.

[30] C. L. Bennett et al. Nine-Year Wilkinson Microwave Anisotropy Probe (WMAP) Observations: Final Maps and Results. *Astrophys. J. Suppl.*, 208:20, 2013.

[31] P. Cushman et al. Working Group Report: WIMP Dark Matter Direct Detection. In *Proceedings, 2013 Community Summer Study on the Future of U.S. Particle Physics: Snowmass on the Mississippi (CSS2013): Minneapolis, MN, USA, July 29-August 6, 2013*, 2013.

[32] E. Aprile et al. Dark Matter Results from 225 Live Days of XENON100 Data. *Phys. Rev. Lett.*, 109:181301, 2012.

[33] D. S. Akerib et al. First results from the LUX dark matter experiment at the Sanford Underground Research Facility. *Phys. Rev. Lett.*, 112:091303, 2014.

[34] Andi Tan et al. Dark Matter Results from First 98.7 Days of Data from the PandaX-II Experiment. *Phys. Rev. Lett.*, 117(12):121303, 2016.

[35] Oscar Adriani et al. An anomalous positron abundance in cosmic rays with energies 1.5-100 GeV. *Nature*, 458:607–609, 2009.

[36] M. Ackermann et al. Measurement of separate cosmic-ray electron and positron spectra with the Fermi Large Area Telescope. *Phys. Rev. Lett.*, 108:011103, 2012.

[37] M. Aguilar et al. First Result from the Alpha Magnetic Spectrometer on the International Space Station: Precision Measurement of the Positron Fraction in Primary Cosmic Rays of 0.5?350 GeV. *Phys. Rev. Lett.*, 110:141102, 2013.

[38] Esra Bulbul, Maxim Markevitch, Adam Foster, Randall K. Smith, Michael Loewenstein, and Scott W. Randall. Detection of An Unidentified Emission Line in the Stacked X-ray spectrum of Galaxy Clusters. *Astrophys. J.*, 789:13, 2014.

[39] Alexey Boyarsky, Oleg Ruchayskiy, Dmytro Iakubovskyi, and Jeroen Franse. Unidentified Line in X-Ray Spectra of the Andromeda Galaxy and Perseus Galaxy Cluster. *Phys. Rev. Lett.*, 113:251301, 2014.

[40] Sean Tulin and Hai-Bo Yu. Dark Matter Self-interactions and Small Scale Structure. 2017.

[41] M. Passera, W. J. Marciano, and A. Sirlin. The muon g-2 discrepancy: Errors or new physics? *AIP Conf. Proc.*, 1078:378–381, 2009.

[42] Maxim Pospelov. Secluded U(1) below the weak scale. *Phys. Rev.*, D80:095002, 2009.

[43] Rouven Essig et al. Working Group Report: New Light Weakly Coupled Particles. In *Proceedings, 2013 Community Summer Study on the Future of U.S. Particle Physics: Snowmass on the Mississippi (CSS2013): Minneapolis, MN, USA, July 29-August 6, 2013*, 2013.

[44] Brian Batell, Maxim Pospelov, and Adam Ritz. Multi-lepton Signatures of a Hidden Sector in Rare B Decays. *Phys. Rev.*, D83:054005, 2011.

[45] John McDonald. Gauge singlet scalars as cold dark matter. *Phys. Rev.*, D50:3637–3649, 1994.

[46] C. P. Burgess, Maxim Pospelov, and Tonnis ter Veldhuis. The Minimal model of nonbaryonic dark matter: A Singlet scalar. *Nucl. Phys.*, B619:709–728, 2001.

[47] Sergey Alekhin et al. A facility to Search for Hidden Particles at the CERN SPS: the SHiP physics case. *Rept. Prog. Phys.*, 79(12):124201, 2016.

[48] C. Patrignani et al. Review of Particle Physics. *Chin. Phys.*, C40(10):100001, 2016.

[49] Paola Arias, Davide Cadamuro, Mark Goodsell, Joerg Jaeckel, Javier Redondo, and Andreas Ringwald. WISPy Cold Dark Matter. *JCAP*, 1206:013, 2012.

[50] K. N. Abazajian et al. Light Sterile Neutrinos: A White Paper. 2012.

[51] Emmanuel Paschos. Open Issues in Neutrino Reactions. *PoS*, CORFU2016:043, 2017.

[52] Michael Klasen, Martin Pohl, and Gnter Sigl. Indirect and direct search for dark matter. *Prog. Part. Nucl. Phys.*, 85:1–32, 2015.

[53] Teresa Marrodn Undagoitia and Ludwig Rauch. Dark matter direct-detection experiments. *J. Phys.*, G43(1):013001, 2016.

[54] Xiangyi Cui et al. Dark Matter Results From 54-Ton-Day Exposure of PandaX-II Experiment. 2017.

[55] E. Aprile et al. First Dark Matter Search Results from the XENON1T Experiment. 2017.

[56] D. C. Malling et al. After LUX: The LZ Program. 2011.

[57] Jianglai Liu, Xun Chen, and Xiangdong Ji. Current status of direct dark matter detection experiments. *Nature Phys.*, 13(3):212–216, 2017.

[58] E. Aprile et al. Physics reach of the XENON1T dark matter experiment. *JCAP*, 1604(04):027, 2016.

[59] Tracy R. Slatyer. TASI Lectures on Indirect Detection of Dark Matter. In *Theoretical Advanced Study Institute in Elementary Particle Physics: Anticipating the Next Discoveries in Particle Physics (TASI 2016) Boulder, CO, USA, June 6-July 1, 2016*, 2017.

[60] M. Ackermann et al. Searching for Dark Matter Annihilation from Milky Way Dwarf Spheroidal Galaxies with Six Years of Fermi Large Area Telescope Data. *Phys. Rev. Lett.*, 115(23):231301, 2015.

[61] Lars Bergstrom, Torsten Bringmann, Ilias Cholis, Dan Hooper, and Christoph Weniger. New limits on dark matter annihilation from AMS cosmic ray positron data. *Phys. Rev. Lett.*, 111:171101, 2013.

[62] Galle Giesen, Mathieu Boudaud, Yoann Gnolini, Vivian Poulin, Marco Cirelli, Pierre Salati, and Pasquale D. Serpico. AMS-02 antiprotons, at last! Secondary astrophysical component and immediate implications for Dark Matter. *JCAP*, 1509(09):023, 2015.

[63] Lisa Goodenough and Dan Hooper. Possible Evidence For Dark Matter Annihilation In The Inner Milky Way From The Fermi Gamma Ray Space Telescope. 2009.

[64] Dan Hooper and Lisa Goodenough. Dark Matter Annihilation in The Galactic Center As Seen by the Fermi Gamma Ray Space Telescope. *Phys. Lett.*, B697:412–428, 2011.

[65] Kevork N. Abazajian. Sterile neutrinos in cosmology. 2017.

[66] Tesla E. Jeltema and Stefano Profumo. Discovery of a 3.5 keV line in the Galactic Centre and a critical look at the origin of the line across astronomical targets. *Mon. Not. Roy. Astron. Soc.*, 450(2):2143–2152, 2015.

[67] Vardan Khachatryan et al. Search for long-lived particles that decay into final states containing two electrons or two muons in proton-proton collisions at $\sqrt{s} =$ 8 TeV. *Phys. Rev.*, D91(5):052012, 2015.

[68] Georges Aad et al. Search for massive, long-lived particles using multitrack displaced vertices or displaced lepton pairs in pp collisions at $\sqrt{s} = 8$ TeV with the ATLAS detector. *Phys. Rev.*, D92(7):072004, 2015.

[69] Maxim Pospelov and Josef Pradler. Metastable GeV-scale particles as a solution to the cosmological lithium problem. *Phys. Rev.*, D82:103514, 2010.

[70] Le Zhang, Xuelei Chen, Marc Kamionkowski, Zong-guo Si, and Zheng Zheng. Constraints on radiative dark-matter decay from the cosmic microwave background. *Phys. Rev.*, D76:061301, 2007.

[71] Xue-Lei Chen and Marc Kamionkowski. Particle decays during the cosmic dark ages. *Phys. Rev.*, D70:043502, 2004.

[72] Tracy R. Slatyer and Chih-Liang Wu. General Constraints on Dark Matter Decay from the Cosmic Microwave Background. *Phys. Rev.*, D95(2):023010, 2017.

[73] Tracy R. Slatyer. Indirect Dark Matter Signatures in the Cosmic Dark Ages II. Ionization, Heating and Photon Production from Arbitrary Energy Injections. *Phys. Rev.*, D93(2):023521, 2016.

[74] Anthony Fradette, Maxim Pospelov, Josef Pradler, and Adam Ritz. Cosmological Constraints on Very Dark Photons. *Phys. Rev.*, D90(3):035022, 2014.

[75] Torsten Bringmann, Felix Kahlhoefer, Kai Schmidt-Hoberg, and Parampreet Walia. Strong constraints on self-interacting dark matter with light mediators. *Phys. Rev. Lett.*, 118(14):141802, 2017.

[76] Anthony Fradette and Maxim Pospelov. BBN for the LHC: constraints on lifetimes of the Higgs portal scalars. *Phys. Rev.*, D96(7):075033, 2017.

[77] Bob Holdom. Two U(1)'s and Epsilon Charge Shifts. *Phys. Lett.*, 166B:196–198, 1986.

[78] Javier Redondo and Marieke Postma. Massive hidden photons as lukewarm dark matter. *JCAP*, 0902:005, 2009.

[79] Haipeng An, Maxim Pospelov, and Josef Pradler. New stellar constraints on dark photons. *Phys. Lett.*, B725:190–195, 2013.

[80] Haipeng An, Maxim Pospelov, and Josef Pradler. Dark Matter Detectors as Dark Photon Helioscopes. *Phys. Rev. Lett.*, 111:041302, 2013.

[81] Javier Redondo and Georg Raffelt. Solar constraints on hidden photons revisited. *JCAP*, 1308:034, 2013.

[82] James D. Bjorken, Rouven Essig, Philip Schuster, and Natalia Toro. New Fixed-Target Experiments to Search for Dark Gauge Forces. *Phys. Rev.*, D80:075018, 2009.

[83] Hooman Davoudiasl, Hye-Sung Lee, and William J. Marciano. Dark Side of Higgs Diphoton Decays and Muon g-2. *Phys. Rev.*, D86:095009, 2012.

[84] Motoi Endo, Koichi Hamaguchi, and Go Mishima. Constraints on Hidden Photon Models from Electron g-2 and Hydrogen Spectroscopy. *Phys. Rev.*, D86:095029, 2012.

[85] D. Babusci et al. Limit on the production of a light vector gauge boson in phi meson decays with the KLOE detector. *Phys. Lett.*, B720:111–115, 2013.

[86] F. Archilli et al. Search for a vector gauge boson in $\phi$ meson decays with the KLOE detector. *Phys. Lett.*, B706:251–255, 2012.

[87] P. Adlarson et al. Search for a dark photon in the $\pi^0 \to e^+e^-\gamma$ decay. *Phys. Lett.*, B726:187–193, 2013.

[88] S. Abrahamyan et al. Search for a New Gauge Boson in Electron-Nucleus Fixed-Target Scattering by the APEX Experiment. *Phys. Rev. Lett.*, 107:191804, 2011.

[89] H. Merkel et al. Search for Light Gauge Bosons of the Dark Sector at the Mainz Microtron. *Phys. Rev. Lett.*, 106:251802, 2011.

[90] Matthew Reece and Lian-Tao Wang. Searching for the light dark gauge boson in GeV-scale experiments. *JHEP*, 07:051, 2009.

[91] James B. Dent, Francesc Ferrer, and Lawrence M. Krauss. Constraints on Light Hidden Sector Gauge Bosons from Supernova Cooling. 2012.

[92] Herbert K. Dreiner, Jean-Franois Fortin, Christoph Hanhart, and Lorenzo Ubaldi. Supernova constraints on MeV dark sectors from $e^+e^-$ annihilations. *Phys. Rev.*, D89(10):105015, 2014.

[93] Johannes Blumlein and Jurgen Brunner. New Exclusion Limits for Dark Gauge Forces from Beam-Dump Data. *Phys. Lett.*, B701:155–159, 2011.

[94] Rouven Essig, Roni Harnik, Jared Kaplan, and Natalia Toro. Discovering New Light States at Neutrino Experiments. *Phys. Rev.*, D82:113008, 2010.

[95] Brian Batell, Maxim Pospelov, and Adam Ritz. Exploring Portals to a Hidden Sector Through Fixed Targets. *Phys. Rev.*, D80:095024, 2009.

[96] S. N. Gninenko. Stringent limits on the $\pi^0 -> \gamma X, X -> e + e-$ decay from neutrino experiments and constraints on new light gauge bosons. *Phys. Rev.*, D85:055027, 2012.

[97] S. N. Gninenko. Constraints on sub-GeV hidden sector gauge bosons from a search for heavy neutrino decays. *Phys. Lett.*, B713:244–248, 2012.

[98] J. P. Lees et al. Search for a Dark Photon in $e^+e^-$ Collisions at BaBar. *Phys. Rev. Lett.*, 113(20):201801, 2014.

[99] D. Babusci et al. Search for light vector boson production in $e^+e^- \to \mu^+\mu^-\gamma$ interactions with the KLOE experiment. *Phys. Lett.*, B736:459–464, 2014.

[100] H. Merkel et al. Search at the Mainz Microtron for Light Massive Gauge Bosons Relevant for the Muon g-2 Anomaly. *Phys. Rev. Lett.*, 112(22):221802, 2014.

[101] Johannes Blmlein and Jrgen Brunner. New Exclusion Limits on Dark Gauge Forces from Proton Bremsstrahlung in Beam-Dump Data. *Phys. Lett.*, B731:320–326, 2014.

[102] Joshua Berger, Karsten Jedamzik, and Devin G. E. Walker. Cosmological Constraints on Decoupled Dark Photons and Dark Higgs. *JCAP*, 1611:032, 2016.

[103] Max Pettini and Ryan Cooke. A new, precise measurement of the primordial abundance of Deuterium. *Mon. Not. Roy. Astron. Soc.*, 425:2477–2486, 2012.

[104] Ryan Cooke, Max Pettini, Regina A. Jorgenson, Michael T. Murphy, and Charles C. Steidel. Precision measures of the primordial abundance of deuterium. *Astrophys. J.*, 781(1):31, 2014.

[105] Scott Burles and David Tytler. The Deuterium abundance toward QSO 1009+2956. *Astrophys. J.*, 507:732–744, 1998.

[106] David Kirkman, David Tytler, Nao Suzuki, John M. O'Meara, and Dan Lubin. The Cosmological baryon density from the deuterium to hydrogen ratio towards QSO absorption systems: D/H towards Q1243+3047. *Astrophys. J. Suppl.*, 149:1, 2003.

[107] N. Prantzos, E. Vangioni-Flam, and M. Casse, editors. *Origin and evolution of the elements*, January 1993.

[108] Y. I. Izotov and T. X. Thuan. The primordial abundance of 4He: evidence for non-standard big bang nucleosynthesis. *Astrophys. J.*, 710:L67–L71, 2010.

[109] Erik Aver, Keith A. Olive, R. L. Porter, and Evan D. Skillman. The primordial helium abundance from updated emissivities. *JCAP*, 1311:017, 2013.

[110] F. Spite and M. Spite. Abundance of lithium in unevolved halo stars and old disk stars: Interpretation and consequences. *Astron. Astrophys.*, 115:357–366, 1982.

[111] Diego Blas, Julien Lesgourgues, and Thomas Tram. The Cosmic Linear Anisotropy Solving System (CLASS) II: Approximation schemes. *JCAP*, 1107:034, 2011.

[112] Benjamin Audren, Julien Lesgourgues, Karim Benabed, and Simon Prunet. Conservative Constraints on Early Cosmology: an illustration of the Monte Python cosmological parameter inference code. *JCAP*, 1302:001, 2013.

[113] P. A. R. Ade et al. Planck 2013 results. XV. CMB power spectra and likelihood. *Astron. Astrophys.*, 571:A15, 2014.

[114] E. Komatsu et al. Seven-Year Wilkinson Microwave Anisotropy Probe (WMAP) Observations: Cosmological Interpretation. *Astrophys. J. Suppl.*, 192:18, 2011.

[115] R. Keisler et al. A Measurement of the Damping Tail of the Cosmic Microwave Background Power Spectrum with the South Pole Telescope. *Astrophys. J.*, 743:28, 2011.

[116] Nikhil Padmanabhan and Douglas P. Finkbeiner. Detecting dark matter annihilation with CMB polarization: Signatures and experimental prospects. *Phys. Rev.*, D72:023508, 2005.

[117] Tracy R. Slatyer, Nikhil Padmanabhan, and Douglas P. Finkbeiner. CMB Constraints on WIMP Annihilation: Energy Absorption During the Recombination Epoch. *Phys. Rev.*, D80:043526, 2009.

[118] Tracy R. Slatyer. Energy Injection And Absorption In The Cosmic Dark Ages. *Phys. Rev.*, D87(12):123513, 2013.

[119] James M. Cline and Pat Scott. Dark Matter CMB Constraints and Likelihoods for Poor Particle Physicists. *JCAP*, 1303:044, 2013. [Erratum: JCAP1305,E01(2013)].

[120] Brian Batell, Maxim Pospelov, and Adam Ritz. Probing a Secluded U(1) at B-factories. *Phys. Rev.*, D79:115008, 2009.

[121] Maxim Pospelov, Adam Ritz, and Mikhail B. Voloshin. Bosonic super-WIMPs as keV-scale dark matter. *Phys. Rev.*, D78:115012, 2008.

[122] E. Aprile et al. Study of the electromagnetic background in the XENON100 experiment. *Phys. Rev.*, D83:082001, 2011. [Erratum: Phys. Rev.D85,029904(2012)].

[123] K. Arisaka, P. Beltrame, C. Ghag, J. Kaidi, K. Lung, A. Lyashenko, R. D. Peccei, P. Smith, and K. Ye. Expected Sensitivity to Galactic/Solar Axions and Bosonic Super-WIMPs based on the Axio-electric Effect in Liquid Xenon Dark Matter Detectors. *Astropart. Phys.*, 44:59–67, 2013.

[124] K. Abe et al. Search for bosonic superweakly interacting massive dark matter particles with the XMASS-I detector. *Phys. Rev. Lett.*, 113:121301, 2014.

[125] Alejandro Ibarra, David Tran, and Christoph Weniger. Indirect Searches for Decaying Dark Matter. *Int. J. Mod. Phys.*, A28:1330040, 2013.

[126] Arman Esmaili, Alejandro Ibarra, and Orlando L. G. Peres. Probing the stability of superheavy dark matter particles with high-energy neutrinos. *JCAP*, 1211:034, 2012.

[127] Kohta Murase and John F. Beacom. Constraining Very Heavy Dark Matter Using Diffuse Backgrounds of Neutrinos and Cascaded Gamma Rays. *JCAP*, 1210:043, 2012.

[128] Eric Braaten and Daniel Segel. Neutrino energy loss from the plasma process at all temperatures and densities. *Phys. Rev.*, D48:1478–1491, 1993.

[129] H. Arthur Weldon. Simple Rules for Discontinuities in Finite Temperature Field Theory. *Phys. Rev.*, D28:2007, 1983.

[130] J. P. Lees et al. Precise Measurement of the $e^+e^- \to \pi^+\pi^-(\gamma)$ Cross Section with the Initial-State Radiation Method at BABAR. *Phys. Rev.*, D86:032013, 2012.

[131] J. P. Lees et al. Precision measurement of the $e^+e^-?K^+K^-(?)$ cross section with the initial-state radiation method at BABAR. *Phys. Rev.*, D88(3):032013, 2013.

[132] J. I. Kapusta and Charles Gale. *Finite-temperature field theory: Principles and applications*. Cambridge University Press, 2011.

[133] Vyacheslav S. Rychkov and Alessandro Strumia. Thermal production of gravitinos. *Phys. Rev.*, D75:075011, 2007.

[134] Lawrence Kawano. Let's go: Early universe. 2. Primordial nucleosynthesis: The Computer way. 1992.

[135] Richard H. Cyburt, John R. Ellis, Brian D. Fields, and Keith A. Olive. Updated nucleosynthesis constraints on unstable relic particles. *Phys. Rev.*, D67:103521, 2003.

[136] A. Antonelli et al. The first measurement of the neutron electromagnetic formfactors in the timelike region. *Nucl. Phys.*, B517:3–35, 1998.

[137] Earle L. Lomon and Simone Pacetti. Time-like and space-like electromagnetic form factors of nucleons, a unified description. *Phys. Rev.*, D85:113004, 2012. [Erratum: Phys. Rev.D86,039901(2012)].

[138] Gianfranco Bertone and Dan Hooper. A History of Dark Matter. *Submitted to: Rev. Mod. Phys.*, 2016.

[139] Jrg Diemand, Marcel Zemp, Ben Moore, Joachim Stadel, and Marcella Carollo. Cusps in cold dark matter haloes. *Mon. Not. Roy. Astron. Soc.*, 364:665, 2005.

[140] Anatoly A. Klypin, Andrey V. Kravtsov, Octavio Valenzuela, and Francisco Prada. Where are the missing Galactic satellites? *Astrophys. J.*, 522:82–92, 1999.

[141] Michael Boylan-Kolchin, James S. Bullock, and Manoj Kaplinghat. Too big to fail? The puzzling darkness of massive Milky Way subhaloes. *Mon. Not. Roy. Astron. Soc.*, 415:L40, 2011.

[142] Marcel S. Pawlowski et al. Co-orbiting satellite galaxy structures are still in conflict with the distribution of primordial dwarf galaxies. *Mon. Not. Roy. Astron. Soc.*, 442(3):2362–2380, 2014.

[143] Till Sawala et al. The APOSTLE simulations: solutions to the Local Group's cosmic puzzles. *Mon. Not. Roy. Astron. Soc.*, 457(2):1931–1943, 2016.

[144] Azadeh Fattahi, Julio F. Navarro, Till Sawala, Carlos S. Frenk, Laura V. Sales, Kyle Oman, Matthieu Schaller, and Jie Wang. The cold dark matter content of Galactic dwarf spheroidals: no cores, no failures, no problem. 2016.

[145] Kyle A. Oman et al. The unexpected diversity of dwarf galaxy rotation curves. *Mon. Not. Roy. Astron. Soc.*, 452(4):3650–3665, 2015.

[146] Jose Oorbe, Michael Boylan-Kolchin, James S. Bullock, Philip F. Hopkins, Duan Ker?s, Claude-Andr Faucher-Gigure, Eliot Quataert, and Norman Murray. Forged in FIRE: cusps, cores, and baryons in low-mass dwarf galaxies. *Mon. Not. Roy. Astron. Soc.*, 454(2):2092–2106, 2015.

[147] Marcel S. Pawlowski, Benoit Famaey, David Merritt, and Pavel Kroupa. On the persistence of two small-scale problems in ΛCDM. *Astrophys. J.*, 815(1):19, 2015.

[148] Antonino Del Popolo and Morgan Le Delliou. Small scale problems of the ΛCDM model: a short review. *Galaxies*, 5(1):17, 2017.

[149] Jesper Sommer-Larsen and Alexandre Dolgov. Formation of disk galaxies: warm dark matter and the angular momentum problem. *Astrophys. J.*, 551:608–623, 2001.

[150] Paul Bode, Jeremiah P. Ostriker, and Neil Turok. Halo formation in warm dark matter models. *Astrophys. J.*, 556:93–107, 2001.

[151] David N. Spergel and Paul J. Steinhardt. Observational evidence for selfinteracting cold dark matter. *Phys. Rev. Lett.*, 84:3760–3763, 2000.

[152] Jesus Zavala, Mark Vogelsberger, and Matthew G. Walker. Constraining Self-Interacting Dark Matter with the Milky Way's dwarf spheroidals. *Mon. Not. Roy. Astron. Soc.*, 431:L20–L24, 2013.

[153] Miguel Rocha, Annika H. G. Peter, James S. Bullock, Manoj Kaplinghat, Shea Garrison-Kimmel, Jose Onorbe, and Leonidas A. Moustakas. Cosmological Simulations with Self-Interacting Dark Matter I: Constant Density Cores and Substructure. *Mon. Not. Roy. Astron. Soc.*, 430:81–104, 2013.

[154] Maxim Markevitch, A. H. Gonzalez, D. Clowe, A. Vikhlinin, L. David, W. Forman, C. Jones, S. Murray, and W. Tucker. Direct constraints on the dark matter self-interaction cross-section from the merging galaxy cluster 1E0657-56. *Astrophys. J.*, 606:819–824, 2004.

[155] Scott W. Randall, Maxim Markevitch, Douglas Clowe, Anthony H. Gonzalez, and Marusa Bradac. Constraints on the Self-Interaction Cross-Section of Dark Matter from Numerical Simulations of the Merging Galaxy Cluster 1E 0657-56. *Astrophys. J.*, 679:1173–1180, 2008.

[156] David Harvey, Richard Massey, Thomas Kitching, Andy Taylor, and Eric Tittley. The non-gravitational interactions of dark matter in colliding galaxy clusters. *Science*, 347:1462–1465, 2015.

[157] Mark Vogelsberger, Jesus Zavala, and Abraham Loeb. Subhaloes in Self-Interacting Galactic Dark Matter Haloes. *Mon. Not. Roy. Astron. Soc.*, 423:3740, 2012.

[158] Annika H. G. Peter, Miguel Rocha, James S. Bullock, and Manoj Kaplinghat. Cosmological Simulations with Self-Interacting Dark Matter II: Halo Shapes vs. Observations. *Mon. Not. Roy. Astron. Soc.*, 430:105, 2013.

[159] Abraham Loeb and Neal Weiner. Cores in Dwarf Galaxies from Dark Matter with a Yukawa Potential. *Phys. Rev. Lett.*, 106:171302, 2011.

[160] Sean Tulin, Hai-Bo Yu, and Kathryn M. Zurek. Resonant Dark Forces and Small Scale Structure. *Phys. Rev. Lett.*, 110(11):111301, 2013.

[161] Sean Tulin, Hai-Bo Yu, and Kathryn M. Zurek. Beyond Collisionless Dark Matter: Particle Physics Dynamics for Dark Matter Halo Structure. *Phys. Rev.*, D87(11):115007, 2013.

[162] Manoj Kaplinghat, Sean Tulin, and Hai-Bo Yu. Self-interacting Dark Matter Benchmarks. 2013.

[163] Manoj Kaplinghat, Sean Tulin, and Hai-Bo Yu. Direct Detection Portals for Self-interacting Dark Matter. *Phys. Rev.*, D89(3):035009, 2014.

[164] Xiaoyong Chu, Camilo Garcia-Cely, and Thomas Hambye. Can the relic density of self-interacting dark matter be due to annihilations into Standard Model particles? *JHEP*, 11:048, 2016.

[165] Eric D. Carlson, Marie E. Machacek, and Lawrence J. Hall. Self-interacting dark matter. *Astrophys. J.*, 398:43–52, 1992.

[166] Yonit Hochberg, Eric Kuflik, Tomer Volansky, and Jay G. Wacker. Mechanism for Thermal Relic Dark Matter of Strongly Interacting Massive Particles. *Phys. Rev. Lett.*, 113:171301, 2014.

[167] Nicolas Bernal, Xiaoyong Chu, Camilo Garcia-Cely, Thomas Hambye, and Bryan Zaldivar. Production Regimes for Self-Interacting Dark Matter. *JCAP*, 1603(03):018, 2016.

[168] Kimberly K. Boddy, Jonathan L. Feng, Manoj Kaplinghat, and Tim M. P. Tait. Self-Interacting Dark Matter from a Non-Abelian Hidden Sector. *Phys. Rev.*, D89(11):115017, 2014.

[169] Robyn Campbell, Stephen Godfrey, Heather E. Logan, Andrea D. Peterson, and Alexandre Poulin. Implications of the observation of dark matter self-interactions for singlet scalar dark matter. *Phys. Rev.*, D92(5):055031, 2015.

[170] Zhaofeng Kang. View FImP miracle (by scale invariance) la self-interaction. *Phys. Lett.*, B751:201–204, 2015.

[171] Seyed Yaser Ayazi, S. Mahdi Firouzabadi, and S. Peyman Zakeri. Freeze-in production of Fermionic Dark Matter with Pseudo-scalar and Phenomenological Aspects. *J. Phys.*, G43(9):095006, 2016.

[172] Rouven Essig, Jeremy Mardon, and Tomer Volansky. Direct Detection of Sub-GeV Dark Matter. *Phys. Rev.*, D85:076007, 2012.

[173] Rouven Essig, Marivi Fernandez-Serra, Jeremy Mardon, Adrian Soto, Tomer Volansky, and Tien-Tien Yu. Direct Detection of sub-GeV Dark Matter with Semiconductor Targets. *JHEP*, 05:046, 2016.

[174] Rouven Essig, Jeremy Mardon, Oren Slone, and Tomer Volansky. Detection of sub-GeV Dark Matter and Solar Neutrinos via Chemical-Bond Breaking. *Phys. Rev.*, D95(5):056011, 2017.

[175] Henri Ruegg and Marti Ruiz-Altaba. The Stueckelberg field. *Int. J. Mod. Phys.*, A19:3265–3348, 2004.

[176] C. Patrignani et al. Review of Particle Physics. *Chin. Phys.*, C40(10):100001, 2016.

[177] Lawrence J. Hall, Karsten Jedamzik, John March-Russell, and Stephen M. West. Freeze-In Production of FIMP Dark Matter. *JHEP*, 03:080, 2010.

[178] Paolo Gondolo and Graciela Gelmini. Cosmic abundances of stable particles: Improved analysis. *Nucl. Phys.*, B360:145–179, 1991.

[179] Clifford Cheung, Gilly Elor, Lawrence J. Hall, and Piyush Kumar. Origins of Hidden Sector Dark Matter I: Cosmology. *JHEP*, 03:042, 2011.

[180] Eugenio Del Nobile, Manoj Kaplinghat, and Hai-Bo Yu. Direct Detection Signatures of Self-Interacting Dark Matter with a Light Mediator. *JCAP*, 1510(10):055, 2015.

[181] Jim Alexander et al. Dark Sectors 2016 Workshop: Community Report. 2016.

[182] N. Fornengo, P. Panci, and M. Regis. Long-Range Forces in Direct Dark Matter Searches. *Phys. Rev.*, D84:115002, 2011.

[183] Tai Li, Sen Miao, and Yu-Feng Zhou. Light mediators in dark matter direct detections. *JCAP*, 1503(03):032, 2015.

[184] R. Agnese et al. Search for Low-Mass Weakly Interacting Massive Particles with SuperCDMS. *Phys. Rev. Lett.*, 112(24):241302, 2014.

[185] D. S. Akerib et al. Results from a search for dark matter in the complete LUX exposure. *Phys. Rev. Lett.*, 118(2):021303, 2017.

[186] D. S. Akerib et al. LUX-ZEPLIN (LZ) Conceptual Design Report. 2015.

[187] Jae Hyeok Chang, Rouven Essig, and Samuel D. McDermott. Revisiting Supernova 1987A Constraints on Dark Photons. *JHEP*, 01:107, 2017.

[188] Edward Hardy and Robert Lasenby. Stellar cooling bounds on new light particles: plasma mixing effects. *JHEP*, 02:033, 2017.

[189] Cameron Mahoney, Adam K. Leibovich, and Andrew R. Zentner. Updated Constraints on Self-Interacting Dark Matter from Supernova 1987A. *Phys. Rev.*, D96(4):043018, 2017.

[190] Demos Kazanas, Rabindra N. Mohapatra, Shmuel Nussinov, Vigdor L. Teplitz, and Yongchao Zhang. Supernova Bounds on the Dark Photon Using its Electromagnetic Decay. *Nucl. Phys.*, B890:17–29, 2014.

[191] Ermal Rrapaj and Sanjay Reddy. Nucleon-nucleon bremsstrahlung of dark gauge bosons and revised supernova constraints. *Phys. Rev.*, C94(4):045805, 2016.

[192] D. S. Akerib et al. Improved Limits on Scattering of Weakly Interacting Massive Particles from Reanalysis of 2013 LUX Data. *Phys. Rev. Lett.*, 116(16):161301, 2016.

[193] J. Barreto et al. Direct Search for Low Mass Dark Matter Particles with CCDs. *Phys. Lett.*, B711:264–269, 2012.

[194] R. Agnese et al. Search for Low-Mass Weakly Interacting Massive Particles Using Voltage-Assisted Calorimetric Ionization Detection in the SuperCDMS Experiment. *Phys. Rev. Lett.*, 112(4):041302, 2014.

[195] David Curtin, Rouven Essig, Stefania Gori, and Jessie Shelton. Illuminating Dark Photons with High-Energy Colliders. *JHEP*, 02:157, 2015.

[196] Hendrik Vogel and Javier Redondo. Dark Radiation constraints on minicharged particles in models with a hidden photon. *JCAP*, 1402:029, 2014.

[197] Peter W. Graham, David E. Kaplan, Surjeet Rajendran, and Prashant Saraswat. Displaced Supersymmetry. *JHEP*, 07:149, 2012.

[198] Nathaniel Craig, Andrey Katz, Matt Strassler, and Raman Sundrum. Naturalness in the Dark at the LHC. *JHEP*, 07:105, 2015.

[199] Eder Izaguirre and Brian Shuve. Multilepton and Lepton Jet Probes of Sub-Weak-Scale Right-Handed Neutrinos. *Phys. Rev.*, D91(9):093010, 2015.

[200] Brian Batell, Maxim Pospelov, and Brian Shuve. Shedding Light on Neutrino Masses with Dark Forces. *JHEP*, 08:052, 2016.

[201] Georges Aad et al. Search for long-lived, weakly interacting particles that decay to displaced hadronic jets in proton-proton collisions at $\sqrt{s} = 8$ TeV with the ATLAS detector. *Phys. Rev.*, D92(1):012010, 2015.

[202] John Paul Chou, David Curtin, and H. J. Lubatti. New Detectors to Explore the Lifetime Frontier. *Phys. Lett.*, B767:29–36, 2017.

[203] Richard H. Cyburt, Brian D. Fields, Keith A. Olive, and Tsung-Han Yeh. Big Bang Nucleosynthesis: 2015. *Rev. Mod. Phys.*, 88:015004, 2016.

[204] Karsten Jedamzik and Maxim Pospelov. Big Bang Nucleosynthesis and Particle Dark Matter. *New J. Phys.*, 11:105028, 2009.

[205] Donal O'Connell, Michael J. Ramsey-Musolf, and Mark B. Wise. Minimal Extension of the Standard Model Scalar Sector. *Phys. Rev.*, D75:037701, 2007.

[206] Maxim Pospelov, Adam Ritz, and Mikhail B. Voloshin. Secluded WIMP Dark Matter. *Phys. Lett.*, B662:53–61, 2008.

[207] Kai Schmidt-Hoberg, Florian Staub, and Martin Wolfgang Winkler. Constraints on light mediators: confronting dark matter searches with B physics. *Phys. Lett.*, B727:506–510, 2013.

[208] Jackson D. Clarke, Robert Foot, and Raymond R. Volkas. Phenomenology of a very light scalar (100 MeV ¡ $m_h$ ¡ 10 GeV) mixing with the SM Higgs. *JHEP*, 02:123, 2014.

[209] Vanda Silveira and A. Zee. SCALAR PHANTOMS. *Phys. Lett.*, 161B:136–140, 1985.

[210] James M. Cline, Kimmo Kainulainen, Pat Scott, and Christoph Weniger. Update on scalar singlet dark matter. *Phys. Rev.*, D88:055025, 2013. [Erratum: Phys. Rev.D92,no.3,039906(2015)].

[211] Peter Athron et al. Status of the scalar singlet dark matter model. *Eur. Phys. J.*, C77(8):568, 2017.

[212] G. Belanger, B. Dumont, U. Ellwanger, J. F. Gunion, and S. Kraml. Global fit to Higgs signal strengths and couplings and implications for extended Higgs sectors. *Phys. Rev.*, D88:075008, 2013.

[213] John R. Ellis, Mary K. Gaillard, and Dimitri V. Nanopoulos. A Phenomenological Profile of the Higgs Boson. *Nucl. Phys.*, B106:292, 1976.

[214] John R. Ellis, M. K. Gaillard, Dimitri V. Nanopoulos, and Christopher T. Sachrajda. Is the Mass of the Higgs Boson About 10-GeV? *Phys. Lett.*, 83B:339–344, 1979.

[215] Stuart Raby and Geoffrey B. West. The Branching Ratio for a Light Higgs to Decay Into $\mu^+\mu^-$ Pairs. *Phys. Rev.*, D38:3488, 1988.

[216] Tran N. Truong and R. S. Willey. Branching Ratios for Decays of Light Higgs Bosons. *Phys. Rev.*, D40:3635, 1989.

[217] Manuel Drees and Ken-ichi Hikasa. NOTE ON QCD CORRECTIONS TO HADRONIC HIGGS DECAY. *Phys. Lett.*, B240:455, 1990. [Erratum: Phys. Lett.B262,497(1991)].

[218] A. Djouadi, J. Kalinowski, and M. Spira. HDECAY: A Program for Higgs boson decays in the standard model and its supersymmetric extension. *Comput. Phys. Commun.*, 108:56–74, 1998.

[219] F. Bezrukov and D. Gorbunov. Light inflaton Hunter's Guide. *JHEP*, 05:010, 2010.

[220] M. B. Voloshin. Once Again About the Role of Gluonic Mechanism in Interaction of Light Higgs Boson with Hadrons. *Sov. J. Nucl. Phys.*, 44:478, 1986. [Yad. Fiz.44,738(1986)].

[221] H. Leutwyler and Mikhail A. Shifman. Light Higgs Particle in Decays of $K$ and $\eta$ Mesons. *Nucl. Phys.*, B343:369–397, 1990.

[222] John F. Donoghue, J. Gasser, and H. Leutwyler. The Decay of a Light Higgs Boson. *Nucl. Phys.*, B343:341–368, 1990.

[223] B. Hyams et al. $\pi\pi$ Phase Shift Analysis from 600-MeV to 1900-MeV. *Nucl. Phys.*, B64:134–162, 1973.

[224] Michael Spira. QCD effects in Higgs physics. *Fortsch. Phys.*, 46:203–284, 1998.

[225] John F. Gunion, Howard E. Haber, Gordon L. Kane, and Sally Dawson. The Higgs Hunter's Guide. *Front. Phys.*, 80:1–404, 2000.

[226] David McKeen. Constraining Light Bosons with Radiative Upsilon(1S) Decays. *Phys. Rev.*, D79:015007, 2009.

[227] Gary Steigman, Basudeb Dasgupta, and John F. Beacom. Precise Relic WIMP Abundance and its Impact on Searches for Dark Matter Annihilation. *Phys. Rev.*, D86:023506, 2012.

[228] Kim Griest and David Seckel. Three exceptions in the calculation of relic abundances. *Phys. Rev.*, D43:3191–3203, 1991.

[229] Viatcheslav F. Mukhanov. Nucleosynthesis without a computer. *Int. J. Theor. Phys.*, 43:669–693, 2004.

[230] Mark Srednicki, Richard Watkins, and Keith A. Olive. Calculations of Relic Densities in the Early Universe. *Nucl. Phys.*, B310:693, 1988.

[231] M. H. Reno and D. Seckel. Primordial Nucleosynthesis: The Effects of Injecting Hadrons. *Phys. Rev.*, D37:3441, 1988.

[232] Kazunori Kohri. Primordial nucleosynthesis and hadronic decay of a massive particle with a relatively short lifetime. *Phys. Rev.*, D64:043515, 2001.

[233] Masahiro Kawasaki, Kazunori Kohri, and Takeo Moroi. Big-Bang nucleosynthesis and hadronic decay of long-lived massive particles. *Phys. Rev.*, D71:083502, 2005.

[234] M. Kawasaki, Kazunori Kohri, and Naoshi Sugiyama. MeV scale reheating temperature and thermalization of neutrino background. *Phys. Rev.*, D62:023506, 2000.

[235] M. Kawasaki, Kazunori Kohri, and Naoshi Sugiyama. Cosmological constraints on late time entropy production. *Phys. Rev. Lett.*, 82:4168, 1999.

[236] A. D. Dolgov. Neutrinos in cosmology. *Phys. Rept.*, 370:333–535, 2002.

[237] Masahiro Kawasaki, Kazunori Kohri, and Takeo Moroi. Hadronic decay of late - decaying particles and Big-Bang Nucleosynthesis. *Phys. Lett.*, B625:7–12, 2005.

[238] Karsten Jedamzik. Big bang nucleosynthesis constraints on hadronically and electromagnetically decaying relic neutral particles. *Phys. Rev.*, D74:103509, 2006.

[239] John R. Ellis, Keith A. Olive, and Elisabeth Vangioni. Effects of unstable particles on light-element abundances: Lithium versus deuterium and He-3. *Phys. Lett.*, B619:30–42, 2005.

[240] Savas Dimopoulos, Rahim Esmailzadeh, Lawrence J. Hall, and G. D. Starkman. Is the Universe Closed by Baryons? Nucleosynthesis With a Late Decaying Massive Particle. *Astrophys. J.*, 330:545, 1988.

[241] Maxim Pospelov and Josef Pradler. Primordial beryllium as a big bang calorimeter. *Phys. Rev. Lett.*, 106:121305, 2011.

[242] Mykhailo Lisovyi, Andrii Verbytskyi, and Oleksandr Zenaiev. Combined analysis of charm-quark fragmentation-fraction measurements. *Eur. Phys. J.*, C76(7):397, 2016.

[243] R. Barate et al. A Measurement of the semileptonic branching ratio BR(b-baryon —¿ p lepton anti-neutrino X) and a study of inclusive pi+-, K+-, (p,anti-p) production in Z decays. *Eur. Phys. J.*, C5:205–227, 1998.

[244] Edward K. G. Sarkisyan, Aditya Nath Mishra, Raghunath Sahoo, and Alexander S. Sakharov. Multihadron production dynamics exploring the energy balance in hadronic and nuclear collisions. *Phys. Rev.*, D93:054046, 2016. [Addendum: Phys. Rev.D93,no.7,079904(2016)].

[245] Projections for measurements of Higgs boson signal strengths and coupling parameters with the ATLAS detector at a HL-LHC. Technical Report ATL-PHYS-PUB-2014-016, CERN, Geneva, Oct 2014.

[246] Daniel Enrique De Florian Sabaris, Christophe Grojean, Fabio Maltoni, Chiara Mariotti, Alexandre Nikitenko, Marco Pieri, Pierre Savard, Markus Schumacher, and Rei Tanaka. Handbook of LHC Higgs cross sections: 4. Deciphering the nature of the Higgs sector. Sep 2016.

[247] Nicolas Bernal and Xiaoyong Chu. $\mathbb{Z}_2$ SIMP Dark Matter. *JCAP*, 1601:006, 2016.

[248] Toru Kanzaki, Masahiro Kawasaki, Kazunori Kohri, and Takeo Moroi. Cosmological Constraints on Neutrino Injection. *Phys. Rev.*, D76:105017, 2007.

[249] A. D. Dolgov, S. H. Hansen, and D. V. Semikoz. Nonequilibrium corrections to the spectra of massless neutrinos in the early universe. *Nucl. Phys.*, B503:426–444, 1997.

[250] Peter W. Graham, David E. Kaplan, and Surjeet Rajendran. Cosmological Relaxation of the Electroweak Scale. *Phys. Rev. Lett.*, 115(22):221801, 2015.

[251] Thomas Flacke, Claudia Frugiuele, Elina Fuchs, Rick S. Gupta, and Gilad Perez. Phenomenology of relaxion-Higgs mixing. *JHEP*, 06:050, 2017.

[252] Abdelhak Djouadi. The Anatomy of electro-weak symmetry breaking. I: The Higgs boson in the standard model. *Phys. Rept.*, 457:1–216, 2008.

[253] A. Pich. Chiral perturbation theory. *Rept. Prog. Phys.*, 58:563–610, 1995.

[254] H. Leutwyler and Mikhail A. Shifman. GOLDSTONE BOSONS GENERATE PECULIAR CONFORMAL ANOMALIES. *Phys. Lett.*, B221:384–388, 1989.

[255] M. E. Carrington. The Effective potential at finite temperature in the Standard Model. *Phys. Rev.*, D45:2933–2944, 1992.

[256] Kari Enqvist, Sami Nurmi, Tommi Tenkanen, and Kimmo Tuominen. Standard Model with a real singlet scalar and inflation. *JCAP*, 1408:035, 2014.

[257] Michela D'Onofrio, Kari Rummukainen, and Anders Tranberg. Sphaleron Rate in the Minimal Standard Model. *Phys. Rev. Lett.*, 113(14):141602, 2014.

[258] Michela D'Onofrio and Kari Rummukainen. Standard model cross-over on the lattice. *Phys. Rev.*, D93(2):025003, 2016.

[259] Joakim Edsjo and Paolo Gondolo. Neutralino relic density including coannihilations. *Phys. Rev.*, D56:1879–1894, 1997.

[260] John M. Cornwall, David N. Levin, and George Tiktopoulos. Derivation of Gauge Invariance from High-Energy Unitarity Bounds on the s Matrix. *Phys. Rev.*, D10:1145, 1974. [Erratum: Phys. Rev.D11,972(1975)].

[261] Benjamin W. Lee, C. Quigg, and H. B. Thacker. Weak Interactions at Very High-Energies: The Role of the Higgs Boson Mass. *Phys. Rev.*, D16:1519, 1977.

[262] David J. Gross, Robert D. Pisarski, and Laurence G. Yaffe. QCD and Instantons at Finite Temperature. *Rev. Mod. Phys.*, 53:43, 1981.

[263] J. R. Espinosa, M. Quiros, and F. Zwirner. On the nature of the electroweak phase transition. *Phys. Lett.*, B314:206–216, 1993.

[264] O. K. Kalashnikov. Infrared behavior of the gluon polarization tensor at finite temperature. *Phys. Lett.*, B279:367–372, 1992.

[265] R. Mertig, M. Bohm, and Ansgar Denner. FEYN CALC: Computer algebraic calculation of Feynman amplitudes. *Comput. Phys. Commun.*, 64:345–359, 1991.

[266] Vladyslav Shtabovenko, Rolf Mertig, and Frederik Orellana. New Developments in FeynCalc 9.0. *Comput. Phys. Commun.*, 207:432–444, 2016.

[267] Ernestos N. Argyres, Wim Beenakker, Geert Jan van Oldenborgh, Ansgar Denner, Stefan Dittmaier, Jiri Hoogland, Ronald Kleiss, Costas G. Papadopoulos, and Giampiero Passarino. Stable calculations for unstable particles: Restoring gauge invariance. *Phys. Lett.*, B358:339–346, 1995.

[268] N. Kauer and D. Zeppenfeld. Finite width effects in top quark production at hadron colliders. *Phys. Rev.*, D65:014021, 2002.

[269] Christian Schwinn. *Gauge checks, consistency of approximation schemes and numerical evaluation of realistic scattering amplitudes*. PhD thesis, Wurzburg U., 2003.

[270] V. B. Berestetskii, E. M. Lifshitz, and L. P. Pitaevskii. *QUANTUM ELECTRODYNAMICS*, volume 4 of *Course of Theoretical Physics*. Pergamon Press, Oxford, 1982.

[271] T. Kinoshita. Mass singularities of Feynman amplitudes. *J. Math. Phys.*, 3:650–677, 1962.

[272] T. D. Lee and M. Nauenberg. Degenerate Systems and Mass Singularities. *Phys. Rev.*, 133:B1549–B1562, 1964. [,25(1964)].

[273] Eric Braaten and Tzu Chiang Yuan. Calculation of screening in a hot plasma. *Phys. Rev. Lett.*, 66:2183–2186, 1991.

[274] Per Elmfors, Kari Enqvist, and Iiro Vilja. Thermalization of the Higgs field at the electroweak phase transition. *Nucl. Phys.*, B412:459–478, 1994.

[275] J. R. Espinosa, D. Racco, and A. Riotto. A Cosmological Signature of the Standard Model Higgs Vacuum Instability: Primordial Black Holes as Dark Matter. 2017.

[276] D. J. Kapner, T. S. Cook, E. G. Adelberger, J. H. Gundlach, Blayne R. Heckel, C. D. Hoyle, and H. E. Swanson. Tests of the gravitational inverse-square law below the dark-energy length scale. *Phys. Rev. Lett.*, 98:021101, 2007.

[277] R. S. Decca, D. Lopez, E. Fischbach, G. L. Klimchitskaya, D. E. Krause, and V. M. Mostepanenko. Novel constraints on light elementary particles and extra-dimensional physics from the Casimir effect. *Eur. Phys. J.*, C51:963–975, 2007.

[278] Andrew A. Geraci, Sylvia J. Smullin, David M. Weld, John Chiaverini, and Aharon Kapitulnik. Improved constraints on non-Newtonian forces at 10 microns. *Phys. Rev.*, D78:022002, 2008.

[279] A. O. Sushkov, W. J. Kim, D. A. R. Dalvit, and S. K. Lamoreaux. New Experimental Limits on Non-Newtonian Forces in the Micrometer Range. *Phys. Rev. Lett.*, 107:171101, 2011.

[280] Gordan Krnjaic. Probing Light Thermal Dark-Matter With a Higgs Portal Mediator. *Phys. Rev.*, D94(7):073009, 2016.

[281] Federico Piazza and Maxim Pospelov. Sub-eV scalar dark matter through the super-renormalizable Higgs portal. *Phys. Rev.*, D82:043533, 2010.

[282] Rouven Essig, Eric Kuflik, Samuel D. McDermott, Tomer Volansky, and Kathryn M. Zurek. Constraining Light Dark Matter with Diffuse X-Ray and Gamma-Ray Observations. *JHEP*, 11:193, 2013.

[283] D. E. Gruber, J. L. Matteson, L. E. Peterson, and G. V. Jung. The spectrum of diffuse cosmic hard x-rays measured with heao-1. *Astrophys. J.*, 520:124, 1999.

[284] L. Bouchet, E. Jourdain, J. P. Roques, A. Strong, R. Diehl, F. Lebrun, and R. Terrier. INTEGRAL SPI All-Sky View in Soft Gamma Rays: Study of Point Source and Galactic Diffuse Emissions. *Astrophys. J.*, 679:1315, 2008.

[285] Elena Pierpaoli. Decaying particles and the reionization history of the universe. *Phys. Rev. Lett.*, 92:031301, 2004.

[286] Douglas P. Finkbeiner, Silvia Galli, Tongyan Lin, and Tracy R. Slatyer. Searching for Dark Matter in the CMB: A Compact Parameterization of Energy Injection from New Physics. *Phys. Rev.*, D85:043522, 2012.

[287] Vivian Poulin, Julien Lesgourgues, and Pasquale D. Serpico. Cosmological constraints on exotic injection of electromagnetic energy. *JCAP*, 1703(03):043, 2017.

[288] A. Kogut et al. The Primordial Inflation Explorer (PIXIE): A Nulling Polarimeter for Cosmic Microwave Background Observations. *JCAP*, 1107:025, 2011.

[289] J. Chluba and R. A. Sunyaev. The evolution of CMB spectral distortions in the early Universe. *Mon. Not. Roy. Astron. Soc.*, 419:1294–1314, 2012.

[290] Jens Chluba. Distinguishing different scenarios of early energy release with spectral distortions of the cosmic microwave background. *Mon. Not. Roy. Astron. Soc.*, 436:2232–2243, 2013.

[291] Jens Chluba and Donghui Jeong. Teasing bits of information out of the CMB energy spectrum. *Mon. Not. Roy. Astron. Soc.*, 438(3):2065–2082, 2014.

[292] Jens Chluba. Which spectral distortions does ΛCDM actually predict? *Mon. Not. Roy. Astron. Soc.*, 460(1):227–239, 2016.

[293] D. J. Fixsen, E. S. Cheng, J. M. Gales, John C. Mather, R. A. Shafer, and E. L. Wright. The Cosmic Microwave Background spectrum from the full COBE FIRAS data set. *Astrophys. J.*, 473:576, 1996.

[294] Gianpiero Mangano, Gennaro Miele, Sergio Pastor, Teguayco Pinto, Ofelia Pisanti, and Pasquale D. Serpico. Relic neutrino decoupling including flavor oscillations. *Nucl. Phys.*, B729:221–234, 2005.

[295] Alain Coc and Elisabeth Vangioni. Primordial nucleosynthesis. *Int. J. Mod. Phys.*, E26(08):1741002, 2017.

[296] Masahiro Kawasaki, Kazunori Kohri, Takeo Moroi, and Yoshitaro Takaesu. Revisiting Big-Bang Nucleosynthesis Constraints on Long-Lived Decaying Particles. 2017.

[297] Ryan J. Cooke, Max Pettini, Kenneth M. Nollett, and Regina Jorgenson. The primordial deuterium abundance of the most metal-poor damped Ly$\alpha$ system. *Astrophys. J.*, 830(2):148, 2016.

[298] Steen Hannestad and Jes Madsen. Neutrino decoupling in the early universe. *Phys. Rev.*, D52:1764–1769, 1995.

[299] Mark Hindmarsh and Owe Philipsen. WIMP dark matter and the QCD equation of state. *Phys. Rev.*, D71:087302, 2005.

[300] Szabocls Borsanyi, Zoltan Fodor, Christian Hoelbling, Sandor D. Katz, Stefan Krieg, and Kalman K. Szabo. Full result for the QCD equation of state with 2+1 flavors. *Phys. Lett.*, B730:99–104, 2014.

[301] Najmul Haque, Aritra Bandyopadhyay, Jens O. Andersen, Munshi G. Mustafa, Michael Strickland, and Nan Su. Three-loop HTLpt thermodynamics at finite temperature and chemical potential. *JHEP*, 05:027, 2014.

[302] Szabolcs Borsanyi, Gergely Endrodi, Zoltan Fodor, Antal Jakovac, Sandor D. Katz, Stefan Krieg, Claudia Ratti, and Kalman K. Szabo. The QCD equation of state with dynamical quarks. *JHEP*, 11:077, 2010.

[303] Y. Aoki, G. Endrodi, Z. Fodor, S. D. Katz, and K. K. Szabo. The Order of the quantum chromodynamics transition predicted by the standard model of particle physics. *Nature*, 443:675–678, 2006.